INVESTIGATION OF ANOMALOUS ELECTRON PHENOMENA IN THE ACCELERATION REGION OF A HALL EFFECT THRUSTER VIA LASER THOMSON SCATTERING

A Dissertation
Presented to
The Academic Faculty

by

Julian Lopez-Uricoechea

In Partial Fulfillment
of the Requirements for the Degree
Doctor of Philosophy in the
School of Aerospace Engineering

Georgia Institute of Technology
August 2026

INVESTIGATION OF ANOMALOUS ELECTRON PHENOMENA IN THE ACCELERATION REGION OF A HALL EFFECT THRUSTER VIA LASER THOMSON SCATTERING

Approved by:

Dr. Mitchell L. R. Walker, Advisor
School of Aerospace Engineering
Georgia Institute of Technology

Dr. Wensheng Huang
Electric Propulsion Group
NASA Glenn Research Center

Dr. Sedina Tsikata
School of Aerospace Engineering
Georgia Institute of Technology

Dr. Vernon Chaplin
Electric Propulsion Group
Jet Propulsion Laboratory

Dr. Wenting Sun
School of Aerospace Engineering
Georgia Institute of Technology

Date Approved: July 21, 2026

ACKNOWLEDGEMENTS

Primero, a mis papás, muchas gracias por todo el apoyo que siempre me han dado. Mamá, gracias por ese mes que estuviste en Atlanta mientras estudiaba para los exámenes. Papá, gracias por siempre estar pendiente de mí. Adelaida, gracias también por el apoyo, por siempre querer estar al día de mi progreso, y por los consejos al principio con la escritura.

To my labmates, thank you for making this an unforgettable experience and for making this all possible. David, thank you for being so welcoming at the beginning and for teaching me so much. Truly the big brother of the lab, in every meaning. Jean Luis, thank you for teaching me everything about Thomson and for tolerating me while teaching me how to use a wrench. See you in the DMV! Chhavi, thank you showing me that I didn't know flow features to the point that I needed ice cream and for your daily flow features examples. Naia, I'm very proud of our teamwork during this last test campaign amidst all the challenges. I couldn't have done it without you. Muhannad, you'll probably disagree with whatever I say, but I hope we continue our long conversations. Thank you for always making yourself available to help and for your well-timed naps. Adrian, thank you for being such a great and patient teacher in all the stuff that you taught me. So many memories, some are a blur, but those few months holed up in that office together studying for quals were something. Will, thank you for all your annoyingly tough questions while we were studying for quals, for always being willing to help around the lab, and for being a great friend outside the lab. Janice, thank you for teaching me how to put on a flange! Arega, as much as you tried to explain your problems with CNTs, I still don't think I understand. Stay safe in your car and thank you so much! Jacob, thank you for tolerating my (and others') refusal to learn Labview, for being our dungeon master, and for engaging in our physics discussions that rarely reached a satisfying conclusion. Hope to see you in the DMV! Richeek, thank you for being so helpful and curious. This work wouldn't have been possible without you. We've probably had too many all-nighters at the lab. Good luck with Thomson! Ebise, Devin, and Trevor, good luck!

Professor Walker, thank you for all the support and guidance you've given me throughout the entire process. Dan, thank you for your help around the lab, and I think you were the first person to suggest I make 2-D measurements for the drift velocity. Jeremy, I don't think any of the projects I did in the lab would have been possible without you, so thank you so much! To everyone on the committee, thank you for reviewing my work and for helping me improve it. Wensheng, thank you for your help these last three years and for welcoming me at GRC last summer. Your input throughout was essential.

This work was supported by a NASA Space Technology Graduate Research Opportunity (No. 80NSSC23K1217)

TABLE OF CONTENTS

SUMMARY

The main goal of this work was to provide a better understanding of anomalous electron momentum transport along magnetic field lines in a Hall effect thruster (HET) for the purpose of improving the predictive capabilities of simulations regarding HET lifetime. Along the way, we were also able to investigate anomalous electron heating, anomalous electron heat flux, and nonequilibrium electron phenomena. The study was carried out experimentally with a magnetically shielded HET and with incoherent laser Thomson scattering (ILTS) as the plasma diagnostic. We developed an ILTS data processing method that directly quantifies the electron nonequilibrium through the skew and excess and kurtosis of the electron velocity distribution function (EVDF). We also developed a solver to quantify anomalous electron momentum transport and anomalous electron heating with ILTS measurements in a HET. The HET was operated with a low discharge voltage to push the acceleration region outside of the HET channel, which allowed us to make a 2-D (axial-radial) map of ILTS measurements the azimuthal (EVDF) across the entire acceleration region.

Regarding the variation of the anomalous electron Hall parameter along magnetic field lines, we found that it was not constant along magnetic field lines, was not proportional to the azimuthal electron drift velocity along magnetic field lines, and could not be described by existing closure models. Regarding anomalous electron heat flux, we confirmed previous experimental and simulation findings that the electron temperature is not constant along magnetic field lines, indicating that the classical conductive electron heat flux does not apply along magnetic field lines. Regarding anomalous electron heating, we found that for the five different heat flux models used, the anomalous electron heating cannot be described by

anomalous resistive heating. Regarding electron nonequilibrium, we measured significant departures from equilibrium, with both the skew and excess kurtosis of the azimuthal EVDF being nonzero in the upstream region of the acceleration region. While significant attention has been given to anomalous electron momentum transport in the attempt to develop predictive HET simulations, we have found that anomalous electron heating and electron nonequilibrium are also present in the acceleration region of a HET, indicating that they need to be accounted for in predictive HET simulations.

CHAPTER 1. Introduction

1.1. Orbital Mechanics Background

The two most important performance parameters of an in-space propulsion device are thrust and specific impulse (I_{sp}). This is because thrust and I_{sp} are closely tied to the change in velocity, ΔV, required to perform a certain orbital maneuver. While thrust determines how fast a ΔV is achieved and which types of orbital maneuvers are possible, I_{sp} determines the amount of propellant mass needed to achieve the ΔV of a certain orbital maneuver. Importantly, as shown in Section 1.2, the choice of propulsion device is essentially a choice between a high-thrust, low-I_{sp} device and a low-thrust, high-I_{sp} device.

In high-thrust orbital maneuvers, thrust is the dominant force acting on the spacecraft, such that all external forces, including gravity, can be neglected [1]. In this case, one can derive the ideal rocket equation, which states that for a maneuver with a given ratio of the propellant mass used in the maneuver, m_p, to the final spacecraft mass without the used propellant, m_f, the ΔV is given by

$$\Delta V = I_{sp} g_0 \ln\left(1 + \frac{m_p}{m_f}\right), \tag{1-1}$$

where g_0 is the standard acceleration due to gravity. Alternatively, for a high-thrust maneuver of a given ΔV, $\frac{m_p}{m_f}$ is given by

$$\frac{m_p}{m_f} = \exp\left(\frac{\Delta V}{g_0 I_{sp}}\right) - 1. \tag{1-2}$$

High-thrust devices are often used for impulsive maneuvers, which assume that the ΔV is achieved instantaneously. The most common type of orbital transfer that uses impulsive maneuvers is the Hohmann transfer.

In low-thrust orbital maneuvers, gravity is no longer negligible [1], and there is no general closed-form expression, like Eq. 1-1, that relates $\Delta V, I_{sp},$ and $\frac{m_p}{m_f}$. The most common type of low-thrust orbital maneuver is the spiral transfer between two orbits. The analysis of a spiral trajectory can often be approximated by representing the transfer as a circular orbit with a slowly changing radius and with a constant thrust being applied tangential to the orbit [1]. It turns out that in this approximation, Eqs. 1-1 and 1-2 hold for orbit raising using a low-thrust spiral transfer [1]. This is because, in this approximation, the acceleration due to gravity is purely radial and is perpendicular to the thrust and orbital velocity vectors, such that gravity plays no role in the acceleration of the spacecraft. Consequently, Eqs. 1-1 and 1-2 serve as useful approximations for low-thrust maneuvers. to illustrate the benefits of high-I_{sp} propulsion devices, even when low-thrust maneuvers are used.

However, it is important to note that optimal low-thrust orbital transfers require a higher ΔV, which we will call ΔV_{LT}, than the Hohmann transfer between the same two orbits. For an orbital transfer between two circular orbits with radii R_1 and $R_2 = 10R_1$, the ΔV is approximately 30% higher for the optimal low-thrust transfer when compared to the Hohmann transfer [2]. For orbital transfers between two circular orbits with radii R_1 and $R_2 > 1000R_1$, the ΔV of the optimal low-thrust transfer approaches twice that of the Hohmann transfer [2]. Also, depending on the optimization constraints, the increase in ΔV for optimal low-thrust transfer to Mars can be less than double the Δv of the corresponding Hohmann transfers shown in Table 1 [3]. As a result, we can use Eqs. 1-1 and 1-2 to illustrate the benefits of low-thrust, high-I_{sp} devices where we take $\Delta V_{LT} = 2\Delta V$ to be the worst-case corrected low-thrust ΔV when compared to a high-thrust transfer.

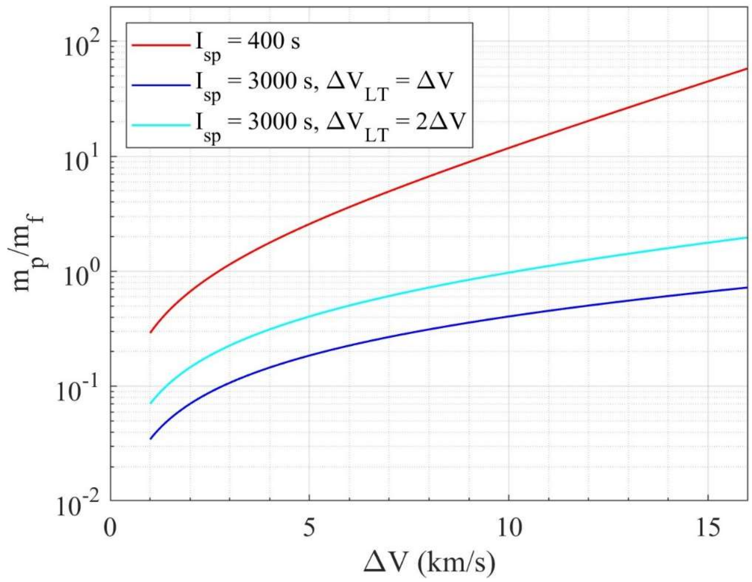

Figure 1-1: Comparison of m_p/m_f as a function of ΔV between low-I_{sp} devices and high-I_{sp} devices, ΔV is representative of the ΔV required for a given high-thrust orbital transfer. 400 s is representative of the I_{sp} in chemical propulsion devices, and 3000 s is representative of the I_{sp} in electric propulsion devices. Two cases are shown for the high-I_{sp} case: one that assumes the same ΔV for low-thrust and high-thrust orbital transfers, and one that assumes that low-thrust orbital transfers require twice the ΔV as high-thrust orbital transfers.

Eq. 1-2 illustrates that for a given destination orbit, a higher I_{sp} exponentially decreases the required propellant mass, as shown in Fig. 1-1. As a result, as ΔV increases, the mass savings from high-I_{sp} devices increase. The propellant mass savings due to high I_{sp} has similar implications for the planning of orbital transfers or satellite station-keeping. The propellant mass savings provide mission planners with two options: either they can use the large mass savings to decrease the total mass of the spacecraft and thus significantly decrease launch costs, or they can maintain the same initial mass of the spacecraft and instead carry more equipment and instrumentation onboard. Also, when multiple launches are required to send cargo to a destination, a reduction in propellant mass can increase the cargo mass per launch and thus decrease the number of launches required to deliver a set amount of cargo. Consequently, one of the main benefits of high-I_{sp} propulsion devices is the savings on launch costs due to the reduction in propellant mass.

Eq. 1-1 illustrates that for a given $\frac{m_p}{m_f}$, the ΔV increases linearly with I_{sp}. From Table 1, we can see that orbital transfers to further orbits generally require a larger ΔV. As a result, high-I_{sp} propulsion devices can enable science missions to a wider variety of destination orbits than their low-I_{sp} counterparts. In addition, for satellite station-keeping, the required ΔV can be budgeted annually to account for drag of the residual atmosphere and for gravitational perturbations due to Earth's oblateness and the gravity of the Sun and the Moon. Consequently, the lifetime of a satellite scales linearly with I_{sp}, which can decrease the launch costs of replacing satellites.

Table 1: ΔV of various Hohmann transfers

Orbital Transfer	ΔV (km/s) for Hohmann transfer
LEO to GEO	3.90 [1]
LEO to Lunar orbit	3.96 [4]
Earth orbit to Mercury orbit	17.14 [5]
Earth orbit to Venus orbit	5.20 [5]
Earth orbit to Mars orbit	5.59 [5]
Earth orbit to Jupiter orbit	14.44 [5]
Earth orbit to Saturn orbit	15.73 [5]
Earth orbit to Uranus orbit	15.94 [5]
Earth orbit to Neptune orbit	15.71 [5]

1.2. Types of In-Space Propulsion

The three main types of in-space propulsion are chemical propulsion, nuclear thermal propulsion, and electric propulsion (EP). We will briefly summarize chemical propulsion and nuclear thermal propulsion and will go into further detail on EP, which is the focus of this thesis.

1.2.1. Chemical Propulsion

Chemical propulsion consists of using combustion reactions to heat a gas that is then accelerated through a converging-diverging nozzle. The high thermal energy in the combustion chamber is converted into directed kinetic energy through the converging-diverging nozzle, such that the exhaust velocity scales approximately as $\sqrt{\frac{T_c}{M}}$, where T_c is the combustion chamber temperature, and M is the mass of the propellant. I_{sp} is then related to the exhaust velocity by $u_{ex} = g_0 I_{sp}$. The key limitation on the I_{sp} of chemical propulsion devices is that the propellant is the source of both the chemical energy released by the combustion reactions and of the gas that is accelerated. T_c is higher for heavier molecules, such that a low molecular weight tends to be sacrificed in favor of high combustion temperatures, with common choices of oxidizer and fuel being oxygen and hydrogen or oxygen and methane. Therefore, the I_{sp} of chemical propulsion devices is fundamentally limited by the temperature that can be reached through combustion reactions and is practically limited by material considerations, such that the combustion chamber temperature in chemical propulsion engines can be as high as around 3500 K [6]. Consequently, chemical propulsion is characterized by a low I_{sp} but can produce high thrust, with the state-of-the-art SpaceX's Starship capable of an I_{sp} of around 400 s and a thrust of around 15 MN. As such, chemical propulsion is the preferred choice of propulsion for launch vehicles and for missions to the Moon and has also been considered for crewed missions to Mars. Chemical propulsion devices have also been used on science missions to the outer solar system by using gravity-assist maneuvers, most famously in the Voyager 1, Voyager 2, and Cassini missions.

1.2.2. Nuclear Thermal Propulsion

Nuclear thermal propulsion (NTP) consists of flowing the propellant through a nuclear fission reactor to heat a gas that is then accelerated through a converging-diverging nozzle. The acceleration principle is the same as that of chemical propulsion, but, in NTP, the nuclear reactor is the energy source. As a result, to maximize I_{sp}, NTP systems usually use hydrogen as the propellant. Even though the reactor could theoretically heat the hydrogen to temperatures significantly higher than the combustion temperatures in chemical propulsion, the temperature of the hydrogen in an NTP device is limited by material temperature limits of around 2500 K in the reactor-heat exchanger [6,7]. As a result, current NTP systems are limited to an I_{sp} of around 900 s [8]. While an NTP system has not flown yet, NASA has plans to test an NTP system with a thrust as high as 67 kN [8]. As a result, NTP is being considered for decreasing the travel time for crewed missions to Mars and for science missions to the outer solar system.

1.2.3. Electric Propulsion

There are many variants of EP devices that can be categorized as electrothermal, electrostatic, or electromagnetic devices. As in NTP, the energy source is separate from the propellant in EP devices. Electrothermal devices use electrical power to heat a gas passing through a converging-diverging nozzle, and state-of-the-art systems can provide as high as I_{sp} of around 1400 s and thrust of around 4 N [9] at 100 kW of electrical power. Electrostatic and electromagnetic devices use electrical power to generate an ionized gas from the propellant and to generate electrostatic or electromagnetic forces, respectively, to accelerate the charged particles. Electrostatic and electromagnetic forces are able to accelerate charged particles to significantly higher exit velocities such that EP can offer significantly higher I_{sp} than chemical propulsion and

NPT. State-of-the-art electrostatic systems can offer as high as either around 3 N of thrust and 3000 s of I_{sp} at 70 kW of electrical power for Hall effect thrusters (HETs) or around 450 mN of thrust and 7500 s of I_{sp} at 20 kW of electrical power for gridded ion engines (GIEs) [9]. In electrostatic devices, the I_{sp} is so high that the devices can afford to lower the I_{sp} by using heavy propellants such as xenon to increase the thrust. Because of the high I_{sp}, electric propulsion is the most common type of propulsion used on satellites, has been used on Dawn and Deep Space 1 science missions to the outer solar system, and is planned to be used as the propulsion system for the Lunar Gateway space station.

While EP can offer high I_{sp}, increasing the thrust of an EP device comes at the cost of increased electrical power requirement. As a result, EP systems are limited by the state-of-the-art in-space electrical power systems. While solar power of 100 kW would allow EP to be used for cargo transportation to Mars as support for crewed missions to Mars, space nuclear reactors would enhance EP capabilities in the outer solar system and enable EP for crewed missions to Mars. However, significant development in EP technology is still needed to take advantage of anticipated advances in in-space power systems. Electromagnetic devices are not flight-qualified and need significant development, but they are promising technologies for high-power EP of 100 kW and above. Flight-qualified EP systems have not exceeded 10s of kW of electrical power, and in this range of powers, GIEs and HETs are the most mature EP technology.

1.2.3.1. Gridded Ion Engines

GIEs operate with three distinct stages: the ionized gas is generated in the ionization chamber; ions are then extracted and accelerated through the acceleration grids; and an external cathode then emits electrons to create a neutral exhaust such that the spacecraft does not become negatively charged. Importantly, the acceleration grids only extract ions, such that a finite space-charge develops between the acceleration grids. Due to the Child-Langmuir law, there is then a limit on the amount of ion current density that can be extracted by the acceleration grids [10]. Because of this limit on the current density and vacuum breakdown limitations on the voltage between the acceleration grids, the thrust of GIEs can only be increased by increasing the cross-sectional area of the device [10]. There are then practical limits on the size of GIEs such that GIEs are not suitable for generating high thrust.

1.2.3.2. Hall Effect Thrusters

While the discharges generated by HETs have different regions, there are no definitive boundaries separating these regions that preferentially extract either ions or electrons. The discharge thus remains quasi-neutral everywhere away from the surfaces such that space-charge effects do not limit the acceleration mechanism in a HET. As a result, HETs can achieve higher thrust densities than GIEs and are thus better suited for scaling to high power than GIEs. The thrust scales approximately as $\dot{m}_{anode}\sqrt{V_d}$, the discharge current scales approximately linearly with $\dot{m}_{anode}$, and the discharge power is given as $P_d = V_d I_d$. Consequently, it is preferred to increase the thrust by increasing the mass flow rate to maintain a constant thrust-to-power ratio. However, increasing the mass flow rate with a given geometry of the discharge channel increases the current density, which directly reduces the operational lifetime of a HET [11].

Understanding a HET's lifetime is an important part of flight qualification to ensure that the HET can last the duration of the planned mission. While recent developments have significantly increased the lifetime of HETs [13] and thus facilitated high current density operation of HETs [16], HETs have not been flight-qualified at high current densities. One of the major challenges in designing next-generation HETs is that the complex physics governing HET operation is not well understood.

1.3. Operating Principles of Hall Effect Thrusters

1.3.1. Fundamentals of HET Operating Principles

Because of the high I_{sp} of HETs, HET flight heritage, and the potential for even higher power HET operation, this work will focus on HETs. A notional schematic of a conventional HET with a center-mounted cathode is shown in Fig. 1-2. The main components of a HET are the following: an annular discharge channel with a black plate that acts as the anode electrode and through which most of the propellant is fed; a hollow cathode that emits electrons that sustain the discharge by ionizing the neutral propellant and that neutralize the plume; a magnetic circuit that establishes a magnetic field that is predominantly radial near the channel exit plane and whose radial component peaks near the channel exit plane. A DC discharge voltage, V_d, is applied between the anode and the cathode, and a DC discharge current, I_d, of electrons exits the cathode and is collected by the anode. Because of the applied radial magnetic field, an axial electric field is established and peaks near the exit plane of the discharge channel that accelerates the ions for thrust. The HET discharge constitutes a plasma, and so to understand the basics of HET operating principles, it is necessary to understand some basic plasma physics.

A plasma consists of positively and negatively charged particles and can include neutral particles. When averaged over large enough length scales and time scales, the plasma can be assumed to be quasi-neutral, that is that the charge density of positively charged particles and negatively charged particles are approximately equal. In HETs, these limiting scales for quasi-neutrality are around 70 μm and 25 ps. Also, because a plasma consists of charged particles,

particles can exert forces on each other over large distances, and particle motion is coupled to local electric and magnetic fields; this behavior is called collective behavior. In fact, collective behavior is essential for maintaining quasi-neutrality because if there were a charge imbalance such that there were locally more ions than electrons, this would locally increase the electrostatic potential, which would attract electrons and restore quasi-neutrality. While other plasma parameters play a role in maintaining quasineutrality, the plasma potential can be thought of as the local electrostatic potential necessary to maintain quasineutrality.

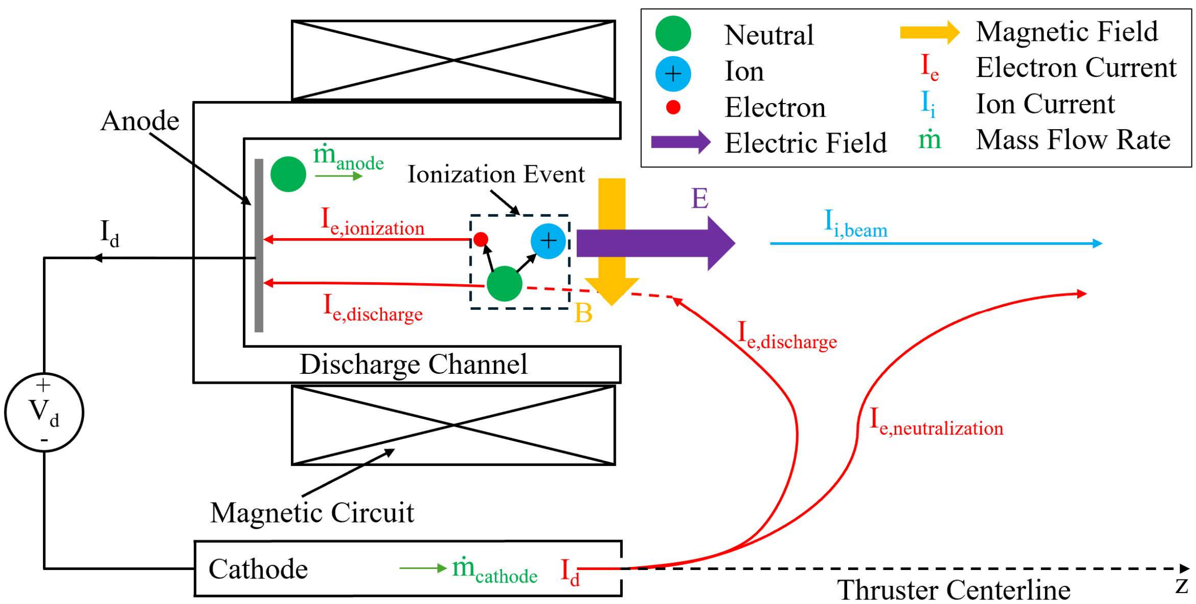

Figure 1-2: Schematic of the operating principles of Hall effect thruster

Returning to Fig. 1-2, once fully accelerated, the beam of ions carries the ion beam current, $I_{i,beam}$. To maintain quasineutrality in the plume, a part of the electron current emitted from the cathode, $I_{e,neutralization}$, which is equal and opposite to $I_{i,beam}$ goes into the plume. The remaining electron current emitted from the cathode, $I_{e,discharge}$, enters the discharge channel, provides the seed electrons for the ionization events inside the discharge channel, and eventually reaches the anode. We will call this part of the electron current the discharge electron current as a nonzero $I_{e,discharge}$ is needed to sustain the HET discharge. The electrons produced inside the discharge channel from the ionization events backstream toward the anode and must contribute an electron current, $I_{e,ionization}$, at the anode equal to the ion beam current to maintain quasineutrality.

It is important to note that while the discharge electron current does not directly contribute to thrust since it backstreams towards the anode, this electron current is necessary to sustain the discharge. This produces an inherent inefficiency in HETs because part of the discharge power must go to sustaining the plasma instead of entirely producing thrust; this inefficiency is quantified using the current utilization efficiency, $\frac{I_{i,beam}}{I_d} = 1 - \frac{I_{e,discharge}}{I_d}$ [17]. Another important inefficiency in HETs is the voltage utilization efficiency, which arises because the average ion in the plume is not accelerated by the entire discharge voltage [17]. The underlying physics that cause the inefficiencies in the current utilization and in the voltage utilization will be introduced in the next section.

1.3.2. Hall Effect Thruster as a Cross-Field Discharge

Because the magnetic field and electric field are predominantly perpendicular to each other, the HET discharge is classed as a cross-field discharge and contains rich but poorly understood physics [18]. Without the applied magnetic field, the strongest electric fields would be in the regions by the anode and cathode surfaces with a strong space charge, which are called sheaths. This would produce little thrust as the ions would be predominantly accelerated into the cathode instead of axially away from the thruster. To understand the physics governing HET operation, it is thus critical to understand how the magnetic field establishes a strong axial electric field that efficiently accelerates the ions to produce thrust.

In standard HET operation, the magnetic field strength is set such that the electrons are magnetized and that the ions are unmagnetized. Because of this, HET discharges are considered partially magnetized plasmas. Assuming negligible particle inertia, magnetized particles gyrate around magnetic field lines at the cyclotron frequency (or gyrofrequency) and with an orbit the size of a Larmor radius. In a HET, the maximum electron cyclotron frequency, ω_{ce}, is typically around 3 GHz and the maximum electron Larmor radius, r_{Le}, is typically around 1 mm. Electrons are considered magnetized because their Larmor radius is significantly smaller than the width of the discharge channel, while ions are considered unmagnetized because their Larmor radius is significantly larger than the channel width.

Due to the magnetic $q\vec{u} \times \vec{B}$ force, forces perpendicular to the magnetic field generate particle drifts for magnetized particles in the direction mutually perpendicular to the force and the magnetic field. For a general force, $\vec{\xi}$, the resultant particle drift is [19]

$$\vec{u}_{drift} = \frac{\vec{\xi} \times \vec{B}}{qB^2}, \tag{1-3}$$

where $\vec{B}$ is the magnetic field, B is the magnetic field strength, and q is the charge of the particle. For example, considering an annular coordinate system, a radial magnetic field, and magnetized electrons, as in a HET, an axial force produces an azimuthal electron drift velocity, and an azimuthal force produces an axial electron drift velocity.

In a HET, an axial electric field thus produces an azimuthal electron drift velocity responsible for the eponymous Hall current, and electron collisions that dampen electron motion in the azimuthal direction are the dominant contribution to the backstreaming axial electron drift velocity that is responsible for the current inefficiency in a HET. Analytically, these drift velocities can be written as

$$u_{ExB} = \frac{E_z}{B_r} \tag{1-4}$$

$$u_{ez,\nu} = \frac{u_{e\theta}}{\Omega_e}, \tag{1-5}$$

where

$$\Omega_e \equiv \frac{\omega_{ce}}{\nu_e} \tag{1-6}$$

is the electron Hall parameter, ν_e is the total electron collision frequency, $\omega_{ce} \equiv \frac{eB}{m_e}$, e is the elementary charge, and m_e is the electron mass. It is important to note that in a HET, $u_{e\theta} \gg u_{ez}$ generally holds, such that it can be said that the electron motion from the cathode to the anode is mostly redirected into the azimuthal direction. As a result, the discharge current is significantly less when there is an applied magnetic field compared to the case with no magnetic field.

If the only axial force on electrons we consider is the Lorentz force, we can write $u_{e\theta} = u_{ExB}$, and if the only azimuthal forces on electrons we consider are the magnetic force and the force from collisional damping, we can write $u_{ez} = u_{ez,\nu}$. We can then rewrite Eqs. 1-4 and 1-5 to arrive at a common approximation [20] for the axial electric field in a HET,

$$E_z = \frac{e u_{ez} B^2}{m_e \nu_e}, \tag{1-7}$$

which is a simplified version of the axial component of generalized Ohm's law in a HET [20].

Taking the axial derivative of Eq. 1-7 and neglecting the azimuthal and radial of the electric field, we arrive at an expression in the form of Gauss's law, where the sources of an axial electric field are $\frac{\partial B^2}{\partial z}$, $\frac{\partial u_{ez}}{\partial z}$, and $-\frac{\partial \nu_e}{\partial z}$. Therefore, we expect the axial electric field to increase in regions where the magnetic field strength and backstreaming velocity of electrons increase and where the electron collision frequency decreases. From Eq. 1-7, we can now say that due to particle drifts, an axial varying radial component of the magnetic field with a strong peak can produce a strong axial electric field. It is then no surprise that the magnetic circuit of HETs indeed produces an axially varying radial component of the magnetic field with a strong peak.

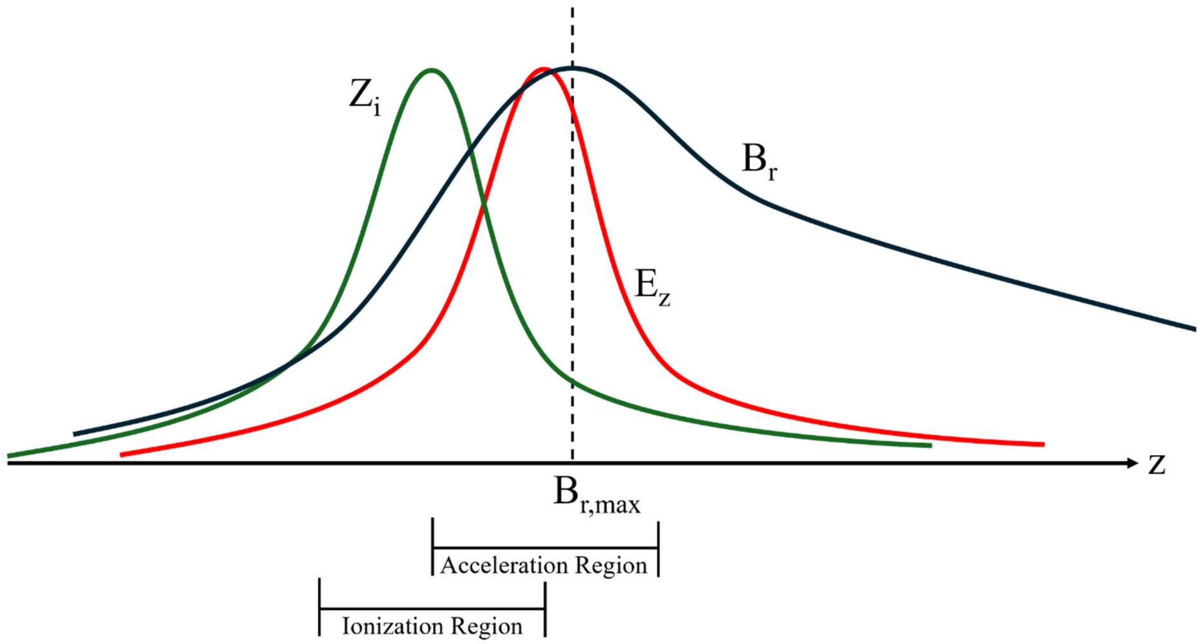

Figure 1-3: Notional axial variations in a HET of the radial magnetic field strength (B_r), axial electric field strength (E_z), and ionization rate (Z_i). Approximate locations of the acceleration region and the ionization region are denoted.

Experimental measurements in HETs observe that a strong electric field exists over a narrow region whose axial location and axial width depend on various operating conditions, including the location of the peak magnetic field [12-15], magnetic field strength, and discharge voltage [14,21,22]. This region exhibits most of the potential drop seen by the ions and is thus traditionally called the acceleration region, or acceleration zone. It is important to note for this work that the acceleration region shifts substantially downstream at low discharge voltages and for magnetically shielded HETs (MS-HET). Upstream of the acceleration region is the ionization region, defined as the region with a strong ionization rate. The ionization rate is proportional to the product of the electron density, neutral density, and the ionization reaction rate, and, for the range of electron temperatures in a HET, it increases with an increase in electron temperature. Consequently, the extent of the ionization region is limited downstream because the neutral density is mostly depleted after the ionization region and is limited upstream due to the low electron temperature and low electron density near the anode.

Per Eq. 1-7, the relative positions of the ionization and acceleration regions depend on the axial profiles of the ionization rate, magnetic field strength, electron collision frequency, and axial electron velocity. The ionization and acceleration regions are known to overlap, as shown in Fig. 1-3, which, combined with the fact that each axial location in the acceleration region has different plasma potential, means that ions are produced at locations with a different potential. A notional potential profile along the channel centerline of a HET is shown in Fig. 1-4. In a HET, an ion's acceleration potential is given by

$$\phi_{acc} = \phi_{prod} - \phi_{plume}, \tag{1-8}$$

where ϕ_{prod} is the local plasma potential where the ion is produced and ϕ_{plume} is the plasma potential in the plume, as shown in Fig. 1-4. As such, the further downstream an ion is produced, the smaller its acceleration potential and the lower its velocity in the plume, which is given by

$$u_{i,ex} = \sqrt{\frac{2e\phi_{acc}}{m_i}}, \tag{1-9}$$

where m_i is the mass of the ion. Also, the plume potential is greater than the cathode potential such that the plume can attract enough electrons to ensure a quasi-neutral plume. For these reasons, the average ion velocity in the plume, $\langle u_{i,ex} \rangle$, corresponds to an average acceleration potential, $\langle \phi_{acc} \rangle$, that is less than the discharge voltage, resulting in a voltage utilization efficiency of $\langle \phi_{acc} \rangle / V_d$. Thrust is also directly related to the average ion velocity in the plume through

$$T = \dot{m}_{i,ex} \langle u_{i,ex} \rangle, \tag{1-10}$$

where $\dot{m}_{i,ex}$ is the mass flow rate of ions in the plume. Thus, the exact values of the thrust and the voltage utilization efficiency are strongly dependent on the axial profiles of the ionization rate, magnetic field strength, electron collision frequency, and axial electron velocity.

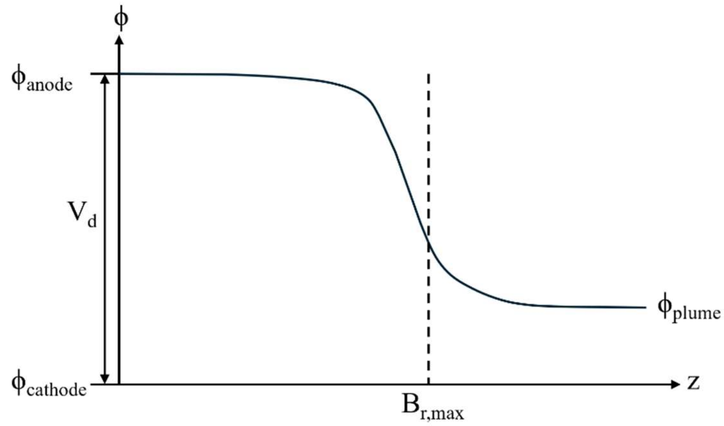

Figure 1-4: Notional axial potential profile across the channel centerline of a HET

1.4. Challenges with Predicting HET Performance

For an EP device, the three critical performance parameters are discharge power, thrust, and lifetime. In a HET where the discharge voltage and mass flow rate are known, the discharge power can be calculated from the discharge current, and the I_{sp} can be calculated from the thrust and mass flow rate. Also, in a HET, erosion rates of surfaces that protect the magnetic circuit from the discharge are a measure of the thruster lifetime.

Ideally, if HET simulations could accurately predict the discharge current, thrust, and erosion rates at various operating conditions, then the design of HETs could be robustly optimized computationally. However, given only a HET's operating condition, state-of-the-art HET simulations cannot reproduce the measured discharge current, thrust, or erosion rates. Instead, expensive test campaigns must be carried out to flight-qualify every new HET design. Lifetime qualification tests are the most time-consuming and most expensive parts of developing EP, as long-lifetime tests can take 1000s of hours [23-26], and accelerated lifetime tests can take 100s of hours [27]. For clarity, the operating condition is defined by the thruster parameters that are directly controlled when operating a given HET, such as discharge voltage, mass flow rate, magnetic field strength, magnetic field topology, flow fraction between anode and cathode, and electrical configuration of the thruster body. A given HET is then specified by the channel geometry, thruster materials exposed to the plasma, cathode properties, and position and orientation of the cathode. Environmental conditions that influence facility-thruster coupling in ground testing or space-thruster coupling in space flight should also be considered when predicting thruster performance.

1.4.1. Experimental Evidence of Anomalous Momentum Electron Transport

It was first noted by Ref. 28 in a conference in 1962 that the discharge electron current in a HET discharge was higher than that predicted by classical electron collisions. Shortly after, Ref. 29 published the results from Ref. 28 and showed that the discharge electron current could be as much as 100 times higher than that predicted by classical electron collisions. More than 60 years of research have since been dedicated to improving the understanding of the physical mechanisms behind this enhanced electron current, dubbed anomalous electron momentum transport, and to incrementally improving HET performance through extensive testing. An experimental inference of the axial profile of the electron Hall parameter later showed that classical electron collisions could only account for the measurements near the anode [30]. As a result, to accurately predict the discharge current and thrust, HET simulations must be able to accurately model the axial profile of the effective electron collision frequency, ν_e.

1.4.2. Overview of Techniques to Infer the Effective Electron Collision Frequency

It is important to clarify the difference between a measurement and an inference of ν_e in a HET. A measurement of ν_e would require a plasma diagnostic that directly calculate ν_e from a raw measurement of the plasma. To our knowledge, the only plasma diagnostic capable of such a measurement is terahertz time-domain spectroscopy (THz-TDS), however THz-TDS is yet to be used on a HET. An inference of ν_e is done by measuring other plasma properties and using the governing equations of a HET plasma to calculate ν_e from the measured plasma properties. To date, all experimental values of ν_e have been inferences.

To evaluate models of ν_e it is necessary to have accurate measurements of ν_e. Initial inferences of the axial profile of the electron Hall parameter relied heavily on measurements of electrostatic probes [30, 31]. However, for measurements in a HET, electrostatic probes have three main drawbacks. First, probes are directly inserted into the plasma and are known to perturb the plasma [32,33], possibly changing the plasma properties that are measured and thus making the measurements ambiguous. Second, theories used to extract plasma properties from the raw data of electrostatic probe measurements do not fully account for the effects of a magnetic field [34-36]. Third, probes are quickly damaged in regions of high electron temperature, which makes probe measurements in regions of high electron temperature challenging [37,38]. The second and third drawbacks are particularly important when considering measurements in the acceleration region of a HET, since this region contains the highest electron temperatures and the strongest magnetic fields. Given the importance of ν_e in establishing the electric field per Eq. 1-7, it is crucial to have the ability to make unambiguous inferences of ν_e in the acceleration region. This can be achieved with laser diagnostics, which can make noninvasive measurements of plasma properties that do not perturb the plasma and that do not depend on the magnetic field.

Recent efforts to infer the effective electron collision frequency have used noninvasive laser diagnostics. While some techniques have been able to empirically infer the effective collision frequency from predominantly noninvasive laser diagnostics of a HET discharge [39,40], semi-empirical techniques have combined noninvasive measurements with simulations to obtain a profile of ν_e that results in the best match between these calibrated simulations and the measured discharge current, thrust, and axial profile of the average ion velocity [41,42]. The main benefit of obtaining semi-empirical profiles of the effective electron collision frequency from calibrated simulations is that the semi-empirical profiles are accompanied by values of all the other plasma properties. This allows for the comparison between the semi-empirical profile and models of the effective electron collision frequency that depend on the local plasma properties [43-49].

However, these calibrated simulations that match the measured discharge current and thrust do not consistently reproduce the measured erosion rates [50] and do not self-consistently reproduce the exact LIF measurements [41,42,51]. Although anomalous electron momentum transport does influence erosion rates in a HET [41,52], other anomalous phenomena are thought to also influence HET lifetime [53-55]. The lack of self-consistency points to some missing physics in the uncalibrated plasma properties that may also explain why the simulations do not reproduce the measured erosion rates. If some of the uncalibrated plasma properties are inaccurate within a supposedly calibrated simulation, then models for the anomalous electron collision frequency cannot be properly checked against the semi-empirical profile. This is because a correct model would not match the semi-empirical profile if some of the uncalibrated plasma properties are inaccurate. Therefore, to advance the understanding of anomalous electron momentum transport, it is critical to make measurements of plasma properties that, when directly inputted into a HET simulation, self-consistently reproduce the measured values of discharge current and thrust.

1.5. Overview of Research

1.5.1. Research Question

As will be discussed in more detail in Section 3.3, we have identified that the lack of self-consistency of state-of-the-art calibrated simulations can be partially attributed to the fact that these 2-D simulations are calibrated with 1-D measurements. Because 2-D simulations are calibrated with 1-D measurements, a model is used to extrapolate the values of the anomalous electron collision frequency along the channel centerline to those off-centerline. The model is typically employed in a manner that is equivalent to assuming that the anomalous electron Hall parameter, Ω_{ea}, is constant along magnetic field lines. However, this model has not been experimentally validated. Alternatively, from Eq. 1-5, if the axial electron drift velocity is constant, then the electron Hall parameter is only proportional to the azimuthal electron drift velocity. While the axial electron current density and electron density are known to vary radially, the validity of assuming a constant axial electron drift velocity along magnetic field lines is unknown. However, if in the axial electron drift velocity is in fact constant along magnetic field lines, it would lead to a simplified model for the variation of the electron Hall parameter along magnetic field lines. As such, our research question is the following:

> In a HET, is the anomalous electron Hall parameter directly proportional to the azimuthal electron drift velocity along magnetic field lines?

1.5.2. Research Hypothesis

As will be expanded upon in Section 2.2, it is widely believed that anomalous momentum transport in HETs is due to plasma turbulence. If so, Ω_{ea} should be the same in two locations if the characteristics of the turbulence are the same in the two locations. However, the local characteristics of the plasma turbulence should depend on the local plasma properties. In addition, we expect the azimuthal electron drift velocity to vary along magnetic field lines and hypothesize that the axial electron drift velocity is constant along magnetic field lines, such that our research hypothesis is the following:

> In a HET, the anomalous electron Hall parameter is directly proportional to the azimuthal electron drift velocity along magnetic field lines.

1.5.3. Thesis Outline

The purpose of this is to elucidate some of the physics that is not captured by the previous techniques of inferring the effective electron Hall parameter. We plan to use incoherent laser Thomson scattering (ILTS) to make a 2-D map of noninvasive measurements of electron properties and to obtain a 2-D map of the anomalous electron Hall parameter by calibrating a HET simulation with the ILTS measurements. Chapter 2 reviews the theory of anomalous electron phenomena in HETs and analyzes several common assumptions made in HET research. After this review, Chapter 3 evaluates techniques that have been used to infer the electron Hall parameter and identifies avenues to improve these state-of-the-art techniques. Chapter 4 presents the research question, research hypothesis in more detail, along with an overview and justification of the methodology. The experimental and inference methodology are described in Chapter 5 and 6, respectively. Chapter 7 presents and discusses the experimental measurements and the inference results. Lastly, Chapter 8 summarizes the research contributions and discusses suggested future work.

CHAPTER 2. Background: Review of Anomalous Electron Phenomena in the Acceleration Region of HETs

In this chapter, we will discuss different theories of anomalous electron transport, and we will scrutinize several common assumptions used in electron fluid simulations of HETs. This will shed light on the plasma properties that are closely tied to certain anomalous electron phenomena and will clarify which electron phenomena should not be neglected in the fluid formulation of electrons. By the end of this chapter, we will have developed the framework necessary to evaluate the assumptions made by state-of-the-art techniques used to infer the electron Hall parameter and to develop a new technique for inferring the electron Hall parameter. The chapter is structured as follows: Section 2.1 presents a physical description of classical electron transport; Section 2.2 presents an overview of different theories of anomalous electron momentum transport and analyzes the electron momentum equation; Section 2.3 analyzes the electron energy equation in the context of anomalous electron heating; and Sections 2.4 discusses sources of anomalous electron transport due to electron nonequilibrium effects..

2.1. Introduction to Cross-Field Electron Transport

To understand anomalous cross-field electron transport, it is necessary to first understand classical electron transport in a partially magnetized plasma. We first qualitatively describe electron transport for unmagnetized electrons before continuing to the case of magnetized electrons. Among the various types of electron transport (Fick's law, Ohm's law, Fourier's law, Soret effect, Peltier effect, and Dufour effect), we will focus on Ohm's law, which is associated with the transport coefficient of mobility, since it is the most relevant transport effect for anomalous electron current in a HET.

2.1.1. Physical Picture of Classical Electron Mobility

In this section, we will present a qualitative picture of classical electron mobility from the point of view of single-particle motion, first in an unmagnetized plasma and then in a magnetized plasma. Collisions between electrons conserve electron momentum, so classical electron transport in plasma is governed by electron collisions with neutrals and ions. Because of the large difference in mass between electrons and atoms, collisions of electrons with neutrals and ions effectively bring electrons to a halt. With this in mind, we can qualitatively derive the transport coefficients of electron mobility for unmagnetized and magnetized electrons. For conciseness, we summarize the different types of electron collisions and their respective equations in Appendix A. We note that the physical description of electron transport is often made through the diffusion coefficient and is treated as a random walk process [19]. However, because electron mobility is the dominant contribution to electron transport in a HET, we will focus on the physical description of electron mobility.

2.1.1.1. Mobility of Unmagnetized Electrons

Electron mobility is defined as the transport coefficient that describes the ability of the electrons to move through an electric field. If only electrostatic acceleration is considered, then we can write

$$\vec{u}_e = -\mu_e \vec{E}, \tag{2-1}$$

where $\vec{u}_e$ is the electron drift velocity, μ_e is the electron mobility, and $\vec{E}$ is the electric field. To understand the physical principle behind electron mobility, we consider the time-interval between electron momentum-transfer collisions of time τ_c. If an electric field is present, then in this time-interval, the equation of motion of an electron is

$$m_e \frac{\partial \vec{u}_e}{\partial t} = -e\vec{E}. \tag{2-2}$$

Taking the average of Eq. 2-2 over the time interval of time τ_c and recalling that the initial electron velocity in this time interval is zero, we find that

$$\vec{u}_{e,f} = -\frac{\tau_c e\langle \vec{E} \rangle}{m_e}, \tag{2-3}$$

where $\vec{u}_{e,f}$ is the final velocity in this time interval and $\langle \, \rangle$ denotes a time-averaged quantity. Noting that the average time-interval between collisions is the inverse of the electron collision frequency, ν_e, we can qualitatively recover the definition of the mobility for unmagnetized electrons,

$$\mu_e = \frac{e}{m_e \nu_e}. \tag{2-4}$$

Physically, collisions prevent the free acceleration of electrons due to an electric field. Consequently, we recover an expected inverse relation between the electron mobility and the electron collision frequency.

2.1.1.2. Mobility of Magnetized Electrons

To understand the mobility of magnetized electrons, we again consider the motion of a single electron in the time interval between two collisions. Considering only the Lorentz force, the equation of motion of the electron is

$$m_e \frac{\partial \vec{u}_e}{\partial t} = -e\left(\vec{E} + \vec{u} \times \vec{B}\right). \tag{2-5}$$

The magnetic force term creates the well-known gyration of electrons in the plane perpendicular to the magnetic field. Also, the combination of the electric and magnetic fields creates a drift velocity given by

$$\vec{u}_{E\times B} = \frac{\vec{E}\times\vec{B}}{B^2} \tag{2-6}$$

that is superimposed onto the electron gyrating motion.

If we consider the motion perpendicular to a static magnetic field in the z-direction and only consider a static electric field in the x-direction, then Eq. 2-5 can be decomposed into

$$m_e \frac{\partial u_{ex}}{\partial t} = -eE + eu_{ey}B \tag{2-7a}$$

$$m_e \frac{\partial u_{ey}}{\partial t} = -eu_{ex}B \tag{2-7b}$$

Even though the electron will start with zero velocity right after the collision, it will immediately begin to gyrate in the x-y plane and will accelerate up to its drift velocity of $u_{E\times B}$ in the y-direction within the first gyration. Averaging Eq. 2-7 over the time interval between collisions, we find that

$$u_{ex,f} = -\frac{e\tau_c}{m_e}\left(E - \langle u_{ey}\rangle B\right) \tag{2-8a}$$

$$u_{E\times B} = -\frac{eB}{m_e}\tau_c\langle u_{ex}\rangle, \tag{2-8b}$$

where we used the facts that $u_{ey}(0) = 0$ and that if τ_c is greater than the gyration period, then $u_{ey}(\tau_c) = u_{E\times B}$. If we further assume that the gyrofrequency is much greater than the collision frequency, then $u_{ex,f} \approx \langle u_{ex}\rangle$ and $u_{E\times B} \approx \langle u_{ey}\rangle$, such that Eq. 2-8b can be substituted into Eq. 2-8a to get

$$\langle u_{ex}\rangle = -\frac{e\tau_c}{m_e}\left(E + \frac{eB}{m_e}\tau_c\langle u_{ex}\rangle B\right). \tag{2-9}$$

If we substitute in the definition for ω_{ce}, then we can rearrange Eq. 2-9 to solve for $\langle u_{ex}\rangle$ and arrive at

$$\langle u_{ex}\rangle = -\frac{\mu_e E}{1+\Omega_e^2}. \tag{2-10}$$

With the previous assumption that $\omega_{ce} \gg \nu_e$ such that $\Omega_e \gg 1$, we find that Eq. 2-10 reduces to

$$\langle u_{ex}\rangle = -\frac{e\nu_e E}{m_e\omega_{ce}^2}, \tag{2-11}$$

such that collisions enhance electron motion in the direction perpendicular to magnetic field, which is the opposite effect of collisions for unmagnetized electrons. If we were to carry out the analysis, we would also find that there are different effective electron mobilities in the different directions, and the electron mobility is unaffected by the magnetic field in the direction parallel to the magnetic field.

To try to explain the physical interpretation of our derivation of cross-field electron transport in terms of guiding center drifts, we note that the electron inertia plays a critical role in our derivation. Thus, the enhanced cross-field transport can be interpreted as an inertia drift, which can be tied to the polarization drift due to a time-varying electric field [56]. An explanation for why collisions cause a polarization drift is because if $\vec{E} = \vec{u}_e \times \vec{B}$, where $\vec{u}_e$ is the average velocity of electrons, then constant collisions will cause periodic small dips in $\vec{u}_e$ and thus also in $\vec{E}$. The electric field will remain strong enough to reestablish the drift of the electrons that had collided, and so $\vec{u}_e$ will begin to increase and so will $\vec{E}$, thus causing a time-varying electric field and the polarization drift.

2.1.2. Fluid Formulation of Electron Transport in a Cross-Field Discharge

It will be useful to first define some terminology of the cross-field coordinate system that is often used to analyze cross-field discharges with 2-D magnetic fields like conventional HETs. The cross-field coordinate system is defined locally by three directions: the parallel-field direction, the cross-field direction, and the E×B direction. The parallel-field direction, denoted by unit vector $\hat{\beta}_{\parallel} \equiv \frac{\vec{B}}{B}$, is the direction parallel to the magnetic field. The E×B direction, denoted by unit vector $\hat{\beta}_{\vartheta} \equiv \frac{\vec{E}\times\hat{\beta}}{E}$, is in the direction parallel to the E×B velocity. For a magnetic field in the r-z plane, $\hat{\beta}_{\vartheta}$ is always $\pm\hat{\theta}$, where $\hat{\theta}$ is the cylindrical azimuthal unit vector and the sign of $\hat{\beta}_{\vartheta} \cdot \hat{\theta}$ depends on the sign of the magnetic field in the cylindrical coordinate system. The cross-field direction, denoted by unit vector $\hat{\beta}_{\perp} = \hat{\beta}_{\parallel} \times \hat{\beta}_{\vartheta}$, is the direction perpendicular to the magnetic field, within the r-z plane. We note that the E×B direction is sometimes referred to as the cross-field direction, as the name “cross-field discharge” is due to crossed electric and magnetic fields. However, cross-field transport often refers to the transport across the magnetic field lines, which is why we choose to call $\hat{\beta}_{\perp}$ the cross-field direction. In addition, we define the cross-field plane as the plane perpendicular to the magnetic field, defined locally by $\hat{\beta}_{\vartheta}$ and $\hat{\beta}_{\perp}$. Quantities related to the cross-field direction will be denoted as $A_{\hat{\perp}}$, while quantities related to the cross-field plane will be denoted as $A_{\perp}$. Figures 2-1 and 2-2 help visualize the cross-field coordinate system.

In partially magnetized plasmas, it is often appropriate to treat the electrons as their own fluid, separate from the ions. For electrons to be able to be approximated as a fluid, their local thermal relaxation time must be significantly smaller than the characteristic time for electrons to pass through regions with gradients in fluid properties. The collisional thermal relaxation time of electrons is the inverse of the electron-electron Coulomb collision frequency, ν_{ee}, given in in Eq.

A-2. The region in a HET with the most gradients is the acceleration region. Given characteristic values of electron density and electron temperature found in the acceleration region of a HET of 10^{17} m^{-3} and 30 eV, we find that ν_{ee} is approximately 100 kHz. Next, using a characteristic length of the acceleration region of 1 cm and characteristic value of the electron drift velocity in the cross-field direction of around 10 km/s, we find that the characteristic time for electrons to pass through the acceleration region is 1 μs $< \nu_{ee}^{-1}$. Consequently, collisions are not expected to maintain the thermal equilibrium of electrons as they traverse the acceleration region.

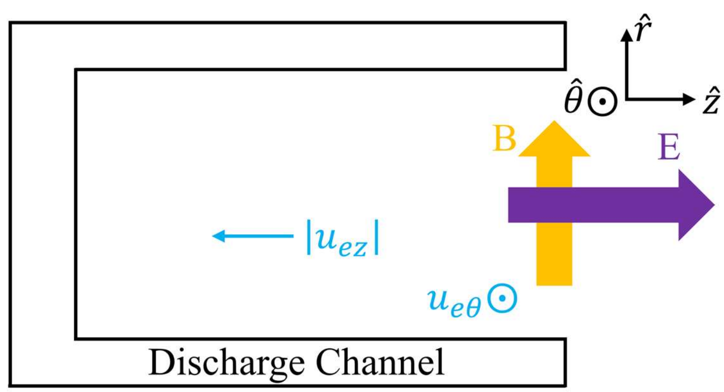

Figure 2-1: Basic schematic of electric, magnetic, and electron velocity fields in a HET discharge channel.

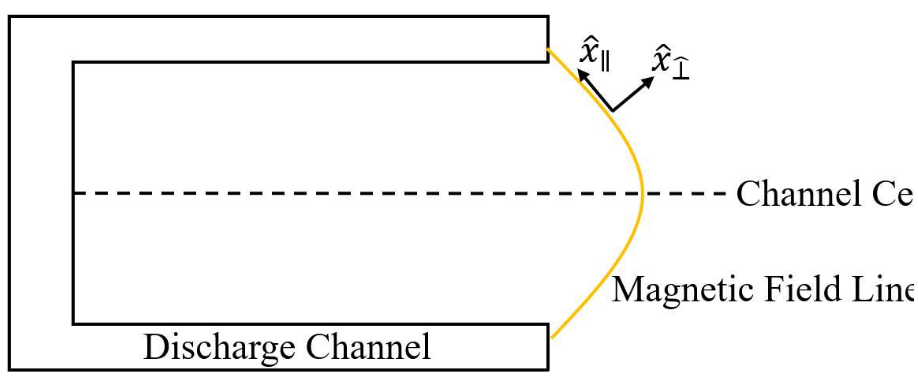

Figure 2-2: Basic schematic of cross-field coordinate system

Regarding experimental evidence, measurements of the EVDF in the parallel-field direction have not shown significant departures from an equilibrium EVDF. However, for the azimuthal EVDF, measurements in the acceleration region of one HET showed no significant departures from thermal equilibrium [40], while measurements in the acceleration region of another HET showed clear departures from an equilibrium EVDF [22]. This shows that while the fluid formulation might be better in certain HETs or operating conditions, the fluid formulation can be used as a general approximation, which is unexpected given the low electron-electron collision frequency in the acceleration region. This phenomenon of anomalous thermal equilibrium of electrons has been observed in space plasmas, and it is generally thought to be caused by plasma instabilities [57].

In addition, because ω_{ce} is the dominant frequency that governs quasineutral electron dynamics in a HET and $E_{\perp} \gg E_{\parallel}$ in a HET, the most general equilibrium electron pressure tensor in the cross-field coordinate system is [58]

$$\vec{\vec{P}}_e = \begin{bmatrix} p_{e\perp} & 0 & 0 \\ 0 & p_{e\perp} & 0 \\ 0 & 0 & p_{e\parallel} \end{bmatrix}, \tag{2-12}$$

where we have aligned $\hat{\beta}_{\parallel}$ with the third index. Assuming an ideal gas law for electrons, this also creates anisotropic terms for the electron temperature, $T_{e\perp}$ and $T_{e\parallel}$. The isotropization in the cross-field plane can be explained through gyromotion, as motion in one direction within the cross-field plane will lead to motion in all directions in the cross-field plane. Thus, the anisotropic relaxation time in the cross-field plane is ω_{ce}^{-1}, which is around 1 GHz with a magnetic field strength of 100 G. Because 1 μs ≫ ω_{ce}^{-1}, isotropic random electron motion in the cross-field direction is a good assumption. Lastly, we note that the fluid equations are derived from taking up to second-order moments of the Boltzmann equation and by providing a closure for third-order moments of the EVDF. In theory, infinitely many moments of the kinetic Boltzmann equation would be able to fully represent non-equilibrium phenomena [59], but this representation of kinetic effects is not practical. However, systems of up to fourth-order moment equations of the Boltzmann equation have been used to successfully model non-equilibrium electron phenomena [60,61], but these methods have yet to be extended for simulations in a HET.

Now that we have established that the fluid picture of electrons is a good approximation in HETs, the electron momentum equation assuming only a single species of singly charged ions is given by

$$\begin{aligned} m_e n_e \frac{\partial \vec{u}_e}{\partial t} + m_e n_e (\vec{u}_e \cdot \nabla)\vec{u}_\mathrm{e} \\ = -e n_e\left(\vec{E} + \vec{u}_\mathrm{e} \times \vec{B}\right) - \nabla \cdot \vec{\vec{P}}_e - m_e n_e \nu_{en} \vec{u}_\mathrm{e} - m_e n_e \nu_{iz} \vec{u}_\mathrm{e} \\ - m_e n_e \nu_{ei}^m (\vec{u}_e - \vec{u}_i) \end{aligned} , \qquad (2\text{-}13)$$

where ν_{en} is the electron-neutral momentum-transfer collision frequency, ν_{iz} is the ionization frequency, and ν_{ei}^m is the electron-ion momentum-transfer collision frequency. Assuming steady state and negligible electron inertia due to the small electron mass, we can neglect the left-hand side of Eq. 2-13 and solve for $\vec{u}_e$, such that

$$\vec{u}_\mathrm{e} = -\frac{e}{m_e(\nu_{en}+\nu_{ei})}\left(\vec{E} + \vec{u}_e \times \vec{B}\right) - \frac{\nabla \cdot \vec{\vec{P}}_e}{m_e n_e (\nu_{en}+\nu_{ei})} + \frac{\nu_{ei}^m}{\nu_{en}+\nu_{ei}} \vec{u}_i, \qquad (2\text{-}14)$$

where we note that the magnetic field couples the different components of $\vec{u}_e$.

Assuming azimuthal symmetry, which enforces $E_\vartheta = -\partial_\vartheta \phi = 0$, and negligible azimuthal ion momentum, the $\hat{\beta}_\vartheta$ component of Eq. 2-14 is

$$u_{e\vartheta} = -\frac{e}{m_e\nu_c}u_{e\hat{\perp}}B = -\Omega_c u_{e\hat{\perp}}, \tag{2-15}$$

where we define $\nu_c = \nu_{en} + \nu_{ei}^m$ as the classical electron collision frequency, and $\Omega_c = \frac{\omega_{ce}}{\nu_c}$. Negligible azimuthal ion momentum is an appropriate assumption because the ions are unmagnetized. Using Eq. 2-15, the component of Eq. 2-14 in the cross-field direction can be written as

$$u_{e\hat{\perp}} = -\frac{e}{m_e\nu_c}\left(E_{\hat{\perp}} + \Omega_c u_{e\hat{\perp}}B\right) - \frac{e\,\partial_{\hat{\perp}}\left(T_{eV,\perp}n_e\right)}{m_e n_e \nu_c} + \frac{\nu_{ei}^m}{\nu_c}u_{i\hat{\perp}}, \tag{2-16}$$

where we have substituted in Eq. 2-12 for the pressure tensor. Rearranging to solve for $u_{e\hat{\perp}}$, we find that

$$u_{e\hat{\perp}} = -\frac{\Omega_c}{\left(1+\Omega_c^2\right)}\frac{E_{\hat{\perp}}}{B} - \frac{\Omega_c}{\left(1+\Omega_c^2\right)}\frac{\partial_{\hat{\perp}}\left(T_{eV,\perp}n_e\right)}{Bn_e} + \frac{\nu_{ei}^m}{\nu_c\left(1+\Omega_c^2\right)}u_{i\hat{\perp}}. \tag{2-17}$$

In addition, the parallel-field component of Eq. 2-14 is

$$u_{e\parallel} = -\frac{e}{m_e\nu_c}E_{\parallel} - \frac{e\,\partial_{\parallel}\left(T_{eV,\parallel}n_e\right)}{m_e n_e \nu_c} + \frac{\nu_{ei}^m}{\nu_c}u_{i\parallel}. \tag{2-18}$$

Comparing Eqs. 2-17 and 2-18, we see that collisions dampen parallel-field motion and enhance cross-field motion, as we showed in Section 2.1.1.2.

To understand the fluid interpretation of this enhanced cross-field transport, we need to return to Eqs. 2-15 and 2-16. Using Eq. 2-15 and rearranging Eq. 2-16 to solve for $u_{e\vartheta}$, we find that

$$u_{e\vartheta} = \frac{E_{\hat{\perp}}}{B} + \frac{\partial_{\hat{\perp}}\left(T_{eV,\perp}n_e\right)}{n_e B} + \frac{u_{e\hat{\perp}}}{\Omega_c} - \frac{m_e\nu_{ei}u_{i\hat{\perp}}}{eB}, \tag{2-19}$$

and rearranging Eq. 2-15 to solve for $u_{e\hat{\perp}}$, we find that

$$u_{e\hat{\perp}} = -\frac{u_{e\vartheta}}{\Omega_c}. \tag{2-20}$$

Eqs. 2-19 and 2-20 are simply made of drift velocities, and we can write

$$u_{e\hat{\perp}}\hat{\beta}_{\perp} + u_{e\vartheta}\hat{\beta}_{\vartheta} = \frac{\vec{E}\times\vec{B}}{B^2} + \frac{\nabla\cdot\vec{\vec{P}}_e\times\vec{B}}{en_eB^2} + \frac{m_e\nu_c\vec{u}_e\times\vec{B}}{eB^2} + \frac{m_e\nu_{ei}\vec{u}_i\times\vec{B}}{eB^2}, \tag{2-21}$$

where $\frac{\vec{E}\times\vec{B}}{B^2}$ is the E×B drift velocity ($v_{E\times B}$), $\frac{\nabla\cdot\vec{\vec{P}}_e\times\vec{B}}{en_eB^2}$ is the diamagnetic electron drift velocity ($v_{\nabla p_e}$), and the second two terms are electron drift velocities due to electron-neutral and electron-ion collisions. Consequently, in a magnetized plasma of a HET, cross-field forces cause an azimuthal electron drift velocity, and azimuthal forces cause a cross-field electron drift velocity. We can then conclude that if we assume azimuthal symmetry and negligible electron inertia, then the enhanced classical cross-field electron transport in a magnetized plasma corresponds to the drift velocity that arises from collisions that dampen the azimuthal electron motion.

2.2. Anomalous Electron Momentum Transport in HETs

The cause of anomalous electron momentum transport is widely believed to be due to plasma turbulence and electron-wall collisions. Electron shear and anomalous electron temperatures can also play a role in anomalous electron momentum transport. In addition, while this section focuses on cross-field electron transport, we will also briefly cover the contributions of the magnetic mirror force and the centrifugal (or swirl) force to the parallel-field electron momentum equation. In this section, we will present the theory of how these phenomena can cause anomalous electron momentum transport and review the experimental and theoretical evidence of each phenomenon. In addition, because electron shear, the magnetic mirror force, and the centrifugal force are often neglected in HET simulations, we will provide an order of magnitude analyses to check the approximate significance of each phenomenon.

2.2.1. Electron Transport Due to Plasma Turbulence

Turbulence can be described as the chaotic final state of instabilities following the initial growth of instabilities at certain length and time scales and the subsequent saturation of the instabilities across a wide range of scales. Plasma turbulence is inherently more complicated than fluid turbulence, as, while liquids and gases only have one main type of instability, Tollmien Schlichting waves, and one type of saturation mechanism, viscosity, plasmas can have a wide variety of instabilities (often described as a zoo of instabilities) and saturation mechanisms.

While a full description of the plasma fluctuations observed in HETs is beyond the scope of this review and can be found in Ref. 62, we will briefly mention five main types of fluctuations observed in HETs. The breathing mode is an axial oscillation with a frequency typically between 5 and 20 kHz that is attributed to the neutral transit time through the discharge channel [62]. While the breathing mode is a critical plasma oscillation in HETs as it leads to large fluctuations in the discharge current, it is typically not considered a turbulent fluctuation because it occurs at a single frequency depending on the HET discharge condition. Rotating spokes are azimuthal fluctuation at typically around 25-100 kHz [62] that exhibits a range of scales [63], but whose nature is not fully understood. The ion transit time instability (ITTI) is an axial fluctuation typically between 100 and 500 kHz [62], and as evidenced by its name, is tied to the ion transit time through the acceleration region. The electron cyclotron drift instability (ECDI) is an azimuthal instability that typically grows between 2 and 5 MHz, and it can exhibit resonances relating to the length of the azimuthal path covered by electrons traveling at the $E \times B$ velocity during a single cyclotron gyration [62]. Lastly, the modified two-stream instability is predominantly parallel-field instability, typically between 5 and 10 MHz, which has been shown to couple the ECDI [62].

While in the subsequent analysis we will focus on the effect of azimuthal fluctuations, radial and axial fluctuations can still be important. In general, azimuthal fluctuations attract more attention for anomalous electron momentum transport, because the terms in the azimuthal electron momentum equations are significantly smaller than in the parallel or cross-field electron momentum equations. As a result, even a small additional azimuthal force will significantly affect the azimuthal force balance.

While axial fluctuations do not directly cause significant anomalous transport in the acceleration region, axial correlations can indirectly affect the magnitude of anomalous electron momentum transport in the acceleration region. In fact, it was shown by Ref. 39 that the anomalous electron collision frequency oscillates with the breathing mode. The simplest way that axial oscillations can couple to azimuthal correlations is if the azimuthal fluctuations occur at a significantly higher frequency than the axial oscillations. Considering that there exists some unknown time-averaged closure model for the azimuthal correlations and that "time-averaged" on the timescale of the azimuthal fluctuations could be considered instantaneous on the timescale of the axial fluctuations, then the azimuthal correlations fluctuate according to the axial fluctuations of the plasma properties in the hypothetical closure model. If the average of the fluctuating azimuthal correlation is not the same as the closure model evaluated with the time-averaged plasma properties, then the axial oscillations have changed the magnitude of the anomalous electron momentum transport. A more complicated coupling between the oscillations could be a direct coupling between different types of instabilities that change the behavior of the instabilities, as shown by Ref. 64.

2.2.1.1. Analytical Description of Turbulent Transport in HETs

In the presence of turbulence, plasma properties fluctuate in space and time, such that the local or instantaneous values of a plasma property can be decomposed into

$$x = \langle x \rangle + \delta x, \tag{2-22}$$

where $\langle x \rangle$ is the time-and-space averaged value and δx is the fluctuation about the average. δx has the property that $\langle \delta x \rangle = 0$. It is possible to gain insight into the nature of fluctuating plasma properties with time-resolved experimental [65-68] and computational studies [64, 69-85]. However, numerical simulations with high temporal and azimuthal resolution are very time consuming, so the ultimate goal is to gain enough insight to be able to model the plasma with reduced resolution.

In a HET, the self-induced magnetic field from the Hall current is often neglected, so we will neglect fluctuations in the magnetic field. As a result, turbulence in a HET is usually considered electrostatic. For illustrative purposes, we will only consider azimuthal fluctuations in electron density and in the electric field, since azimuthal fluctuations are considered to be a significant driver of anomalous electron momentum transport in HETs. In fact, Ref. 78 studied the coupling between axial and azimuthal fluctuations but did not report on the electron transport due to the correlation of axial fluctuations, which justifies the assumption of negligible axial anomalous electron momentum transport due to the correlation of axial fluctuations.

We start by considering the E×B component of Eq. 2-13 with negligible electron inertia. When also using the ideal gas law and neglecting azimuthal ion velocity, we arrive at

$$m_e n_e \frac{\partial u_{e\vartheta}}{\partial t} = -e n_e (E_\vartheta + u_{e\hat{\perp}} B) - \partial_\vartheta \left(e T_{eV,\perp} n_e \right) - m_e n_e \nu_c u_{e\vartheta} \tag{2-23}$$

While azimuthal symmetry holds in the time-averaged operation of a HET, due to the possibility of azimuthal instabilities, azimuthal symmetry does not necessarily hold instantaneously. As a result, we can assume that $\langle E_\vartheta \rangle = 0$. We can then write the azimuthally-averaged forms of Eqs. 2-23 as

$$0 = -e\langle \delta n_e \delta E_\vartheta \rangle - e\langle n_e \rangle \langle u_{e\hat{\perp}} \rangle B - m_e \langle n_e \rangle \langle \nu_c \rangle \langle u_{e\vartheta} \rangle \tag{2-24}$$

Due to turbulence, the correlation term of $\langle \delta n_e \delta E_\vartheta \rangle$ causes an additional azimuthally-averaged force in the azimuthal direction. Consequently, $\langle \delta n_e \delta E_\vartheta \rangle$ causes an additional drift in the cross-field direction. Now that we have established the relevant turbulent correlation in the electron momentum equations, for simplicity, we will now exclude $\langle\ \rangle$ when writing the azimuthally-averaged quantities that are not turbulent correlations. Anomalous electron momentum transport is often represented as an anomalous collision frequency, so it is instructive to convert $\langle \delta n_e \delta E_\vartheta \rangle$ to equivalent collision frequencies. $\nu_{a\vartheta}$ represents the anomalous collision frequency due to $\langle \delta n_e \delta E_\vartheta \rangle$ and is given by

$$\nu_a = \frac{e\langle \delta n_e \delta E_\vartheta \rangle}{m_e n_e u_{e\vartheta}}. \tag{2-25}$$

To derive an analogous expression to Eq. 2-17, we start by rewriting Eq. 2-24 to solve for $u_{e\hat{\perp}}$, such that

$$u_{e\hat{\perp}} = -\frac{u_{e\vartheta}}{\Omega_e}, \tag{2-26}$$

where Ω_e is the electron Hall parameter that accounts for the effective collision frequency due to forces in the E×B direction, ν_e. In this case, $\nu_e = \nu_c + \nu_a$. Substituting Eq. 2-26 for $u_{e\vartheta}$ into the cross-field component of Eq. 2-14 and solving for $u_{e\hat{\perp}}$, we get

$$u_{e\hat{\perp}} = -\frac{e}{m_e \nu_c (1+\Omega_e \Omega_c)} E_{\hat{\perp}} - \frac{\partial_{\hat{\perp}} (e T_{eV,\perp} n_e)}{m_e n_e \nu_c (1+\Omega_e \Omega_c)} + \frac{\nu_{ei}^m}{\nu_c (1+\Omega_e \Omega_c)} u_{i\hat{\perp}}. \tag{2-27}$$

If $\Omega_e \Omega_c \gg 1$, then Eq. 2-27 can be approximated as

$$u_{e\hat{\perp}} = -\frac{1}{\Omega_e}\frac{E_{\hat{\perp}}}{B} - \frac{1}{\Omega_e}\frac{\partial_{\hat{\perp}} (T_{eV,\perp} n_e)}{B n_e} + \frac{1}{\Omega_e}\frac{\nu_{ei}^m}{\omega_{ce}} u_{i\hat{\perp}}. \tag{2-28}$$

From Eq. 2-28, we can conclude that in strongly magnetized regions of a HET, the anomalous momentum electron transport is entirely due to anomalous azimuthal forces and can be captured by an anomalous electron collision frequency, ν_a. The main takeaway from ν_a being the key property dictating anomalous electron momentum transport in a HET, is that with Eq. 2-26, we can see that the key property of anomalous electron momentum transport can be found from only $u_{e\vartheta}$ and $u_{e\hat{\perp}}$.

2.2.1.2. Evidence of Electron Transport Due to Plasma Turbulence

To our knowledge, the first indication that plasma turbulence is largely responsible for anomalous electron momentum transport in a HET was the work by Ref. 86. They measured azimuthal fluctuations in the electron density and used theory to relate $\langle \delta n_e^2 \rangle$ to the electron Hall parameter. They then inferred the electron Hall parameter from time-averaged plasma properties, similar to the techniques described in Section 3.2, and found that the electron Hall parameter calculated from $\langle \delta n_e^2 \rangle$ was in remarkable agreement with that inferred from the time-averaged plasma properties. Decades later, a similar technique was carried out by Ref. 30, and they came to similar conclusions as Ref. 86.

While Ref. 86 attributed the azimuthal fluctuations to azimuthally rotating spokes with a base frequency of 16 kHz, kinetic simulations [69] later predicted the presence of high-frequency azimuthal fluctuations on the order of 1 MHz, attributed to the electron cyclotron drift instability

(ECDI) [70], that could lead to anomalous electron momentum transport. Experimental observation of the ECDI in a HET [65] has since sparked over a decade of research into high-frequency azimuthal fluctuations in HETs [64, 67, 68, 71-85]. Since computational cost limits kinetic simulations of the high-frequency azimuthal fluctuations to domains smaller than that of a HET, these simulations cannot capture azimuthal fluctuations at frequencies relevant to spokes. However, these kinetic simulations have shown that, at least within the simulation domain, the turbulent correlation of $\langle \delta n_e \delta E_\theta \rangle$ captures the effective anomalous electron momentum transport when they time-average the results of the kinetic simulation [76]. We note, however, that the transport due to spokes and ECDI are not necessarily competing theories, as the resulting turbulence from these phenomena is thought to occur in a distinct region of the HET discharge [62]. In addition, there is experimental and computational evidence that high-frequency azimuthal fluctuations can transition into low-frequency azimuthal fluctuations between 100 and 500 kHz [68], characterized by a modified ion-acoustic turbulence that propagates with the ion beam [78].

To be able to capture the effects of $\langle \delta n_e \delta E_\vartheta \rangle$ in simulations that do not resolve high-frequency oscillations but that can simulate over the entire HET discharge, it is necessary to relate $\langle \delta n_e \delta E_\vartheta \rangle$ to the more common fluid terms variables of $\vec{u}_e$, $\vec{u}_i$, $\vec{E}$, n_e, n_n, and $\vec{\vec{P}}_e$; this is referred to as the closure problem for anomalous electron momentum transport in HETs because without a model for $\langle \delta n_e \delta E_\vartheta \rangle$, then the typical system of fluid equations has more unknowns than there are equations. While several attempts [43-49,87,] have been made to find a closure model for $\langle \delta n_e \delta E_\vartheta \rangle$, a fully predictive closure model for turbulent transport in a HET is still elusive.

2.2.2. Electron Transport Due to Electron-Wall Collisions

2.2.2.1. Basics of Plasma-Wall Interactions

At every boundary, whether a dielectric or a conductor, charge continuity needs to be satisfied. If a current density j_w flows through a boundary, then current conservation at the boundary requires

$$j_w = (\vec{j}_e \cdot \hat{n})_w + (\vec{j}_i \cdot \hat{n})_w = j_{ew} + j_{iw} - j_{SEE}, \tag{2-29}$$

where $\hat{n}$ is the normal vector to the surface, j_{ew} and j_{iw} correspond to the current fluxes from the plasma to the wall, and j_{SEE} represents the current density of secondary electron emission (SEE) from the boundary. Eq. 2-29 assumes no backscattering of ions or electrons at the wall, such that charged particle fluxes to the boundary are fully accommodated. In addition, if the electrostatic potential of the wall, ϕ_w, is not equal to the local plasma potential, then a region, called a sheath, with finite space charge will develop between the plasma and the wall. For an unmagnetized plasma with negligible collisions, isothermal electrons, and cold ions, j_{ew} and j_{iw} are given by [10]

$$j_{ew} = \begin{cases} j_{e0} & , \quad \phi_w \geq \phi_0 \\ j_{e0} \exp\left(-\frac{\phi_0 - \phi_w}{k_B T_e}\right), & \phi_w < \phi_0 \end{cases} \tag{2-30}$$

$$j_{iw} = \begin{cases} 0 & , \quad \phi_w \geq \phi_0 \\ -\exp\left(-\frac{1}{2}\right) e n_{e0} \sqrt{\frac{k_B T_e}{m_i}}, & \phi_w < \phi_0 \end{cases} , \tag{2-31}$$

where "0" denotes the plasma properties in the quasineutral plasma adjacent to the boundary. Secondary electron emission is modeled with a yield coefficient, γ, that depends on a variety of parameters, including wall material, $\phi_0 - \phi_w$, and the ion mass, such that

$$j_{ew} - j_{SEE} = j_{ew}(1-\gamma). \tag{2-32}$$

2.2.2.2. Near-Wall Conductivity

Early studies of electron transport in HETs suggested that the rate of electron flux to the channel walls could lead to an effective electron-wall collision frequency. This phenomenon is called near-wall conductivity (NWC). The basics of near-wall conductivity is best modeled by assuming that electrons lose their mean momentum upon colliding with the wall and by incorporating wall fluxes into the electron continuity equation and by assuming that SEE electrons do not provide a source of mean momentum [88]. In this manner, steady-state electron continuity and momentum equations for a control volume adjacent to the wall can be written as

$$\nabla \cdot (n_e \vec{u}_e) = n_e \nu_{iz} - \frac{j_{ew}(1-\gamma)A_w}{eV_w} \tag{2-33}$$

$$\nabla \cdot (m_e n_e \vec{u}_e \otimes \vec{u}_e) - en_e\left(\vec{E} + \vec{u}_e \times \vec{B}\right) - \nabla \cdot \vec{\vec{P}}_e - m_e \frac{j_{ew}A_w}{eV_w} \vec{u}_e, \tag{2-34}$$

where A_w is the surface area of the wall within the control volume, V_w is the control volume, and we have neglected classical collisions in the momentum equation. If we combine Eqs. 2-33 and 2-34, we can write the momentum equation in non-conservative form as

$$m_e n_e (\vec{u}_e \cdot \nabla)\vec{u}_e = -en_e\left(\vec{E} + \vec{u}_e \times \vec{B}\right) - \nabla \cdot \vec{\vec{P}}_e - m_e n_e \nu_{iz} \vec{u}_e - m_e \frac{j_{ew}\gamma A_w}{eV_w} \vec{u}_e. \tag{2-35}$$

From Eq. 2-35, we can see that the effective momentum-transfer collision frequency of electron-wall collisions, when writing the momentum equation in non-conservative form, is

$$\nu_w = \frac{j_{ew}\gamma A_w}{en_e V_w}. \tag{2-36}$$

Approaches like the one outlined above have been used in fluid models of electrons to study the effect of electron-wall collisions on the HET discharge [88-90], and Ref. 88 was able to recover the measured trends in the discharge current versus material of the channel wall. However, in a calibrated fluid simulation in Ref. 90, it was found that the contribution of NWC was at most half of the anomalous collision frequency but that it was almost negligible in most regions of the discharge.

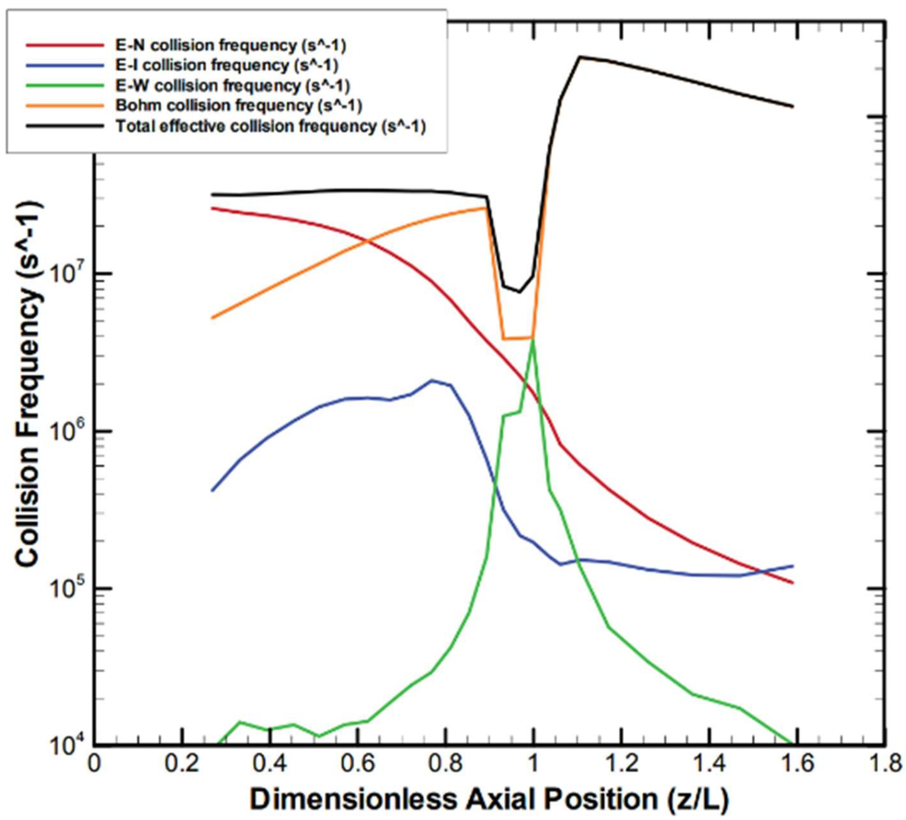

Figure 2-3: Reproduced from Ref. [90]. Axial profiles of different types of electron collision frequencies in a HET simulation, including electron-neutral (E-N) collisions, electron-ion (E-I) collisions, electron-wall (E-W) collisions, and an empirical collision frequency due plasma turbulence (Bohm)

While the contribution of ν_w is expected to only occur near the channel walls, NWC has also been shown to significantly affect the radial profile of the axial electron current density [91]. Moreover, Refs. 92 and 93 found that the SEE beams from one channel wall could traverse the discharge and reach the opposing wall. This could potentially manifest in an effective SEE coefficient away from the channel walls based on the time-averaged radial distribution of j_{SEE}. Consequently, NWC could influence the radial distribution of the electron current density.

Lastly, there have also been kinetic simulation studies about the coupling of SEE with the ECDI [71,72]. Ref. 72 found that, via electron cooling, SEE could reduce the electron mobility attributed to ECDI in the bulk plasma by 20%, but ECDI was the dominant cause of the electron transport in their simulation. Consequently, even if NWC does not contribute significantly to electron transport, SEE can modify plasma properties that can in turn change the characteristics of turbulent fluctuations.

2.2.2.3. Experimental Evidence of Wall Effects on Electron Transport in a HET

Experimental evidence of electron transport due to electron-wall collisions is mainly in the form of changes in the time-averaged discharge current and in the discharge current oscillations due to changes in the channel wall material [94]. When changing the channel material in an unshielded HET between borosil, alumina, silicon carbide, and graphite, Ref. 94 observed 25% variations in the time-averaged discharge current and 100% variations in the discharge current oscillations. However, for a MS-HET, virtually no change in the discharge current was observed when changing between a boron nitride channel and a graphite channel [95,96]. In fact, Ref. 96 demonstrated that such a change in the channel wall material also had no significant change on the discharge current oscillations or on the plasma properties. Therefore, while SEE and NWC may play a significant role in electron transport in an unshielded HET, it appears that they may not play a significant role in MS-HETs.

2.2.3. Electron Transport Due to Electron Shear

2.2.3.1. Electron Inertia Considerations

While electron inertia is often neglected in HET simulations, it is instructive to write out the material derivative in cylindrical coordinates to try to identify the most significant electron inertia terms in a HET. The steady-state cylindrical material derivative is written out as

$$\begin{aligned}\vec{u}\cdot\nabla\vec{u} = &\left(u_r\frac{\partial u_r}{\partial r} + \frac{u_\theta}{r}\frac{\partial u_r}{\partial \theta} - \frac{u_\theta^2}{r} + u_z\frac{\partial u_r}{\partial z}\right)\hat{r} \\ &+ \left(u_r\frac{\partial u_\theta}{\partial r} + \frac{u_\theta}{r}\frac{\partial u_\theta}{\partial \theta} + \frac{u_\theta u_r}{r} + u_z\frac{\partial u_\theta}{\partial z}\right)\hat{\theta}\ \cdot \\ &+ \left(u_r\frac{\partial u_z}{\partial r} + \frac{u_\theta}{r}\frac{\partial u_z}{\partial \theta} + u_z\frac{\partial u_z}{\partial z}\right)\hat{z}\end{aligned} \tag{2-37}$$

Given that we expect a large azimuthal electron drift velocity and a large axial gradient in the E×B velocity in the acceleration region, two terms in Eq. 2-37 stick out: $u_{ez}\frac{\partial u_{e\theta}}{\partial z}\hat{\theta}$ and $-\frac{u_{e\theta}^2}{r}\hat{r}$. From now on, we will refer to $u_{ez}\frac{\partial u_{e\theta}}{\partial z}\hat{\theta}$ as the electron shear term and to $-\frac{u_{e\theta}^2}{r}\hat{r}$ as the centrifugal force term.

In the cross-field coordinate system, the total shear of the azimuthal electron drift velocity is

$$u_{er}\frac{\partial u_\theta}{\partial z} + u_z\frac{\partial u_\theta}{\partial z} = u_{e\parallel}\,\partial_\parallel u_{e\theta} + u_{e\perp}\,\partial_\perp u_{e\theta}, \tag{2-38}$$

and we expect the cross-field term to dominate in Eq. 2-38. The centrifugal force can also be expressed as

$$-\frac{u_{e\theta}^2}{r}\hat{r} = -\frac{u_{e\vartheta}^2}{r}\left[\left(\hat{\beta}_\perp \cdot \hat{r}\right)\hat{\beta}_\perp + \left(\hat{\beta}_\parallel \cdot \hat{r}\right)\hat{\beta}_\parallel\right], \tag{2-39}$$

and we expect the parallel-field term to dominate with a predominantly radial magnetic field. Consequently, electron shear is most relevant to cross-field electron transport, while the centrifugal force term is most relevant for parallel-field physics, so we will discuss the centrifugal force in more detail in Section 2.2.5. The two effects of electron shear that have been studied regarding electron transport in HETs are the shear suppression of turbulence and the shear-modified electron Hall parameter.

2.2.3.2. Shear-Modified Electron Hall Parameter

Accounting for cross-field electron shear, the electron azimuthal equation can be written as

$$m_e n_e u_{e\hat{\perp}}\, \partial_{\hat{\perp}} u_{e\vartheta} = -e n_e u_{e\hat{\perp}} B - m_e n_e \nu_e u_{e\vartheta}, \tag{2-40}$$

where we have also accounted for the effects of wall and turbulent transport in ν_e. Solving Eq. 2-40 for the ratio of $u_{e\theta}$ to $u_{e\hat{\perp}}$, we find that

$$\frac{u_{e\vartheta}}{|u_{e\hat{\perp}}|} = \frac{\omega_{ce} + \partial_{\hat{\perp}} u_{e\vartheta}}{\nu_e}, \tag{2-41}$$

where define the modified azimuthal electron Hall parameter as

$$\Omega_e^* \equiv \frac{u_{e\vartheta}}{|u_{e\hat{\perp}}|} = \Omega_e\left(1 + \frac{\partial_{\hat{\perp}} u_{e\vartheta}}{\omega_{ce}}\right). \tag{2-42}$$

Therefore, $\frac{\partial_{\perp} u_{e\vartheta}}{\omega_{ce}}$ determines by how much electron shear modifies Ω_e. To estimate the maximum effect of electron shear on the Hall parameter, we estimate $\partial_{\perp} u_{e\vartheta}$ being approximately equal to $\frac{V_d}{L_{acc}^2 B_{max}}$, where we approximate V_d as 300 V, L_{acc} as 1 cm, and B_{max} as 100 G. This results in $\partial_{\perp} u_{e\vartheta}$ being approximately 300 MHz, which is approximately 17% of ω_{ce} evaluated at 100 G. We thus expect electron shear to have non-negligible effect on Ω_e, and we expect the effect to increase with the discharge voltage. The effect of electron shear on Ω_e is to reduce Ω_e in the downstream portion of the acceleration region and to increase Ω_e in the upstream portion of the acceleration region, where a decrease in $\Omega_{e\vartheta}$ corresponds to an increase in cross-field transport. To our knowledge, electron shear was first inferred in a HET by Ref. 97, and they found a peak $\frac{\partial_{\perp} u_{e\vartheta}}{\omega_{ce}}$ of 0.12 at a discharge voltage of 200 V. Their results are reproduced in Fig. 2-4.

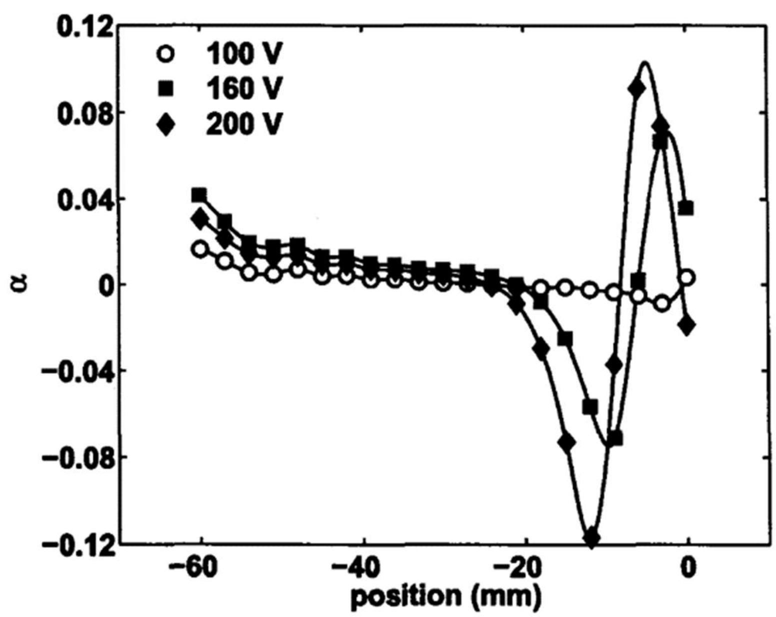

Figure 2-4: Reproduced from Ref. [97]. Measured axial profiles of $\frac{\partial_{\perp} u_{e\vartheta}}{\omega_{ce}}$ in a HET at three different discharge conditions.

2.2.3.3. Shear Suppression of Plasma Turbulence

While the modified electron Hall parameter can be an important consequence of electron shear, shear-suppressed turbulence could be more significant. The concept of shear-suppressed turbulence is that electron shear decreases the magnitude of turbulent correlations [98]. Consequently, in this theory, electron shear does not produce anomalous electron momentum transport, but it can modify already-existing anomalous electron momentum transport. This phenomenon has been studied extensively in the field of magnetic-confinement fusion, and an empirical scaling law that captures the effect of shear suppression is [99]

$$\nu_{a,shear} = \frac{\nu_{a,fluc}}{1+(Cs)^{\alpha}}, \tag{2-43}$$

where $\nu_{a,fluc}$ is the anomalous collision frequency due to turbulence in the absence of shear, $\nu_{a,shear}$ is the anomalous collision frequency accounting for shear suppression, C and α are empirical constants, and s the electron shear. Interestingly, in Ref. 97, an expression for shear-suppressed turbulence similar to Eq. 2-43 was derived from principles. It was found in Ref. 97 that

$$\nu_{a,shear} = \frac{\nu_{a,fluc}}{1+f\left(\frac{|C|s}{\omega_{ce}}\right)\left(\frac{|C|s}{\omega_{ce}}\right)^{2}}, \tag{2-44}$$

where f is a function less than 1 and $|C|$ is a constant that depends on the characteristics of the turbulence.

In the HET community, Eq. 2-43 has been considered as a model for anomalous electron momentum transport, but only with $\nu_{a,fluc} = \nu_{Bohm}$, where ν_{Bohm} is the Bohm collision frequency. The Bohm model is

$$\nu_{a,fluc} = \alpha\omega_{ce}, \tag{2-45}$$

where α is a constant of proportionality typically taken to be around 16 [100] that is reflective of the characteristics of turbulence [101]. Equation 2-45 in combination with Eq. 2-43 has been compared to empirical values of the anomalous electron collision frequency and has in fact shown among the best agreement when compared with other models of anomalous electron momentum transport in a HET [46]. Surprisingly, Eq. 2-43 in combination with a more sophisticated model for $\nu_{a,fluc}$ has not been compared with experiments, but this has been suggested by Ref. 87.

2.2.4. Electron Transport Due to Anomalous Electron Temperatures

The cause of anomalous electron temperatures is evidently not well-understood, so we will treat electron energy transport more in-depth in Section 2.3. However, its effect on cross-field electron momentum transport is clear. If the maximum cross-field electron temperature in a HET is higher than expected, this will increase the cross-field pressure gradient. Per Eq. 2-27, this will directly affect $u_{e\hat{\perp}}$ via the term $-\frac{\partial_{\hat{\perp}}(eT_{eV,\perp}n_e)}{m_e n_e \nu_c(1+\Omega_e\Omega_{e\vartheta})}$. In this manner, since electron temperature peaks in the acceleration region and $u_{e\hat{\perp}} < 0$, anomalously high peak electron temperatures would decrease $|u_{e\hat{\perp}}|$ in the downstream region of the acceleration region and would increase $|u_{e\hat{\perp}}|$ in the upstream region of the acceleration region.

Regarding evidence of anomalously high electron temperatures, recent ILTS measurements in a HET have shown electron temperatures corresponding to around 20% of the discharge voltage. However, scaling laws based on Langmuir probe measurements in HETs suggest that the maximum electron temperature in a conventional HET should be around 10% of the discharge voltage [17], and this has also been found by simulations [12]. For magnetic shielding, this scaling has been found to be around 13% [12,102]. Consequently, ILTS measurements strongly suggest the presence of anomalous electron energy transport in a HET that is not currently captured by HET models and that approximately doubles the maximum electron temperature. In Section 3.1, we consider why electron temperatures from ILTS are considered more accurate than Langmuir probe in addition to the fact that Langmuir probes are an invasive diagnostic that can perturb the plasma, while ILTS in a non-invasive diagnostic.

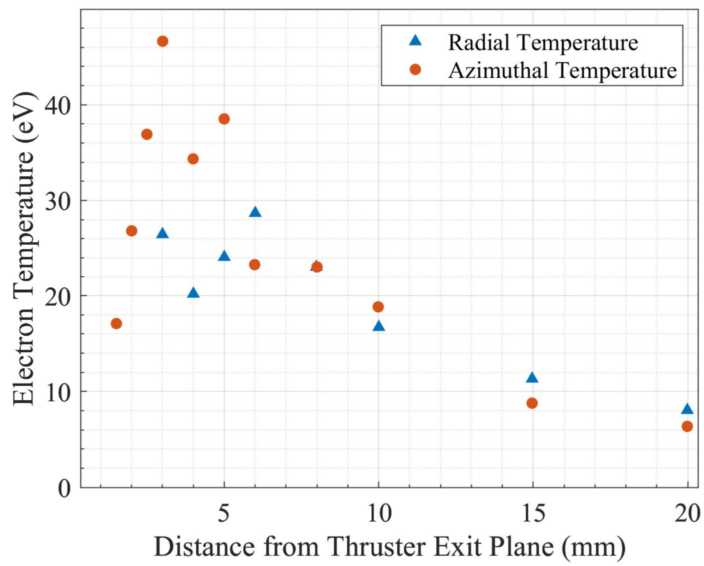

Figure 2-5: Data extracted from Ref. 22. Axial profile of azimuthal and radial electron temperatures in a MS-HET operating at 150 V.

Lastly, ILTS measurements in a HET (replicated in Fig. 2-5) have also shown anisotropy in the electron temperatures between the parallel-field and cross-field directions [22]. These measurements show that the azimuthal electron temperature is generally higher than the parallel-field electron temperature. This is significant, since if electron temperature anisotropy exists in a HET, it needs to be accurately modeled for simulations to capture the effect of the cross-field divergence of the electron pressure tensor on cross-field electron transport. In addition, as will be discussed in Section 2.2.5, electron temperature anisotropy can play a role in the parallel-field electron momentum equation.

2.2.5. Parallel-Field Considerations

2.2.5.1. Motivation for Studying Parallel-Field Electron Dynamics

Even though parallel-field physics is not significant for electron transport, we are generally concerned with understanding the electron phenomena that limit the predictive capability state-of-the-art HET models. Radial dynamics inside the discharge channel play a significant role in the understanding of discharge channel erosion, which is the main life-limiting mechanism of conventional HETs. Since the magnetic field lines in an unshielded HET are predominantly radial in the acceleration region, parallel-field physics determines the electron temperature and electrostatic potential near the channel wall. These are properties of importance to discharge channel erosion, as $T_{e\parallel}$ determines the ion flux to the wall, through Eq. 2-31, and through electrostatic acceleration, the potential drop from the plasma to the wall determines the ion velocity at the wall.

In addition, simulations of MS HETs have shown that small changes in the ion divergence at the edges of the exit plane of the discharge channel produce large changes in the predicted erosion of the inner and outer front pole covers, which is the main life-limiting mechanism in MS HETs. Deviations from zero ion divergence are determined by the radial electric field, of which the parallel-field electric field is a significant component. Therefore, accurate modeling of electron dynamics in the parallel-field direction is a critical component of the predictive capability of the lifetime of MS-HETs. Lastly, while plume divergence usually represents a small thrust inefficiency of around 5% [10,103], we note that the radial electric field also determines the plume divergence.

2.2.5.2. Modified Parallel-Field Electron Momentum Equation

In this section, we present modifications to Eq. 2-18, which is a common representation of parallel-field electron dynamics in state-of-the-art HET simulations. These modifications are due to the centrifugal force, which was introduced in Section 2.2.3.1, and the magnetic mirror force. The centrifugal force is commonly neglected because electron inertia is commonly neglected. The magnetic mirror force is often not modeled in HET simulations because it is zero in the case of an isotropic electron temperature, which is also a common assumption in HET simulations. While the magnetic mirror force is well-known from magnetized single-particle motion [19], it only arises in the fluid formulation of electrons from the divergence of an anisotropic pressure tensor given by

$$P_{ij} \ = \ p_{\parallel}\beta_i\beta_j + p_{\perp}\left(\delta_{ij} - \beta_i\beta_j\right), \tag{2-46}$$

where δ_{ij} is the Kronecker delta and β_i is the normalized magnetic field in tensor notation [104]. We note that the pressure tensor used in Eq. 2-12 is of the form of Eq. 2-46 with $\beta_1 = 0$, $\beta_2 = 0$, and $\beta_3 = 1$. Accordingly, the modified form of Eq. 2-18 is

$$u_{e\parallel} = \ -\frac{e}{m_e\nu_c}E_{\parallel} - \frac{e\,\partial_{\parallel}(T_{eV,\parallel}n_e)}{m_e n_e \nu_c} + \frac{e\left(T_{eV,\parallel} - T_{eV,\perp}\right)\partial_{\parallel}B}{m_e B \nu_c} + \frac{u_{e\vartheta}^2}{r\nu_c}\left(\hat{\beta}_{\parallel}\cdot\hat{r}\right) + \frac{\nu_{ei}^m}{\nu_c}u_{i\parallel}. \tag{2-47}$$

We note that the $T_{eV,\parallel}\,\partial_{\parallel}B$ is not due to the magnetic mirror effect [104], but that it cancels the magnetic mirror force in the case of an isotropic pressure tensor, such that we will refer to the third term on the right-hand side of Eq. 2-47 as the net magnetic mirror term.

Evaluating the relative contributions of the pressure term, magnetic mirror term, and centrifugal term, we approximate $T_{eV,\parallel} = \frac{V_d}{10}$ as a constant along the magnetic field lines and approximate $\partial_{\parallel}(\ln n_e)$ and $\partial_{\parallel}(\ln B)$ as $\frac{1}{R_{chann}}$. With this approximation, the ratio of the pressure gradient to the net magnetic mirror force is $\left|\frac{T_{eV,\parallel}}{T_{eV,\perp}-T_{eV,\parallel}}\right|$. Assuming radial magnetic field lines, we can approximate the centrifugal contribution by $\frac{u_{e\theta}^2}{r}$ being approximately equal to $\frac{V_d}{L_{acc}R_{mean}B_{max}}$ and use the previous estimates of V_d approximately 300 V, L_{acc} approximately 1 cm, and B_{max} approximately 100 G along with R_{mean} approximately 50 cm for the mean channel diameter. We find that $m_e \frac{u_{e\theta}^2}{r}$ is approximately 1 eV/cm, and approximating R_{chann} as 10 cm, we find that $\frac{eT_{eV,\parallel}\,\partial_\parallel(n_e)}{n_e}$ is approximately 3 eV/cm, such that the centrifugal contribution is expected to be of the same order of magnitude as the pressure gradient. In fact, at the channel centerline, we expected $\partial_\parallel(n_e) \approx 0$ due to approximate radial symmetry of the channel, such that the centrifugal force is expected to be greater than the electron pressure gradient at the channel centerline. In fact, in Ref. 105, the net magnetic mirror force and the centrifugal force were incorporated into a 1-D radial model of a HET and were found to be of a similar magnitude as the radial pressure gradient. Also, in Ref. 106, a form of the magnetic mirror force was included into 2-D HET simulation, and they found that the magnetic mirror force altered the equipotential lines away from the magnetic field lines. Consequently, the centrifugal force is expected to be non-negligible, and the net magnetic mirror force will be non-negligible in the presence of significant electron temperature anisotropy, so it should be important to incorporate these terms in the parallel-field momentum equation.

2.3. Anomalous Electron Energy Transport in HETs

Having previously mentioned the consequence of anomalous electron temperatures and the strong evidence in support of it, in this section, we will first briefly present the electron energy equation. We will then review potential mechanisms of anomalous electron energy transport.

2.3.1. Electron Energy Equation

The total (thermal and bulk flow) electron energy equation is given by

$$\frac{\partial}{\partial t}\left(\frac{3}{2}p_e + \frac{1}{2}m_e n_e u^2\right) + \nabla\cdot\left(\frac{5}{2}\vec{u}_e p_e + \frac{1}{2}m_e n_e u_e^2 \vec{u}_e\right) = \vec{j}_e \cdot \vec{E} - \nabla\cdot\vec{q}_e - Q_{in} - Q_{el}, \tag{2-48}$$

where $\vec{q}_e$ is the heat flux vector, Q_{in} is the energy loss rate from inelastic electron-impact collisions of electrons with heavy species, and Q_{el} is the energy loss due to the relaxation of the thermal nonequilibrium between the electrons and the heavy species. Electron inertia is commonly excluded in HET models, so the form of Eq. 2-48 usually considered in HET models that represent electrons as fluids [20,102] is

$$\frac{\partial}{\partial t}\left(\frac{3}{2}p_e\right) + \nabla\cdot\left(\frac{5}{2}\vec{u}_e p_e\right) = \vec{j}_e \cdot \vec{E} - \nabla\cdot\vec{q}_e - Q_{in} - Q_{el}. \tag{2-49}$$

2.3.2. Anomalous Joule Heating Due to Plasma Turbulence

In radial-axial electron fluid models, the Joule heating term in Eq. 2-49, $\vec{j}_e \cdot \vec{E}$, is typically evaluated as $\vec{j}_e \cdot \vec{E} = j_{e\parallel}E_{parallel} + j_{e\perp}E_{\perp}$, neglecting the azimuthal contribution to the dot product under the assumption of $E_\vartheta = 0$. However, if we consider azimuthal fluctuations of the electron density, electric field, and azimuthal electron drift velocity, then the azimuthally-averaged Joule heating is

$$\langle \vec{j}_e \cdot \vec{E} \rangle = j_{e\parallel}E_{parallel} + j_{e\perp}E_{\perp} - eu_{e\vartheta}\langle \delta n_e \delta E_\vartheta \rangle - en_e\langle \delta u_{e\vartheta}\delta E_\vartheta \rangle\,, \tag{2-50}$$

where we have neglected third-order correlations. Since $eu_{e\vartheta}\langle \delta n_e \delta E_\vartheta \rangle$ is not independently anomalous from anomalous electron momentum transport, the true anomalous electron heating comes from $en_e\langle \delta u_{e\vartheta}\delta E_\vartheta \rangle$. Assuming that anomalous momentum transport can be represented by an anomalous collision frequency, then Eq. 2-50 can be rewritten as

$$\langle \vec{j}_e \cdot \vec{E} \rangle = j_{e\parallel} E_{parallel} + j_{e\hat{\perp}} E_{\hat{\perp}} - \eta_a j_{e\vartheta}^2 + Q_a \,, \tag{2-51}$$

where we have defined the anomalous Joule heating as $Q_a = -en_e \langle \delta u_{e\vartheta} \delta E_\vartheta \rangle$. It is also common to try to define the anomalous Joule heating by an anomalous electron energy transfer collision frequency, ν_a^E, such that $Q_a = \eta_a^E j_{e\vartheta}^2$. Therefore, when fluid simulations use the model of $\vec{j}_e \cdot \vec{E} = j_{e\parallel} E_{parallel} + j_{e\hat{\perp}} E_{\hat{\perp}}$ it is equivalent to assuming that $\nu_a^E = \nu_a$.

Because HET simulations use a phenomenological model for Q_a that has little physical basis, it is not surprising that ILTS measurements of electron temperature do not agree with simulations. In addition, when ILTS measurements disagree with simulations it does not imply that there is anomalous electron heating, but instead that the anomalous heating is different from the arbitrary model used in simulations. To reiterate, while Langmuir probe measurements have better agreement with simulations [12], these simulations already account for anomalous electron heating, so ILTS measurements simply suggest that simulations should use a different anomalous electron heating model.

2.3.2.1. Evidence of Anomalous Joule Heating Due to Plasma Turbulence

While it is standard to assume that $\nu_a^E = \nu_a$ and such that anomalous Joule heating exists, little work exists to quantify any deviation of Q_a from $\eta_a j_{e\vartheta}^2$. While high peak electron temperatures measured with ILTS could be a sign that Q_a is different from $\eta_a j_{e\vartheta}^2$, it could also be a sign anomalous energy transport due to anomalous electron heat flux. However, results from a recent kinetic simulation in Ref. 107 included the axial distribution of $\langle j_{e\theta} E_\theta \rangle$, as shown in Fig. 2-6. Ref. 107 found that $\langle j_{e\theta} E_\theta \rangle$ was not equal to zero, implying that Q_a differs from $\eta_a j_{e\vartheta}^2$. In particular, regions of negative $\langle j_{e\theta} E_\theta \rangle$ imply $Q_a < \eta_a j_{e\vartheta}^2$, and regions of positive $\langle j_{e\theta} E_\theta \rangle$ imply $Q_a > \eta_a j_{e\vartheta}^2$.

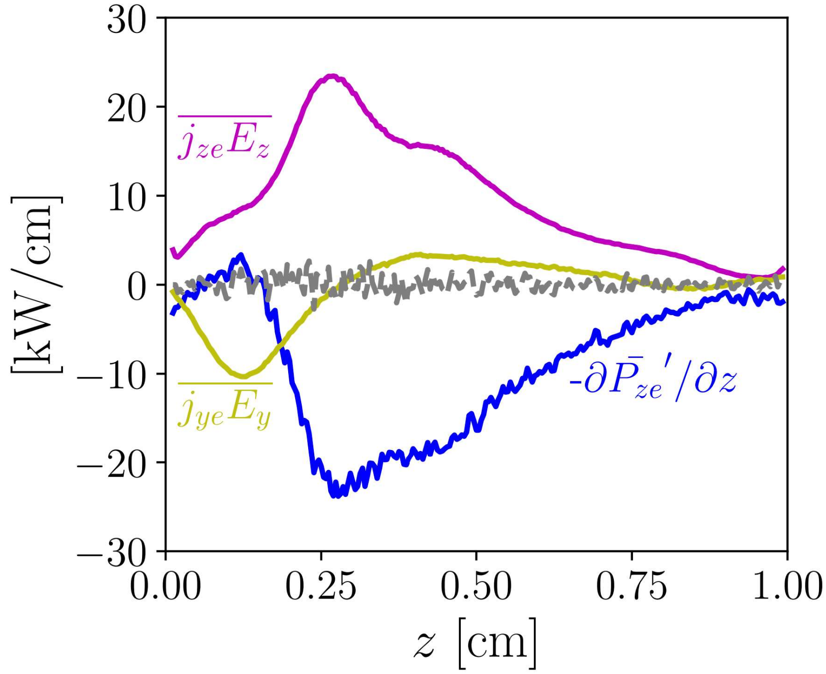

Figure 2-6: Reproduced from Ref. 107. z corresponds to the axial direction, and y corresponds to the azimuthal direction. $P_{ze}{}'$ is the total axial energy flux.

2.3.2.2. Kinetic Explanation of Anomalous Electron Heating

In this section, we will briefly discuss the kinetic interpretation of how azimuthal fluctuations heat electrons. Specifically, we will explain the mechanism by which the ECDI has been shown to provide significant electron heating in the cross-field plane.

The first thing to establish is that when an electromagnetic wave propagates through a magnetized plasma and has a frequency corresponding to an integer multiple of ω_{ce}, the electrons will resonate with the wave, such that they gain energy in the direction of the wave's propagation [108]. Averaged over the electron population, this will heat the electrons in the propagation direction of the wave. This is known as electron cyclotron heating.

A plasma instability can be characterized by its wavevector, $\vec{k}$, and its dispersion relation, $\omega(\vec{k})$, which describes the frequency, ω, at a given wavevector. An electron moving at a certain velocity, $\vec{v}$, will feel such an instability at a Doppler-shifted frequency, $\omega - \vec{k} \cdot \vec{v}$. If an electron satisfies the condition

$$\omega - \vec{k} \cdot \vec{v} = n\omega_{ce}, \tag{2-52}$$

then it resonates with the plasma instability [109], where n is a positive integer. Thus, when electrons satisfy the cyclotron resonance condition, Eq. 2-52, with the ECDI, the electrons will be heated predominantly in the azimuthal direction because, in a HET, the ECDI propagates predominantly in the azimuthal direction. We note that this heating mechanism only occurs for electrons in the portion of the EVDF that satisfies Eq. 2-52.

In addition, as an electron resonates with the ECDI, it will gain energy, which will increase its azimuthal velocity, such that the resonance condition is no longer met. However, as the electron gyrates in cross-field plane, its azimuthal velocity will eventually decrease to the point where the resonance condition is once again met, and the electron will once again gain energy. This is the efficient heating mechanism of the ECDI described by Refs. 110 and 79 as the trapping and untrapping of electrons. The complexities of how long the resonance condition is met in comparison to ω_{ce}^{-1} and how these complexities affect the heating are described in Ref. 111. Then, as previously discussed in Section 2.1.2, the gyromotion will isotropize the thermal electron energy in the cross-field plane. It is also interesting to note that both the resonance condition and the definition $Q_a = -en_e\langle \delta u_{e\vartheta} \delta E_\vartheta \rangle$ show that relation between electron velocities and the instability are central to anomalous electron heating, suggesting a direct connection between the two explanations may be possible.

While electron heating in the cross-field plane is expected to be most significant and more relevant to cross-field transport, it is still important to consider possible sources of anomalous electron heating in the parallel-field direction. First, experiments have shown that the wavevector of the ECDI contains a parallel-field component [66,68]. When simulations first accounted for this feature of the ECDI, it was found that the ECDI could heat electrons in the parallel-field direction, although the physical heating mechanism could not be explained [71]. Later, 2-D PIC simulations of the ECDI showed that the MTSI also developed and that it produced intense fluctuations in the parallel-direction that would couple with the 2-D ECDI [80]. Ref. 80 showed that the MTSI produced strong parallel-field heating of electrons, and the authors mentioned that this heating is due to parallel-field electric field, suggesting that this parallel-field is due to turbulent Joule heating. Interestingly, while the 2-D simulation in Ref. 80 was in the context of conventional HETs, with the radial field lines being bounded by dielectric walls, the MTSI is thought to also exist in the front pole regions of MS-HETs [53], which is where the magnetic field lines terminate in MS-HETs. Lastly, in conventional HETs, SEE is expected to contribute to significant electron cooling in the radial direction [92,93].

2.4. Anomalous Electron Transport in HETs Due to Nonequilibrium

In this section, we will cover electron transport due to nonequilibrium effects, which we call anomalous since fluid simulations typically do not account for these effects. Nonequilibrium phenomena have broadly two categories, non-Maxwellian and anisotropic. While we have already covered an anisotropic effect in the magnetic mirror effect, here we will provide a review of anomalous heat flux transport and briefly cover higher-order non-Maxwellian and anisotropic phenomena.

2.4.1. Electron Heat Flux Transport Equation

Here, we will present the electron heat flux transport equation for an isotropic electron temperature and derive the parallel and perpendicular components of the electron heat flux vector accounting for turbulent effects. Formulations of electron heat flux transport for anisotropic electron temperatures can be found in Ref. 112 and 113. Neglecting inertial terms, the electron heat flux transport equation is given in Ref. 114

$$0 = -\nabla\left(\frac{5p_eT_e}{2e}\right) - \frac{5}{2}p_e\vec{E} - \left(\vec{q}_e + \frac{5}{2}p_e\vec{u}_e\right) \times \vec{B} - \frac{m_e\nu_c}{e}\vec{q}_e, \tag{2-53}$$

The parallel-field component is calculated simply from Eq. 2-53, as

$$q_{e\parallel} = \frac{e}{m_e\nu_c}\left(-\nabla_\parallel\left(\frac{5p_eT_e}{2e}\right) - \frac{5}{2}p_eE_\parallel\right). \tag{2-54}$$

Recognizing that $\frac{5}{2}T_{eV}(en_eE_\parallel + \nabla p_e) = -\frac{5}{2}T_{eV}m_en_e\nu_cu_{e\parallel}$ from the parallel component of the electron momentum equation, Eq. 2-18, then Eq. 2-54 can be rewritten as

$$q_{e\parallel} = -\frac{5p_e}{2m_e\nu_c}\nabla_\parallel T_{eV} + \frac{5}{2}p_eu_{e\parallel}, \tag{2-55}$$

which recovers Fourier's Law modified by a convective heat flux term. For the azimuthally-averaged azimuthal component of Eq. 2-53, we assume that the p_eE_ϑ term is the one most affected by turbulent effects, such that the azimuthal component of $\vec{q}_e$ is given by

$$q_{e\vartheta} = \frac{e}{m_e\nu_c}\left(-\frac{5}{2}eT_{eV}\langle\delta n_e\delta E_\vartheta\rangle - \frac{5}{2}en_e\langle\delta T_{eV}\delta E_\vartheta\rangle - q_{e\hat{\perp}}B - \frac{5}{2}p_eu_{e\hat{\perp}}B\right), \tag{2-56}$$

where we have neglected triple-product correlations. Recognizing that $\frac{5}{2}T_{eV}(e\langle\delta n_e\delta E_\vartheta\rangle + n_eu_{e\hat{\perp}}B) = -\frac{5}{2}T_{eV}m_en_e\nu_cu_{e\vartheta}$ from the azimuthal component of the electron momentum equation, Eq. 2-24, then Eq. 2-56 can be rewritten as

$$q_{e\vartheta} = -\frac{e}{m_e\nu_c}\left(\frac{5}{2}en_e\langle\delta T_{eV}\delta E_{\vartheta}\rangle + q_{e\hat{\perp}}B - \frac{5m_e\nu_c}{2e}p_e u_{e\vartheta}\right). \tag{2-57}$$

Next, the cross-field component of $\vec{q}_e$ calculated from Eq. 2-53 is given by

$$q_{e\hat{\perp}} = \frac{e}{m_e\nu_c}\left(-\nabla_{\hat{\perp}}\left(\frac{5p_eT_e}{2e}\right) - \frac{5}{2}p_eE_{\hat{\perp}} + \left(q_{e\vartheta} + \frac{5}{2}p_e u_{e\vartheta}\right)B\right), \tag{2-58}$$

Again, recognizing the presence of the electron momentum equation in Eq. 2-58, Eq. 2-58 can be rewritten as

$$q_{e\hat{\perp}} = -\frac{5p_e}{2m_e\nu_c}\nabla_{\hat{\perp}}T_{eV} + \frac{5}{2}p_e u_{\hat{\perp}} - \left(\frac{e}{m_e\nu_c}\right)^2\left(\frac{5}{2}en_e\langle\delta T_{eV}\delta E_{\vartheta}\rangle + q_{e\hat{\perp}}B - \frac{5m_e\nu_c}{2e}p_e u_{e\vartheta}\right)B, \tag{2-59}$$

where we have also substituted Eq. 2-57 for $q_{e\vartheta}$. Rearranging Eq. 2-59 to solve for $q_{e\hat{\perp}}$, we find

$$q_{e\hat{\perp}} = -\frac{5p_e}{2m_e\nu_c(1+\Omega_c^2)}\nabla_{\hat{\perp}}T_{eV} + \frac{5}{2}\frac{p_e u_{\hat{\perp}}}{(1+\Omega_c^2)} + \frac{5}{2}\frac{p_e u_{e\vartheta}\Omega_c}{(1+\Omega_c^2)} - \frac{5e^2n_e\langle\delta T_{eV}\delta E_{\vartheta}\rangle\Omega_c}{2m_e\nu_c(1+\Omega_c^2)}. \tag{2-60}$$

A common assumption in electron fluid models is that $\frac{5}{2}en_e\langle\delta T_{eV}\delta E_{\vartheta}\rangle = \frac{m_e\nu_a}{e}q_{e\vartheta}$, which should warrant investigation similar to checking whether $Q_a = \eta_a^E j_{e\vartheta}^2$.

2.4.2. Higher-Order Non-Maxwellian Effects on Heat Flux Transport

Section 2.4.1 assumed that there were no higher-order non-Maxwellian effects on heat flux transport. Accounting for these effects can be done with higher-order fluid models, as in Refs. 60 and 61. Perhaps the most important effect of higher-order moments of the electron EVDF on heat flux is on the parallel-field heat flux. As written, Eq. 2-55 indicates a high thermal conductivity along magnetic field lines, which in the discharge plasma is usually high enough to justify the assumption of or result in isothermal magnetic field lines [115,12]. It is important to note that the assumption of isothermal magnetic field lines has guided a significant amount of HETs design principles [12,13,17,115], but it is unclear how the invalidation of this assumption would affect the quality of these design principles. Both kinetic simulations [116,117] and ILTS measurements [118,119] have found that the electron temperature is not constant along magnetic field lines, indicating that Eq. 2-55 does not typically hold in the acceleration region of a HET. There can be ambiguity regarding whether deviation from Eq. 2-55 is due to non-Maxwellian effects or correlations due to parallel-field fluctuations. However, the simulation in Ref. 117 was explicitly studying non-Maxwellian effects and did not self-consistently simulation the azimuthal fluctuations and was able to capture non-isothermal magnetic field lines.

2.4.3. Other Higher-Order Non-Maxwellian Effects

Another significant effect of non-Maxwellian EVDFs is their impact on classical collision rates. This should have a significant effect on the continuity equations via the ionization rates, a likely minor effect on the electron equation via classical electron resistivity, and a non-negligible effect on the electron energy equation via the inelastic energy loss rate.

2.4.4. Anisotropic Effects

Beyond the magnetic mirror effect, it has been found that there can be significant effects from non-zero off-diagonal terms in the electron pressure tensor in a HET [117,120]. Particularly, the azimuthal component of the divergence produced by these off-diagonal pressure tensor terms can be significant in the azimuthal electron momentum equation, causing anomalous momentum transport that is not a direct consequence of plasma turbulence. Refs. 112 and 113 can be used as a reference for the transport equations for each component of the pressure tensor for magnetized electrons, Ref. 112 can be used as reference for the classical anisotropic relaxation rate, and Ref. 121 derived an anomalous anisotropic relaxation rate which could potentially be used as guide to derive a similar equation for the plasma conditions typical of a HET.

2.5. Chapter Summary

Regarding the review of the different causes of anomalous electron momentum transport in a HET, there is overwhelming evidence that plasma turbulence is the main cause, but other phenomena can still play a role. After reviewing the theoretical description of anomalous electron momentum transport, anomalous electron momentum transport can be accurately captured through Eq. 2-20, such that $u_{e\hat{\perp}}$ and $u_{e\vartheta}$ are directly related to anomalous electron momentum transport in a HET. In addition, we discuss and present experimental evidence of how anomalous electron heating and electron shear can indirectly influence anomalous electron momentum transport. We have also provided an order of magnitude analysis that supports the inclusion of inertial effects and the net magnetic mirror force in the parallel-field electron momentum equation. Importantly, we observe that these additional electron phenomena of electron heating, electron inertia, and the net magnetic mirror force can all be described through $u_{e\vartheta}$, $T_{e\perp}$, and $T_{e\parallel}$. Lastly, we have described how plasma turbulence can produce anomalous electron heating and anomalous electron heat flux transport, and we have reviewed how electron nonequilibrium effects can affect the electron continuity, momentum, energy, and heat flux equations. The main conclusion from this chapter is that state-of-the-art electron fluid models of HETs neglect several phenomena that can significantly affect electron transport in a HET and the predictive capability of calibrated HET simulations.

CHAPTER 3. Background: Review of Experimental Techniques

As we plan to make our own inference of the electron Hall parameter, we will review the previous techniques in the literature. The goal of this chapter is to learn from these previous techniques to gain some insight into how to improve the accuracy of empirical inferences of the electron Hall parameter. We will review the techniques on the basis of the theoretical assumptions made and on the accuracy of the direct measurements of plasma properties. Section 3.1 discusses the advantages and disadvantages of various plasma diagnostics in the context of measurements in the acceleration region of a HET. Section 3.2 reviews previous experimental techniques of inferring the electron Hall parameter, and Section 3.3 reviews semi-empirical techniques for inferring the electron Hall parameter.

3.1. Plasma Diagnostics in the Acceleration Region of a HET

To evaluate the quality of different inferences of the electron Hall parameter, in this section, we discuss the advantages and disadvantages of different plasma diagnostics from a theoretical perspective. However, from a practical perspective, we note that laser diagnostics are more complicated and expensive to implement. For the measurement of local plasma properties with electrostatic probes in the acceleration region, we will consider Langmuir probes and emissive probes. The optical diagnostics we will consider are those that have been used in EP testing for measurement of bulk plasma properties, namely laser-induced fluorescence (LIF), ILTS, optical emission spectroscopy (OES), and interferometry. We will first discuss the invasive nature of some of these diagnostics, and we will then discuss how the presence of a magnetic field affects each diagnostic.

3.1.1. Electrostatic Probes

Electrostatic probes are known to perturb the local plasma properties that they are trying to measure [32, 33]. This can be explained through plasma-wall interactions. As described in Section 2.2.2.1, a surface in contact with a plasma will attract different amounts of electron and ion current, depending on the difference in potential between the surface and the local plasma and the local electron temperature. In addition, the energy associated with these electron and ion current fluxes will also represent an energy loss to the plasma. Thus, if a probe is large enough, then the particle flux and energy flux from the plasma to the probe will represent a non-negligible contribution to the local conservation equations of the plasma, therefore changing the local plasma properties.

In addition to plasma perturbation, if placed in the acceleration region of a HET, a probe will experience significant energy flux from the plasma, which heats up and quickly damages the probe. Two solutions to this problem have been proposed. First, emissive probes and Langmuir probes have been placed on a high-speed axially reciprocating motion stage [37,38], which limits the time that the probes spend in the acceleration region; however, this does not solve the problem of plasma perturbation [33]. Second, Langmuir probes have been placed on the channel walls, which, using the assumption of isothermal magnetic field lines [115], can be used to infer the electron temperature across the acceleration region in an unshielded HET. Wall-mounted Langmuir probes have been shown to induce significantly less plasma perturbation than other configurations, and they are also not exposed to the high-energy ions in the acceleration region. Thus, wall-mounted Langmuir probes are an attractive option for electron temperature measurements across the acceleration region. However, we note that because of the magnetic field topology in MS HETs, wall-mounted Langmuir probes cannot be used to infer the electron temperature across the acceleration region in an MS HET.

In addition, the presence of a magnetic field requires clarification on the interpretation of the measurements of wall-mounted Langmuir probes. The direction normal to the surface of wall-mounted Langmuir probes is the radial direction, which in unshielded HETs, is approximately the parallel-field direction. The temperature measurement from Langmuir probes relies on the plasma-wall interaction theory described in Section 2.2.2.1 [34], and this theory assumes an isothermal electron temperature. Furthermore, in a good approximation, the electron flux arriving at the wall-mounted Langmuir probe is governed by parallel-field dynamics, such that the isothermal electron temperature appearing in Eq. 2-30 is the parallel-field electron temperature, $T_{e\parallel}$. Thus, while wall-mounted Langmuir probes seem to be able to provide an approximate measurement of $T_{e\parallel}$, they are unable to measure $T_{e\perp}$.

3.1.2. Optical Diagnostics

As opposed to electrostatic probes, optical diagnostics are known to be noninvasive, in that they do not perturb the plasma. Optical diagnostics can be divided into passive diagnostics and laser diagnostics. OES is a passive diagnostic that directly measures the natural emission spectrum of a plasma. Using collisional-radiative (CR) model, the electron density and electron temperature can then be inferred from the plasma emission spectrum [122]. While OES is in principle a line-of-sight diagnostic, tomographic techniques [123] have been used to make local measurements of electron density and temperature using OES [124]. However, because CR models depend on the rate of certain processes averaged over the EVDF, CR models are not well suited to distinguish between $T_{e\parallel}$ and $T_{e\perp}$, and the inferred electron temperature should be interpreted as the mean electron temperature.

Laser diagnostics are those that direct a laser beam through a plasma and either measure how the laser beam changes after passing through the plasma or measure the plasma's response to the laser beam. As such, laser diagnostics can be invasive, but at a low laser power density, the plasma perturbations are negligible. LIF and plasma interferometry methods for HETs both use continuous wave lasers with a power density of around 1 mW/mm^2 [125,126], while ILTS in HETs uses pulsed lasers with a power density of around 10^{15} W/m^2 during the pulse [127]. As such, LIF and plasma interferometry are essentially noninvasive, and care needs to be taken with ILTS measurements to ensure minimal plasma perturbation. Chapter 3 of Ref. 127 analyzes the laser-induced perturbations and presents bounds of the plasma conditions necessary for minimal perturbation based on the laser power density.

Plasma interferometry directly measures the phase shift of the laser beam that traverses the plasma relative to a reference beam and relates this phase shift to the path-averaged plasma density [126]. While the theory used in plasma interferometry neglects the magnetic field and electron pressure gradients [128], this can be justified for microwave sources since the magnetic force and the pressure gradient will be negligible on the fast time scale of the microwave [126]. In addition, using tomographic techniques, the local electron density can also be inferred from plasma interferometry measurements [126].

In LIF, a laser beam is injected into the plasma at a certain wavelength to induce a particular photon-absorption transition, and then light from spontaneous emission from the excited state is collected [129]. If the neutrals or ions are moving at a certain velocity, then photons from the laser beam will only excite the targeted transition if the Doppler-shifted laser wavelength is equal to the excitation wavelength [129]. As such, by varying the laser wavelength, the distribution of the collected light versus the laser wavelength is directly related to the VDF of the heavy species. While a magnetic field can complicate the LIF measurement via the Zeeman effect, it has been shown that if incident radiation is polarized parallel to the magnetic field, the effect is negligible.

In incoherent ILTS, a monochromatic laser beam is injected into the plasma, and this incident radiation elastically scatters off of free electrons. The mechanism of this scattering is that the electric field of the incident radiation accelerates the free electrons, and the accelerating free electrons then emit their own radiation, which is the scattered light. If an electron is moving at a given velocity, then there will be Doppler effects associated with the acceleration due to the incident radiation and with the emission process, such that the wavelength of the scattered light is Doppler shifted from the wavelength of the incident radiation [127]. Consequently, the spectrum of the scattered light is directly related to the EVDF. Because Thomson scattering is related to the acceleration of free charges due to the electric field of the incident radiation, electrons experience a significantly stronger acceleration than the significantly heavier ions, such that Thomson scattering from ions can be neglected [130]. In addition, if the electrons are moving at a velocity that is negligible compared to the speed of light, then the magnetic field does not influence the Thomson scattering [130]; this approximation is valid for electron temperatures below 5 keV. At the electron densities typical in a HET, Thomson scattering is a weak signal, which is why high-power lasers are needed for ILTS in a HET. Lastly, because the wavelength of the scattered light is only spectrally shifted by the velocities of the electrons, the incident wavelength is included in the collected spectrum of the scattered light, such that stray light from reflections at the incident wavelength can significantly distort the spectrum. Thus, unlike in LIF where the collected spectrum is away from the incident wavelength, in ILTS, the complete EVDF cannot be collected due to distortions around the center wavelength.

3.2. Experimental Techniques for Inferring the Effective Electron Hall Parameter

Having covered the necessary theoretical background, we are now in a position to analyze techniques that have been used to infer the electron Hall parameter. For each technique, we will summarize its shortcomings regarding underlying assumptions, uncertainty, and ambiguity of the measurements. As we will see, the essence of these inferences is to use Eq. 2-20 for the Hall parameter in terms of $u_{e\hat{\perp}}$ and $u_{e\vartheta}$. While there are no big differences between the techniques in how $u_{e\hat{\perp}}$ is inferred, the main differences between the methods are how $u_{e\vartheta}$ is inferred or measured.

3.2.1. First Axial Profile

Meezan *et al*. [30] built on the first inference of the effective electron Hall parameter made in Ref. 86 by measuring the axial ion velocity with LIF instead of inferring it from emissive probe measurements of the plasma potential and by making measurements at several axial locations along the channel centerline. Meezan *et al*. assume a purely radial magnetic field along the channel centerline such that the cross-field direction is the axial direction. As a result, Eq. 2-20 can be written to solve for the electron Hall parameter,

$$\Omega_e = -\frac{u_{e\theta}}{u_{ez}}. \tag{3-1}$$

To solve for $u_{e\theta}$, they assume a collisionless form of Eq. 2-19 with a negligible axial electron pressure gradient, such that

$$u_{e\theta} \approx \frac{E_z}{B}. \tag{3-2}$$

To solve for u_{ez}, they use the relation

$$u_{ez} = u_{iz} - \frac{I_d}{en_e A_c}. \tag{3-3}$$

Eq. 3-3 is derived from the current continuity equation,

$$\nabla \cdot j = 0, \tag{3-4}$$

where azimuthal gradients are neglected due to azimuthal symmetry and radial gradients are neglected due to symmetry at the channel centerline, such that

$$\frac{\partial j_{ez}}{\partial z} = -\frac{\partial j_{iz}}{\partial z}. \tag{3-5}$$

Integrating Eq. 3-5 from the anode to an axial position with anode boundary conditions of $j_{ez,0} = \frac{I_d}{A_c}$ and $j_{iz,0} = 0$ yields

$$j_{ez} - \frac{I_d}{A_c} = -j_{iz}, \tag{3-6}$$

from which the derivation of Eq. 3-3 is straightforward.

Meezan *et al*. directly measured u_{iz} with LIF, n_e with a Langmuir probe, and the plasma potential axial profile with an emissive probe. E_z can then be extracted from the plasma potential axial profile. Using an integrated neutral continuity equation similar to Eq. 3-3 and with LIF measurements of the neutral velocity, they were also able to infer ν_{en} to estimate ν_c. This allowed a comparison between the effective electron Hall parameter with the classical Hall parameter. Their results are shown in Fig. 3-1.

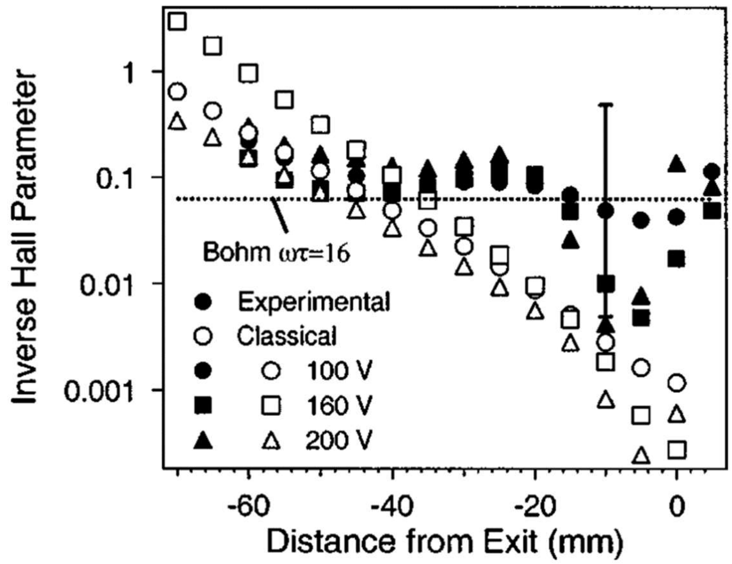

Figure 3-1: Reproduced from Ref. 30. Comparison of axial profile of experimentally inferred effective Hall parameter to classical Hall parameter at several discharge conditions.

The work by Meezan *et al*. was significant as their results were the first axial profiles of the effective electron Hall parameter in a HET. The main conclusions are that the Ω_e has strong axial variations, which contradicts the Bohm model of anomalous electron momentum transport, Eq. 2-45, and that the classical electron collision frequency can reasonably account for electron transport near the anode. While the work by Meezan *et al*. was an important step in understanding anomalous electron momentum transport in a HET, they make several simplifying assumptions (notably no diamagnetic drift), there are large uncertainties in the results, and the results are made ambiguous by the use of electrostatic probes.

3.2.2. First 2-D Map

Linnell *et al*. [31] built upon the measurements done by Meezan *et al*. [30] by reducing the number of assumptions in the electron momentum equations and by making a 2-D map of electron measurements that spanned across the entire acceleration region and the width of the discharge channel. They used Eq. 2-20 to solve for the electron Hall parameter in terms of $u_{e\theta}$ and $u_{e\hat{\perp}}$. To solve for $u_{e\theta}$, they plug Eq. 2-20 into Eq. 2-17, assuming an isotropic electron pressure tensor and neglecting the ion velocity term, to obtain

$$u_{e\theta} = \frac{\Omega_e}{(1+\Omega_e^2)} \frac{E_{\hat{\perp}}}{B} + \frac{\Omega_e}{(1+\Omega_e^2)} \frac{\partial_{\hat{\perp}} p_e}{eB\ {}_e}. \tag{3-8}$$

They then use the ideal gas law to write $p_e = n_e k_b T_e$.

To solve for $u_{e\hat{\perp}}$, Linnell *et al.* start by using Eq. 3-6 to solve for j_{ez} at a given axial location. Because they made a 2-D map of measurements, using Eq. 3-6 requires assuming that the radial electron and ion current densities are radially uniform. Although it is not explicitly stated in their formulation, we assume that Linnell *et al.* related $u_{e\perp}$ to j_{ez} through

$$j_{ez} \approx e n_e (z_{\hat{\perp}} u_{e\hat{\perp}} + z_{\parallel} u_{e\parallel}), \tag{3-9}$$

where $z_{\hat{\perp}} = \hat{\beta}_{\perp} \cdot \hat{z}$ and $z_{\parallel} = \hat{\beta}_{\parallel} \cdot \hat{z}$. To solve for $u_{e\parallel}$, Linnell *et al.* used a modified form of Eq. 2-18,

$$u_{e\parallel} = -\mu_e E_{\parallel} - D_e \frac{\partial_{\parallel} n_e}{n_e} - D_e \frac{\partial_{\parallel} \mathrm{B}}{B}, \tag{3-10}$$

where the ion resistivity is neglected, as in Eq. 3-8, the electron temperature is assumed be isothermal along magnetic field lines, and $D_e = \frac{k_B T_e}{m_e \nu_e}$ is the electron diffusion coefficient. The last term, $D_e \frac{\partial_{\parallel} \mathrm{B}}{B}$ is the magnetic mirror force term, written in the same form as in Ref. 106. This form of the magnetic mirror force is incomplete, however, as it is not the manifestation of an anisotropic pressure tensor.

From Eqs. 2-20, 3-6, 3-8-3-10, a numerical solver could be used to solve for Ω_e, $u_{e\theta}$, $u_{e\perp}$, $u_{e\parallel}$, and j_{ez} if values for $E_{\perp}$, n_e, T_e, and j_{iz} are provided. Linnell and Gallimore measured n_e and T_e with a Langmuir probe and the plasma potential with an emissive probe. From the 2-D measurements of ϕ, $E_{\parallel}$ and $E_{\perp}$ can be calculated through $\vec{E} = -\nabla\phi$, and the ion velocity is found through 1-D electrostatic acceleration with an upstream boundary condition. j_{iz} is then assumed to be radially uniform and is calculated through $j_{iz} = \frac{\int en_i u_{iz} dA}{A_c}$ where the integral is taken over the entire cross-sectional area of the channel and the ion density is obtained through assuming quasineutrality. To make probe measurements inside the discharge channel and in the acceleration region, they used high-speed axially reciprocating probes. Linnell *et al*. carried out these measurements and analysis at two operating conditions, and the 2-D maps of Ω_e are shown in Figs. 3-2 and 3-3.

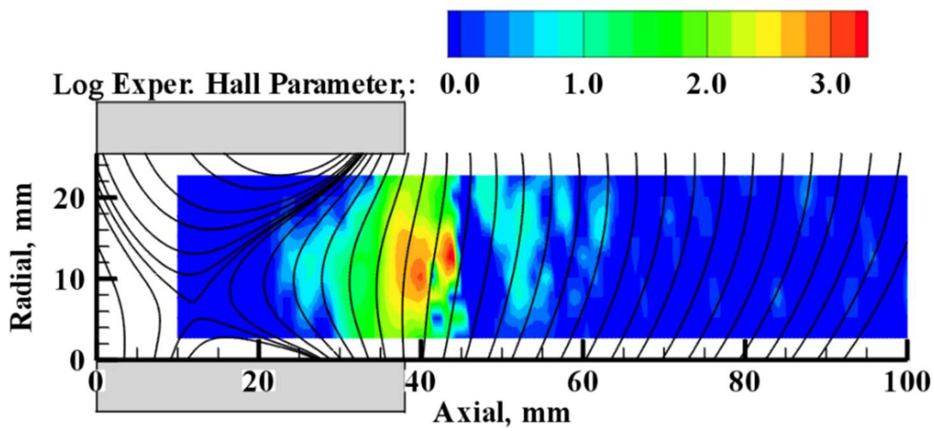

Figure 3-2: Reproduced from Ref. 31. 2D map of experimentally inferred effective Hall parameter at a discharge voltage of 300 V.

These were the first inferences of the electron Hall parameter across the entire acceleration region, both axially and radially. Linnell *et al*. stated that Eq. 3-6 overestimates j_{ez} downstream of the channel exit because neglecting ion divergence underestimates the ion current. While they do not neglect electron pressure like Meezan *et al*., Linnell *et al*. exclusively rely on probe measurements, which increases the ambiguity of the measurements. Also, even though their assumption of isothermal electron temperature along magnetic field lines should not have significantly affected their results, it has been shown that this assumption does not always hold in a HET [131,132]. In addition, they assume an isotropic electron collision frequency, which, as discussed in Section 2.2.1, is not expected to be accurate due to plasma turbulence. However, the effect of assuming an isotropic electron collision frequency is not well understood. Lastly, because of the reliance on probes, the uncertainty in the results is likely large, although the uncertainties are not shown.

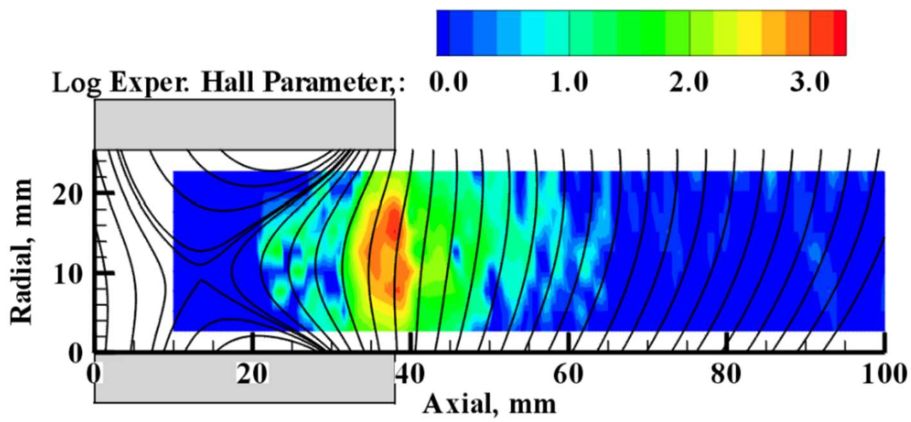

Figure 3-3: Reproduced from Ref. 31. 2D map of experimentally inferred effective Hall parameter at a discharge voltage of 500 V.

3.2.3. First Noninvasive and Time-Resolved Inference

Instead of focusing on Ω_e, Dale *et al*. [39] focused on the electron collision frequency. Dale *et al*. made the first experimental inference of the anomalous electron collision frequency using almost exclusively optical diagnostics. In addition, they made the first (and still the only) time-resolved inference of the anomalous electron collision frequency. For the cross-field electron momentum equation, they made similar assumptions to Linnell *et al*. [31], using Eq. 2-17 with an isotropic electron pressure tensor, but including the ion velocity term. Like Meezan *et al*. [30], they only made channel centerline measurements such that they approximated the cross-field and parallel-field directions as the axial and radial directions, respectively. As such, Eq. 2-17 can be rearranged into a typical form of the axial component of generalized Ohm's law,

$$E_z = \eta j_{ez}(1 + \Omega_e^2) - \frac{\partial_z p_e}{e n_e} + \eta_{ei} j_{iz}. \tag{3-11}$$

To relate j_{ez} to j_{iz}, they made the same assumptions of radial symmetry and radially uniform discharge current to use Eq. 3-6. In this manner, assuming that the magnetic field, discharge current, and channel geometry are known, then the effective electron collision frequency is a function of E_z, u_{iz}, n_e, and T_e. Next, to calculate the anomalous electron collision frequency, they break up the effective electron collision frequency into

$$\nu_e = \nu_{en} + \nu_{ei}^m + \nu_a. \tag{3-12}$$

Calculating ν_{en} requires the additional unknown of the neutral density, such that the anomalous electron collision frequency is a function of E_z, u_{iz}, n_e, n_n, and T_e.

While LIF offers direct measurements of u_{iz}, Dale *et al*. developed a method to use LIF to also infer E_z, n_e, n_n, and T_e. The method is based on the LIF measurement of the axial IVDF and takes the zeroth, first, and second moments of the unsteady Boltzmann equation to directly relate the moments of the axial IVDF to E_z, $n_e n_n \langle \sigma_{iz} v_e \rangle$, and $\frac{\partial n_e}{\partial z}$, where $\langle \sigma_{iz} v_e \rangle$ is a function of the electron temperature. To calculate n_e everywhere, a boundary condition for n_e was required. This boundary condition was obtained with a Faraday probe measurement of j_{iz} combined with the LIF measurement of u_{iz}. With knowledge of the ionization rate, the neutral density was then calculated via the neutral continuity and momentum equations and appropriate boundary conditions for the neutral density and velocity. These boundary conditions were based on the anode mass flow rate and the neutral temperature. Then, with knowledge of n_e, n_n, and $n_e n_n \langle \sigma_{iz} v_e \rangle$, the electron temperature could then be inferred assuming Maxwellian electrons. Like CR models used in OES, because this inference of electron temperature is based on a rate coefficient, this inference of the electron temperature is representative of the mean electron temperature, so the axial electron pressure gradient is likely underestimated. The main finding from Dale *et al*. was that the ν_a oscillates strongly with the breathing mode. As discussed in Section 2.2.1.1, this is not surprising, as strong oscillations in the fluid plasma properties will change the characteristics of the turbulence and thus cause oscillations in ν_a.

Due to the phase-resolved and noninvasive measurements, the work by Dale *et al*. represented significant progress in experimental inferences of the electron Hall parameter (or electron collision frequency). While the assumptions are mostly sound, the inference is limited by two main assumptions. First, because they only made measurements at the channel centerline, they assumed radial symmetry at the channel centerline and a radially uniform discharge current. Known radial asymmetries are the position of the cathode and the radial distribution of the magnetic field strength. Second, they assume an isotropic electron temperature. In addition, they assume an isotropic electron collision frequency, but this should not have influenced their results, as they only made measurements in regions where $\Omega_e \gg 1$. Lastly, regarding assumptions in their time-resolved measurements, Dale and Jorns acknowledge that the Faraday probe measurement is a time-averaged measurement, such that they have a static boundary condition for the ion flux.

3.2.4. First Inference with Thomson Scattering

Roberts *et al*. [40] made direct measurements of the azimuthal electron drift velocity using ILTS. This greatly simplifies the inference of the electron Hall parameter using Eq. 3-1, because the form of Eq. 3-8 no longer needs to be used to first infer $u_{e\theta}$ from other plasma properties. Roberts and Jorns made channel centerline measurements such that the cross-field direction could be assumed to be purely axial. To infer u_{ez}, Roberts *et al*. use a form of Eq. 3-3 with a downstream boundary condition of $j_{ez,0} = \frac{en_e u_{iz,ex}}{\eta_B}$, where $en_e u_{iz,ex}$ represents the ion beam current density at the measurement point furthest downstream at the channel centerline. The axial ion velocity was obtained with LIF, and η_B was measured using a Faraday probe. To convert between j_{ez} and u_{ez}, electron density was measured using ILTS. Roberts *et al*. denote the inferred electron Hall parameter from this method as Ω_B.

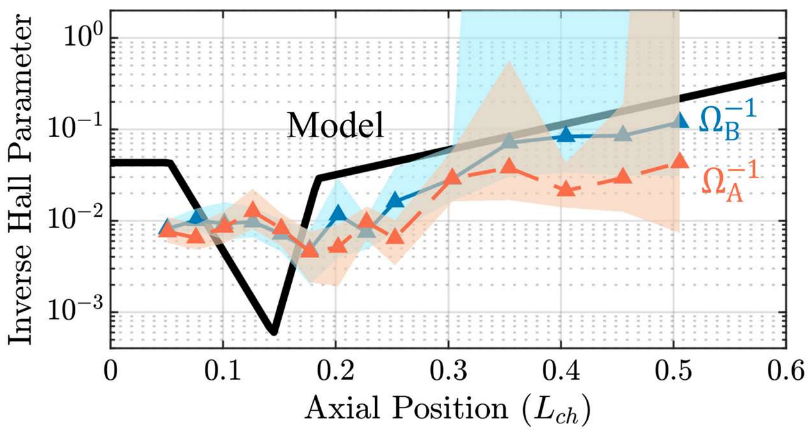

Figure 3-4: Reproduced from Ref. 40. Comparison of the LIF-calibrated axial profile of the Hall parameter (Model) with the two experimentally inferred axial profiles of the Hall parameter using two different methods (Ω_A and Ω_B)

Roberts *et al*. made a second inference of Ω_e, denoted Ω_A, using the collisionless form of Eq. 2-19 to solve for $u_{e\theta}$. For this inference, the electron pressure was calculated using the ideal gas law and ILTS measurements of n_e and $T_{e\perp}$, E_z was inferred from the LIF measurements of u_{iz}, and u_{ez} was inferred in the same way as for Ω_B. The inferred profiles of Ω_A and Ω_B are shown in Fig. 3-4 alongside an LIF-calibrated profile of Ω_e from a simulation.

The profile of Ω_A is the first profile of Ω_e that uses electron temperature measurements from ILTS, and the profile of Ω_B is the first profile of Ω_e that uses azimuthal electron drift velocity measurements from ILTS. Critically, Roberts *et al*. measured the azimuthal electron temperature, which is expected to be representative of $T_{e\perp}$, such that Ω_A is the first inference of Ω_e that correctly accounts for the anisotropy in electron temperature. The first finding is that both experimental values agree within their uncertainties, which is a validation of both methods. The second finding is that the experimental profiles don't exhibit the strong peak in Ω_e that the calibrated profile does. Roberts and Jorns reason that a possible reason for this discrepancy is that the ILTS measurements of $T_{e\perp}$ are around double that of the isotropic electron temperature from the calibrated simulation. These results indicate the importance of having an accurate measurement of $T_{e\perp}$ when inferring the effective electron collision frequency, which we had suggested in Section 2.2.4. Therefore, because Langmuir probes and simulations are currently unable to capture the same electron temperatures as ILTS, ILTS measurements are critical to making accurate inferences of the electron Hall parameter. Another important finding by Roberts *et al*. shown in Fig. 3-5, although not entirely surprising, is that the measured $u_{e\theta}$ from ILTS used to calculate Ω_B was in very close agreement with the inferred $u_{e\theta}$ used to calculate Ω_A, which is equal to the sum of the E×B and diamagnetic drifts. The main conclusion from this finding is that an isotropic electron temperature within the cross-field plane is an accurate assumption. While the initial implication from this is that $u_{e\theta}$ can be inferred from only E_z, n_e, and $T_{e\perp}$, an alternative conclusion is that E_z can be inferred from $u_{e\theta}$, n_e, and $T_{e\perp}$, which can all be measured with ILTS.

However, the Hall parameter profiles have an especially large uncertainty in the downstream portion of the profiles. These large uncertainties can be attributed to large relative uncertainties in the downstream measurements of $u_{e\theta}$ and E_z for Ω_B and Ω_A, respectively. In fact, when $u_{e\theta}$ crosses zero, this creates an unphysical singularity in Ω_e^{-1}. The main drawback of the measurements is that ILTS is unable to probe inside the discharge channel. This prevents the measurement technique from measuring across the entire axial extent of the acceleration region; this can be seen in their measured $u_{e\theta}$, with the most upstream point being the peak value. As these inferences are made noninvasively and are the first to directly measure $u_{e\theta}$ and to accurately measure the diamagnetic drift, the work by Roberts *et al*. represents the most accurate inferences of the electron Hall parameter to date. However, the main limitation of these inferences is the 1-D nature of channel centerline measurements, which influences the accuracy of the inferred u_{ez}. Lastly, while the inference of Ω_B is robust to an anisotropic electron Hall parameter, the inference of Ω_A assumes an isotropic Hall parameter, but like Dale *et al*. [39], they only made measurements in regions of $\Omega_e \gg 1$, so this should not have influenced their results.

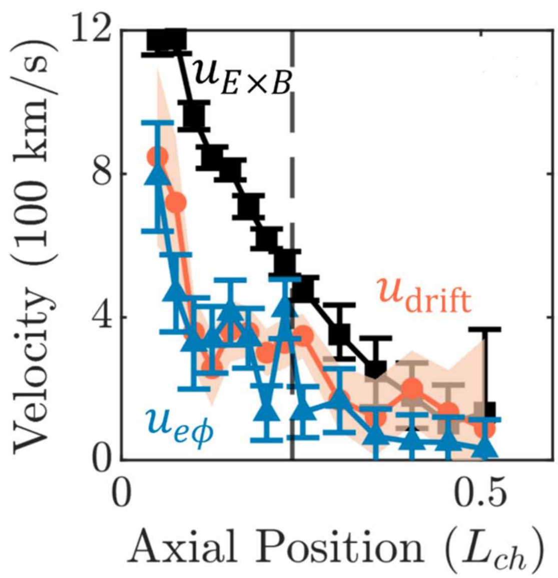

Figure 3-5: Reproduced from Ref. 40. Comparison of different inferences and measurements of the axial profile of the azimuthal electron. Direct measurement from ILTS is denoted as $u_{e\phi}$. E×B velocity with E_z obtained from LIF measurements is denoted as $u_{E\times B}$. u_{drift} is the sum of the E×B drift and the diamagnetic drift, where LIF measurements are used to obtain the E×B drift and ILTS measurements are used to obtain the diamagnetic drift.

3.3. Semi-Empirical Techniques for Inferring the Effective Electron Collision Frequency

Semi-empirical techniques use direct plasma measurements to calibrate a HET simulation in order to obtain an axial profile of the anomalous electron collision frequency, ν_a, that produces a simulation that matches the plasma measurements. The key to calibrating simulations is to provide plasma measurements across the entire acceleration region that are strongly dependent on the ν_a.

By rearranging Eq. 2-17 to solve for the cross-field electric field, we arrive at common form of generalized Ohm's Law,

$$E_{\hat{\perp}} = \eta_e j_{e\hat{\perp}}(1 + \Omega_e^2) - \frac{\partial_{\hat{\perp}} p_{e\perp}}{en_e} + \eta_{ei} j_{i\hat{\perp}}, \tag{3-13}$$

which shows that the electron Hall parameter plays an important role in establishing the cross-field electric field. Consequently, measurements of plasma properties that are closely tied to $E_\perp$ are well-suited for calibrating HET simulations. In this section, we will present some LIF-calibrated and Langmuir probe-calibrated profiles of ν_a and will then discuss the limitations of state-of-the-art calibrated HET simulations and the need for improved calibrated HET simulations. Regarding the limitations of calibrated HET simulations, we will focus on the unknown physics regarding the off-centerline ν_a and regarding anomalous electron heating.

3.3.1. Calibrated Results

Measurement techniques for direct measurement of the electric field are not sensitive enough to work on HETs, so the plasma properties chosen for calibration are those that depend strongly on the electric field. As a result, the two plasma properties that have been used to calibrate simulations are the axial ion velocity and the electron temperature. u_{iz} is the most common choice for calibrating simulations because ions are approximately accelerated electrostatically and because LIF is able to provide noninvasive measurements of u_{iz} across the entire acceleration region. Electron temperature has been used to calibrated simulations assuming that the dominant source of electron heating is the phenomenological model of anomalous Joule heating. Wall-mounted Langmuir probes have been used to provide electron temperature measurements across the entire acceleration region of an unshielded HET. However, as we analyzed in Section 2.3.1, $E_{\perp}$ may not play a significant role in electron heating, bringing into doubt the usefulness of using electron temperature to calibrate for ν_a.

Figure 3-6 shows the calibrated channel-centerline axial profile of ν_a for an LIF-calibrated simulation and Langmuir probe-calibrated simulation for the same HET at the same discharge condition. It can be seen that the two calibrations have a discrepancy in the location of the minimum anomalous electron collision frequency of around a quarter of a channel length. In addition, for the wall-mounted Langmuir probe-calibrated simulation, the entire acceleration region is shifted around a quarter of a channel length upstream with respect to the LIF-calibrated simulation. Given that LIF measurements are noninvasive and are insignificantly influenced by the magnetic field in a HET, the LIF measurements are reliable, which suggests that the Langmuir probe-calibrated simulation is inaccurate. Consequently, LIF is the most common choice for calibrating HET simulations. The inaccuracy of the Langmuir probe-calibrated simulation is likely due to two issues. First, as discussed in Section 3.1.1, wall-mounted Langmuir probes cannot give an accurate measurement of $T_{e\perp}$. Second, in the presence of anomalous electron heating, the electric field cannot be properly inferred from accurate electron temperature measurements, since Joule heating would not be able to be distinguished from anomalous heating.

Lastly, it is important to note that even for the LIF-calibrated simulations, Fig. 3-7 shows that the calibrated profiles of the measured plasma properties do not exactly match the measured profiles of the same properties. As a result, these calibrations are not self-consistent. This indicates that there is still some missing physics in the LIF-calibrated simulations.

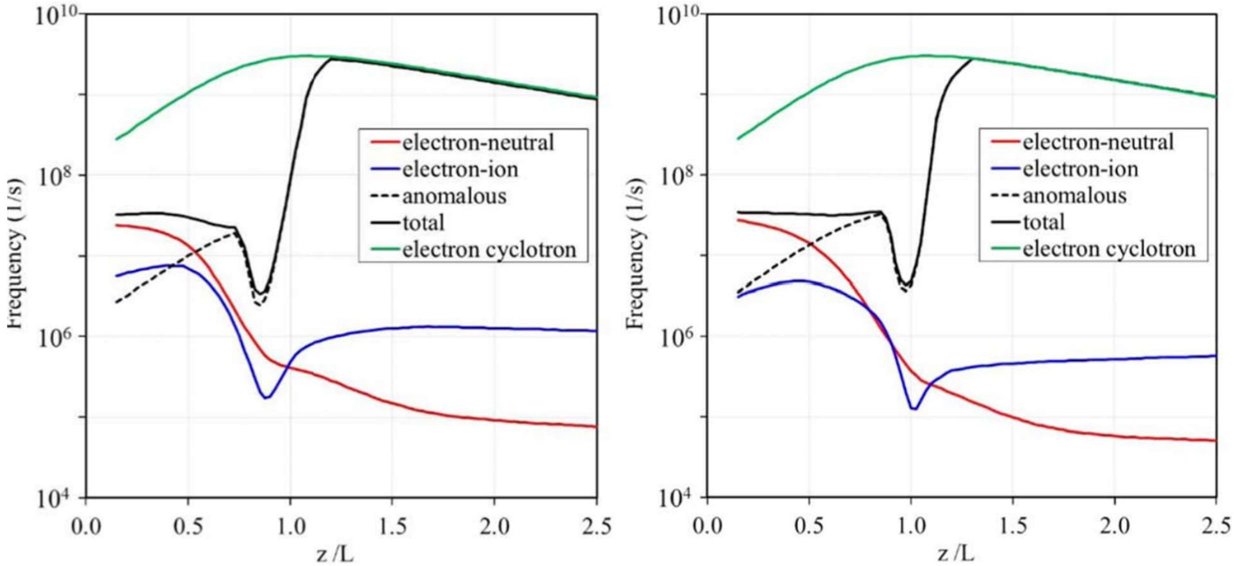

a) b)

Figure 3-6: Reproduced from Ref. 41. a) Axial profile of different electron collision frequencies in a HET simulation calibrated with wall-mounted Langmuir probe measurements of the electron temperature. b) Axial profile of different electron collision frequencies in a HET simulation calibrated with LIF measurements of the axial ion velocity.

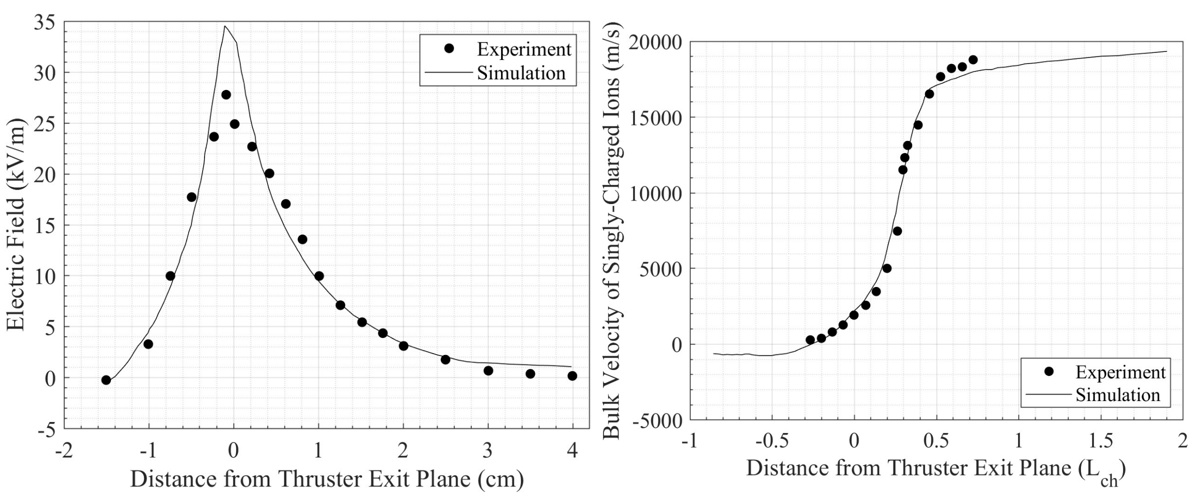

a) b)

Figure 3-7: a) Data extracted from Ref. 42. Comparison between experimental inference of the electric field from LIF measurements and electric field from a simulation calibrated on those same LIF measurements. b) Data extracted from Ref. 51. Comparison between LIF measurement of ion bulk axial velocity and ion bulk axial velocity from a simulation calibrated on those same LIF measurements. Axial distance is normalized by the length of the discharge channel, L_{ch}.

3.3.2. Limitations of State-of-the-Art Calibrated HET Simulations

The most in-depth presentation of the calibrated HET simulations is Ref. 41, so this section will mostly use Ref. 41 and related work as an example of state-of-the-art calibrated HET simulations. Also, because LIF measurements are the most common choice for calibrating simulations, unless otherwise specified, "calibrated" simulations will be used to refer to "LIF-calibrated" simulations. It is important to point out that calibrated HET simulations do not directly input the LIF measurements as the solution for u_{iz} in the simulation. Instead, they use a piece-wise curve for the anomalous collision frequency with multiple fitting parameters and manually tune the fitting parameters until the simulation close matches the LIF profile of u_{iz} and measurements of thrust and discharge current. This is the preferred method because simply inputting the LIF measurements into the simulation would not self-consistently produce the measured discharge current and thrust, so an exact match to the LIF measurements is sacrificed in favor of the simulation reproducing the measured values of discharge current and thrust. While Ref. 41 uses a leading constant on the piece-wise anomalous collision frequency to tune for the discharge current, they noticed that they could scale the upstream portion of the anomalous electron collision frequency to tune for the thrust with minimal effect on the axial ion velocity profile. It is important to note the insensitivity of the axial ion velocity profile to upstream portion of the anomalous electron collision frequency, but it is equally important to note some of the missing physics in the simulations that prevent the LIF measurements from producing self-consistent calibrated simulations.

To date, calibrated simulations are almost exclusively calibrated on measurements at the channel centerline. For 2-D (axial-radial) simulations it is then important to consider how to relate the centerline measurements to the off-centerline values of ν_a. This is because the off-centerline anomalous electron collision frequency directly influences the discharge current and the thrust.

From Eq. 2-20, the local $u_{e\perp}$ is approximately proportional to the local ν_e, so the radial distribution of ν_e is closely tied to radial distribution of the cross-field electron current density. Consequently, incorrect off-centerline values of ν_e would produce an incorrect value for the discharge current even if the channel centerline values of ν_e is correct. In addition, the magnetic field lines are not purely radial away from the channel centerline, so $E_\perp$ has a non-negligible radial component. The radial electric field is responsible for the divergence in the plume of a HET, which can produce thrust inefficiencies around 5%. As a result, since $E_\perp$ is strongly tied to the anomalous electron collision frequency and off-centerline values of $E_\perp$ contribute to plume divergence, the off-centerline values of ν_e can influence the thrust of a calibrated simulation.

Additionally, accurate off-centerline plasma properties are critical to accurately model life-limiting erosion rates. In unshielded HETs, the main life-limiting erosion mechanism is high energy ions striking and gradually eroding the discharge channel walls through sputtering, such that accurate plasma properties close to the discharge channel walls are necessary for accurate erosion predictions. Specifically, ion flux to the wall scales as $\sqrt{T_e}$, and the ion velocity as it strikes the wall scales as $\sqrt{\Delta\phi_w}$, where $\Delta\phi_w$ is the potential drop across the sheath that separates the wall from the plasma. To accurately capture T_e and ϕ near the channel walls it is then necessary to have a calibrated simulation that accurately captures the off-centerline physics. For MS HETs, the magnetic field topology is designed with the assumptions of isothermal and equipotential magnetic field line in minds to substantially reduce T_e and ϕ near the channel walls. As such, in MS HETs, the T_e and ϕ near the channel walls are approximately the same as those near the anode, which reduces channel erosion by 2-3 orders of magnitude [12,13]. However, the magnetic field topology in MS-HETs also shifts the plasma downstream which makes the inner and outer front pole covers on the front face of the thruster more susceptible to erosion [51]. As a result, while pole erosion in

MS HETs is much slower and thus easier to mitigate than channel erosion in unshielded HETs, it is the life-limiting mechanism in MS HETs and has become the subject of several research efforts [50-55, 133-135].

Recent simulations that account for anomalous ion heating in the front pole regions due to a lower-hybrid drift instability and for the global oscillation of plasma during the breathing mode have been able to successfully match erosion rates at the inner front pole at several discharge conditions [55]. However, these simulations still cannot account for erosion rates at the outer front pole [50]. Ref. 50 explains that the erosion rate at the outer pole is very sensitive to the upstream values of the anomalous electron collision frequency and to global oscillations due to the breathing mode. Because these simulations are calibrated on time-averaged LIF measurements, they cannot self-consistently account for the breathing mode, and as previously mentioned, the ion velocity that is used for the calibration with the LIF measurements is not very sensitive to large changes in the upstream anomalous electron collision frequency. As a result, Ref. 50 stresses the importance of finding a closure for anomalous electron momentum transport to be able to self-consistently account for the effect of the breathing mode on pole erosion. In addition, we note that the model for anomalous ion heating used in Ref. 55 depends on electron temperature, which indicates the importance of having accurate values of electron temperature to properly evaluate a model of anomalous ion heating. Also, it was observed in Refs. 41 and 52 that the predicted pole erosion was dependent on the electric field near the edges of the discharge channel and near the channel exit plane. This can be explained by the fact that the electric field in this region determines the ion divergence at the outer edges of the acceleration region, which influences the ion flux to the front poles. In fact, Ref. 52 showed that if finite-sheath effects are considered near the edges of the front poles, then predicted pole erosion rates are even more dependent on the electric field near the edges of the discharge channel and, in certain cases, can account for the pole erosion. This is because an increased ion divergence caused by the electric field in this region could substantially increase the number of ions that enter the sheath at the edges of the front poles. The size of the sheath also depends on the local electron temperature. Consequently, to accurately assess the mechanisms that cause pole erosion in MS-HETs, it is necessary to have calibrated simulations that accurately capture the off-centerline physics of anomalous electron momentum transport and anomalous electron heating near the channel exit plane.

For off-centerline anomalous electron momentum transport in Ref. 41, they use

$$\nu_a(\beta) = \nu_a(\beta_{CL})\left(\frac{B(\beta)}{B(\beta_{CL})}\right)^d \tag{3-14}$$

to scale the anomalous electron collision frequency along a magnetic field line, where β_{CL} is the field line coordinate at the channel centerline and β is a general field line coordinate. In Ref. 41, the authors assume $d = 1$, which forces a Bohm-like scaling for the off-centerline anomalous electron collision frequency. However, the authors acknowledge that this choice of d is arbitrary. It is thus clear that a good understanding of the off-centerline scaling of the anomalous electron collision frequency is needed to improve the self-consistency and accuracy of simulations calibrated with centerline measurements.

Regarding anomalous electron heating, state-of-the-art calibrated simulations use the phenomenological model of $Q_a = \eta_a j_{e\vartheta}^2$, which can have two main effects on a LIF-calibrated simulation. First, even with accurate LIF measurements, electron temperature influences both $E_\perp$ and $E_\parallel$. Second, as shown in Section 3.2.4, even if $E_\perp$ is correct, an incorrect electron temperature can significantly affect the accuracy of the calibrated profile of ν_a.

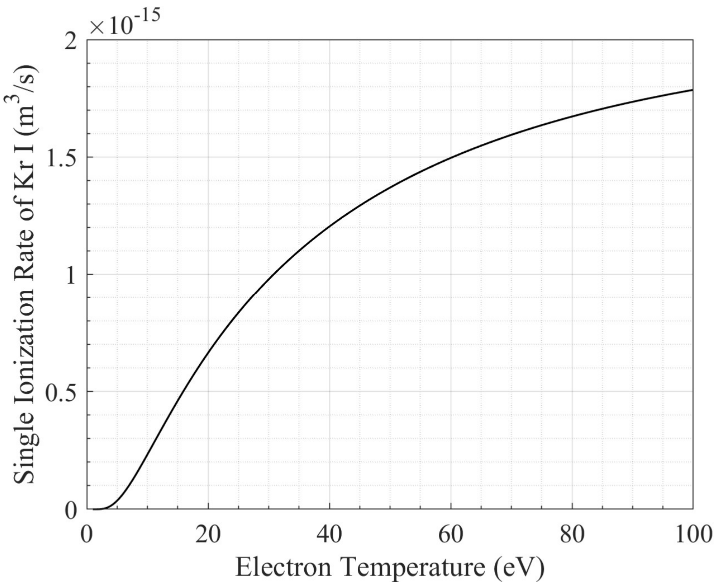

Figure 3-8: Electron-impact single ionization rate, $\langle \sigma_{iz} v_e \rangle$, of a krypton atom as a function of electron temperature. Calculated assuming a Maxwell-Boltzmann speed distribution for electrons and using the cross-sections from Ref. 136.

To see the effect of electron temperature on $E_{\hat{\perp}}$ inferred from LIF measurements, we consider a simplified form of the steady-state cross-field ion momentum equation

$$m_i n_i u_{i\hat{\perp}} \nabla_{\hat{\perp}} u_{i\hat{\perp}} = e n_i E_{\hat{\perp}} - m_i n_e n_n \langle \sigma_{iz} v_e \rangle u_{i\hat{\perp}}, \tag{3-15}$$

where ions collisions, ion pressure, radial gradients, and neutral velocity are neglected, and we have written out the ionization frequency. Physically, the second term on the right-hand side of Eq. 3-15 represents the reduction of the average ion velocity due to ions that are born with zero velocity, which is directly related to voltage utilization efficiency, as discussed in Section 1.3.2. As seen in Fig. 3-8, $\langle \sigma_{iz} v_e \rangle$ increases approximately linearly in the region of electron temperatures observed in a HET. At the peak of the acceleration region, the ionization term is negligible compared to the electrostatic acceleration term, but if the electron temperature is incorrectly too low, then $E_{\hat{\perp}}$ would artificially decrease at the outer portions of the acceleration region. In addition, if the electron temperature is incorrectly too low where the ionization and acceleration regions overlap, then the voltage utilization efficiency and the thrust would artificially increase. Therefore, an accurate electron temperature axial profile is necessary for an accurate axial profile of $E_{\perp}$ and for an accurate voltage utilization efficiency.

Regarding the effect of anomalous electron heating on $E_{\parallel}$, it is important to also consider the net magnetic mirror force, which cannot be considered in LIF-calibrated simulations that do not account for an anisotropic electron temperature. Accounting for electron temperature anisotropy and adding the net magnetic mirror force and the centrifugal force, we recall our modified parallel-field electron momentum equation, Eq. 2-47, and rearrange it to solve for $E_{\parallel}$

$$E_{\parallel} = \eta_e j_{e\parallel} - \frac{\partial_{\parallel}(n_e T_{eV,\parallel})}{n_e} + \left(T_{eV,\parallel} - T_{eV,\perp}\right)\frac{\partial_{\parallel} B}{B} + \frac{m_e u_{e\vartheta}^2}{er}\left(\hat{\beta}_{\parallel} \cdot \hat{r}\right) + \eta_{ei} j_{i\parallel}. \qquad (3\text{-}16)$$

Evidently, anisotropic anomalous electron heating can create a nonzero net magnetic mirror force, which, from the discussion in Section 2.2.5, implies that anomalous electron heating can influence the ion beam divergence, mostly influencing life-limiting erosion rates, but also influencing thrust. Because of its impact on erosion rates and thrust, anomalous electron heating needs to be correctly accounted for to improve the predictive capability of LIF-calibrated simulations. However, given accurate LIF-measurements of u_{iz}, inferring the axial electron current density at the channel centerline from Eq. 3-3 should not depend strongly on the electron temperature. As a result, accounting for anomalous electron heating should not be critical for LIF-calibrated simulations to self-consistently reproduce the measured discharge current.

Additionally, even if accurate LIF measurements are able to produce an accurate profile of $E_{\perp}$, anomalous electron heating can strongly influence the inferred effective electron collision frequency. As discussed in Section 2.2.4 and as demonstrated by Ref. 40, anomalous anisotropic electron heating can significantly increase the cross-field pressure gradient. Therefore, it is crucial to account for anomalous electron heating to obtain accurate profiles of ν_a from LIF-calibrated simulations. This has significant implications for using calibrated simulations to assess models of anomalous electron momentum transport.

3.3.3. Path to Improve Calibrated Simulations

Calibrated simulations serve two main goals. One goal is to obtain profiles of the anomalous collision frequency that can be used as the ground truth to which theories of anomalous electron momentum transport can be compared. The benefits of these calibrated simulations compared to the purely experimental techniques are that the calibrated profiles generally require fewer assumptions and that the calibrated simulations also output all the plasma properties. This second benefit is especially important for the validation of theories of anomalous electron momentum transport that depend on a variety of plasma properties. The other main goal of calibrated simulations is to be able to serve as accelerated lifetime tests for HETs [90]. If, given accurate local plasma properties, HET simulations can accurately predict the life-limiting erosion rates, then correctly calibrated simulations could be used to determine the lifetime of the HET. While a long-duration lifetime test can take more than a year of testing, accelerated lifetime tests can still take 800 hours. On the other hand, the process of obtaining the measurements necessary to calibrate simulations would be on the order of a few days, so correctly calibrated simulations would drastically reduce the amount of HET testing time required for a lifetime test.

As previously discussed, calibrated simulations need to account for anomalous electron heating to correctly calibrate ν_a. Since the theory of anomalous electron heating is as unknown as that of anomalous electron momentum transport, the only way to account for anomalous electron heating is to have accurate measurements of the electron temperature. Thus, the combination of an accurate inference of $E_\perp$ with an accurate measurement of the electron temperature is critical for the validation of theories of anomalous electron momentum transport. Also, it is important to note that in the hypothetical case that an accurate profile of ν_a is obtained with an inaccurate electron temperature, a theory of anomalous electron momentum transport that depends on electron temperature would not be able to be properly checked on the accurate profile of ν_a. Since many theories of anomalous electron momentum transport depend on the electron temperature, this is another reason why accurate electron temperatures are needed for the validation of theories of anomalous electron momentum transport.

In addition to neglecting anomalous electron heating, we have also learned that, for the most part, experimental and semi-empirical inferences of Ω_e or ν_a rely exclusively on measurements at the channel centerline. Also, the relationship between ν_a at the channel centerline and the off-centerline ν_a is unknown, and this relationship likely affects the resultant discharge current, thrust, and erosion rates from a simulation calibrated on channel centerline measurements. Therefore, to improve the predictive capability of calibrated simulations, off-centerline measurements that can elucidate the off-centerline physics of anomalous electron momentum transport and anomalous electron heating are required. Lastly, the ideal calibration would temporally resolve large amplitude plasma oscillations.

3.4. Lessons Learned from Review of Techniques

While early techniques of observing anomalous electron momentum transport identified that anomalous electron momentum transport in a HET did not follow Bohm diffusion, these early techniques relied heavily on probe techniques that can perturb the plasma and that do not produce accurate measurements of electron temperature when electrons are magnetized. We then described a technique that almost exclusively uses LIF to infer the time-resolved anomalous electron collision frequency and electron temperature. This technique found that the anomalous electron collision frequency oscillates with the breathing mode and was able to infer electron temperature higher than those measured by Langmuir probes. The technique of inferring electron temperature presented in Ref. 39 has not been compared to direct measurements of electron temperature using ILTS, so the accuracy of the electron temperature in Ref. 39 is in question, especially because it assumes an isotropic electron temperature. However, Ref. 39 did find that the force due to the cross-field electron pressure gradient was comparable to the electrostatic force. This finding was confirmed with simultaneous LIF and ILTS measurements in Ref. 40, which provided experimental evidence that an underestimation of the electron pressure gradient would underestimate the anomalous electron collision frequency in the acceleration region. While the need for ILTS measurements of electron temperature is clear, ILTS measurements are restricted to outside of the discharge channel, so ILTS has not been able to access the entire acceleration region. Also, these noninvasive studies of anomalous electron momentum transport have only made channel centerline measurements, which forces several assumptions in order to infer $u_{e\hat{\perp}}$.

One way to avoid these 1-D assumptions is to use noninvasive measurements to calibrate 2-D simulations, but we have found that these calibrations have two main issues. First, because they are only calibrated on 1-D data, the calibrations assume an arbitrary model for relating ν_a at the channel centerline to the values away from the centerline. Second, these simulations are not calibrated on ILTS measurements of electron temperature and are not able to reproduce the ILTS measurements of electron temperature. We discussed how these two issues may be the reason why LIF-calibrated simulations that also match the measured discharge current and thrust are not self-consistent, and we also analyzed how calibrated simulations with accurate off-centerline plasma properties could improve the prediction of HET lifetime. We also discussed how inaccurate electron temperatures and off-centerline plasma properties could produce inaccurate channel centerline profiles of the calibrated ν_a. Therefore, to improve the predictive capability of calibrated simulations and the accuracy of the calibrated ν_a, there is a pressing need to improve our understanding of anomalous electron heating and of how anomalous electron phenomena at the channel centerline are related to those away from the channel centerline.

CHAPTER 4. Experimental Approach

With the added context from the literature review of Chapters 2 and 3, this chapter will present the research plan. Sections 4.1 discusses the research focus, Section 4.2 will present the research question, and Section 4.3 states the research hypothesis. Section 4.4 provides an overview of the chosen methodology, and Section 4.5 will discuss the justifications for different aspects of the methodology.

4.1. Research Focus

In Sections 3.2 and 3.3, we highlighted three phenomena of electron dynamics in HETs that are either not well-understood or are often not considered in inferences of the electron Hall parameter. We then discussed why we expect an accurate understanding of these phenomena to be necessary for an accurate representation of electron dynamics in the acceleration region of a HET. These phenomena are the following: the anisotropic electron temperatures, anomalous electron heating, and the off-centerline behavior of anomalous electron momentum transport. We will focus primarily on the off-centerline behavior of anomalous electron momentum transport.

To increase the accuracy of our inference of the electron Hall parameter, we plan to make a 2-D map of ILTS measurements. However, a 2-D map of ILTS is very time consuming, so the goal of the research is to improve the understanding of the off-centerline behavior of anomalous electron momentum transport in order to enable more accurate inferences of the electron Hall parameter from only measurements along the channel centerline. As previously discussed, improving the accuracy of inferences of the electron Hall parameter from measurements along the channel centerline has two main benefits. First, it will improve the predictive capability of calibrated HET simulations, and second, it will improve the accuracy of validating theories of anomalous electron momentum transport with only plasma measurements at the channel centerline.

4.2. Research Question

In Section 3.3, we highlighted the fact that to use 1-D measurements to calibrate a 2-D simulation, an arbitrary model, Eq. 3-14, is used to relate the anomalous electron collision frequency at the channel centerline to that off-centerline. By "arbitrary", we mean that that Eq. 3-14 is not based on theory nor has it been experimentally validated. This arbitrariness is reflected by the exponential factor, d, that is not specified but is usually taken to be equal to -1. When $d = -1$, the model is equivalent to assuming that the anomalous contribution to the electron Hall parameter, Ω_{ea} is constant along magnetic field lines.

Alternatively, the electron Hall parameter is given by Eq. 2-26, which if $u_{e\hat{1}}$ is constant along magnetic field lines, implies that electron parameter is directly proportional to the azimuthal electron drift velocity along magnetic field lines. So, the research question is the following:

> In a HET, is the electron Hall parameter directly proportional to the azimuthal electron drift velocity along magnetic field lines?

4.3. Research Hypothesis

While the axial electron current density is known to not be radially constant, this is usually attributed to a reduced electron density away from the channel centerline. If we assume negligible variations in the cross-field electron drift velocity along magnetic field lines, then from Eq. 2-26, we arrive at our research hypothesis:

In a HET, the electron Hall parameter is directly proportional to the azimuthal electron drift velocity along magnetic field lines.

4.4. Methodology Overview

We measured a 2-D map of ILTS measurements of the electron density, azimuthal electron temperature, and azimuthal electron drift velocity across the entire acceleration region of a high-power MS-HET. The thruster was operated at an off-nominal discharge condition of 150 V and 30 A. We developed our own solver for a 2-D inference of the electron Hall parameter based on our ILTS measurements. By making our own solver, the inference also uses the electron density measurements, in addition to the azimuthal electron temperature and azimuthal electron drift velocity measurements that we had already stated were necessary for an accurate calibration. From our own solver, we were also able to evaluate several closure models of anomalous electron momentum transport and compare them to our inferred 2-D inference of the electron Hall parameter. Lastly, due to time constraints, we did not measure a 2-D map of the radial electron temperature, so in our inference we assume an isotropic electron temperature. The experimental methodology is described in detail in Chapter 5, and the computational methodology for the inference and comparison to closure models is described in Chapter 6.

4.5. Justification of Methodology

4.5.1. Requirements for Plasma Diagnostic

As discussed in Section 3.1, optical diagnostics are preferred over electrostatic probes for unambiguous measurements of plasma properties. From the optical diagnostics mentioned in Section 3.1, LIF, ILTS, OES, and interferometry, it is possible to make optical measurements of $\vec{u}_i$, $\vec{u}_e$, n_e, an effective isotropic T_e, and T_e along different directions. To decide which diagnostic(s) to use, we use the theory and methods described in Chapter 2 to see which plasma properties we need to measure to answer the research question.

The main objective of the research is to study the off-centerline anomalous azimuthal electron collision frequency. In Chapter 2, we discussed how the main challenge in inferring the local anomalous azimuthal electron collision frequency is inferring or measuring the azimuthal electron drift velocity, $u_{e\theta}$, and the cross-field electron drift velocity, $u_{e\perp}$. As described in Section Chapter 3, $u_{e\perp}$ can be calculated by combining the current continuity equation with inferences or knowledge of the electron density and the ion velocity. Thus, to infer a 2-D map of $u_{e\perp}$, a 2-D map of n_e and $\vec{u}_i$ is needed. It is important to note that the values of u_{ez} expected in a HET are too low to unambiguously measure with ILTS, given the measurement resolution of ILTS. As shown in Fig. 3-5, $u_{e\theta}$ can be accurately inferred from the sum of the E×B drift and the diamagnetic drift due to $E_\perp$ and $\nabla_\perp \cdot \vec{\vec{P}}_e$, respectively. $E_\perp$ can be inferred from $u_{i\perp}$ and while $\nabla_\perp \cdot \vec{\vec{P}}_e$ can be inferred from n_e and $T_{e\perp}$. Alternatively, ILTS can be used to directly measure $u_{e\theta}$.

At first glance, possible combinations of measurable plasma properties required to infer a 2-D map of the azimuthal anomalous electron collision frequency are

- $\vec{u}_i$, n_e, and $u_{e\theta}$
- $\vec{u}_i$, n_e, and T_e

LIF is the diagnostic of choice for $\vec{u}_i$ while ILTS is the only diagnostic capable of simultaneously measuring n_e and $u_{e\theta}$. So, it would seem that LIF and ILTS are needed to infer a 2-D map of the azimuthal anomalous electron collision frequency. However, as shown in Chapter 6, n_e, T_e, $u_{e\theta}$ can be used to infer $\vec{E}$, which can then be used to infer $\vec{u}_i$ assuming suitable boundary conditions for $\vec{u}_i$. Likewise, Ref. 39 was able to infer n_e, T_e, $u_{e\theta}$ from LIF measurements from the axial ion

VDF. However, the inference in Ref. 39 included using the transport equation of the total axial ion pressure. Because there is no fully verified closure model for the significant anomalous ion heating in the acceleration region of a HET [49], the methodology in Ref. 39 inherently introduces some inaccuracy via the modeling of the transport equation of the total axial ion pressure. While LIF measurements typically have lower uncertainty than ILTS measurements, the ILTS-based inference method that we will present makes fewer assumptions in the transport equations. Therefore, by using ILTS for this work, we believe that we are prioritizing accuracy over precision.

4.5.2. Justification of Thruster Operating Condition

An important caveat is that this potential capability of ILTS is only valid if ILTS can access the entire acceleration region. This is because the solver needs an upstream boundary condition for $\vec{u}_i$, so if the upstream boundary is upstream of the acceleration region, the uncertainty on the boundary condition is reduced. Recent ILTS measurements on the magnetically shielded H9 operating at 300 V were not able to access the entire acceleration region [40]. However, multiple studies have shown a downstream shift of the acceleration region with a decreasing discharge voltage [14, 21, 31], and magnetic shielding also shifts the acceleration region downstream with respect to conventional HETs [12, 14, 15]. Indeed, ILTS on a MS HET operating at 150 V was able to measure across the entire acceleration region [22]. In addition, a high discharge current will increase the ILTS signal, which is helpful because the ILTS is a low signal diagnostic. So, because we need optical access of the entire acceleration region and because we wanted to increase the ILTS signal, we chose to do the experiment on an MS-HET operating at a low discharge voltage and high current density.

However, an important consideration is whether our findings regarding anomalous transport at this off-nominal discharge condition are applicable to nominal discharge conditions.

Indeed, the presence and importance of different plasma instabilities and oscillations depends on the thruster operating condition. Any theory regarding the anomalous transport from these types of instabilities should be general enough for a wide set of discharge conditions. A 3-D kinetic simulation of a HET at 200 V was able to capture the ECDI and MTSI, two kinetic instabilities believed to drive anomalous transport in a HET [116]. Therefore, it is reasonable to believe that these instabilities will still be present at 150 V. So, while nature of the large-amplitude and low-frequency oscillations, such as the breathing mode or rotating spokes, will be different than in nominal conditions, the critical task is understanding the anomalous transport due to higher frequency oscillations. This is because having a closure for the effects of higher frequency oscillations will relax that temporal resolution requirements for accurate HET simulations. We believe that the findings from our work will be mainly attributed to anomalous transport from kinetic or high-frequency instabilities. We believe this because the peak-to-peak discharge current and rms discharge current were relatively low at 14% and 2% of the mean discharge current, respectively, which reduces the effect of how large-amplitude plasma oscillations couple nonlinearly to high-frequency oscillations.

4.5.3. Custom Solver Justification

We were initially planning to calibrate a 2-D HET simulation with our measurements. However, we realized that while calibrations of HET simulations can be calibrated with channel-centerline measurements, a calibration based on a 2-D map of data poses extremely high precision and accuracy requirements on the measurements. These requirements appear because the simulation requires the electric field to be conservative. If the electric field corresponding to the Lorentz force and the pressure gradient is not conservative, then the simulation generates a conservative electric field by increasing the electron current density. The electron resistivity term is supposed to be significantly less than the Lorentz force or the pressure gradient, so its magnitude is artificially increased by the solver of the electric potential. As a result, we cannot trust the electron current density from a 2-D calibration. This is why we chose to make a custom solver of the anomalous Hall parameter based on our measurements. While there will be some uncertainty due to choices of boundary conditions and inherent inaccuracies if the electric field is not conservative, we are confident that our uncertainty bounds of our inferred anomalous Hall parameter will be representative of the uncertainty in our boundary conditions and in our measurements.

CHAPTER 5. Experimental Setup

This chapter presents the experimental methodology. Section 5.1 describes the vacuum test facility in which the experiment was conducted, and Section 5.2 presents the setup and description of the test article. Section 5.3 describes the setup of the ILTS diagnostic, Section 5.4 presents a new ILTS data processing technique developed for this work, Section 5.5 covers how the data processing technique was implemented in this work, and Section 5.6 explains the test matrix.

5.1. Vacuum Test Facility

The experiment was conducted in VTF-2 at HPEPL. VTF-2 is 9.2 m long and 4.9 m in diameter. A 495 CFM rotary-vane pump is used to reach 5 Torr, and a 3800 CFM blower is then used to reach rough vacuum of around 10 mTorr. 10 LN2-cooled CVI TMI reentrant cryopumps are used to reach high-vacuum with a nominal pumping speed of 350,000 l/s on krypton. We used a Kurt J Lesker XCG-BT-FB-1 capacitance manometer with a range of 1000 to 1 Torr to measure the chamber pressure during the Raman scattering measurements (for an intensity calibration of the ILTS diagnostic), which were taken at 10 Torr on the residual atmosphere. At high vacuum, the chamber pressure will be monitored with an Agilent Bayard-Alpert 571 hot-filament ion gauge on the side of the chamber near the exit plane of the thruster. For this experiment, VTF-2 achieved a base pressure of 9.5×10^{-9} Torr-N_2 and an operating pressure of 1.2×10^{-5} Torr-Kr at a Kr flow rate of 345 sccm.

5.2. Test Article

The study was performed on the H9, a 9-kW class MS HET [137], with a center-mounted heaterless LaB_6 cathode. The Jet Propulsion Laboratory, the University of Michigan, and the Air

Force Research Laboratory designed the H9, which has a boron nitride channel. The H9 was chosen for this experiment because magnetic shielding shifts the acceleration region downstream [12-15], which helps the ILTS diagnostic to probe across the entire acceleration region.

Research-grade (99.999% purity) krypton was supplied to the anode via an MKS GE50A00650S8V020 mass flow controller and to the cathode via an MKS GE50A006102S8V020 mass flow controller. The mass flow controllers were calibrated by measuring the flow upstream of the thruster with a MesaLabs DryCal 800-10 volumetric flow meter.

The H9 discharge was powered with an EMI / TDK-Lambda EMHP 600-100 DC power supply. To prevent discharge current oscillations above 1.4 kHz from going into the discharge power supply, a filter with a 95-μF capacitor and a 1.3-Ω resistor is connected to the discharge power supply. The discharge voltage is measured in the control room at a location in the thruster circuit between the discharge filter and the thruster. The discharge current and its oscillations are measured by a Teledyne LeCroy CP150 current clamp connected to a Teledyne LeCroy HDO6104 oscilloscope at a sampling rate of 5 MS/s for one second. The thruster operating condition used in the experiment was 4.5 kW, 150 V, 30.3 A, inner coil current of 4.11 A, outer coil current of 2.27 A, an anode flow rate of 322.9 $\pm$ 3.06 sccm, a cathode flow rate of 22.4 $\pm$ 3.67 sccm. The thruster body was isolated from electrical ground and is configured to be electrically floating. The polarity of the magnet coils was configured to create a magnetic field predominantly in the negative radial direction along the channel centerline. The resultant discharge current peak-to-peak and discharge current rms were 4.3 A and 0.68 A, respectively, and the discharge current trace and power spectral density are shown in Figs. 5-1 and 5-2. ILTS measurements were taken when the discharge had reached steady-state, determined by waiting until the drift in the discharge current peak-to-peak drops below 1% per minute.

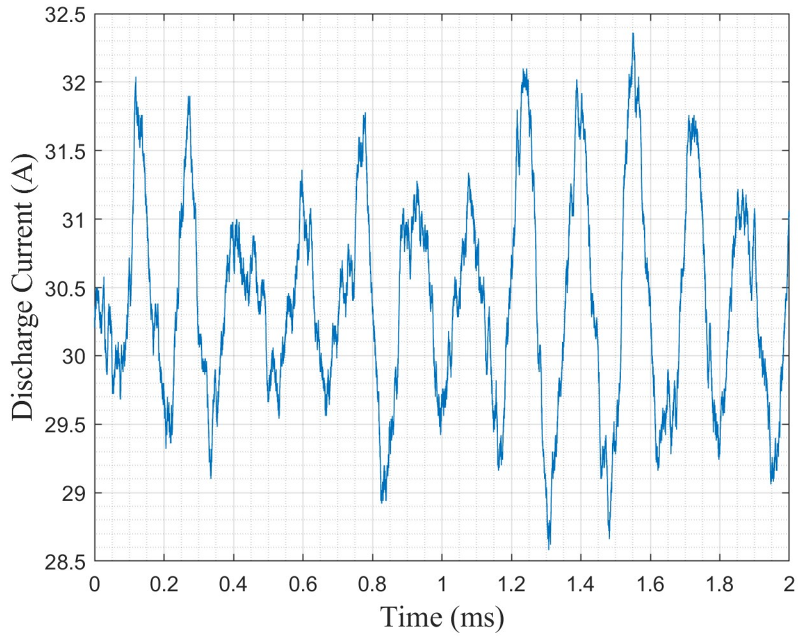

Figure 5-1: Discharge current time series over 2 ms.

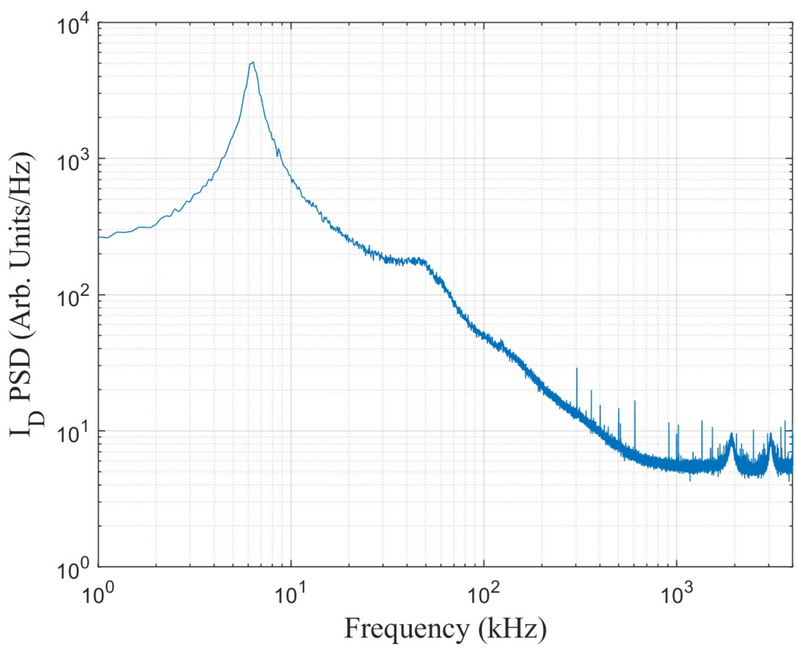

Figure 5-2: Power spectral density of the discharge current.

To probe various locations in the H9 discharge, the H9 was moved with respect to the fixed ILTS observation volume. The H9 was mounted atop three motion stages, which allowed threedirectional movement of the thruster. To move the H9 in the $\mathbf{x}_{chamber}$ and $\mathbf{z}_{chamber}$ directions, as defined in Fig. 5-3, we used two Parker 4062000XR motion stages, and to move in the $\mathbf{y}_{chamber}$ direction, as described in Fig. 5-3, we used an Optics Focus MOZ-300-150.

5.3. ILTS Setup

Thomson scattering is the elastic scattering of electromagnetic radiation off free charged particles. For low-density plasmas, only Thomson scattering from free electrons is considered since the scattered power of the light scattered by free ions is negligible compared to that scattered by free electrons [130].

An ILTS diagnostic is typically composed of three primary optical systems: the interrogation beam optical system, the collection optical system, and the detection optical system. The interrogation beam system generates the incident radiation with a laser and focuses the incident laser beam at the observation volume, which produces intense scattering at the observation volume. The observation volume is the portion of the incident laser beam imaged by the collection system. If an optical fiber is used, as in our setup, then the collection system images the scattered light from the observation volume to the face of the fiber and transports the collected light to the detection system via the optical fiber. Alternatively, if no optical fiber is used, the collection system can be directly coupled with the detection system. If no optical fiber is used, then the collection and detection systems can be treated as one combined system, as done in Ref. 138. An optical fiber was used in this work because of the large distance between the observation volume and the spectrometer due to the size of the vacuum chamber. The detection optical system filters out the light near the wavelength of the interrogation beam. It images the light from the optical fiber to the slit of a spectrometer that is coupled to a detector. The detector then records the spectrum of the collected light. Before the commercialization of volume Bragg grating notch filters (VBG-

NFs), a triple grating spectrometer was often used to filter out the light around the laser wavelength [139]. Figure 5-3 shows the three optical systems.

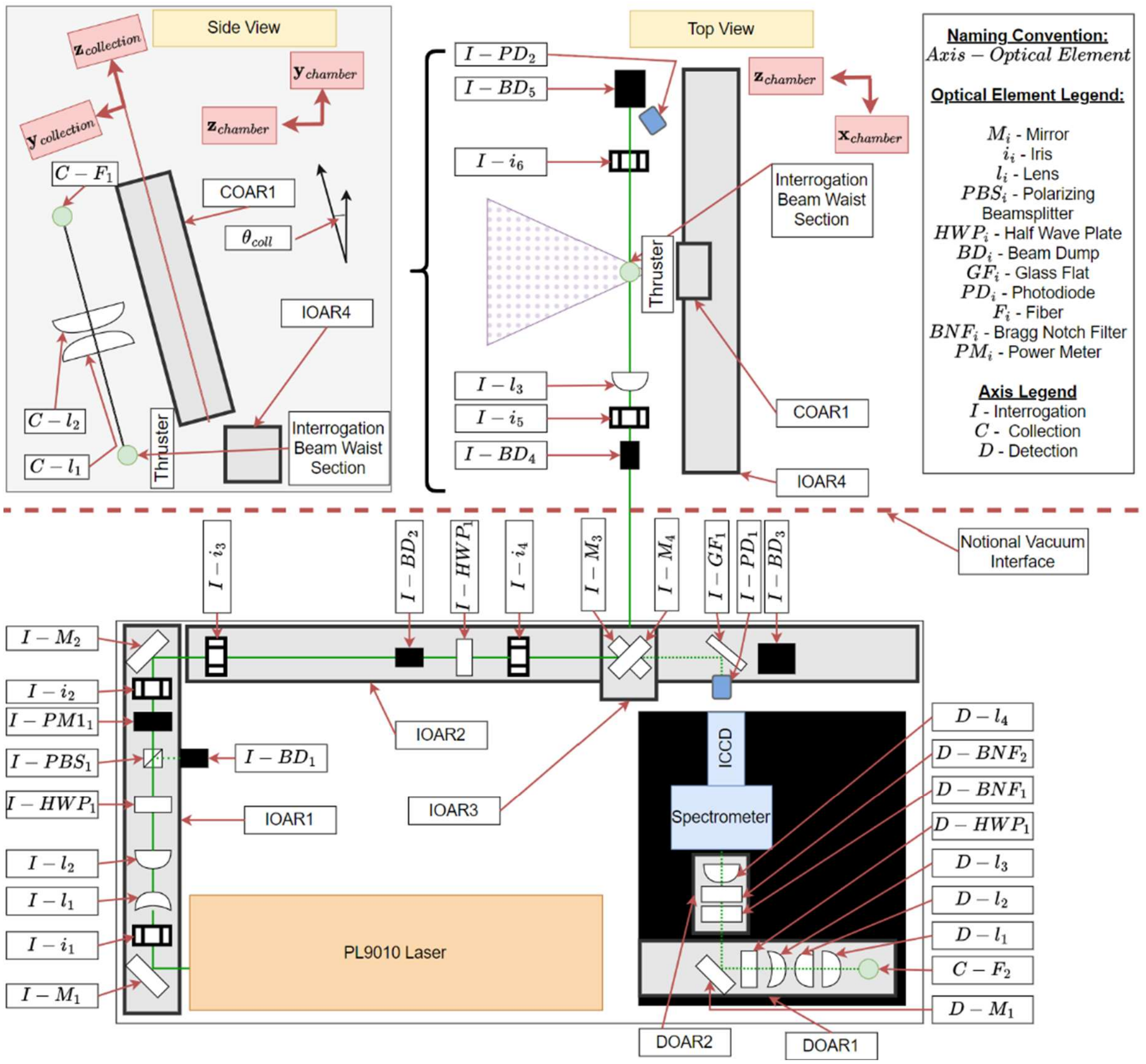

Figure 5-3: Master optical diagram for the interrogation beam, collection, and detection optical systems. θ_{coll} is the angle between $\mathbf{y}_{chamber}$ and $\mathbf{z}_{collection}$. Adapted from Ref. 132.

The laser source used in the interrogation beam optical system was an Amplitude DLS Powerlite 9010 injection seeded Nd:YAG laser. The laser is operated with a second harmonic generator that outputs a 532-nm laser beam with a 9-mm beam width and a beam pulse width between 5 and 8 ns. The laser is rated for a maximum output energy of 1 J/pulse with a 10 Hz repetition rate. To avoid perturbing the plasma, we delivered 600 mJ/pulse into the interrogation volume throughout this work. During a five-minute window, the laser energy had a peak-to-peak stability of 3.1% and an rms stability of 0.69%. The beam goes through a 1.5:1 beam expander formed by the lenses I-l_1 and I-l_2 so as not to damage the polarizing beamsplitter cube, I-PBS1. The polarizing beamsplitter cube and the half wave plate I-HWP_1 modulate the beam power together, which is measured by a power meter on a flip mount, I-PM_1. The beam then passes through a second half wave plate, I-HWP_2, to control the polarization of the incident light in the observation volume. Once the collection and detection systems are aligned, the orientation of I-HWP_2 is optimized to maximize Rayleigh scattering. To align the beam with the interrogation beam optical axis defined inside VTF-2, the beam goes through a periscope formed by the mirrors I-M_3 and I-M_4. The interrogation beam then enters VTF-2 via a custom Torr Scientific NSQ1462-25 KF-flanged Brewster window. Once the incident polarization at the observation volume was optimized without the Brewster window in place, the Brewster window was then oriented to minimize reflections at the window. Inside VTF-2, the beam is focused onto the observation volume with a 600 mm focal length lens, I-l_3, resulting in a beam width of around 100 μm in the observation volume. For more details on the interrogation beam optical system and the alignment practices, see Ref. 132.

The collection optical system forms a 1:1 image of the observation volume at the fiber face with two 250-mm focal length 50-mm diameter lenses, C-l_1 and C-l_2. A custom Thorlabs FG200LEA-FBUNDLE fiber bundle in a 7×1 array of 200-μm diameter FG200LEA multimode fibers transports the collected light to outside VTF-2 via a custom SQS Fiber Optics HEM048727 4.5-in. CF flange. This creates an observation volume with a length of 1.5 mm in the x_{chamb} direction. A second set of the same custom fiber bundle then transports the collected light from the flange to the detection system. To be able to correct for small chamber movements between the atmosphere and high vacuum or thermal drift while the thruster was on, the fiber bundle is placed atop three motorized stages. To protect the collection optics from deposits from sputtering, lens tubes were mounted on the lens mounts, and an AR-coated window was placed at the front of the lens tube. For more details on the collection optical system and the alignment practices, see Ref. 132.

In the detection optical system, the light exiting the optical fiber bundle is first collimated by a 150-mm focal length lens, D-l_1, and then passes through a 2:1 beam reducer formed by D-l_2 and D-l_3. Due to the beam reducer, all the collected light is able to pass through the two 25 mm OptiGrate OD-4 VBG-NFs. The collected light is then focused onto the entrance slit of the spectrometer with a 100-mm focal length lens. The spectrometer slit width was set to 500 μm to maximize light throughput at the cost of a lower spectral resolution. Our setup uses a Princeton Instruments ISOPLANE-320A spectrometer coupled to a Princeton Instruments PM4-1024i-HB-FG-18-P46 PIMAX4 camera. For more details on the detection optical system and the alignment practices, see Ref. 132 and Ref. 140 for more information on the VBG-NFs.

Figure 5-4 shows the scattering configuration. The observation wavevector is defined as $\vec{k} = \vec{k}_s - \vec{k}_i$, where $\vec{k}_i$ is the wavevector of the incident light and $\vec{k}_s$ is the wavevector of the scattered light, which is colinear with the collection optical axis. To measure electron properties along the azimuthal and radial directions, we measured at the two different azimuthal locations shown in Fig. 5-4. Although the observation wavevector is the same at both azimuthal locations in terms of the chamber coordinate system, the observation wavevectors are different in the thruster's cylindrical coordinate system.

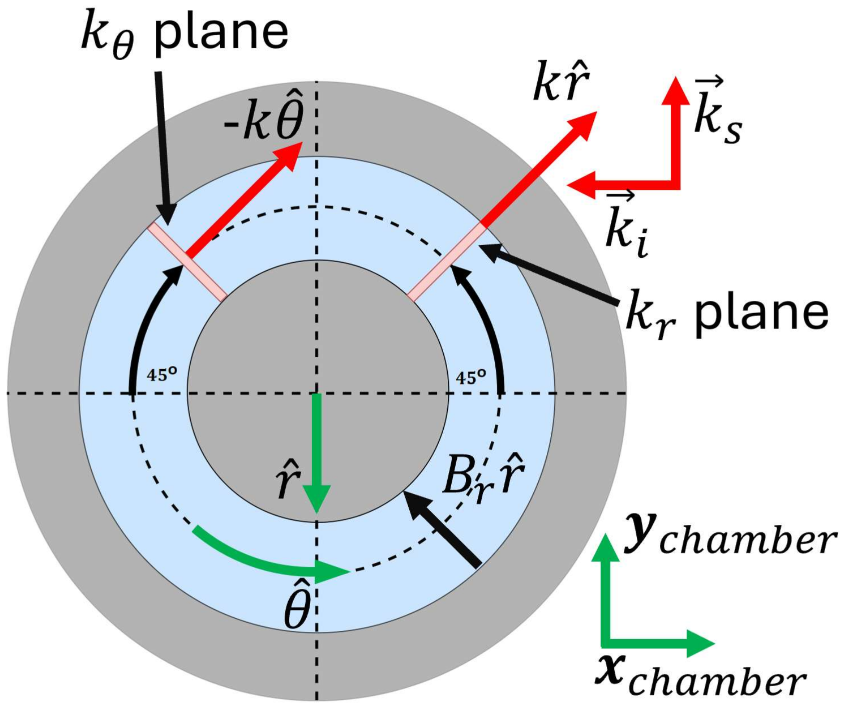

Figure 5-4: ILTS scattering configuration. Wavevectors are shown in red. The chamber coordinate system, the azimuthal direction, and the radial direction are shown in green. The radial component of the magnetic field is shown in black. The incident and scattering wavevectors are positioned arbitrarily to show the relative orientation of $\vec{k}_i$ and $\vec{k}_s$. The k_r and k_θ planes are also defined.

5.3.1. Comments on Modifications to Setup

Compared to the work in Ref. 132, we made a few modifications to the ILTS setup. First, while Ref. 132 had a subtended collection axis with a θ_{coll} in Fig. 5-3 of 17°, the ILTS setup in this experiment was 0° in order to measure the azimuthal EVDF. The rest of the changes had to do with reducing stray light from fluorescence.

While stray light at 532 nm can be filtered out by the VBG-NFs, stray light from fluorescence is dispersed and is not filtered out. The fluorescence can be accurately subtracted out if it is repeatable, but this repeatability error must be negligible compared to the Thomson scattering signal. With the previous setup, this criterion for repeatability error was not met, especially in the wings of the Thomson scattering spectrum, as shown by the distorted ILTS spectrum in Fig. 5-5 with a significant amount of negative intensity values. The data from the previous setup was salvageable in part because the fluorescence spectrum has a relatively simple shape [141], but we did not want to rely on this correction method for this experiment. So, we implemented two parallel solutions, one to reduce the amount of stray light collected and another to make the stray light more repeatable.

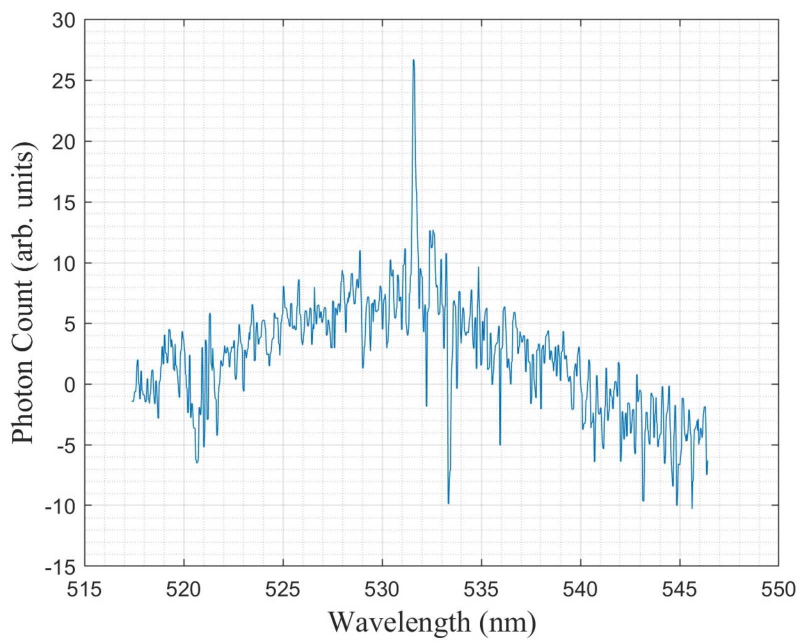

Figure 5-5: ILTS spectrum distorted by stray light.

To reduce the amount of stray light collected, we changed the lenses in the collection system, C-l_1 and C-l_2, from 350-mm focal length 150-mm diameter lenses. While the modified collection solid angle is significantly lower than in the previous setup, the signal with the modified setup is actually slightly higher than with the previous setup. This is because the larger lenses produce large spherical aberrations, significantly increasing the imaging spot size and reducing the coupling efficiency into the fiber optic. The increased spherical aberrations also increase the collection efficiency from intended areas, which increases stray light. As a result, the previous setup had a severely unoptimized ratio of ILTS signal to fluorescence signal, essentially requiring exact repeatability of the fluorescence signal for good Thomson scattering data. To further reduce the amount of stray light collected, we moved $I - i_6$ and $I - BD_5$ further away from the thruster, and we opened the $I - i_6$ a little to reduce the intensity of the light that clipped the iris. We believe that much of the fluorescence comes from the interrogation being clipped by $I - i_6$ and hitting $I - BD_5$. The optical configuration inside the VTF-2 can be seen in Figs. 5-6 and 5-7.

To increase the repeatability of the stray light signal, we note that we think that the repeatability issue comes from thermal drift in the interrogation beam alignment. We identified the lens inside the chamber, $I - l_3$, as being the main source of thermal drift in the entire optical system since it has a high heat load from interrogation beam and no convective cooling. As a result, we acquired a custom water-cooled lens mount for $I - l_3$. This significantly reduced thermal drift in alignment, evidenced by the fact that in the previous setup we had to realign around every 40 minutes, while in the new setup, our ILTS signal could be maintained for around three hours before needing realignment. We briefly describe this realignment process in Section 5.3.3.

In the future, it would be ideal to place the laser in a temperature-controlled environment. The laser energy would oscillate throughout the day, with maximum peak energy in the middle of the day and minimum energy in the middle of the night. During the day, we would modulate the power to keep it around 600 mJ/pulse with the laser occasionally creeping up to 640 mJ/pulse, but during the night, the maximum laser energy decreased steadily to a minimum of 550 mJ/pulse. Given the evidence of thermal drift of the laser energy, this is likely the source of the thermal drift in the alignment and the repeatability issues with the stray light. Putting all the optics outside the chamber in a temperature-controlled environment would further decrease thermal drift.

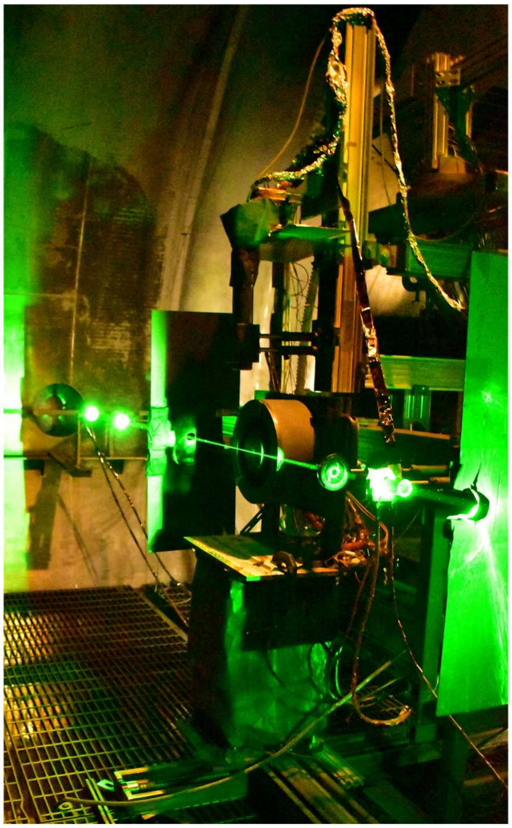

Figure 5-6: ILTS setup inside VTF-2, facing the beam dump.

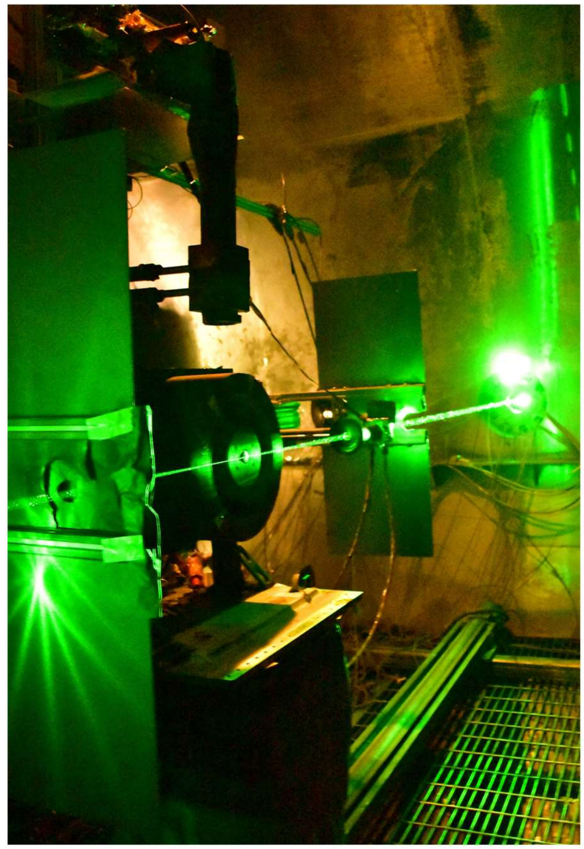

Figure 5-7: ILTS setup inside VTF-2, facing the Brewster window.

5.3.2. Acquisition Strategy

Due to the low dark current produced by the ICCD in our setup, the minimization of the read noise of the detector guided our acquisition strategy. For each acquisition, we acquired 3,000 shots, corresponding to an acquisition time of five minutes. At each point, we used 150 on-CCD accumulations to prevent saturating the pixels with the pattern noise of the detector. Our detector has a 1024 × 1024 imaging array, but our acquisition was done by vertically on-chip-binning the center 300 pixels. A bin height of 300 pixels was chosen to include the image of all seven fibers.

To obtain the ILTS spectrum, four spectra must be acquired for each point. This is done to isolate the Thomson signal from the other sources of signal, such as plasma emission, stray light, and the detector DC bias. Spectrum A is the laser on, plasma on condition, spectrum B is the laser off, plasma on condition, spectrum C is the laser on, plasma off condition, and spectrum D is the laser off, plasma off condition. We will refer to the spectrum resulting from subtracting spectrum B from spectrum A as spectrum AB. We will refer to the spectrum resulting from subtracting spectrum D from spectrum C as spectrum CD. We will refer to the spectrum resulting from subtracting spectrum CD from spectrum AB as spectrum ABCD. Spectrum AB contains a signal due to Thomson and stray light, and spectrum CD contains a signal due to stray light, such that spectrum ABCD should only contain a signal due to ILTS. Figures 5-8 - 5-10 show the Thomson spectrum, plasma emission spectrum, and stray light spectrum for a low-temperature and high-density case (closest to thruster), a high-temperature and moderate-density case, and a low-temperature and low-density case (farthest from thruster).

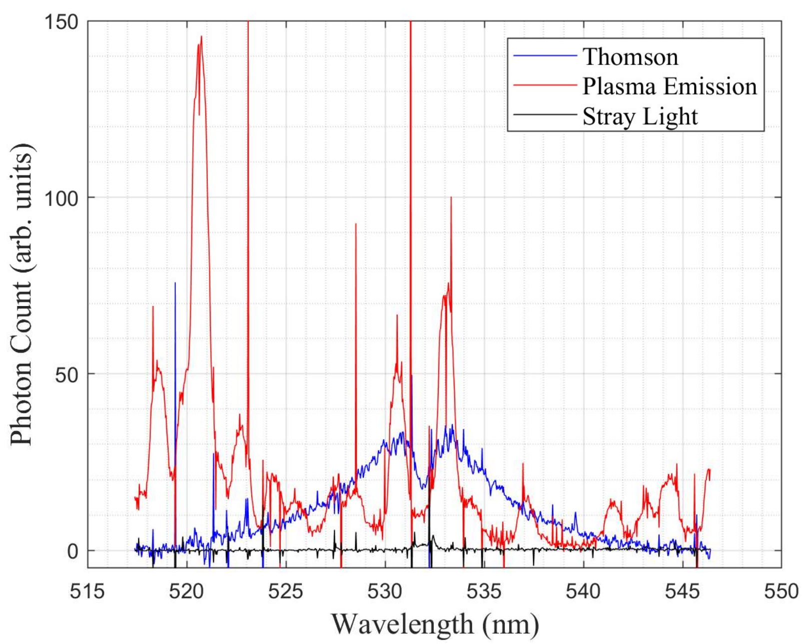

Figure 5-8: Thomson scattering, plasma emission, and stray light spectra. Corresponds to a high-density low-temperature case.

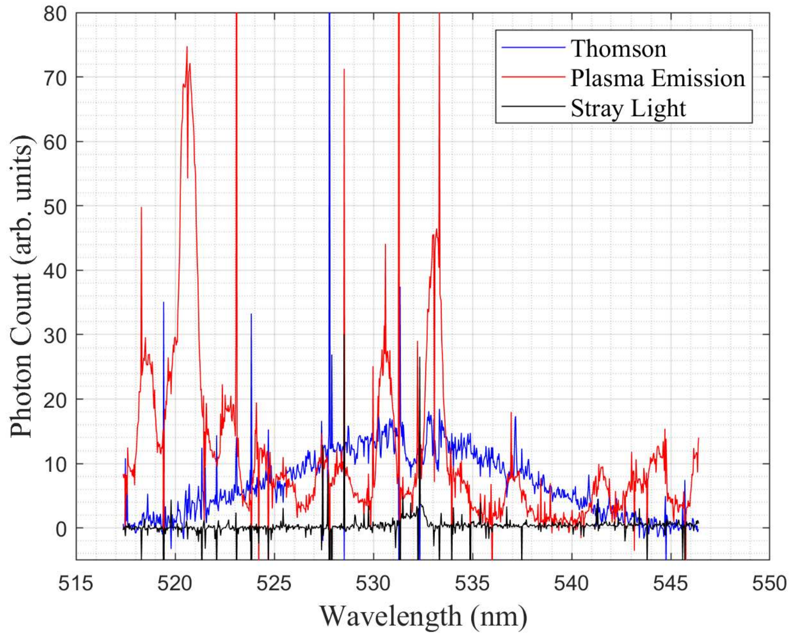

Figure 5-9: Thomson scattering, plasma emission, and stray light spectra. Corresponds to a moderate-density high-temperature case.

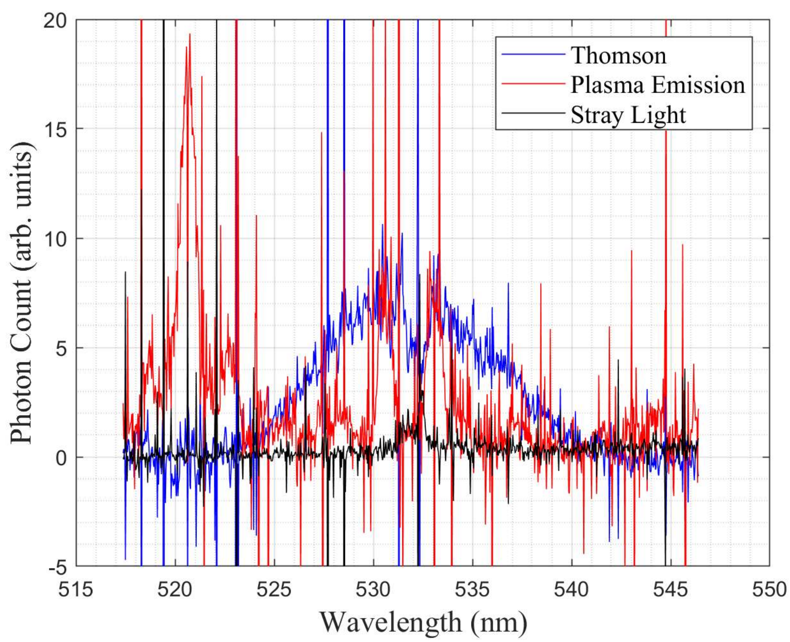

Figure 5-10: Thomson scattering, plasma emission, and stray light spectra. Corresponds to a low-density low-temperature case.

5.3.3. Comments on Alignment Process Under Vacuum

The following three realignment processes are done under vacuum: periodic realignment of the interrogation beam, periodic realignment of the collection fiber, and initial realignment of the thruster position with respect to the interrogation beam. Alignment of the thruster is necessary so that the ILTS interrogation is a known location in the thruster coordinates. Realignment of the interrogation beam and the collection fiber is necessary so that the ILTS volume stays fixed.

Periodic realignment of the interrogation is done using Irises $I - i_5$ and $I - i_6$ (can be viewed from a viewport) as alignment targets inside the vacuum chamber. All misalignments of the interrogation beam with respect to these irises, either due to chamber deformation at vacuum or thermal drift of optical system, could be corrected via translating mirrors $I - M_3$ and $I - M_4$.

Periodic realignment of the collection fiber is done by moving the fiber's motion stages until the ILTS signal is maximized. To do this quickly, the signal maximization is done at the cathode centerline so that we can use a low on-CCD accumulation and frame count see and an immediate response to the signal. The stage that moved the fiber in the z_{cha} direction was the only fiber stage that needed to be periodically realigned, with the overall movement during the experiment being 0.5 mm. We believe that the fiber realignment was not merely moving the fiber to adjust for small interrogation beam drifts that we could not observe on the irises, which would result in a movement in the observation volume. This is because the required fiber position for maximum ILTS signal drifted in a constant direction and would not shift by more than 0.1 mm after a realignment of the interrogation beam. As a result, we think that after each realignment the location of the interrogation beam was fixed with an uncertainty of $\pm$ 0.1 mm.

The thruster location is preliminarily aligned at atmosphere, but the thruster location gets misaligned during pump-down. After thruster ignition, the thruster is realigned in the $x_{chamber}$ and $y_{chamber}$ directions by finding the stages coordinates at which the ILTS signal is maximized, since this corresponds to the observation volume being at the cathode centerline. To align the thruster in the z_{chamb} direction, we have to create a reference at atmosphere. At atmosphere, we make sure the interrogation beam is aligned, move the thruster as close to the beam as possible without the beam hitting the thruster, and then we measure the distance from the thruster face to the beam with a burn paper and calipers. We then lower the laser energy as much as possible with $I - HWP_1$ and move the thruster forward until the point at which we no longer see the interrogation beam on iris $I - i_6$. We make a note of the distance between these two thruster locations at atmosphere. At vacuum, we then repeat the process of finding the position at which thruster full block the beam, which calibrates the thruster with respect to the observation volume in the z_{chamb} direction. The most significant source of uncertainty in the thruster alignment process is identifying the most leftward (in Fig. 5-3) thruster position at which we no longer see the interrogation beam on iris $I - i_6$. We estimate the uncertainty in the thruster's $z_{chamber}$ calibration as $\pm$ 0.5 mm.

5.4. ILTS Data Processing

*This section reproduces the content in the Physics of Plasma journal [*142*].*

In low-temperature plasmas, electrons can often be in non-equilibrium [143]. Such non-equilibrium can produce significant deviations from Maxwellian electron velocity distribution functions (EVDFs). Non-Maxwellian EVDFs can result in reaction rates [60,143,144] and fluxes through sheaths [93,145] that differ significantly from those calculated assuming Maxwellian

EVDFs and in non-conductive electron heat fluxes [117,146,147]. These non-Maxwellian effects can significantly influence plasma composition and spatial distributions of electron temperature [118]. While various simulation methods can capture non-Maxwellian electron effects [60,61,93,117,144,147-149], experimental methods are needed to validate these simulations and to improve the understanding of non-Maxwellian electron behavior in different plasmas.

Langmuir probes are the most common technique used to measure non-Maxwellian electron energy distribution functions (EEDFs) [150-152], and optical emission spectroscopy (OES) has also been used to measure EEDFs [153-156]. Langmuir probes are able to measure the EEDF from low to high electron energies (0-50 eV) [143] and strategies exist to mitigate probe perturbation in certain discharges [150]. However, perturbation from Langmuir probes can be significant [32] and adds ambiguity to the results, even if the perturbation is reduced. On the other hand, while OES is non-invasive, it suffers from reduced spatial resolution as it provides spatially-averaged measurements across the line of sight of the diagnostic, and OES cannot measure the low-energy part of the EEDF [143]. Additionally, measurements of the EEDF cannot be used to calculate odd moments of the EVDF, such as components of the electron drift velocity and electron heat flux vectors.

ILTS can non-invasively measure the one-dimensional EVDF with high spatial resolution, but ILTS has poor signal-to-noise ratio (SNR) in the tails of the EVDF. As a result, ILTS has not been used extensively for non-Maxwellian studies in low-temperature plasmas. Refs. 127, and 157-159 used ILTS to measure non-Maxwellian EVDFs in low-temperature plasmas. In addition, Refs. 127 and 160 showed that incorrectly assuming a Maxwellian EVDF can produce inaccurate ILTS measurements of electron density, drift velocity, and temperature. However, there are two important gaps in the approach to analyzing ILTS measurements of non-Maxwellian EVDFs. First, the authors are not aware of attempts to quantify uncertainty in ILTS measurements of electron density, drift velocity, and temperature that incorporate the uncertainty of the type of EVDF that best describes the data. Second, the authors are not aware of any use of ILTS to quantify the deviation from Maxwellian EVDFs. Given the low SNR in the tails of the EVDF in ILTS measurements, robust uncertainty quantification is necessary to account for the possibility of non-Maxwellian EVDFs in ILTS measurements of electron density, drift velocity, and temperature. Robust uncertainty quantification can also enable quantitative ILTS measurements of the deviation from Maxwellian EVDFs through the electron heat flux and excess kurtosis.

The methods for analyzing non-Maxwellian velocity distribution functions (VDFs) are direct integration, modeling of VDFs with a single alternative distribution, and modeling of VDFs with multiple components. When the VDF can be directly extracted from the raw measurement, as in ILTS when the width of the instrument function is negligible compared to the electron temperature, the moments of the VDF can be calculated directly through integration of the measured signal; Ref. 127 did this with an ILTS measurement of a skewed EVDF, but the main downside of this method is that it does not provide an uncertainty for the calculated moments of the VDF. Analyzing non-Maxwellian VDFs with a single alternative distribution has been done with a Druyvesteyn [159], Kappa [161], super-Gaussian [161-163], and skew-Gaussian [164], among others [60,165-167]. Analyzing non-Maxwellian VDFs with multiple components has been done with two Maxwellians [40,158,160], sum of a Maxwellian and a super-Gaussian [168], and the sum of a Maxwellian, super-Gaussian, and Kappa [169]. While alternative-distribution methods can be enhanced by Bayesian model selection [159,161], these model selection methods are inherently limited in their capability to accurately model VDFs that are not included within the models being selected. As a result, multi-component methods recreate measured VDFs more accurately than alternative-distribution methods [146]. Regarding uncertainty quantification, multi-component methods can be enhanced with Bayesian inference of the moments of the VDF following the Bayesian inference of the parameters that model the VDF [119,168]. However, the highest-order moment that these multi-component Bayesian inference methods have inferred from the VDF is the effective temperature. It is also worth noting that the electron heat flux has been directly calculated from EVDF measurements in the solar wind [170].

This work presents a Bayesian inference method to analyze non-Maxwellian EVDFs with ILTS that assumes that the EVDF is the sum of at most four super-Gaussians. The method was tested against synthetic ILTS spectra representative of Maxwellian, Druyvesteyn, and Kappa distributions as well as skewed versions of these distributions. This study includes Druyvesteyn distributions as they are commonly found in low-temperature plasmas, and it includes Kappa distributions as an example of a leptokurtic distribution, since simulations of Hall thrusters have found EVDFs with positive excess kurtosis [93,117]. The main objective of the study is to demonstrate that ILTS can accurately measure the first five moments of the one-dimensional EVDF for a wide variety of EVDFs, specifically the electron density, drift velocity, electron temperature, heat flux, and excess kurtosis. Section 5.4.1 describes the Bayesian inference method and the generation of the synthetic ILTS spectra. Section 5.4.2 evaluates the accuracy of the proposed method, compares the method's accuracy to simpler methods, and explores the limits of the proposed method regarding spectral resolution and spectral range.

5.4.1. Data Processing Methodology

5.4.1.1. ILTS Model Equations

Thomson scattering is the elastic scattering of light off charged particles, and in the incoherent regime, the scattered spectrum is dominated by scattering off electrons. Thomson scattering is incoherent when $\frac{2\pi}{k} \gg \lambda_{De}$, where k is the observation wavevector and λ_{De} is the Debye length. The observation wavenumber is given by

$$k = \frac{4\pi}{\lambda_i} \sin\left(\frac{\theta}{2}\right), \tag{5-1}$$

where λ_i is the laser's incident wavelength and θ is the scattering angle.

With a perpendicular scattering geometry [127,171], the spectral density of the signal measured by ILTS as function of wavelength is

$$P_s(\lambda) = \frac{C\sigma_T \Delta\lambda n_e}{k} \left[I_s(\lambda) * \hat{f}_k(v)\right], \tag{5-2}$$

where C is the calibration constant provided by laser Raman scattering (LRS) [140], σ_T is the Thomson scattering cross section [171], $\Delta\lambda$ is the spectral resolution of the ILTS spectrum, n_e is the electron density, k is the observation wavenumber, $I_s(\lambda)$ is the normalized ($\Delta\lambda \sum I_s = 1$) instrument function of the detection system and needs to be measured separately, $\hat{f}_k$ is the one-dimensional normalized EVDF along the observation wavevector, and $*$ denotes a discrete convolution. v, the electron velocity corresponding to a given wavelength, is given by

$$v(\lambda) = \frac{2\pi c}{k}\left(\frac{1}{\lambda_i} - \frac{1}{\lambda}\right), \tag{5-3}$$

when using the observation wavevector convention of $\vec{k} = \vec{k}_i - \vec{k}_s$, where $\vec{k}_i$ is the incident wavevector and $\vec{k}_s$ is the scattering wavevector. $f_k = n_e \hat{f}_k$ is defined as the sum of four super-Gaussians,

$$f_k(v) = \sum_{i=1}^{4} f_i^{SG}(v), \tag{5-4}$$

where a super-Gaussian is defined as

$$f_i^{SG}(v) = A_i \exp\left(-\left|\frac{v-v_{D,i}}{\Delta v_i}\right|^{b_i}\right). \tag{5-5}$$

To simplify the numerical implementation of the model equations, the problem is regularized in two ways. First, $v_{D,i}$ and Δv_i are expressed in Mm/s, such that $[f_k] \sim \frac{s}{Mm^4}$. Second, $\log_{10} A_i$ were used as model parameters instead of A_i. Third, from the recorded ILTS spectrum, $P_s^R(\lambda)$, the regularized recorded ILTS spectrum is defined as

$$d(\lambda) = \frac{P_s^R(\lambda)}{\max\left[\frac{P_s^R k}{\sigma_T}\right]}, \tag{5-6}$$

and $B = \max\left[\frac{P_s^R k}{\sigma_T}\right]$. The modeled regularized ILTS spectrum is then similarly defined as

$$M(\lambda, \vec{\theta}, C, I_s) = \frac{C\sigma_T \Delta\lambda n_e}{kB}\left[I_s(\lambda) * \hat{f}_k(v, \vec{\theta})\right], \tag{5-7}$$

where $\vec{\theta} = \left[\log_{10}(A_1), \Delta v_1, v_{D,1}, b_1, \ldots, \log_{10}(A_4), \Delta v_4, v_{D,4}, b_4\right]$.

5.4.1.2. Implementation of Bayesian Inference

The authors chose to implement Bayesian inference to effectively propagate the uncertainty of inferred values of $\vec{\theta}$ to the uncertainty of the moments of f_k. Given $d(\lambda)$ and $I_s(\lambda)$, the joint probability distribution of $\vec{\theta}$ and $\vec{\varphi}$ is given by the posterior probability distribution, $p(\vec{\theta}, \vec{\varphi}|d, I_s)$, where $\vec{\varphi}$ contains the nuisance parameters. In general, nuisance parameters are parameters that need to be inferred but that are not of primary interest. The posterior probability distribution is given by Bayes rule as

$$p(\vec{\theta}, \vec{\varphi}|d, I_s) = \frac{p(d, I_s|\vec{\theta}, \vec{\varphi})\, p(\vec{\theta}, \vec{\varphi})}{p(d, I_s)}, \tag{5-8}$$

where $p(d, I_s|\vec{\theta}, \vec{\varphi})$ is the likelihood of observing the data given a set of model parameters, $p(\vec{\theta}, \vec{\varphi})$ is the prior probability distribution of the model parameters, and $p(d, I_s)$ is the evidence. The evidence does not need to be modeled because it is a normalizing constant of the posterior distribution. The likelihood is constructed by assuming that the errors at each wavelength, $e = d(\lambda) - M(\lambda, \vec{\theta}, C, I_s)$, are independent and identically distributed as $e \sim N(0, s^2)$.

This work uses uninformative priors for $\vec{\theta}$, namely $\log_{10}(A_i) \sim N(0,10)$, $\Delta v_i \sim U\left(420\frac{km}{s}, 5939.7\frac{km}{s}\right)$, $v_{D,i} \sim U\left(-2000\frac{km}{s}, 2000\frac{km}{s}\right)$, and $b_i \sim U(1.5,6)$. In general, uninformative priors, such as uniform distributions and normal distributions with a large standard deviation, are used when no prior information is available on the inferred parameters. The range of values for Δv_i corresponds to an electron temperature range of 0.5 eV to 100 eV for Maxwellian EVDFs and can be changed depending on the expected range of electron temperature. The lower limit for b_i was set below 2 such that a single super-Gaussian could produce positive and negative excess kurtosis and at 1.5 such that that f_k for a single super-Gaussian cannot be unphysically sharp at $v = v_D$. The nuisance parameters are C and s. The prior distribution of C is the posterior distribution of C from Bayesian inference of preliminary LRS measurements, which can be done following the method in Ref. 159. For s, the prior is $s \sim Exp(1)$. The total prior distribution, $p(\vec{\theta}, \vec{\varphi})$, is simply the product of all the individual priors.

Monte Carlo sampling was used to calculate $p(\vec{\theta}, \vec{\varphi}|d, I_s)$ numerically. Specifically, the NumPyro Python package was used to preliminarily transform the posterior distribution to a Gaussian-like one with a trained autoguide and then implement a No-U-Turn sampler (NUTS) to sample from the transformed posterior distribution, as described in Ref. 172 and implemented in the “Neural Transport” NumPyro example [173]. The preliminary transformation of the posterior distribution with a trained autoguide is what is referred to in Refs. 172 and 173 as neural transport. NUTS is a user-friendly extension of Hamiltonian Monte Carlo (HMC) sampling that reduces the number of tuning parameters from 2 to 1 [174]. Instead of relying on random walks to explore the posterior distribution, HMC is a gradient-based Markov chain Monte Carlo method that converges significantly quicker than those that use random walks [174]. The sampling method described above was chosen because of the multimodal nature of the posterior distribution caused by the super-Gaussian mixture model, which makes it difficult for a sampler to efficiently explore the posterior distribution, even for a NUTS sampler on its own.

Implementing this sampling method is around eight lines of code using the code presented in Ref. 174, and to incorporate Eq. 5-7, the observed or synthetic data, and the priors into the code, we refer to the "Bayesian Regression Using NumPyro" NumPyro tutorial [175]. The autoguide was trained on 60,000 samples, and the NUTS sampler was run for four independent chains of 1000 warmup samples followed by 3000 samples. The NUTS sampler was run with a target acceptance probability of 0.99 and a step size of 0.1. While NUTS sampling on the un-transformed posterior distribution was not effective with the presented method, techniques that can combine novel automatic differentiation methods with Hamiltonian Monte Carlo sampling may work with the presented method [176].

Once the samples of $\vec{\theta}$ are generated, the corresponding $f_k(v, \vec{\theta})$ is generated for each sample using Eqs. 5-4 and 5-5. When generating these sampled EVDFs, the lower and upper bounds of the electron velocity are $\pm$ 20,000 km/s and the resolution is 2 km/s. This was done to ensure the accuracy of the moments calculated from the sampled EVDFs. This resolution and the bounds were found to be appropriate for the temperature range considered in this work but should be adapted if the expected range of electron temperature is significantly different. For each sampled EVDF, the electron density, drift velocity along $\vec{k}$, effective temperature along $\vec{k}$, heat flux along $\vec{k}$, and excess kurtosis along $\vec{k}$ are calculated through numerical integration of Eq. 5-9,

$$n_e = \int f_k dv \, , u_{ek} = \frac{1}{n_e} \int v f_k dv \, , T_{ek} = \frac{m_e}{e n_e} \int c_e^2 f_k dv \, , q_{ek} = \frac{m_e}{2} \int c_e^3 f_k dv \, ,$$

$$\Delta_{ek} = \frac{1}{n_e} \left(\frac{m_e}{e T_{ek}} \right)^2 \int c_e^4 f_k dv - 3, \tag{5-9}$$

where $c = v - u_{ek}$. After calculating the moments of each sampled EVDF, the posterior distribution for each moment of interest can then be constructed. The analysis focuses on the excess kurtosis instead of the kurtosis because of its presence in the heat flux transport equation [60] and because the excess kurtosis and the heat flux quantify the first-order deviation from a Maxwellian EVDF. Also, although the analysis focuses on quantifying the heat flux, the heat flux is related to the skewness of the EVDF, β, by $\beta = \frac{2 q_{ek} \sqrt{m_e}}{n_e (e T_{ek})^{3/2}}$.

Next, this study considers the inferred parameters to be the mode of the posterior distributions. For a given posterior distribution of n_e, u_{ek}, T_{ek}, q_{ek}, or Δ_{ek}, the distribution is binned according to the Freedman-Diaconis rule, and the corresponding mode of the distribution

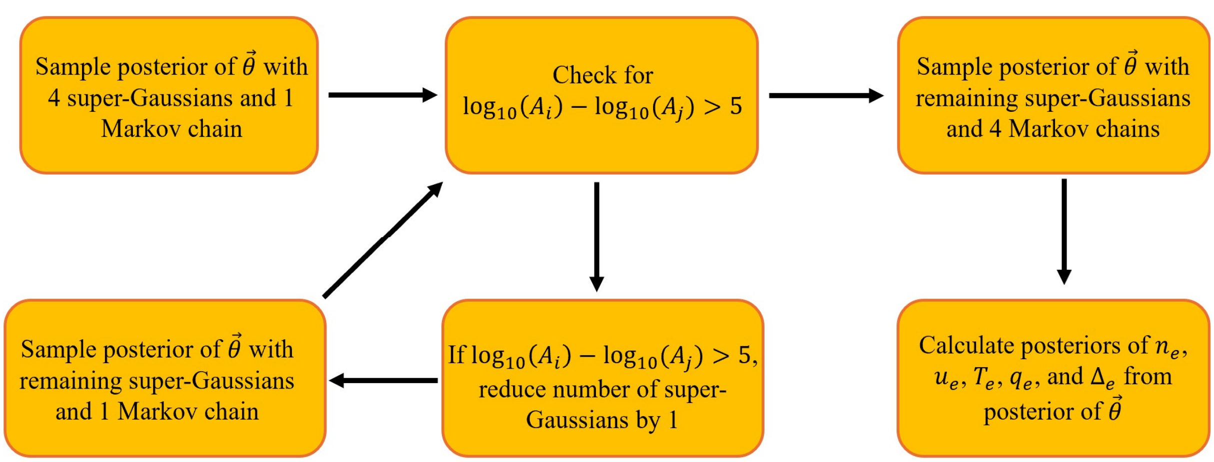

Figure 5-11: Schematic of key steps of the proposed Bayesian inference method

is then found. To quantify the uncertainty of the inferred parameters, this work uses the 95% highest density intervals (HDIs) of the posterior distributions.

Figure 5-11 shows the key steps of the proposed method, including the steps used to determine the number of super-Gaussians used to analyze a given spectrum. To determine how many super-Gaussians to use to analyze a given spectrum, the method first starts by assuming that the EVDF is described by the sum of four super-Gaussians. The previously described sampling procedure is followed, except that the NUTS sampler is only run with one independent chain. If one of the four super-Gaussians has an average $\log_{10}(A_i)$ that is more than five lower than the maximum average $\log_{10}(A_i)$, then the analysis concludes that the given spectrum is described by the sum of at most three super-Gaussians. That is, if $\log_{10}(A_1)$ = -6 and $\log_{10}(A_2) = 0$, then $f_1^{SG}(v)$ is considered negligible. This process is then repeated with three super-Gaussians, and so on, until none of the considered super-Gaussians are negligible. In addition, if the posterior distributions of n_e, u_{ek}, T_{ek}, q_{ek}, or Δ_{ek} are highly skewed, then the method reduces the number of super-Gaussians by one; this prevents the distribution with the smallest $\log_{10}(A_i)$ from trying to match noise in the tails of spectrum. This work defines highly skewed posterior distributions as those where the 95% HDI produces an uncertainty on one side of the mode that is at least five times greater than the uncertainty on the other side of the mode.

In the case where the ILTS spectrum is the average of thousands of laser shots in an unsteady discharge, then $n_e\hat{f}_k$ in Eq. 5-2 should be replaced by $\langle f_k \rangle$, the time-averaged one-dimensional unnormalized EVDF along $\vec{k}$. In this case, the Bayesian inference will produce samples of $\langle f_k \rangle$, and for each sampled time-averaged unnormalized EVDF, the time-averaged electron density, current density along $\vec{k}$, pressure along $\vec{k}$, heat flux along $\vec{k}$ and excess kurtosis along $\vec{k}$ can be unambiguously calculated through numerical integration of Eq. 5-10,

$$\langle n_e \rangle = \int \langle f_k \rangle dv \;, \langle j_{ek} \rangle = e\int v\langle f_k \rangle dv \;, \langle P_{ek} \rangle = m_e \int c_{\langle e \rangle}^2 \langle f_k \rangle dv \;, \langle q_{ek} \rangle = \frac{m_e}{2}\int c_{\langle e \rangle}^3 \langle f_k \rangle dv \;,$$

$$\langle n_e \Delta_{ek} \rangle = \left(\frac{m_e \langle n_e \rangle}{\langle P_{ek} \rangle}\right)^2 \int c_{\langle e \rangle}^4 \langle f_k \rangle dv - 3\langle n_e \rangle, \tag{5-10}$$

where $c_{\langle e \rangle} = v - \frac{\langle j_{ek} \rangle}{e\langle n_e \rangle}$. In the presence of plasma oscillations, the interpretations of $\langle q_{ek} \rangle$ and $\langle n_e \Delta_{ek} \rangle$ are more nuanced as they can be nonzero even if the instantaneous EVDFs are Maxwellian. For example, if n_e and u_{ek} oscillate out of phase, then $\langle q_{ek} \rangle$ can be nonzero even if q_{ek} is zero at every point in time, and if n_e and T_{ek} oscillate out of phase, then $\langle n_e \Delta_{ek} \rangle$ can be nonzero even if Δ_{ek} is zero at every point in time and $\langle T_{ek} \rangle$ can differ from $\frac{\langle P_{ek} \rangle}{e\langle n_e \rangle}$. In the presence of large electron inertia, the interpretation of $\langle P_{ek} \rangle$ calculated from Eq. 5-10 is also more nuanced because it is nonlinear in $\langle f_k \rangle$.

5.4.1.3. Generation of Synthetic ILTS Spectra

To evaluate the capabilities of the Bayesian inference methodology, the method needs to be tested against synthetic ILTS spectra. The first step in creating the synthetic spectra is defining the synthetic EVDFs. The four symmetric EVDFs this study considers are the 1D versions of the Maxwellian, Druyvesteyn, and Kappa distributions [177], defined as

$$\hat{f}^M = \frac{1}{\sqrt{\pi v_{th}^2}} \exp\left(-\frac{(v-v_D)^2}{v_{th}^2}\right), \tag{5-11}$$

$$\hat{f}^D = \sqrt{\frac{\pi\Gamma\left(\frac{5}{4}\right)}{6\Gamma\left(\frac{3}{4}\right)^3 v_{th}^2}} \operatorname{erfc}\left(\frac{2\Gamma\left(\frac{5}{4}\right)(v-v_D)^2}{3\Gamma\left(\frac{3}{4}\right)v_{th}^2}\right), \tag{5-12}$$

$$\hat{f}^{\kappa} = \frac{\Gamma\left(\kappa+\frac{3}{2}\right)}{\Gamma(\kappa+1)} \frac{\left(1+\frac{(v-v_D)^2}{\kappa v_{th}^2}\right)^{-(\kappa+3/2)}}{\sqrt{\pi\kappa v_{th}^2}}, \tag{5-13}$$

respectively, where $v_{th} = \sqrt{\frac{2eT_e}{m_e}}$. Next, from these symmetric EVDFs, skewed versions of Maxwellian, Druyvesteyn, and Kappa distributions are created with the transformation below,

$$\hat{f}^{skew} = \hat{f}\left(1 - a\,\mathrm{erf}\left(\frac{2b(v-v_D)}{v_{th}^2}\right)\right), \tag{5-14}$$

where a and b are parameters that describe the skewness of the distributions. The 9 EVDFs that this work tests the presented methodology against are described in Table 5-1 and plotted in Figs. 5-12 - 5-16. Table 5-1 includes five other distributions that are small variations of the EVDFs corresponding to spectra 1-9. Because a and b in Eq. 5-14 change the effective temperature and drift velocity of the EVDF, the values for v_D and T_e that we input in Eqs. 5-11 - 5-13 are those that ensure the corresponding values of u_e and T_e in Table 5-1.

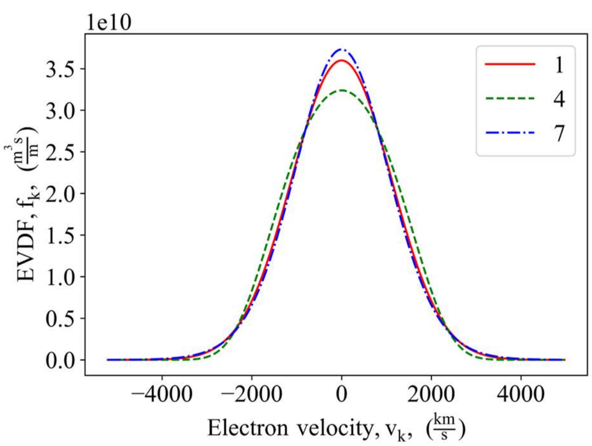

Figure 5-12: EVDFs corresponding to spectra 1, 4, and 7, representing Maxwellian, Druyvesteyn, and Kappa ($\kappa = 10$) distributions, respectively.

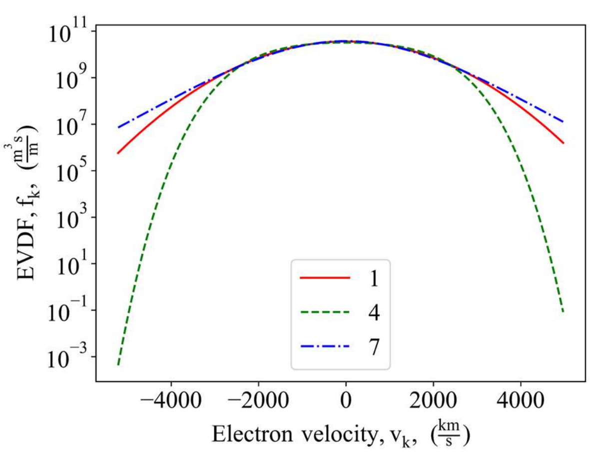

Figure 5-13: EVDFs corresponding to spectra 1, 4, and 7, representing Maxwellian, Druyvesteyn, and Kappa ($\kappa = 10$) distributions, respectively. Y-axis is plotted on a log scale to show the tails of the EVDFs.

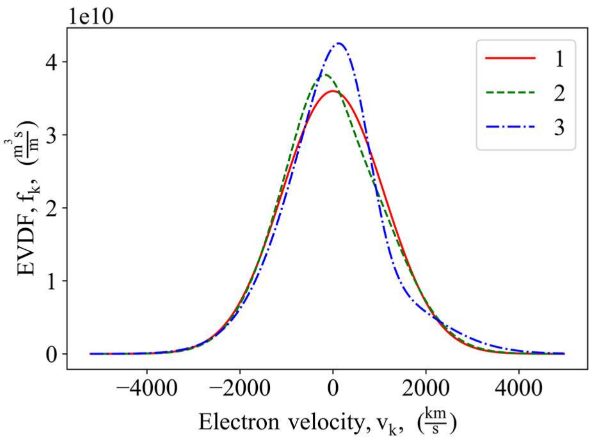

Figure 5-14: EVDFs corresponding to spectra 1, 2, and 3, representing a Maxwellian distribution and its skewed counterparts.

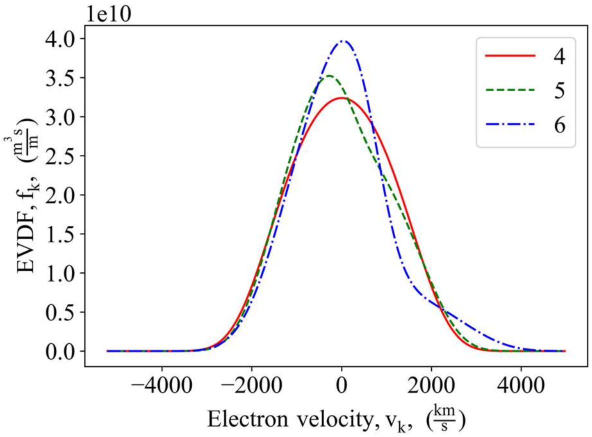

Figure 5-15: EVDFs corresponding to spectra 4, 5, and 6, representing a Druyvesteyn distribution and its skewed counterparts.

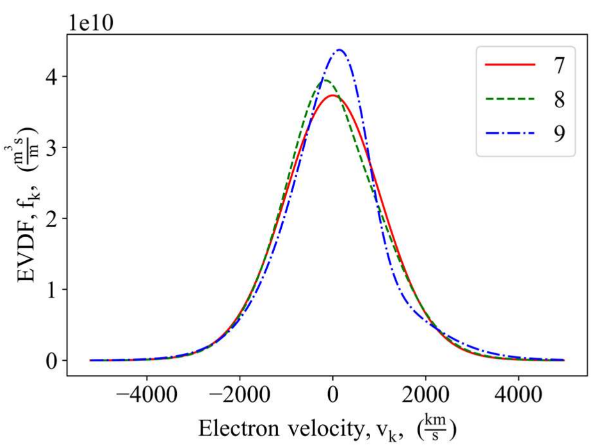

Figure 5-16: EVDFs corresponding to spectra 7, 8, and 9, representing a Kappa distribution (κ =10) and its skewed counterparts.

Spectra 1-12 are meant to evaluate the methodology on EVDFs with different excess kurtosis and skewness. Spectrum 13 is meant to evaluate the methodology with different drift velocities. The impact of the drift velocity is to shift the rejection region within the EVDF, so Spectrum 13 effectively evaluates the methodology when the rejection region is not at the peak of the EVDF. Spectrum 14 has the same EVDF as spectrum 7 but at a higher electron temperature, which evaluates the effect of a smaller rejection region with respect to the width of the EVDF.

Lastly, spectra 15 and 16 have the same EVDF as spectrum 6 but at different temperatures and the same reference detection system, so spectra 15 and 16 are meant to evaluate the flexibility of the methodology on a single detection system. It is important to note that for a given stray light filtering method and detection system, the effect of the rejection region is directly related to the effect of the spectral resolution.

Spectrum #	Distribution type	Detection system	Number of f_i^{SG}	a	b	u_e (km/s)	T_e (eV)	q_e (W/cm^2)	Δ_e
1	Maxwellian	A	1	0	0	0	7	0	0
2	Maxwellian	B	2	0.2	1	0	7	0.525	0.045
3	Maxwellian	B	3	0.7	3	0	7	2.034	1.201
4	Druyvesteyn	B	2	0	0	0	7	0	-0.532
5	Druyvesteyn	D	2	0.2	1	0	7	0.779	-0.483
6	Druyvesteyn	D	4	0.7	3	0	7	3.265	0.716
7	Kappa = 10	D	2	0	0	0	7	0	0.333
8	Kappa = 10	B	2	0.2	1	0	7	0.403	0.379
9	Kappa = 10	D	3	0.7	3	0	7	1.448	1.575
10	Kappa = 30	D	2	0	0	0	7	0	0.103
11	Kappa = 20	D	2	0	0	0	7	0	0.158
12	Kappa = 5	D	2	0	0	0	7	0	0.749
13	Kappa = 10	F	2	0	0	0	25	0	0.333
14	Kappa = 10	E	3	0.7	3	400	7	1.448	1.575
15	Druyvesteyn	D	3	0.7	3	0	1.03	0.183	0.716
16	Druyvesteyn	D	4	0.7	3	0	10.95	6.391	0.716

Table 5-1. Properties of the 16 synthetic spectra, including the underlying type of symmetric EVDF, the values of a and b used in Eq. 14, and the corresponding values of the electron drift velocity, effective temperature, heat flux, and excess kurtosis. For all cases, the electron density was $10^{17}\ m^{-3}$. Also shown are the detection systems that were necessary to accurately analyze the spectra and the number of super-Gaussians required to describe the spectra. For the Kappa distributions, the value of κ is denoted.

To create a realistic synthetic ILTS spectra from a synthetic EVDF, it is necessary to use a realistic rejection region, instrument function, and wavelength array. The choices of rejection region and instrument function are based on a reference detection system from a combination of low-temperature ILTS diagnostics that use VBG-NFs and an ICCD [178,179]. The reference rejection region will have a width of 2.5 nm, and the reference instrument function will be a Gaussian distribution centered at 532 nm with a standard deviation of 0.5 nm. The reference wavelength array will have 1024 elements and will be centered at 532 nm with a range of 17 nm. This reference detection system is denoted as detection system A.

In addition, for an accurate analysis, different EVDFs may require a higher spectral resolution or the same spectra resolution with a wider wavelength range. Because of this, the analysis will also consider different reference detection systems to illustrate the benefit of using different detection systems or acquisition strategies to analyze different EVDFs. Detection system B has the same rejection region, instrument function, and spectral resolution as detection system A, but its wavelength range is 34 nm. Detection system B is representative of acquiring two different spectra with the same detection system but with each spectrum being centered at different wavelengths. Detection system C has half the rejection region of system A, an instrument function with half the standard deviation of that of system A, twice the spectral resolution of system A, and the same spectral range as system A. Detection system C is representative of using a higher resolution grating than that used for system A, but acquiring two different spectra to achieve the same spectral range. Detection system D has the same rejection region, instrument function, and spectral resolution as system C but has 1.5 times the spectral range of system A. Detection system E has the same rejection region, instrument function, and spectral resolution as system C, but has the same spectral range as system B, and detection system F has twice the spectral range of detection system E and is the same otherwise.

Next, since σ_T is constant between the generation of the synthetic spectra and the application of the Bayesian methodology, σ_T was set to 1 in the testing of the methodology. An incident wavelength of 532 nm, a scattering angle of 90°, and a calibration constant of $C = 0.5$ are also assumed. From Eqs. 5-1 - 5-3, the synthetic ILTS spectra for a given synthetic EVDF is then constructed. The last step to generate the realistic ILTS spectra is to add Gaussian noise to the spectra, which is done with an SNR of 20 decibels. These SNR and noise profiles are representative of real ILTS measurements on low-temperature plasmas. Spectra 9 and 14 are shown in Figs. 5-17 and 5-18 to show how the drift velocity changes where the rejection region is with respect to the shape of the spectrum.

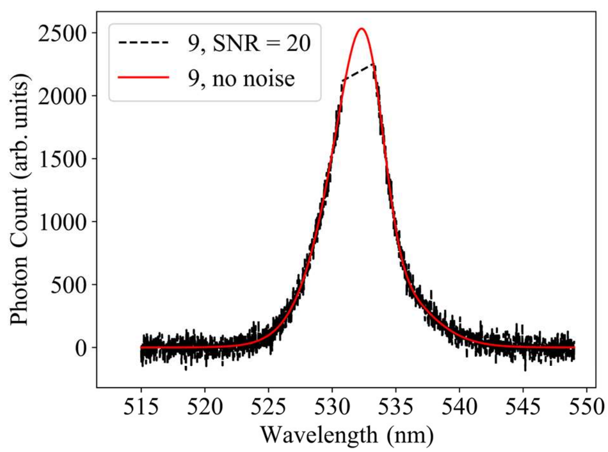

Figure 5-17: Synthetic ILTS spectrum of spectrum 9 on detection system B and an SNR of 20. Also shown is the corresponding synthetic spectrum with no noise and no rejection region.

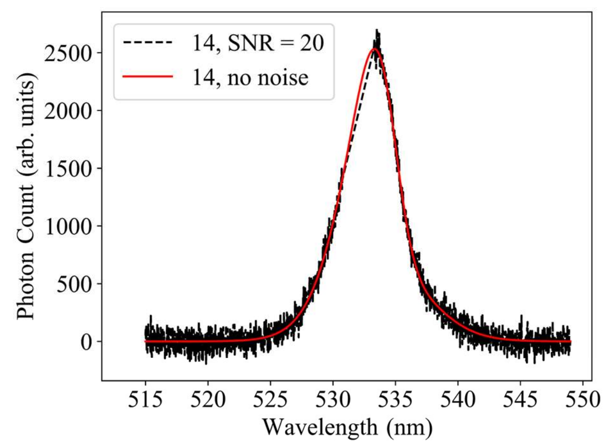

Figure 5-18: Synthetic ILTS spectrum of spectrum 14 on detection system B and an SNR of 20. Also shown is the corresponding synthetic spectrum with no noise and no rejection region.

Lastly, to evaluate the Bayesian inference methodology, an example prior distribution for the LRS calibration constant needs to be defined. The example prior distribution used in this work is a normal distribution centered at $C = 0.5$ with a standard deviation of 0.025. The standard deviation is chosen to represent the 10% uncertainty in the Raman scattering cross section of N_2 that typically dominates the uncertainty in the calibration constant obtained from LRS. In terms of processing time on a standard laptop, if using the sum of four super-Gaussians with the high spectral resolution of detection system D, analysis of a single spectrum takes around 15 minutes, and it takes around 3 minutes for the sum of two super-Gaussians with detection system B.

5.4.2. Results and Discussion of Data Processing Method

In this section, the Bayesian inference method is evaluated on the synthetic spectra shown in Section 5.4.1.3 regarding the method's accuracy and precision. The evaluation primarily focuses on the method's accuracy and precision of inferences of the heat flux and excess kurtosis. It is found that the methodology performs better on certain spectra, and this section also compares the proposed method to a simplified method that treats the EVDFs as sums of Gaussians. The method is considered to have adequate accuracy when the 95% HDIs of the first five moments of the EVDF contain the true values listed in Table 5-1. An important general finding is that for all the spectra considered, the proposed method is adequately accurate for inferences of the electron density, drift velocity, and heat flux. In addition, because the heat flux and excess kurtosis are deviations from Maxwellian EVDFs and thus have true values at or close to zero, it is not always appropriate to assess the method's precision with relative uncertainty. Instead of focusing on relative uncertainty when the inferred values are close to zero, the analysis will relate the bounds of the 95% HDI to the minimum detectable values of the heat flux and excess kurtosis with ILTS.

5.4.2.1. Evaluation of the Proposed Method

At an SNR of 20, the minimum detectable values of the electron heat flux and excess kurtosis can be approximated by the results in Table 5-2 of the analysis on spectra 1 and 4, respectively. From the 95% HDI of the excess kurtosis for spectrum 1, the minimum detectable excess kurtosis at 20 SNR is approximately $\pm$ 0.07. From the 95% HDI of the heat flux for spectrum 4, the minimum detectable excess kurtosis at 20 SNR is approximately $\pm$ 0.04 W/cm^2.

In general, it is more useful to consider the minimum detectable skewness, which in this case would be $\pm$ 0.006. Additionally, whenever the true value of a property is 0 or less than the minimum detectable value, it is found that the 95% HDI includes 0. The analysis can then consider the accuracy and precision of the proposed method for distributions with magnitudes of heat flux or excess kurtosis above these minimum values.

#	n_e (10^{16} m^{-3})	u_e (km/s)	T_e (eV)	q_e (mW/mm^2)	$10\Delta_e$
1	9.8 + 0.9 / - 0.6	1.2 + 8.4 / - 7	6.96 + 0.18 / - 0.13	0	-0.46 + 0.75 / - 0.70
2	9.9 + 0.8 / - 0.6	2.5 + 7.8 / - 7.7	7.00 + 0.15 / - 0.09	4.89 $\pm$ 1.35	0.74 + 0.80 / - 0.68
3	10.0 + 0.9 / - 0.7	-3.1 + 8.8 / - 9.6	6.78 + 0.27 / - 0.14	18.18 + 3.89 / - 3.06	10.19 + 1.82 / - 1.30
4	9.9 $\pm$ 0.7	-1.6 + 6.4 / - 5.9	7.06 $\pm$ 0.10	-0.01 + 0.42 / - 0.35	-5.26 + 0.34 / - 0.38
5	10.3 + 0.5 / - 0.9	-3.1 + 6.0 / - 6.8	7.01 + 0.07 / - 0.10	7.11 + 1.06 / - 0.83	-4.97 + 0.33 / - 0.25
6	9.8 + 0.9 / - 0.6	-2.4 + 9.1 / - 9.5	6.96 + 0.19 / - 0.13	30.34 + 4.47 / - 3.12	6.60 + 1.17 / - 0.92
7	10.1 + 0.3 / - 0.6	1.4 + 4.9 / - 4.1	**6.87 + 0.12 / - 0.11**	-0.19 $\pm$ 0.50	**2.12 + 0.76 / - 0.64**
8	9.9 + 0.8 / - 0.7	2.7 + 7.3 / - 6.6	6.92 + 0.13 / - 0.12	3.85 + 1.02 / - 1.15	**1.84 + 0.80 / - 0.90**
9	9.9 + 0.6 / - 0.5	-8.5 + 10.4 / - 10.3	6.88 + 0.32 / - 0.21	11.37 + 4.68 / - 3.26	14.09 + 3.27 / - 2.19
10	10.1 + 0.4 / - 0.6	2.9 + 4.9 / - 4.8	7.04 + 0.10 / - 0.09	0.15 + 0.56 / - 0.32	1.10 + 0.47 / - 0.36
11	10.0 $\pm$ 0.6	-2.4 + 5.5 / - 5.9	7.06 + 0.12 / - 0.15	-0.38 + 0.60 / - 0.78	1.53 + 0.91 / - 0.71
12	10.0 $\pm$ 0.6	-4.5 + 5.0 / - 5.1	**6.74 + 0.16 / - 0.14**	-0.16 + 0.58 / - 0.68	**4.21 + 1.16 / - 1.11**
13	9.8 + 0.8 / - 0.6	3.9 + 12.6 / - 15.7	24.8 + 0.6 / - 0.5	0.54 + 7.74 / - 11.62	2.93 + 1.63 / - 0.94
14	9.8 + 0.6 / - 0.4	401 + 10 / - 12	6.81 + 0.22 / - 0.15	14.23 + 4.37 / - 5.95	**12.29 + 1.94 / - 1.29**
15	9.7 + 0.8 / - 0.4	-0.3 + 3.3 / - 2.5	1.02 + $\pm$ 0.02	1.83 + 0.26 / - 0.18	5.79 + 1.42 / - 0.90
16	9.9 + 0.9 / - 0.7	-0.8 + 12.6 / - 13.7	11.0 $\pm$ 0.3	61.93 + 10.60 / 7.78	6.93 + 1.28 / - 1.20

Table 5-2. Inferred moments of the EVDF from the synthetic spectra using the presented Bayesian inference method. Inferences are presented as the mode of the posterior distributions and uncertainty bounds based on the 95% HDI of the posterior distributions. Values are bolded when the true value in Table 1 is not within the 95% HDI.

Regarding the accuracy of the proposed method on skewed Maxwellians, Table 5-2 shows that the proposed method achieves adequate accuracy for all properties, and Table 5-3 shows that the proposed method can achieve a relative error of electron heat flux measurements of less than 11%. In addition, when the true value of the excess kurtosis is above the minimum detectable value, as in spectrum 3, the method achieves a relative error of the excess kurtosis of 15.2%. This demonstrates that if the true values of the excess kurtosis and heat flux are above the minimum detectable values for a given SNR, then ILTS can accurately infer the excess kurtosis and heat flux for skewed Maxwellians. In terms of the precision of such inferences, the relative uncertainty of the inferred heat flux and excess kurtosis decreases as the deviation from Maxwellian EVDFs increases, as shown in Table 5-4. Relative uncertainties for the electron heat flux are between 15% and 30%, and when the excess kurtosis exceeds the minimum detectable value, the relative uncertainty is approximately 15%.

#	Relative error in q_e (%)	Relative error in Δ_e (%)
2	6.9	64.4
3	10.6	15.2
4	-	1.1
5	9.7	2.9
6	7.1	7.8
7	-	36.3
8	4.5	51.5
9	21.5	10.5
10	-	6.8
11	-	3.16
12	-	43.8
13	-	12.0
14	1.73	22.0
15	0	19.1
16	3.1	3.2

Table 5-3: Relative errors of the heat flux and excess kurtosis from the presented method for all the spectra with either a nonzero true heat flux or true excess kurtosis. When the true value of the heat flux is zero, the relative error is not shown. Relative error is based on the mode of the posterior distribution with respect to the true value.

#	Relative uncertainty in q_e (%)	Relative uncertainty in Δ_e (%)
2	$\pm$ 27.6	+ 108.1 / - 91.9
3	+ 21.4 / - 16.8	+ 17.9 / - 12.8
4	-	+ 6.5 / - 7.2
5	+ 14.9 / - 11.7	+ 6.6 / - 5.0
6	+ 14.7 / -10.3	+ 17.7 / - 13.9
7	-	+ 35.8 / - 30.2
8	+ 26.5 / - 29.9	+ 43.5 / - 48.9
9	+ 41.2 / - 28.7	+ 23.2 / - 15.5
10	-	+ 42.7 / - 32.7
11	-	+ 40.5 / - 53.6
12	-	27.6 / - 26.4
13	-	+ 55.6 / - 32.1
14	+ 30.7 / - 41.8	+ 15.8 / - 10.5
15	+ 14.2 / - 9.8	+ 24.5 / - 15.5
16	+ 17.1 / - 12.6	+ 18.5 / - 17.3

Table 5-4: Relative uncertainties of the heat flux and excess kurtosis from the presented method for all the spectra with either a nonzero true heat flux or true excess kurtosis. When the true value of the heat flux is zero, the relative uncertainty is not shown. Relative error is based on the uncertainty bounds from the 95% HDI of the posterior relative to the mode of the posterior distribution.

As for the accuracy of the proposed method on Druyvesteyn distributions and their skewed counterparts, Table 5-2 shows that the proposed method achieves adequate accuracy for all properties. From Table 5-3, the relative errors in heat flux and excess kurtosis are all below 10% when $T_e = 7$ eV. From Table 5-4, all relative uncertainties are below 20%, with the excess kurtosis having relative uncertainties below 10% when the heat flux is low and $T_e = 7$ eV. Additionally, the electron temperatures of spectra 15 and 16 represent approximate lower and upper limits of electron temperature, respectively, at which the corresponding shape of the EVDF can be accurately analyzed with the proposed method with detection system D. The increased relative error and relative uncertainty in the excess kurtosis for spectrum 15 are caused by the increased effect of the rejection region. The increased effect of the rejection region can also be visualized in the inferred EVDFs in Figs. 5-19 and 5-20 and is seen to decrease the accuracy of the inferred EVDF both within and outside the rejection region. In this case, the lower limit for the electron temperature corresponded to when one of the super-Gaussians reached the lower limit of Δv_i of 420 km/s. While the analysis of spectrum 16 has a similar accuracy and precision as that on spectrum 6, at even higher electron temperatures, inaccuracies and imprecision are caused by a smaller proportion of the EVDF being included in the analysis.

In general, it is found that the inferences of electron heat flux and excess kurtosis are more precise for Druyvesteyn EVDFs and their skewed counterparts than for skewed Maxwellian EVDFs. This is likely due to the depleted tails of Druyvesteyn distributions. The tails of the EVDFs are generally below the noise floor of ILTS spectra, so with depleted tails, more information is located above the noise floor. Since EVDFs with depleted tails are more common in low-temperature plasmas, this indicates that ILTS is well-suited to infer the higher-order moments of EVDFs in low-temperature plasmas. However, non-Maxwellian EVDFs in low-temperature plasma can have sudden depletion of the tails after the threshold energy of either an inelastic collision [180] or of the sheath potential [93,117], and if this threshold energy occurs below the noise floor of ILTS, then the proposed method would not enable ILTS to detect such EVDFs. In addition, for the case of spectrum 6, the accuracy of the inferred EVDF below the noise floor is surprisingly high, as shown in Fig. 5-21, which is further evidence that Druyvesteyn EVDFs and their skewed counterparts contain a significant amount of information above the noise floor. Lastly, the accurate inference for Druyvesteyn distributions is also seen in Figs. 5-22 and 5-23.

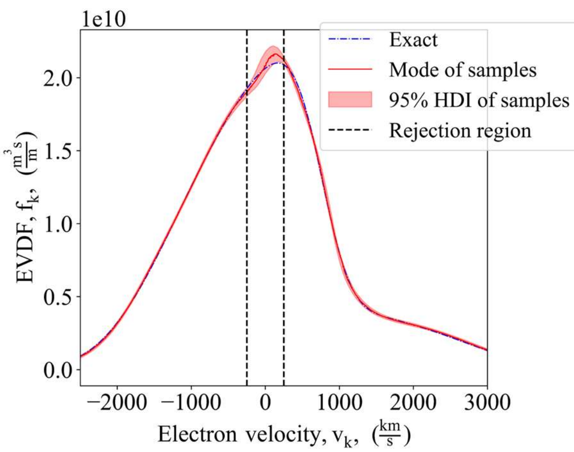

Figure 5-19: Inferred EVDF from spectrum 6 using the presented method. Also shown is the corresponding exact EVDF.

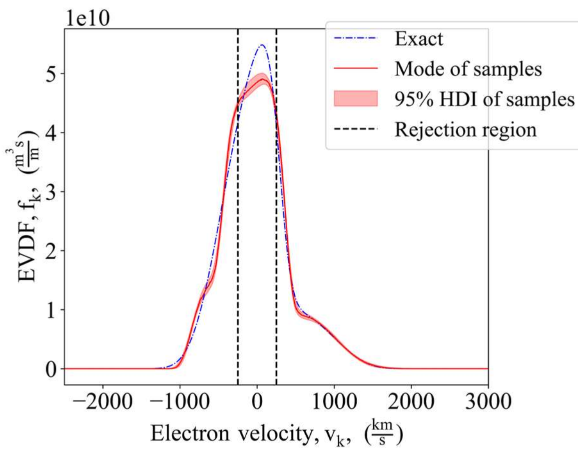

Figure 5-20: Inferred EVDF from spectrum 15 using the presented method. Also shown is the corresponding exact EVDF.

Similar reasoning explains the effects of the spectral resolution, since if the rejection region takes up a larger proportion of the spectrum, then less information is available, which decreases the accuracy and precision. For a constant detection system, the effect of the rejection region becomes greater at lower electron temperatures, such that each type of EVDF has a lower limit for the electron temperature at which a detection system can be used to accurately analyze that type of distribution. In addition, because of the finite bandwidth of VBG-NFs, each type of EVDF has a fundamental lower limit for the electron temperature for which ILTS can be accurately used to analyze that type of EVDF. The Maxwellian and Druyvesteyn distributions analyzed in this work are above these lower limits.

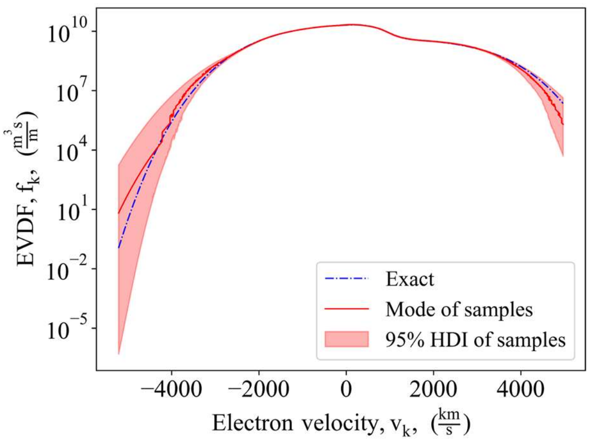

Figure 5-21: Inferred EVDF from spectrum 6 using the presented method. Also shown is the corresponding exact EVDF. Y-axis is plotted on a log scale to show the tails of the EVDFs.

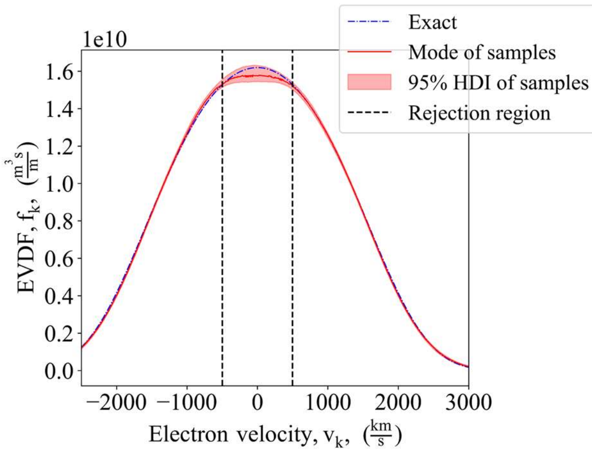

Figure 5-22: Inferred EVDF from spectrum 4 using the presented method. Also shown is the corresponding exact EVDF.

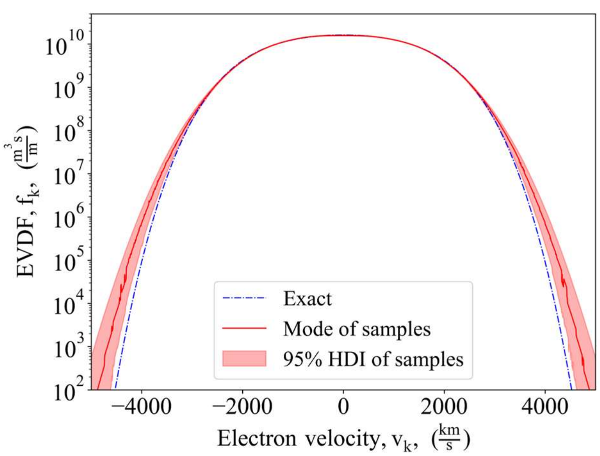

Figure 5-23: Inferred EVDF from spectrum 4 using the presented method. Also shown is the corresponding exact EVDF. Y-axis is plotted on a log scale to show the tails of the EVDFs.

The effect of relative spectral range has competing effects. For a given detection system, as the electron temperature increases, the tails of the EVDF are truncated, which decreases the amount of information in the spectrum, but the effect of the rejection region decreases, which increases the amount of information available. However, for sufficiently high electron temperatures, the increased benefit of a smaller rejection region is negligible, and the increasing effect of truncated tails will produce inaccurate and imprecise inferences. This may explain why spectrum 14 does not experience a noticeable decrease in accuracy or precision with respect to spectrum 6, even though some information above the noise floor in the tails of the EVDF of spectrum 16 is lost when using detection system D.

Regarding its efficacy on Kappa distributions, the method does not accurately capture the electron temperature or the excess kurtosis if the skewness and temperature are too low, as in spectra 7, 8, and 12. Even for these inaccurate cases, the proposed method is adequately accurate for the inferences of the electron density, drift velocity, and heat flux. The relative error in the excess kurtosis decreases to around 10% for sufficiently high heat flux, sufficiently low excess kurtosis, and higher electron temperature, as shown by spectra 9, 10, 11, and 13, respectively. The inferred EVDF for spectrum 11 is shown in Figs. 5-24 and 5-25, as it is the spectrum with the lowest relative uncertainty for the excess kurtosis among all the EVDFs with Kappa distributions. However, even for the accurate cases of spectra 9, 10, 11, and 13, the relative uncertainties for the heat flux and excess kurtosis are higher than for the analysis of Maxwellian distributions. Additionally, the proposed method is not adequately accurate for spectrum 14 for inferences of electron temperature and excess kurtosis; this inaccuracy is due to the drift velocity, which effectively shifts the location of the rejection region along the EVDF, suggesting that different locations of the EVDF contain more important information than others. The importance of the location of the rejection region is also relevant to the effect of poorly subtracted emission spectra when collecting ILTS data, as poorly subtracted emission spectra would lead to additional rejection regions.

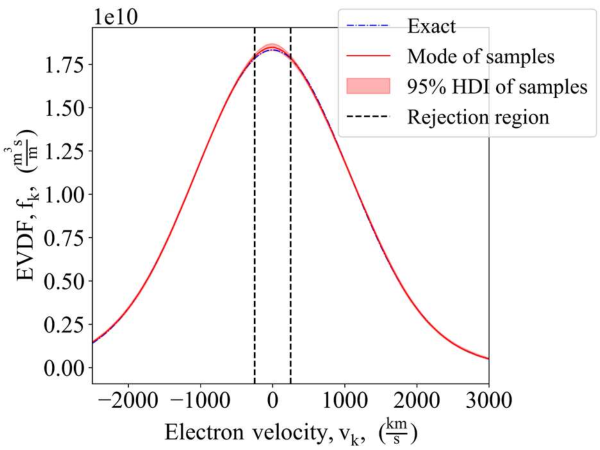

Figure 5-24: Inferred EVDF from spectrum 11 using the presented method. Also shown is the corresponding exact EVDF.

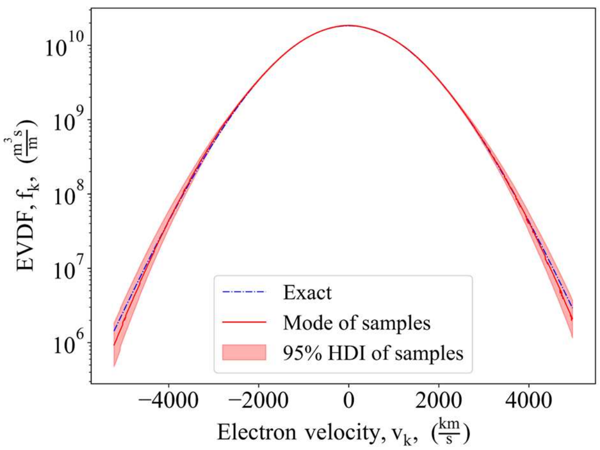

Figure 5-25: Inferred EVDF from spectrum 11 using the presented method. Also shown is the corresponding exact EVDF. Y-axis is plotted on a log scale to show the tails of the EVDFs.

Figures 5-26 and 5-27 compare the inferred ILTS spectra from spectra 9 and 14, respectively, to their corresponding synthetic spectra. The inferred spectra are reconstructed from the inferred EVDFs and the instrument function. Interestingly, the inferred spectrum for spectrum 9 deviates from the exact spectrum within the rejection region, which is not the case for spectrum 14. Although the difference between synthetic spectra 9 and 14 is predominantly the location of the rejection region relative to the shape of the EVDF, the reduced accuracy of the inference on spectrum 14 is not caused by inaccuracies within the rejection region. Instead, the location of the rejection region in spectrum 14 results in reduced accuracy of the inferred spectrum in the tails of the spectrum.

The worse performance of the proposed method on Kappa distributions is for the same reason that the method performs well for Druyvesteyn distributions. For distributions with positive excess kurtosis, more information is in the tails below the noise floor. This explains the improved performance of the method for sufficiently high heat flux, sufficiently low excess kurtosis, and higher electron temperature. If the skewness is high enough, as in spectrum 9, then there is sufficient information above the noise floor for the proposed method to be adequately accurate. For higher electron temperatures, assuming that the same proportion of the EVDF is analyzed but with a constant width of the rejection region, then the effect of the rejection region will reduce, and the same amount of information is lost in the tails. The adequate accuracy of the analysis of spectrum 13 indicates that a smaller rejection region can improve the performance of the proposed method on Kappa distributions. However, in general, careful consideration of the detection system and expected SNR, drift velocity, and temperature is necessary to determine whether ILTS can be used to accurately analyze a specific EVDF with low skewness and positive excess kurtosis. In fact, similar careful consideration of the detection system and acquisition strategy is necessary to accurately measure higher-order moments from EVDFs with negative excess kurtosis. This can be seen in Table 5-1, since several spectra required analysis with reduced rejection regions, such as detection systems D, E, and F.

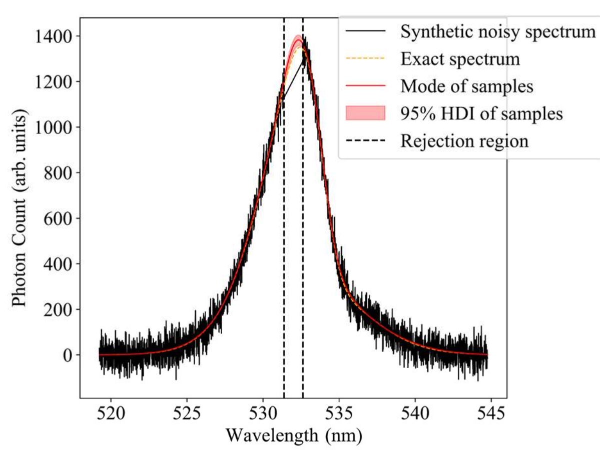

Figure 5-26: Inferred ILTS spectrum from spectrum 9 using the presented method. Also shown are the corresponding exact spectrum and the corresponding synthetic noisy spectrum on detection system D with an SNR of 20.

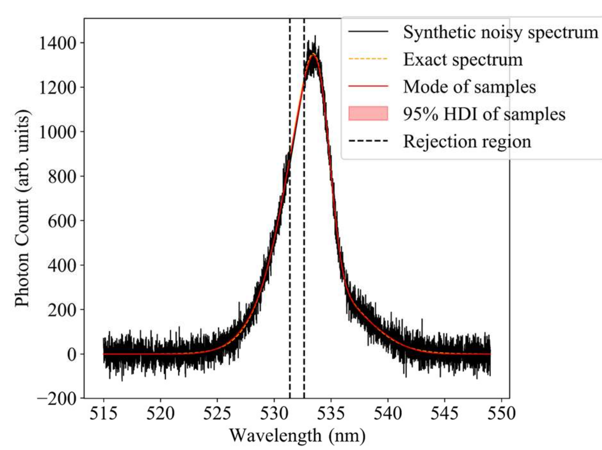

Figure 5-27: Inferred ILTS spectrum from spectrum 14 using the presented method. Also shown are the corresponding exact spectrum and the corresponding synthetic noisy spectrum on detection system E with an SNR of 20.

The parameters of the inferred super-Gaussians are shown in Table 5-5. Unsurprisingly, all the super-Gaussian components inferred for the Druyvesteyn distribution and its skewed counterparts have depleted tails. On the other hand, there is always one super-Gaussian component with depleted tails for the inferences on the Kappa distribution and its skewed counterparts. For the high skew cases of spectra 3, 6, and 9, the super-Gaussian component with the lowest density has the highest temperature by more than a factor of 2.

#	$\vec{\theta}_1\left(-,\frac{Mm}{s},\frac{Mm}{s},-\right)$	$\vec{\theta}_2\left(-,\frac{Mm}{s},\frac{Mm}{s},-\right)$	$\vec{\theta}_3\left(-,\frac{Mm}{s},\frac{Mm}{s},-\right)$	$\vec{\theta}_4\left(-,\frac{Mm}{s},\frac{Mm}{s},-\right)$
2	0.12, 1.28, -0.10, 1.85	-0.09, 1.91, 0.12, 2.42	-	-
3	0.16, 1.03, -0.29, 1.58	0.00, 0.50, 0.36, 2.66	-0.51, 2.60, 0.30, 2.93	-
4	0.23, 1.67, 0.01, 2.48	-0.48, 2.20, -0.04, 5.23	-	-
5	0.00, 2.06, 0.10, 3.71	-0.06, 1.21, -0.20, 2.17	-	-
6	-0.14, 1.04, -0.16, 3.41	-0.31, 1.45, -0.63, 3.58	-0.33, 0.60, 0.28, 3.14	-0.44, 2.34, 0.58, 3.23
9	0.03, 0.57, 0.32, 2.61	0.00, 0.92, -0.41, 1.58	-0.46, 2.39, 0.26, 2.46	-
10	0.27, 1.56, 0.01, 1.96	-1.20, 1.22, -0.26, 3.89	-	-
11	0.25, 1.53, -0.01, 1.85	-0.90, 1.52, 0.11, 3.77	-	-

Table 5-5: Means of the posterior distributions of the super-Gaussian model parameters, $\vec{\theta}$, as defined in Section 5.4.1.1. Results were obtained from the synthetic spectra using the proposed method. For readability, $\vec{\theta}$ is split into $\vec{\theta}_1$, $\vec{\theta}_2$, $\vec{\theta}_4$, and $\vec{\theta}_4$, corresponding to the individual super-Gaussians. As displayed in the table, $\vec{\theta}_i = \left[\log_{10}(A_i), \Delta v_i, v_{D,i}, b_i\right]$. $\vec{\theta}$ is only presented for spectra corresponding to unique non-Maxwellian EVDFs and for spectra for which the proposed method is adequately accurate.

5.4.2.2. Comparison with Simplified Method

For each spectrum, the simplified methodology was implemented with the same detection system and number of distributions as the proposed methodology, but each EVDF was the sum of Gaussians instead of super-Gaussians. As shown in Table 5-6, the simplified method has inadequate accuracy for the excess kurtosis for more spectra than the proposed method, and in some cases, inaccuracies are introduced for the drift velocities and heat flux. In particular, the simplified method is not adequately accurate for Druyvesteyn EVDFs and their skewed counterparts and for the high-skew EVDFs of spectra 3 and 9. Meanwhile, spectra 7 and 8 are the only spectra for which the proposed method does not have adequate accuracy but for which the simplified method does have adequate accuracy. Because the simplified method is only better than the proposed method for a limited range of Kappa distributions, the simplified method is not a general improvement to the proposed method for Kappa distributions. In addition, the simplified method generally has smaller uncertainty bounds than the proposed method, which can be explained by the fact that the proposed method considers more shapes of the EVDF.

#	n_e (10^{16} m^{-3})	u_e (km/s)	T_e (eV)	q_e (mW/mm^2)	$10\Delta_e$
1	10.0 + 0.7 / - 0.8	0.7 + 8.3 / - 8.6	6.98 + 0.13 / - 0.12	0	0
2	10.0 ± 0.7	-3.9 + 7.9 / - 6.5	7.03 + 0.09 / - 0.10	4.35 + 1.27 / - 1.14	0.72 + 0.39 / - 0.38
3	10.2 + 1.0 / - 0.8	-3.6 + 10.9 / - 9.5	7.19 + 0.22 / - 0.19	20.15 + 4.97 / - 3.91	**16.83 + 1.10 / - 0.91**
4	9.9 + 1.0 / - 0.7	3.7 + 8.4 / - 6.9	**7.30 + 0.07 / - 0.08**	-0.17 + 1.14 / - 1.06	**-4.17 + 0.22 / - 0.27**
5	10.0 ± 0.7	-0.9 + 7.8 / - 0.7	**7.30 + 0.07 / - 0.08**	**9.05 + 1.37 / - 1.07**	**-3.42 + 0.22 / - 0.19**
6	9.6 + 0.6 / - 0.5	4.9 + 9.0 / - 9.3	7.02 + 0.15 / - 0.14	31.86 + 2.84 / - 4.23	7.58 + 0.78 / - 1.13
7	9.9 + 0.8 / - 0.7	0.3 + 7.0 / - 8.6	6.94 + 0.15 / - 0.13	-0.7 + 1.33 / - 1.50	2.74 + 0.96 / - 0.74
8	9.8 + 1.0 / - 0.6	4.2 + 7.9 / - 7.8	6.92 + 0.14 / - 0.12	5.38 + 2.29 / - 1.37	2.90 + 0.92 / - 0,77
9	10.0 + 0.8 / - 0.6	-1.4 + 11.6 / - 10.5	**7.37 ± 0.21**	12.51 + 4.08 / - 3.92	**18.26 + 1.23 / - 1.14**
10	9.9 + 0.7 / - 0.5	**-7.7 + 6.3 / - 5.2**	6.97 + 0.08 / - 0.10	-0.25 + 0.44 / - 0.49	**0.42 + 0.35 / - 0.24**
11	10.0 ± 0.6	4.5 + 5.1 / - 6.0	6.92 + 0.08 / - 0.10	0.10 + 0.46 / - 0.47	**0.51 + 0.39 / - 0.21**
12	9.9 + 0.9 / - 0.6	-7.3 + 8.0 / - 7.8	6.82 + 0.19 / - 0.14	-0.64 + 1.27 / - 1.84	**4.75 + 1.44 / - 1.00**
13	10.0 + 0.6 / - 0.8	2.5 + 11.3 / - 9.7	25.1 + 0.3 / - 0.4	3.04 + 8.15 / - 8.35	3.48 + 0.83 / - 0.76
14	10.0 + 0.6 / - 0.7	389 + 11 / - 9	7.04 ± 0.19	**9.42 + 4.17 / - 2.74**	16.69 + 1.25 / - 1.03
15	9.9 ± 0.6	1.1 ± 2.7	**1.09 ± 0.02**	**2.07 + 0.23 / - 0.16**	**8.69 + 0.60 / - 0.50**
16	9.8 ± 0.6	2.2 + 14.4 / - 11.5	**11.2 + 0.3 / - 0.2**	68.46 + 9.49 / - 7.85	**8.51 + 0.95 / - 1.05**

Table 5-6: Inferred moments of the EVDF from the synthetic spectra using the simplified Bayesian inference method. Inferences are presented as the mode of the posterior distributions and uncertainty bounds based on the 95% HDI of the posterior distributions. Values are bolded when the true value in Table 5-1 is not within the 95% HDI.

Due to the inaccuracies of the simplified method, it is useful to consider the general impact of inaccuracies in the inferences of the heat flux and excess kurtosis. For the joint posterior distribution shown in Fig. 5-28, the drift velocity is most strongly correlated with the heat flux, and the temperature is most strongly correlated with the excess kurtosis. These correlations quantify how accounting for non-Maxwellian features is necessary to accurately infer the drift velocity and temperature. This is observed in Table 5-2, as the proposed methodology is adequately accurate for both the heat flux and drift velocity for all cases, but whenever the proposed method is inadequate for the excess kurtosis, the relative error in the temperature inference increases.

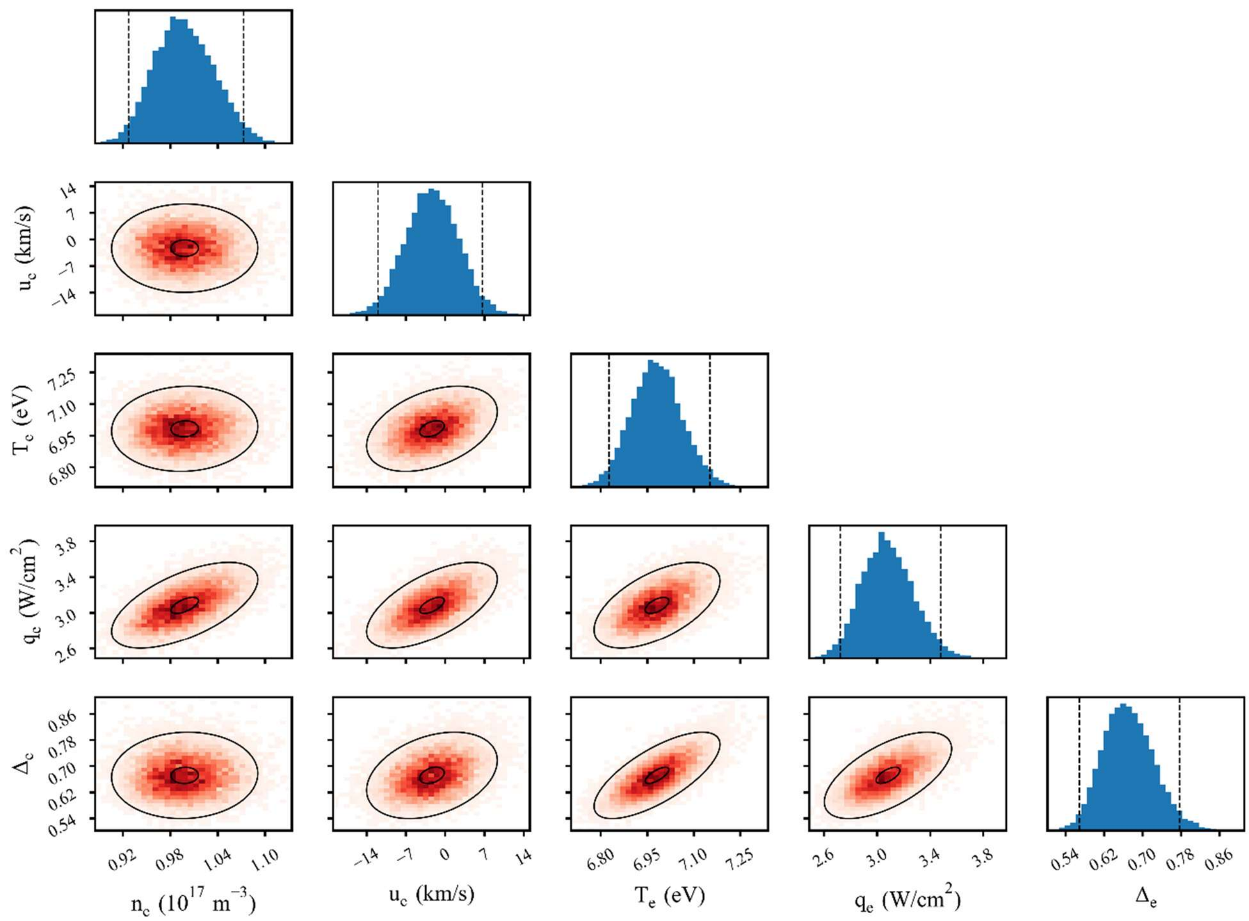

Figure 5-28: Marginal and joint posterior distributions of the electron density, drift velocity, temperature, heat flux and excess kurtosis. In the marginal distributions, the 95% HDIs are denoted with the vertical dashed lines. In the joint distributions, the Mahalanobis contours containing the most probable 10% and 95% of the distribution are shown. Posterior distributions are from the proposed method on spectrum 6.

5.4.3. Conclusion of Data Processing Method

In conclusion, this study has found that the presented Bayesian inference method can accurately expand the capabilities of ILTS to direct measurements of the electron heat flux and excess kurtosis. Specifically, for all the synthetic spectra considered, the presented method is adequately accurate for inferences of the heat flux with uncertainties ranging from around 40% to as low as around 10%. Notably, the method can accurately infer the excess kurtosis of Druyvesteyn distributions with an uncertainty of around 5%. In addition, the presented method performs favorably compared to a simplified method that only uses Gaussian distributions instead of super-Gaussians. However, the presented method does not accurately infer the excess kurtosis of certain Kappa distributions. To accurately infer the excess kurtosis of a wide variety of EVDFs with positive excess kurtosis and low skewness, high SNR measurements are needed in order that a significant portion of the tails are above the noise floor.

Future work should include implementing this method with actual measurements, which would enable high-fidelity validation of simulations that account for non-Maxwellian EVDFs. To do such measurements, it is necessary to carefully select the detection system and acquisition strategy to mitigate the effects of spectral resolution and spectral range. In addition, inferences of higher-order moments will be more affected by improper subtraction of stray light sources when constructing ILTS spectra. Lastly, although the synthetic spectra were constructed to replicate ILTS measurements in low-temperature plasmas, the presented method can be applied to ILTS measurements in high-temperature plasmas.

5.5. Implementation of Data Processing Method

First, we should clarify the spectral density equation, which was presented in a simplified form in Eq. 5-2. The spectral density of the photon counts in the signal measured from Thomson scattering as a function of wavelength is given as [127,132,171]

$$P_s^T(\lambda) = \eta \frac{\lambda_i}{hc} E_i L_{det} \Delta\Omega n_e \frac{d\sigma^T}{d\Omega} \frac{[I_s(\lambda) * \hat{f}_k(v)]}{k}, \quad (5\text{-}15)$$

where η is an efficiency constant, E_i is the incident laser energy, h is Planck's constant, c is the speed of light, L_{det} is the length of observation volume along the axis of the interrogation beam, $\Delta\Omega$ is the detection solid angle, and $\frac{d\sigma^T}{d\Omega}$ is the differential Thomson cross section. With our perpendicular scattering geometry, $\frac{d\sigma^T}{d\Omega}$ is maximized such that $\frac{d\sigma^T}{d\Omega} = r_e^2$, where r_e is the classical electron radius. The equation for $\frac{d\sigma^T}{d\Omega}$ for an arbitrary scattering geometry is given in Ref. 171.

In addition, we note that because there is a strong plasma emission line around 521 nm, as seen in Figs. 5-8 - 5-10, the background subtraction of this emission line was often not perfect and would distort the ILTS spectrum. Given the bad subtraction around 521 nm and the width of the instrument function shown in Section 5.5.2, for all the spectra, we decided to ignore data from 519.5 nm to 522.5 nm. Also, to remove the single pixel high intensity signals seen in Figs. 5-8 - 5-10 that are due to the pattern noise of the detector, we applied a median filter with a window of three pixels.

5.5.1. Intensity Calibration with Laser Raman Scattering

A calibration method is required to calibrate the efficiency constant in Eq. 5-15. This study calibrates the ILTS diagnostic with LRS. Rotational Raman scattering is used instead of Rayleigh scattering to calibrate the ILTS diagnostic because the detection optical setup is the same for both LRS and ILTS. Furthermore, because the detection and collection optical setups are the same for both LRS and ILTS, we use LRS to calibrate the product $\eta L_{det}\Delta\Omega$ instead of just η. To calibrate with Rayleigh scattering, the VBG-NFs must be temporally removed, which would slightly change η. LRS can be used to find η if the gas pressure is known. In this experiment, LRS calibration is done at a facility pressure of 10 Torr, assuming a residual gas composition of 79% N_2 and 21% O_2. The model equations for LRS are described in Appendix B, and an example measurement and fitting are shown in Fig. 5-29. In addition, measurements near the exit plane have a portion of the collection solid angle blocked by the thruster. To calibrate for this effect, we made laser Raman scattering calibration measurements at all measurement locations closer than 10 mm from the exit plane.

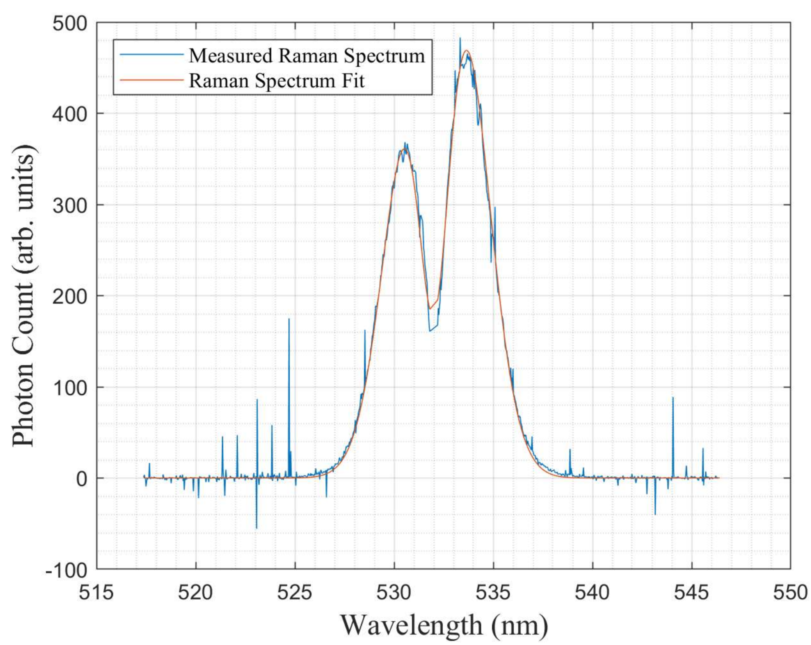

Figure 5-29: Measured LRS spectrum and the fit the data.

5.5.2. Instrument Function Calibration

We measured the instrument function at vacuum in the following manner. We moved the thruster into the path of the laser but reduced the laser energy to not damage the thruster. We then flipped the VBG-NFs out of the way and significantly delayed our detector with respect to the optimum delay and reduced the number of binned pixels to not saturate the detector. The measured instrument function is shown in Fig. 5-30.

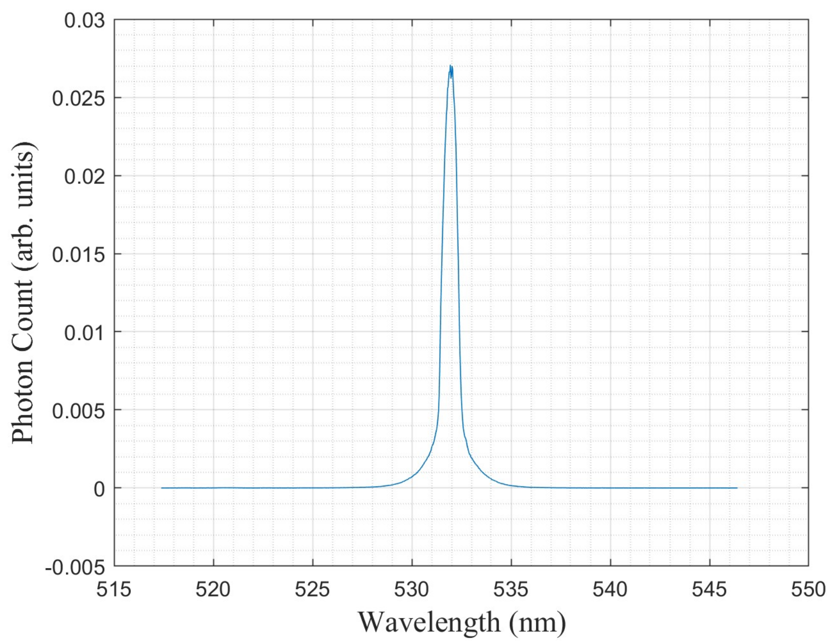

Figure 5-30: Measured normalized instrument function.

5.5.3. Bayesian Inference of Collision Rates

We also decided to calculate collision rates from electron-impact collisions with the Bayesian methodology. Since we are primarily measuring the EVDF in the azimuthal direction, we need a way to convert the azimuthal EVDF, $f_\theta(v_\theta) = \iint_{-\infty}^{\infty} f_{3D}(v_\theta, v_z, v_r) dv_z dv_r$, to an approximate 3-D EVDF. Since the Bayesian inference allows for skewed EVDFs, we cannot use the isotropic analysis that can be used with ILTS [171]. Instead, we assume that the 3-D EVDF is separable and given by

$$f_{3D}(v_z, v_r, v_\theta) = f_\theta(v_z + u_{e\theta}) f_\theta(v_r + u_{e\theta}) f_\theta(v_\theta), \tag{5-16}$$

where we assume that the axial and radial 1-D EVDFs have the same shape as f_θ but with zero drift velocity. From the 3-D EVDF, we calculate the electron speed distribution function through

$$f_v(v) = v^2 \int_0^{2\pi} \int_0^{\pi} f_{3D}(v\cos(\theta), v\sin(\theta)\sin(\theta), v\sin(\theta)\cos(\theta)) \sin(\theta)\, d\theta d\phi, \tag{5-17}$$

and the collision rate is given by

$$k_{col} = \frac{\int_0^\infty \sigma_{col}\left(\frac{1}{2} m_e v^2\right) v f_v dv}{n_e}, \tag{5-18}$$

where $\sigma_{col}\left(\frac{1}{2} m_e v^2\right)$ is the collision cross section as a function of the electron energy. This calculation is carried out for each sampled EVDF in the Bayesian inference, resulting in a mode and a 95% HDI that we define as the inferred collision rate and its uncertainty bounds.

5.6. Test Matrix

In this section, we will outline the test matrix, which will focus on the spatial map of the probed locations. We operated the H9 at 150 V and 30 A and on krypton. The 2-D map, shown in Fig. 5-31, will be made in the k_θ plane, as defined in Fig. 5-4. The 2-D map consists of 14 axial locations and 9 radial locations. We implemented a higher axial resolution in the upstream portion of the domain because we anticipated that region to have larger gradients in the electron properties. In addition, we made channel centerline measurements in the k_r plane.

To make certain trends in the data clearer, we decided to remove certain outliers. We defined outliers in all measurements by clear outliers in the measurements of skew and excess kurtosis, on the basis that clear outliers in skew and excess kurtosis are indicative that the ILTS spectrum was distorted by stray light. In total, this removed 8 points from the test matrix.

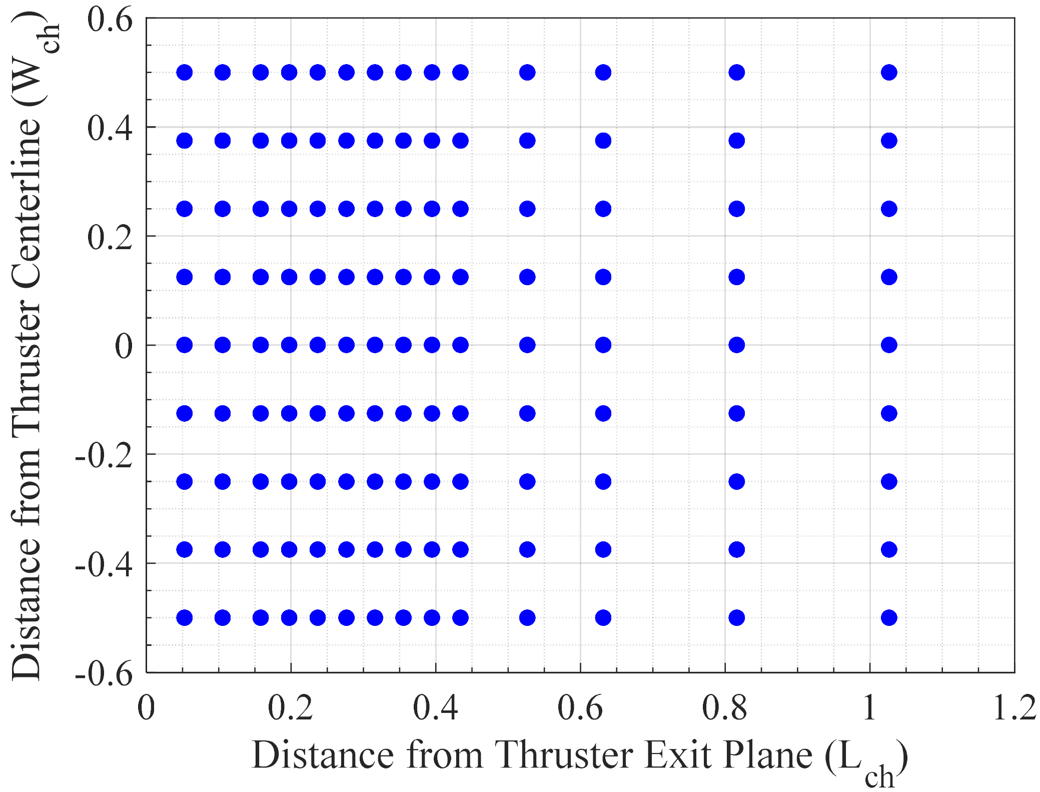

Figure 5-31: Measurements locations for 2-D map. L_{ch} is the H9 channel length, and W_{ch} is the H9 channel width.

CHAPTER 6. Computational Methodology

In this chapter, we will cover the computational methodology for inferring the anomalous electron Hall parameter from our ILTS measurements and for calculating the anomalous electron Hall parameter according to various closure models. Section 6.1 covers the governing equations for Ω_{ea}inference solver, the anomalous heating inference, and of two closure models. Section 6.2 covers the numerical implementation of the Ω_{ea} inference solver and of one of the closure models.

6.1. Governing Equations

6.1.1. Anomalous Electron Hall Parameter Inference

Our inference was carried in cylindrical coordinates instead of field-aligned coordinates. From the azimuthal electron momentum equation, the anomalous electron force density is given by

$$R_{ea} = en_e(u_{ez}B_r - u_{er}B_z) + m_e n_e \nu_c u_{e\theta} + m_e u_{ez}\frac{\partial u_{e\theta}}{\partial z} + m_e u_{er}\frac{\partial u_{e\theta}}{\partial r}. \qquad (6\text{-}1)$$

Assuming that $R_{ea} = -m_e n_e \nu_{ea} u_{e\theta}$, then the anomalous electron Hall parameter is given by

$$\Omega_{ea} = -\frac{eB \quad {}_e u_{e\theta}}{R_{ea}}, \qquad (6\text{-}2)$$

where $\nu_c = \nu_{ei} + n_n k_{en}$ such that, given $\vec{B}$ and the ILTS measurements of n_e, T_e, and $u_{e\theta}$, the unknowns in Eq. 6-1 are u_{ez}, u_{er}, and n_n. Given that we cannot solve for u_{ez} and u_{er} by combining the current continuity equation and axial and radial electron momentum equations (explained in Section 4.5.3), we chose to solve for u_{ez} and u_{er} in the following manner. We first approximate $u_{er} = -u_{ir} \pm 0.2u_{ir}$ motivated by approximate current continuity in just the radial direction. Then, we solve u_{ez} via the electron continuity equation

$$\frac{\partial(n_e u_{ez})}{\partial z} + \frac{\partial(n_e u_{er})}{\partial r} = n_e n_n k_{iz,1} + n_e^2 k_{iz,i} + n_e n_n k_{iz,2}, \tag{6-3}$$

and appropriate boundary conditions, where $k_{iz,1}$ is the ionization coefficient of single ionization of neutrals, $k_{iz,i}$ is the ionization coefficient of single ionization of singly charged ions, and $k_{iz,2}$ is the ionization coefficient of double ionization of neutrals. In this formulation, we have now added a new unknown, u_{ir}. We have also neglected the curvature term in the divergence term in Eq. 6-3, since it will be negligible in the channel. To clarify, even though the research hypothesis of Ω_{ea} being proportional to $u_{e\theta}$ along magnetic field lines has the underlying assumption that $u_{e\hat{\perp}}$ is approximately constant along magnetic field lines, our analysis does not assume that $u_{e\hat{\perp}}$ is constant along magnetic field lines. Instead, we approximate $u_{er} = -u_{ir} \pm 0.2u_{ir}$ and u_{ez} is calculated through Eq. 6-3.

To solve for u_{ir}, we solve it together with u_{iz} via the radial and axial singly charged ion momentum equations, given in conservative form by

$$\nabla \cdot (n_e u_{iz} \vec{u}_i) = e n_e E_z, \tag{6-4}$$

$$\nabla \cdot (n_e u_{ir} \vec{u}_i) = e n_e E_r, \tag{6-5}$$

and appropriate boundary conditions, where charge-exchange collisions are negligible and where $n_e = n_i$. The electric field components are given by the axial and radial electron momentum equations,

$$E_z = u_{e\theta} B_r - \frac{1}{n_e}\frac{\partial(n_e T_{eV})}{\partial z}, \tag{6-6}$$

$$E_r = -u_{e\theta} B_z - \frac{1}{n_e}\frac{\partial(n_e T_{eV})}{\partial r} + \frac{m_e u_{e\theta}^2}{er}. \tag{6-7}$$

To solve for n_n, we solve it together with u_{nz} and u_{nr} via the neutral continuity equation and the axial and radial neutral momentum equations

$$\nabla \cdot (n_n \vec{u}_n) = n_e n_n k_{iz,1} + n_e n_n k_{iz,2}, \tag{6-8}$$

$$\nabla \cdot (n_n u_{nz} \vec{u}_n) = -\frac{k_B T_n}{m_n} \frac{\partial n_n}{\partial z} - n_n n_e k_{CEX}(u_{nz} - u_{iz}), \tag{6-9}$$

$$\nabla \cdot (n_n u_{nr} \vec{u}_n) = -\frac{k_B T_n}{m_n} \frac{\partial n_n}{\partial r} - n_n n_e k_{CEX}(u_{nr} - u_{ir}), \tag{6-10}$$

and appropriate boundary conditions, where we have assumed a constant neutral temperature of 600 K $\pm$ 100 K, k_B is the Boltzmann constant, and k_{CEX} is the charge exchange rate coefficient. We note that using a fluid formulation for neutrals and ions does introduce inaccuracy into the inference, since neutrals and ions are known to be out of equilibrium in the discharge channel [40,181].

6.1.2. Anomalous Electron Heating Inference

Anomalous electron heating, Q_a is calculated by rearranging the electron energy equation, Eq. 2-49, and using the expression for $\langle \vec{j}_e \cdot \vec{E} \rangle$ from Eq. 2-51, such that

$$Q_a = \frac{5}{2}\frac{\partial(u_{ez} e n_e T_{eV})}{\partial z} + \frac{5}{2}\frac{\partial(u_{er} e n_e T_{eV})}{\partial r} - (j_{ez}E_z + j_{er}E_z) + \eta_a j_{e\theta}^2 + \nabla \cdot \vec{q}_e + Q_{in}, \tag{6-11}$$

where we have neglected elastic energy transfer between electron and the heavy species. Q_{in} includes the inelastic loss due to the three ionization mechanisms already included in the continuity equations and due to three effective excitation mechanisms defined by Ref. 182. Because the heat flux closure is unknown, we implemented 5 different heat flux models based on variations of the heat flux components derived in Section 2.4.1 and repeated below,

$$q_{e\hat{\perp}} = -\frac{5p_e}{2m_e\nu_c(1+\Omega_c^2)}\nabla_{\hat{\perp}}T_{eV} + \frac{5}{2}\frac{p_e u_{\hat{\perp}}}{(1+\Omega_c^2)} + \frac{5}{2}\frac{p_e u_{e\vartheta}\Omega_c}{(1+\Omega_c^2)} - \frac{5en_e\langle\delta T_{eV}\delta E_\vartheta\rangle\Omega_c B}{2(1+\Omega_c^2)}, \tag{6-12}$$

$$q_{e\parallel} = -\frac{5p_e}{2m_e\nu_c}\nabla_\parallel T_{eV} + \frac{5}{2}p_e u_{e\parallel}. \tag{6-13}$$

We define the terms $q_{e\hat{\perp},cond} = -\frac{5p_e}{2m_e\nu_c(1+\Omega_c^2)}\nabla_{\hat{\perp}}T_{eV}$, $q_{e\hat{\perp},conv} = \frac{5}{2}\frac{p_e u_{\hat{\perp}}}{(1+\Omega_c^2)}$, $q_{e\hat{\perp},azim} = \frac{5}{2}\frac{p_e u_{e\vartheta}\Omega_c}{(1+\Omega_c^2)}$ $q_{e\hat{\perp},anom} = \left(\frac{1}{1+\Omega_e\Omega_c} - \frac{1}{1+\Omega_c^2}\right)\left(q_{e\hat{\perp},cond} + q_{e\hat{\perp},conv} + q_{e\hat{\perp},azim}\right)$, $q_{e\parallel,cond} = -\frac{5p_e}{2m_e\nu_c}\nabla_\parallel T_{eV}$, and $q_{e\parallel,conv} = \frac{5}{2}p_e u_{e\parallel}$. The five heat flux formulations considered, denoted $\vec{q}_e^{\,1}$, $\vec{q}_e^{\,2}$, $\vec{q}_e^{\,3}$, $\vec{q}_e^{\,4}$, and $\vec{q}_e^{\,5}$, are given by

$$q_{e\hat{\perp}}^1 = q_{e\hat{\perp},cond} + q_{e\hat{\perp},anom}\,, q_{e\hat{\perp},conv} = q_{e\hat{\perp},azim} = 0, \tag{6-14a}$$

$$q_{e\parallel}^1 = q_{e\parallel,cond}, \tag{6-14b}$$

$$q_{e\hat{\perp}}^2 = q_{e\hat{\perp},cond} + q_{e\hat{\perp},anom}\,, q_{e\hat{\perp},conv} = q_{e\hat{\perp},azim} = 0, \tag{6-15a}$$

$$q_{e\parallel}^2 = q_{e\parallel,conv}, \tag{6-15b}$$

$$q_{e\hat{\perp}}^3 = q_{e\hat{\perp},cond} + q_{e\hat{\perp},conv} + q_{e\hat{\perp},azim}\,, \tag{6-16a}$$

$$q_{e\parallel}^3 = q_{e\parallel,conv}, \tag{6-16b}$$

$$q_{e\hat{\perp}}^4 = q_{e\hat{\perp},cond} + q_{e\hat{\perp},conv} + q_{e\hat{\perp},azim}\,, \tag{6-17a}$$

$$q_{e\parallel}^4 = 0, \tag{6-17b}$$

$$q_{e\hat{\perp}}^5 = q_{e\hat{\perp},cond} + q_{e\hat{\perp},conv} + q_{e\hat{\perp},azim} + q_{e\hat{\perp},anom}\,, \tag{6-18a}$$

$$q_{e\parallel}^5 = 0, \tag{6-18b}$$

$\vec{q}_e^1$ is intended to represent the electron heat flux model that is typically used in electron fluid simulations. $\vec{q}_e^2$ is used to show how Q_a changes when $q_{e\parallel,cond}$ is replaced by $q_{e\parallel,conv}$, which is a heat flux model that can recover non-isothermal magnetic field lines. $\vec{q}_e^3$ is used show how Q_a changes when $q_{e\hat{\perp},anom}$ is replaced by the physics based $q_{e\hat{\perp},azim}$ that is not typically used in electron fluid models of HETs. $\vec{q}_e^4$ is used to show how Q_a changes when $q_{e\parallel} = 0$, which is another heat flux model that can recover non-isothermal field lines. $\vec{q}_e^5$ is used to show how Q_a changes when both $q_{e\hat{\perp},azim}$ and $q_{e\hat{\perp},anom}$ are used simultaneously. Lastly, q_{ez} and q_{er} are calculated from $q_{e\hat{\perp}}$ and $q_{e\parallel}$ by

$$q_{ez} = q_{e\parallel}\frac{B_z}{B} - q_{e\hat{\perp}}\frac{B_r}{B}, \tag{6-19}$$

$$q_{er} = q_{e\parallel}\frac{B_r}{B} + q_{e\hat{\perp}}\frac{B_z}{B}. \tag{6-20}$$

6.1.3. Evaluated Closure Models

We evaluated two different closure models for the anomalous electron momentum transport based on plasma turbulence. The first closure model is an algebraic closure for ν_{ea} based on anomalous transport primarily due to the MTSI and is able to match semi-empirical data for ν_{ea} remarkably well across various discharge conditions and thrusters [49]. Algebraic here means that ν_{ea} is a function of previously defined plasma properties such as $\vec{u}_i$, n_e, T_e, etc. The second closure model is a two-equation closure for ν_{ea} based on anomalous transport due to the ECDI and is able to match experimental data for ν_{ea} on a single discharge condition very well [45]. Two-equation here means that ν_{ea} is a function of two turbulence parameters in addition to the previously defined plasma properties and these two turbulence parameters are defined by transport equations. While algebraic and one-equation closures for transport due to the ECDI have been presented [43,44,74], they have not produced satisfactory comparisons to experimental or semi-empirical data.

6.1.3.1. MTSI Closure

Ref. 49 presents two forms of their closure, one when ions are treated as a fluid and another when they are treated kinetically. Since we treat the ions as a fluid in our inference, we will use the fluid closure, which when written as a closure for Ω_{ea}, is

$$\Omega_{ea}^{MTSI} = \frac{u_{e\theta}}{u_B C_1 \exp(C_2 \omega_{LH} \tau_i)}. \tag{6-20}$$

where $u_B = \sqrt{\frac{eT_{eV}}{m_i}}$ is the Bohm velocity, C_1= 0.28 and C_2 = 2.5 × 10^{-3} are constants, ω_{LH} is the lower hybrid frequency, and $\tau_i = \frac{1}{n_n k_{iz,1} + n_n k_{CEX}}$ is the ion production time. $\omega_{LH} = \frac{\omega_{pi}}{\sqrt{1+\frac{\omega_{pe}^2}{\omega_{ce}^2}}}$, where ω_{pi} and ω_{pe} are the ion and electron plasma frequency.

6.1.3.2. ECDI Closure

The two-equation ECDI closure when written as a closure for Ω_{ea} is

$$\Omega_{ea}^{ECDI} = \frac{u_{e\theta} \omega_{ce} n_e T_{eV}}{C_3 \sqrt{2} u_B \langle \omega_i \rangle W_T}. \tag{6-21}$$

where W_T is the total wave energy density and $\langle \omega_i \rangle$ is the average rate at which the waves are able to extract energy from the ambient plasma, and C_3 = 130 is a constant [45]. The time-averaged W_T and $\langle \omega_i \rangle$ evolve according to

$$\nabla \cdot (W_T \vec{u}_i) = 2W_T \left(\langle \omega_i \rangle - \nu_{ei} - \frac{\nabla \cdot \vec{u}_i}{2} \right), \tag{6-22}$$

$$\nabla \cdot (\langle \omega_i \rangle \vec{u}_i) = 2\langle \omega_i \rangle \big(C_4 M_e \omega_{pi} - \langle \omega_i \rangle \big) - C_5 \frac{1}{M_e} \langle \omega_i \rangle^2 \frac{W_T}{n_e T_{eV}} - \langle \omega_i \rangle \nabla \cdot \vec{u}_i, \tag{6-23}$$

where $M_e = \frac{u_{e\theta}}{\sqrt{\frac{2eT_{eV}}{m_e}}}$ is the azimuthal electron Mach number, and C_4 = 0.01 and C_5 = 400 are constants. We note that we expressed Eqs. 6-22 and 6-23 in conservative form so that the discretization scheme is similar to that used for the ion and neutral solvers.

6.1.4. Collision Rates

ν_{ei} is calculated via Eq. A-3, while ν_c and all the inelastic collision rates are calculated via the Bayesian inference method described in Section 5.5.3. The collision cross sections for elastic momentum transfer and excitation of neutral krypton are extracted from the PROGRAM MAGBOLTZ, VERSION 7.1, 2024 [182]. The collision cross sections for single ionization of neutral krypton and single ionization of singly ionized krypton are obtained from Refs. 136 and 183, respectively. For the cross sections double ionization of neutral krypton, we used data from Ref. 184 between 40 and 45 eV, and data from Ref. 136 between 45 and 1000 eV. The collision cross section as a function of collision energy for the charge exchange collision between singly charged krypton and neutral krypton is obtained from the function form provided in Ref. 185 and is evaluated at the local ion energy assuming cold ions.

6.2. Numerical Implementation

6.2.1. Grid and Smoothing ILTS Measurements

For stability, we used a uniform mesh with a grid spacing of 0.0132 channel lengths that covered the entire experimental domain. We interpolated the ILTS measurements to this refined grid. Without smoothing the ILTS data, we would get alternating regions where E_r switched sign. This would create alternating regions where u_{ir} switched sign. Due to the radial convection term in the axial ion momentum equation, the boundaries of these alternating regions concentrated axial ion momentum to a degree that was clearly unphysical. To address this, we smoothed the data on the refined mesh with a 2-D gaussian filter with a window of 20 grid points. A window of 20 grid points was chosen because at 5, 10, and 15 grid points there were still local maximums of axial ion velocity away from the channel centerline. Preliminary results for the axial and radial ion velocities and Ω_{ea} are shown in Appendix C using windows of 10 and 15 for the gaussian filter.

6.2.2. Initialization

The transport equations of the ion solver, the neutral solver, and the ECDI closure solver were solved with separate time-marching sequences, so we needed to provide initialization values for u_{iz}, u_{ir}, n_n, u_{nz}, u_{nr}, W_T, and $\langle\omega_i\rangle$. E_z and E_r are calculated first with Eqs. 6-6 and 6-7. To provide the initial values of u_{iz} and u_{ir} throughout the domain, we set the radial gradients in Eqs. 6-4 and 6-5 to zero and use a simple backwards differencing scheme starting at the upstream boundary. The initial values of n_n are set as the solution to the neutral continuity equation with zero radial gradients and where the axial neutral velocity is assumed constant at the neutral thermal velocity; a simple backwards differencing scheme is used starting at the upstream boundary. The axial neutral velocity is initialized throughout the domain as a constant and equal to the neutral thermal velocity. The radial neutral velocity is initialized throughout the domain as zero. For the ECDI closure, we initialized W_T and $\langle\omega_i\rangle$ as $10^{-4}n_eT_{eV}$ and $C_4M_e\omega_{pi}$ throughout the domain, respectively.

6.2.3. 2-D Discretization

Each transport equation was evaluated by starting at the inner upstream boundary, looping through a radial slice of the grid, and then moving on the next radial slice downstream. Using i to indicate the radial indices and j to indicate the axial indices, $(i = 1, j = 1)$ corresponds to the inner upstream boundary. So, starting at $j = 1$, we solve each transport equation starting at $i = 1$ and sequentially step until $i = N_r$, where N_r is the number of radial points in the grid. Once the radial loop is complete, we then move on to $j = 2$, and so on until $j = N_z$, where N_z is the number of radial points. The electron continuity equation, Eq. 6-3, was solved for u_{ez} with a simple backwards difference discretization.

The sets of Eqs. 6-4 and 6-5, Eqs. 6-8 - 6-10, and Eqs. 6-22 and 6-23 were solved with separate time-marches, and during each time march, the steady-state component of the transport equation at each cell is evaluated semi-implicitly, such that terms from cells that have already been evaluated are evaluated with the updated terms from the following timestep $(t + \Delta t)$, while terms from cells that have not been evaluated (including the cell being evaluated) are evaluated with the terms from the current time step. The divergence of fluxes in Eqs. 6-4, 6-5, 6-8 - 6-10, 6-22, and 6-23 are evaluated as the difference of the fluxes at the cell boundaries, where the fluxes at the cell boundaries are evaluated with an upwinded scheme. For example, when evaluating $\nabla \cdot (X\vec{u})$ at cell (i, j),

$$[\nabla \cdot (X\vec{u})]_{i,j} = \frac{1}{\Delta h}\left(X^{up}_{i,j+\frac{1}{2}} u^{adv}_{z,i,j+\frac{1}{2}} - X^{up}_{i,j-\frac{1}{2}} u^{adv}_{z,i,j-\frac{1}{2}} + X^{up}_{i+\frac{1}{2},j} u^{adv}_{r,i+\frac{1}{2},j} - X^{up}_{i-\frac{1}{2},j} u^{adv}_{r,i-\frac{1}{2},j}\right), \quad (6\text{-}24)$$

where Δh is the grid spacing, the advective velocities at the cell boundaries are the average of the velocities at the cells on either side of the cell boundaries; that is, $u_{z,i,j+\frac{1}{2}} = \frac{1}{2}\left(u_{z,i,j} + u_{z,i,j+1}\right)$. The upwinded values are given by the following

$$X^{up}_{i,j+\frac{1}{2}} = \begin{cases} X_{i,j}, if\ u^{adv}_{z,i,j+\frac{1}{2}} > 0 \\ X_{i,j+1}, if\ else \end{cases}, \quad (6\text{-}25a)$$

$$X^{up}_{i,j-\frac{1}{2}} = \begin{cases} X_{i,j-1}, if\ u^{adv}_{z,i,j-\frac{1}{2}} > 0 \\ X_{i,j}, if\ else \end{cases}, \tag{6-25b}$$

$$X^{up}_{i+\frac{1}{2},j} = \begin{cases} X_{i,j}, if\ u^{adv}_{r,i+\frac{1}{2},j} > 0 \\ X_{i+1,j}, if\ else \end{cases}, \tag{6-25c}$$

$$X^{up}_{i,j-\frac{1}{2}} = \begin{cases} X_{i-1,j}, if\ u^{adv}_{z,i-\frac{1}{2},j} > 0 \\ X_{i,j}, if\ else \end{cases}. \tag{6-25d}$$

In Eqs. 6-22 and 6-23, $\nabla \cdot \vec{u}_i$ was evaluated as $[\nabla \cdot \vec{u}_i]_{i,j} = \frac{1}{\Delta h}\left(u^{adv}_{iz,i,j+\frac{1}{2}} - u^{adv}_{iz,i,j-\frac{1}{2}} + u^{adv}_{ir,i+\frac{1}{2},j} - u^{adv}_{ir,i-\frac{1}{2},j}\right)$.

6.2.4. Solver Steps

After initialization, the ion momentum equations, Eqs. 6-4 and 6-5, are solved for u_{iz} and u_{ir}. u_{er} is defined by u_{ir} and then u_{ez} is solve for via the electron continuity equation, Eq. 6-3. The neutral continuity and momentum equations, Eqs. 6-8 - 6-10, are then solved for n_n, u_{nz}, u_{nr}, after which Eq. 6-2 can be solved for Ω_{ea}. After this, Q_a and the closure models are evaluated.

6.2.5. Time Marching

To clarify, by time-marching we mean that we add the time-varying term back to Eqs. 6-4, 6-5, 6-8 - 6-10, 6-22, and we time-step until the solutions converge. For the convergence criteria for property X, we find the maximum of $\frac{X^{t+\Delta t}_{i,j} - X^{t}_{i,j}}{X^{t}_{i,j}}$ over the domain, and we define convergence as when $\frac{1}{\Delta t}\max\left[\frac{X^{t+\Delta t}_{i,j} - X^{t}_{i,j}}{X^{t}_{i,j}}\right] < 10^{-4}$. We use a CFL number of 0.2 to define the timesteps, such that

$\Delta t = \frac{0.2\Delta}{\max|u_{nz}|+\max|u_{nr}|}$ for the ion momentum solver and for the ECDI closure solver and $\Delta t = \frac{0.2\Delta h}{\max|u_{iz}|+\max|u_{ir}|}$ for the neutral solver.

6.2.6. Boundary Conditions

6.2.6.1. Upstream Boundary Conditions

We assume that at the upstream boundary, we define $u_{iz} = 0.4u_B \pm 0.1u_B$. We use the ILTS measurements of n_e to define $u_{ir} = u_{iz}\frac{\partial n_e/\partial r}{\partial n_e/\partial z}$ at the upstream boundary; this approximation for u_{ir} is loosely based on the ion particle conservation, in the sense that assuming negligible ionization, electron density drops as ions accelerate. We assume a radially uniform current density at the upstream boundary, such that $u_{ez} = u_{iz} - \frac{I_d}{en_eA_c}$ at the upstream boundary, where I_d is the discharge current and A_c is the channel cross-sectional area.

At the upstream boundary, we use the solution of the ion momentum solver to calculate n_n via the ion momentum equation, such that $n_n = \frac{\nabla\cdot(n_e\vec{u}_i)+n_e^2k_{iz,i}}{k_{iz,1}}$. We note that this could be used to solve for n_n throughout the domain. However, throughout a large part of the domain, this would give a negative n_n, which is indicative of inaccuracies in our measurements and subsequent inference of $\vec{u}_i$. To reduce the influence of our assumed boundary conditions for u_{iz} on our boundary condition for n_n, we use the values of $n_n = \frac{\nabla\cdot(n_e\vec{u}_i)+n_e^2k_{iz,i}}{k_{iz,1}}$ one cell inside the domain instead of exactly at the upstream boundary.

For the upstream boundary condition of u_{nz} we use mass conservation of krypton atoms and assume a radially uniform neutral axial flux, such that $u_{nz} = \frac{\dot{m}_a - m_n n_e u_{iz} A_c}{m_n n_n A_c}$, where $\dot{m}_a$ is the anode mass flow rate. For the upstream boundary of u_{nr}, we consider a simplified version of the radial neutral momentum equation, where the $\nabla \cdot (n_n u_{nr} \vec{u}_n) \approx n_n u_{nr} \frac{\partial u_{nz}}{\partial z}$ and with negligible charge exchange collisions, such that $u_{nr} = -\frac{k_B T_n}{n_n \frac{\partial u_{nz}}{\partial z}} \frac{\partial n_n}{\partial r}$. Lastly, for the ECDI closure, the upstream boundary conditions are $W_T = 10^{-4} n_e T_{e,eV}$ and $\langle \omega_i \rangle = C_4 M_e \omega_{pi}$, as in Ref. 45.

6.2.6.2. Radial Boundary Conditions

For Eq. 6-3, $\frac{\partial (n_e u_{er})}{\partial r}$ is calculated via backwards differencing, so no boundary condition is needed at the outer radial boundary. At the inner radial boundary, the boundary condition is $\left[\frac{\partial (n_e u_{er})}{\partial r}\right]_{i=1} = \left[\frac{\partial (n_e u_{er})}{\partial r}\right]_{i=2}$, where $\left[\frac{\partial (n_e u_{er})}{\partial r}\right]_{i=2}$ is known after completing the ion solver. Boundary conditions at both the inner and outer radial boundaries are needed for radial derivatives that are not calculated via backwards differencing, such as the upwinded terms. For the upwinded terms, extrapolation is used such that $X^{up}_{N_r+\frac{1}{2},j} = X_{N_r,j}$ and $X^{up}_{1-\frac{1}{2},j} = X_{1,j}$.

6.2.6.3. Downstream Boundary Conditions

Since $\frac{\partial (n_e u_{ez})}{\partial z}$ is calculated via backwards differencing, no boundary condition is needed at the downstream boundary. For the upwinded terms, extrapolation is used such that $X^{up}_{i,N_z+\frac{1}{2}} = X_{i,N_z}$.

6.2.7. Uncertainty Calculation

There are two main types of uncertainty in the inference of Ω_{ea}. First, there are the measurement uncertainties of each property measured by ILTS, which we define by the bounds of 95% HDI of the posterior distributions of the Bayesian inference. Second, there are the estimates of $u_{iz} = 0.4u_B \pm 0.1u_B$ at the upstream boundary, $u_{er} = -u_{ir} \pm 0.2u_{ir}$ throughout the domain, and $T_n = 600\ \mathrm{K} \pm 100\ \mathrm{K}$ throughout the domain. To propagate these uncertainties into the inference of Ω_{ea}, we make an inference for each combination of estimates and inferences, lower bounds, and upper bounds. Specifically, each inference uses either all the inference values, all the lower bound values, or all the upper bound values for T_e, all the inference values, all the lower bound values, or all the upper bound values for $u_{e\theta}$, all the inference values, all the lower bound values, or all the upper bound values for all the collision rates calculated via the integration method of Eq. 5-18, the estimate, lower bound, upper bound for u_{iz} at the upstream boundary, the estimate, lower bound, upper bound for u_{er}, and the estimate, lower bound, upper bound for T_n. In total, this amounts to 729 inferences, and then at each location of the 2-D map the minimum and maximum inference from the 729 define the uncertainty bounds for the inference. We did not propagate the uncertainty bounds the measurements of n_e because the uncertainty of n_e is dominated by the 10% uncertainty in the Raman scattering cross sections, so all n_e values would be shifted by the same proportion if a more accurate Raman scattering cross section is ever reported.

6.3. Justification and Limitations

In absence of a direct measurement of $u_{e\hat{\perp}}$, u_{ez} and u_{er} need to be inferred from the combination of measurements and governing equations. In Section 4.5.3, we explained that unrealistically precise and accurate measurements are needed to combine the charge continuity with the electron momentum equations to solve for u_{ez} and u_{er}. These unrealistic constraints are we why need to prescribe $u_{er} = -u_{ir} \pm 0.2u_{ir}$ throughout the domain. Direct measurements of u_{er} would be an improvement on this prescription, but the precision of drift velocity measurements of our ILTS system is not high enough to reliably improve on this prescription.

We decided to calculate u_{ez} through the electron continuity equation instead of through the charge continuity equation to account for doubly charged ions without having to solve for or measure the doubly charged ion density and velocity field. As previously explained, solving for the neutral density through $n_n = \frac{\nabla\cdot(n_e \vec{u}_i) + n_e^2 k_{iz,i}}{k_{iz,1}}$ instead of with the neutral continuity and momentum solver would be preferred, but the imprecision in our measurements did not allow this alternative to give physical results. However, a limitation of our implementation of using the electron continuity equation is that our calculation of the ionization rates is based only on measurements of azimuthal EVDF and assuming that the axial and radial EVDFs have the same temperature, skew, and excess kurtosis as the azimuthal EVDF. While it is generally a good assumption that the cyclotron motion equilibrates the azimuthal EVDF with the cross-field EVDF, the assumption that the azimuthal and parallel-field EVDFs are equal is generally inaccurate.

In addition, our quantification of anomalous momentum transport is based entirely on the contribution of azimuthal fluctuations. While correlations of axial fluctuations and of radial fluctuations can produce anomalous momentum transport, we have not attempted to infer these contributions. However, as shown in Ref. 64, the presence of axial fluctuations can change the azimuthal fluctuations. Therefore, even if we have not inferred the effect of axial fluctuations, our inferred anomalous azimuthal momentum transport will include the changes due to the presence of axial and radial fluctuations if such fluctuations are present at the tested operating condition. That is, the methodology does not inherently assume that the azimuthal fluctuations are not affected by axial or radial fluctuations.

Lastly, we should clarify that although we have emphasized the importance of operating at an off-nominal operating condition that pushes the acceleration region outside of the discharge channel, our methodology is generally applicable to all operating conditions. The main purpose of operating at an off-nominal condition was to minimize the effects of the inaccuracy of our boundary conditions for the ion velocity. By having the acceleration region outside the discharge channel, we can be confident that the ions have not experienced a significant potential drop upstream of the experimental domain, which justifies the low ion velocity used as the upstream boundary condition. On the other hand, at nominal operating conditions, the methodology for the interior solution in the experimental domain is valid, but supplemental measurements would be required for accurate boundary conditions of the ion velocity at either the upstream or downstream boundaries.

CHAPTER 7. Results

In this chapter we will cover the main results from this work. Section 7.1 covers the 2-D map of ILTS measurements and Section 7.2 covers the results from our 2-D solver, excluding the results of the inference of Ω_{ea}. Section 7.3 presents the inference of Ω_{ea}, Section 7.4 provides our answer to our research question, and Section 7.5 compares our experimental inference of Ω_{ea} with two closure models of Ω_{ea}. Lastly, Section 7.6 presents our inference of anomalous electron heating, Q_a.

7.1. ILTS Results

In this section, we will present example spectra and velocity distributions along with the 2-D maps of ILTS measurements. We will discuss physical mechanisms that could be responsible for certain features in the 2-D maps, and we will discuss the 2-D maps in the context of other experimental data and HET simulations. While the variation of electron temperature along magnetic field lines is shown in this section, Appendix C shows the variation of the density, azimuthal drift velocity, skew, and excess kurtosis along magnetic field lines. The figures that show the variation along magnetic field lines will also be the main reference for the level of uncertainty in the 2-D maps.

7.1.1. Raw ILTS spectra and inferred EVDFs and EEPFs

Here, we will present the raw ILTS spectra and inferred EVDFs and EEPFs at three locations of the 2-D map that broadly cover the different types of EVDFs that we observed. These locations are along the channel centerline and are at the axial locations of 0.1052, 0.2368, and 1.0263 channel lengths away from the channel exit plane. Between them, these points represent a high density and low temperature case, a moderate density and high temperature case, and a low density and low temperature case. While the inferred EVDFs will be used to compare moderate-to-high signal deviations from Maxwellian EVDFs, the inferred EEPFs will be used to compare deviations from Maxwellian EEPFs in the low signal tails of the distributions.

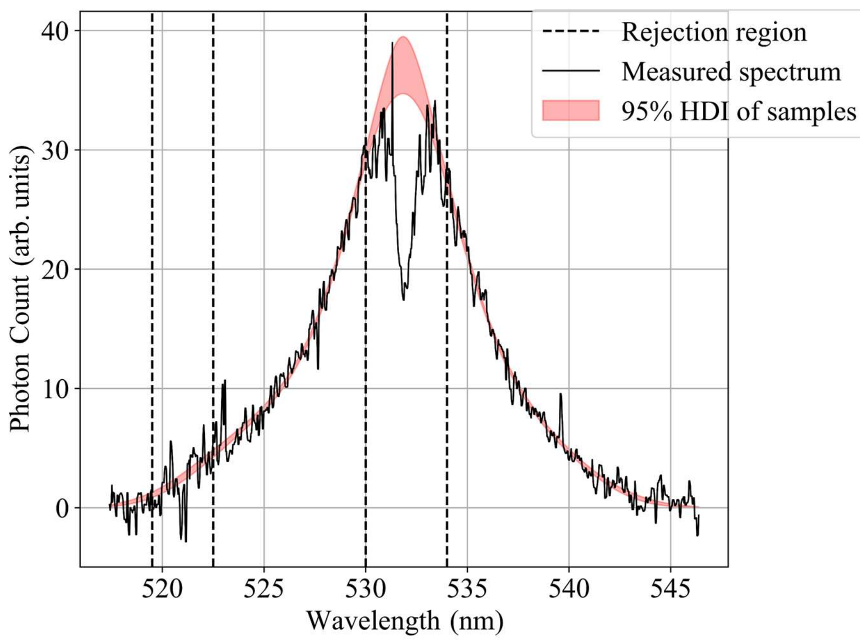

Figure 7-1: Measured ILTS spectrum and the 95% highest density interval of the sampled spectrum posterior distribution. At the channel centerline and 0.1052 channel lengths downstream of exit plane.

Figures 7-1 - 7-3 show the measured that the sampled spectra closely follow measured spectra, indicating that our data processing method is robust enough to handle ILTS spectra measured from HETs. We found that for all the locations in the test matrix, the data processing method required that the EVDFs be represented by the sum of two super gaussians. In addition, even though the peaks of the sampled spectra are within the rejection region around 532 nm in Figs. 7-1 - 7-3, the peaks of the spectra get flatter further away from the channel exit plane. This means that not only are the EVDFs non-Maxwellian, but that the deviation from Maxwellian EVDFs has a spatial distribution. Also, we note that the chosen measured spectra have negligible distortion near the strong emission peak at 521 nm. Lastly, we acknowledge that the measurement of the high temperature spectra can be improved to capture a larger portion of the EVDF. This can be done by either changing the scattering configuration to reduce the spectral width of given EVDF [186,187] or by measuring over a larger spectral range.

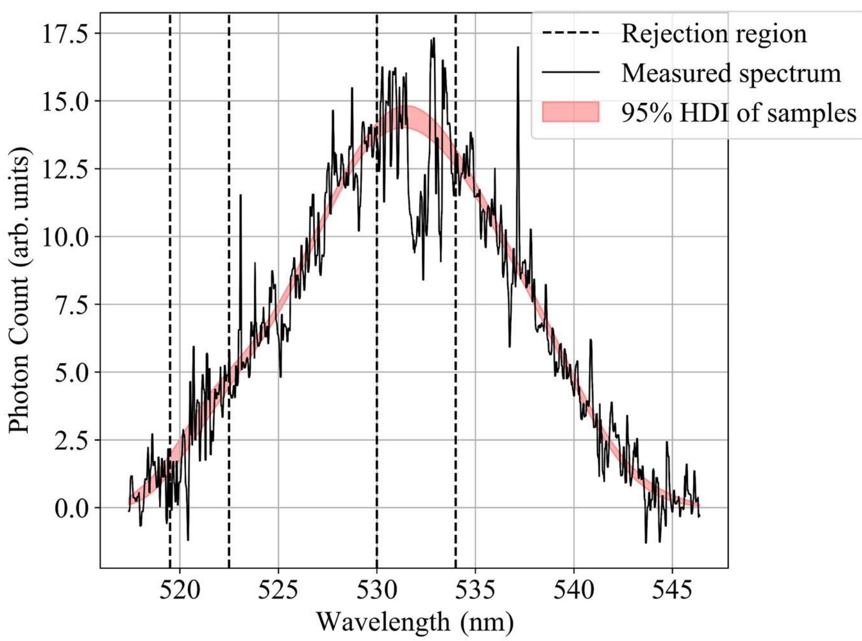

Figure 7-2: Measured ILTS spectrum and the 95% highest density interval of the sampled spectrum posterior distribution. At the channel centerline and 0.2368 channel lengths downstream of exit plane.

Figures 7-4 - 7-6 compare the sampled EVDFs to a corresponding Maxwellian EVDF, showing significant deviation from the Maxwellian EVDFs, particularly in Figs. 7-4 and 7-6. For the sampled EVDFs in Fig. 7-4, the posterior distributions for the skew and excess kurtosis had modes of -0.182 and 0.300, respectively. This negative skew is visible at high negative velocities in Fig. 7-4 and by the fact that the peaks of the sampled EVDFs are to the right of the peak of the Maxwellian EVDF even though they have the same mean velocity. The positive excess kurtosis is most visible in Fig. 7-4 via the sharp peak of the sampled EVDFs. For the sampled EVDFs in Fig. 7-5, the posterior distributions for the skew and excess kurtosis had modes of -0.091 and -0.500, respectively. The negative skew is again visible at high negative velocities in Fig. 7-5 and by the fact that the peaks of the sampled EVDFs are to the right of the peak of the Maxwellian EVDF even though they have the same mean velocity. Interestingly, while the negative excess kurtosis is similar to that of a 1-D Druyvesteyn EVDF, the relative difference in the peaks between the Maxwellian and the sampled EVDFs is lower than that between a Maxwellian and Druyvesteyn. For the sampled EVDFs in Fig. 7-6, the posterior distributions for the skew and excess kurtosis had modes of 0.056 and -0.561, respectively; however, the lower end of the 95% HDI of the skew posterior distribution was negative. This difference in negative and positive skew within the 95% HDI can be seen by the fact the peak of the upper bound of the 95% HDI is to the left of the Maxwellian EVDF, while the peak of the lower bound of the 95% HDI is to the right of the Maxwellian EVDF. Interestingly, while the excess kurtosis is similar to that in Fig. 7-5, the sampled EVDFs in Fig. 7-6 have a significantly flatter peak. This suggests that for the variety of EVDFs seen in a HET, the skew and excess kurtosis are not sufficient to describe the deviation from Maxwellian EVDFs.

Figures 7-7 - 7-9 the deviations from Maxwellian are more intuitive, since a Maxwellian EEPF is linear on a logarithmic scale. However, Figs. 7-7 - 7-9 cover different amounts of the EEPF because of the varying electron temperature. In Fig. 7-7, the positive excess kurtosis is visible through the heavy tail of the sampled EVDFs with respect to the Maxwellian EVDF. In Fig. 7-8, the range of EEPF cover does not allow for measurement in the tails. However, at the highest electron energies in Fig. 7-8, the higher magnitude slope of the sampled EEPFs compared to the Maxwellian EEPF is indicative of depleted tails. In Fig. 7-9, the negative excess kurtosis is evident in the depleted tail of the sampled EVDFs with respect to the Maxwellian EVDF. Because the tail has extremely low signal-to-noise, as seen in Figs. 7-7 - 7-9, the tails of the sampled EVDFs are essentially inferences of what the tail should be given the shape in the high signal-to-noise region. Because of this, our inferred tails would miss any sudden depletion of tails (due to collisional events at high threshold energies) that may occur and that have been observed in simulations of HETs [93,117]. However, the sudden depletion of tails observed in HET simulation has been primarily observed for radial EVDFs due to wall collisions but not for axial EVDFs or azimuthal EVDFs.

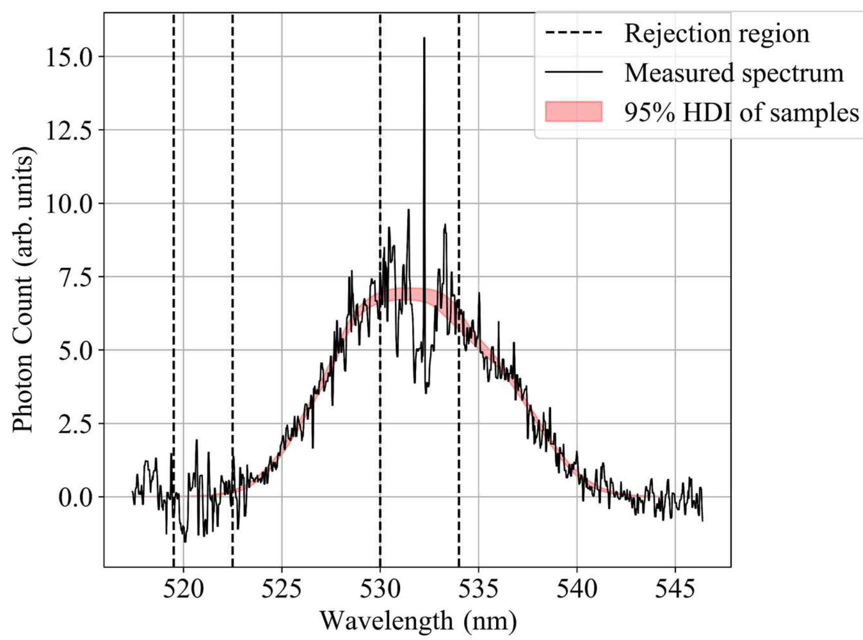

Figure 7-3: Measured ILTS spectrum and the 95% highest density interval of the sampled spectrum posterior distribution. At the channel centerline and 1.0263 channel lengths downstream of exit plane.

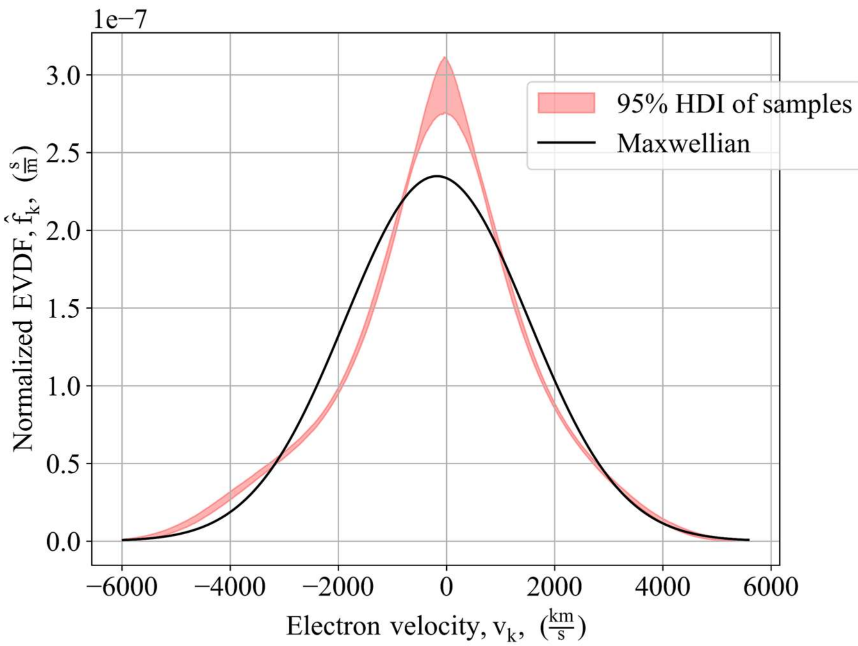

Figure 7-4: 95% highest density interval of the sampled EVDF posterior distribution and a Maxwellian EVDF with an electron temperature and drift velocity equal to the modes of the electron temperature and drift velocity posterior distributions. At the channel centerline and 0.1052 channel lengths downstream of exit plane.

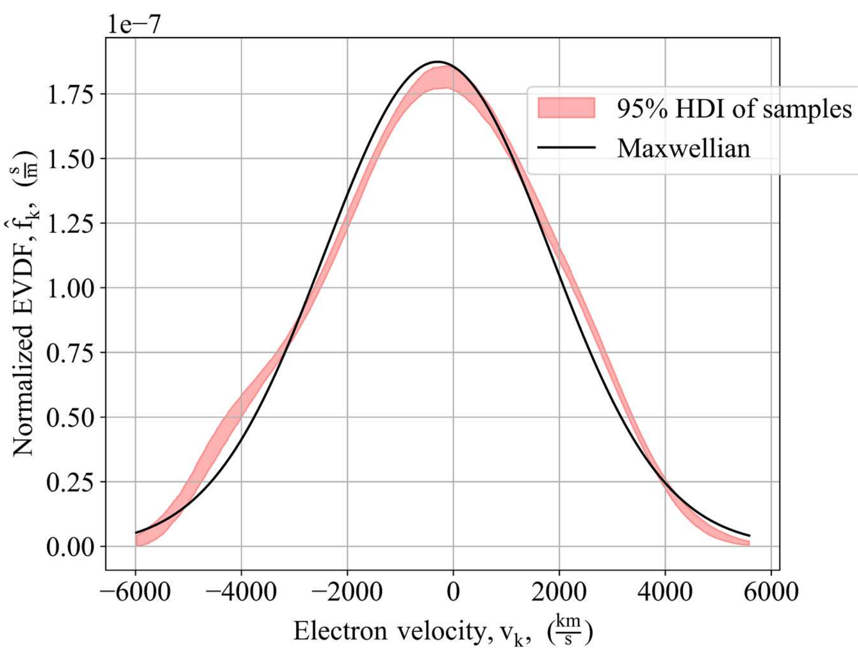

Figure 7-5: 95% highest density interval of the sampled EVDF posterior distribution and a Maxwellian EVDF with an electron temperature and drift velocity equal to the modes of the electron temperature and drift velocity posterior distributions. At the channel centerline and 0.2368 channel lengths downstream of exit plane.

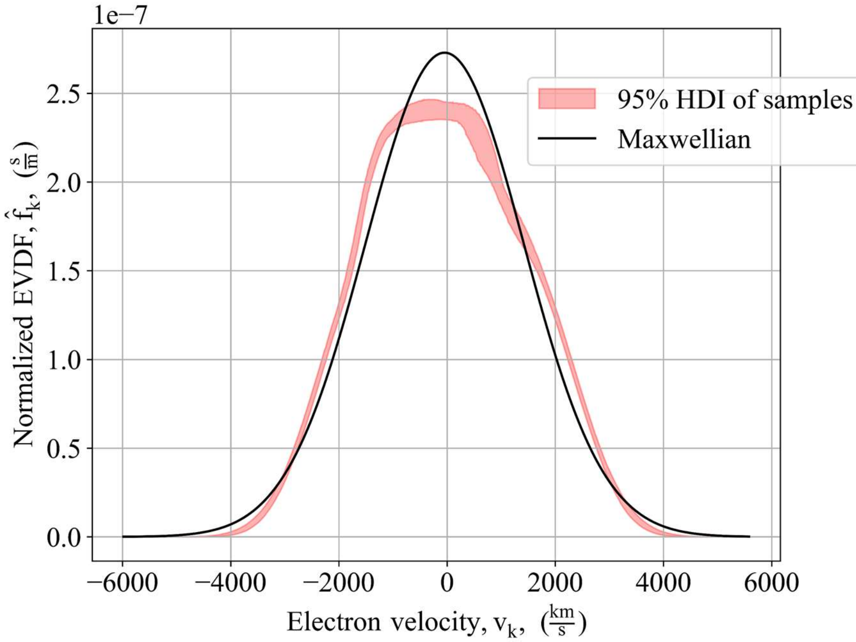

Figure 7-6: 95% highest density interval of the sampled EVDF posterior distribution and a Maxwellian EVDF with an electron temperature and drift velocity equal to the modes of the electron temperature and drift velocity posterior distributions. At the channel centerline and 1.0263 channel lengths downstream of exit plane.

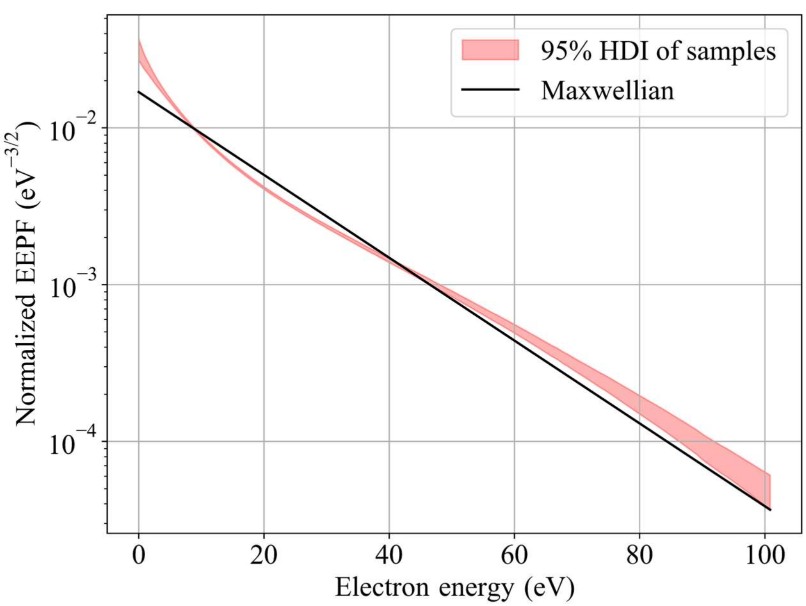

Figure 7-7: 95% highest density interval of the sampled EEPF posterior distribution and a Maxwellian EEPF with an electron temperature equal to the mode of the electron temperature posterior distribution. At the channel centerline and 0.1052 channel lengths downstream of exit plane.

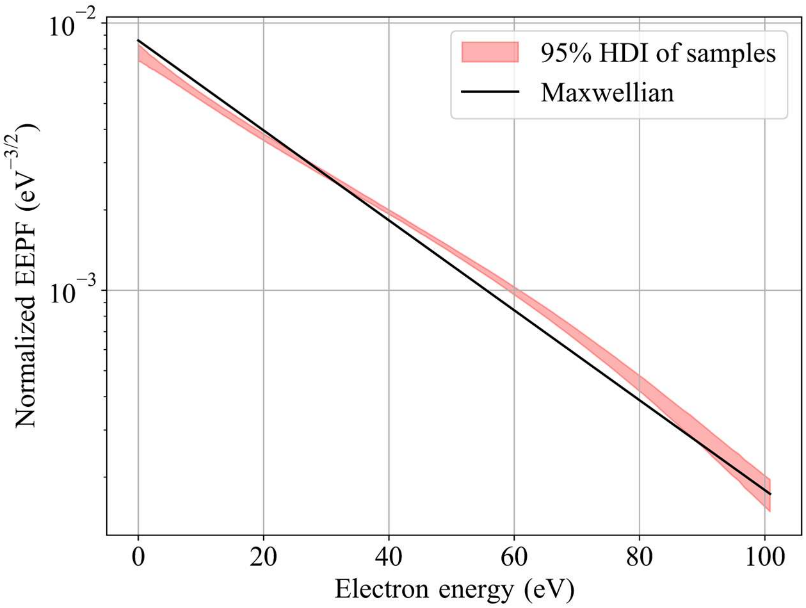

Figure 7-8: 95% highest density interval of the sampled EVDF posterior distribution and a Maxwellian EVDF with an electron temperature equal to the mode of the electron temperature posterior distribution. At the channel centerline and 0.2368 channel lengths downstream of exit plane.

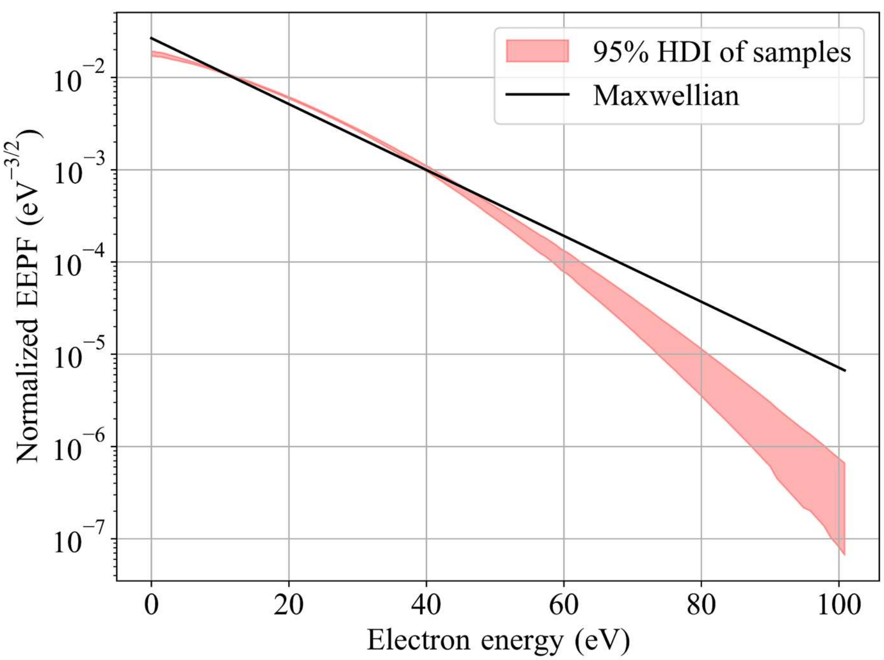

Figure 7-9: 95% highest density interval of the sampled EEPF posterior distribution and a Maxwellian EEPF with an electron temperature equal to the mode of the electron temperature posterior distribution. At the channel centerline and 0.1052 channel lengths downstream of exit plane.

7.1.2. 2-D Maps of ILTS Measurements

In this section, we will present and discuss the 2-D maps of the ILTS measurements of electron density, electron temperature, azimuthal electron drift velocity, skew of the azimuthal EVDF, and excess kurtosis of the azimuthal EVDF. To our knowledge, the measurements of skew and excess kurtosis are the first measurements of the spatial evolution of the higher order moments of the EVDF in a HET. In this section, we will be referring to the azimuthal electron temperature as simply the electron temperature. The 2-D maps are presented as color maps, which are constructed by interpolating the 2-D measurements to a refined grid with a uniform spacing of 0.0132 channel lengths.

In Fig. 7-10, we see the typical drop of electron density across the acceleration region, which is characteristic of axial ion acceleration with an approximately constant ion current density. Regarding the radial variation of electron density, the electron density peaks near the channel centerline and tends to be larger in the inner half of the channel compared to the outer half of the channel. These radial density gradients generate a radial electric field pointing outward from the channel centerline, resulting in divergence of the ion beam. In addition, we see that the minimum density measured is around 10^{17} m^{-3}, which, given the noise level in Fig. 7-3, suggests that the detection limit of the system is around 2×10^{16} m^{-3}.

The peak temperature in Fig. 7-11 of 29 eV is in line with previous ILTS measurements, which show a peak temperature around 20% of the discharge voltage [127,132,187]. Langmuir probes and fluid or hybrid simulations have found peak temperatures of around 13% of the discharge voltage in MS-HETs [12]. The discrepancy between ILTS measurements and fluid or hybrid simulations may suggest that the heat flux models or the phenomenological model for anomalous Joule heating used in electron fluid models should be revised.

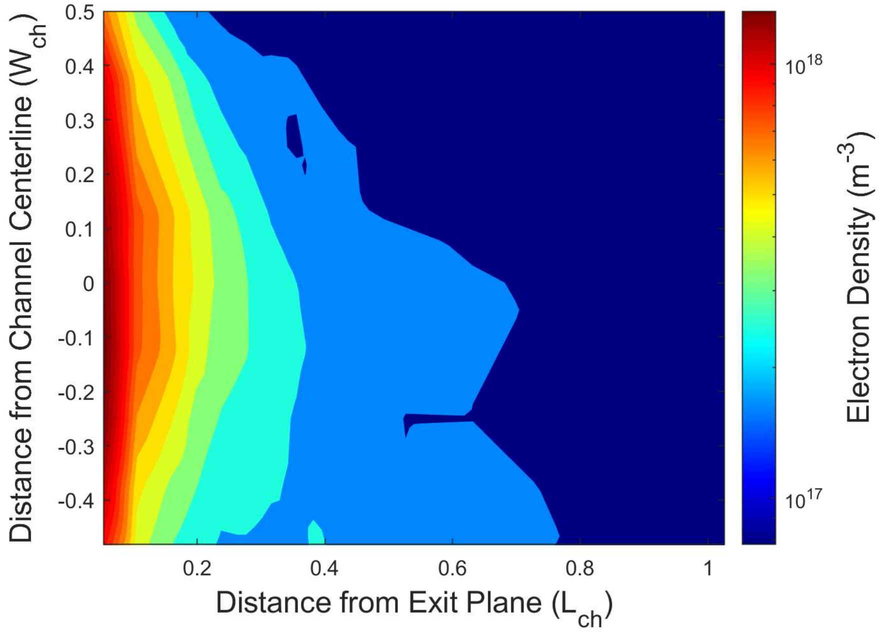

Figure 7-10: 2-D map of ILTS measurements of electron density. Axial coordinate is normalized by the channel length, and the radial coordinate is normalized by the channel width.

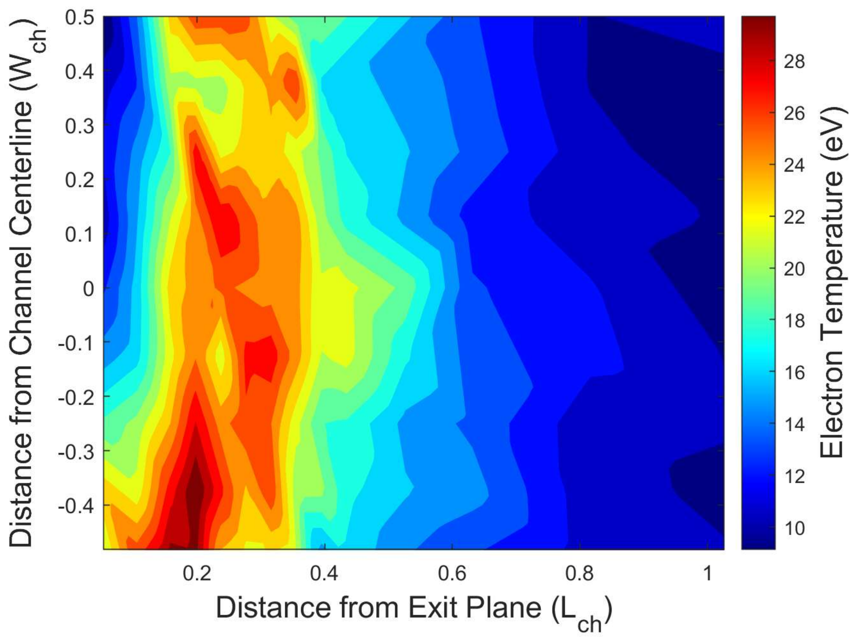

Figure 7-11: 2-D map of ILTS measurements of electron temperature. Axial coordinate is normalized by the channel length, and the radial coordinate is normalized by the channel width.

The high temperature region in the 2-D electron temperature map in Fig. 7-11 resembles a bowed shape, bending outwards away from the thruster. A bowed shape for the electron temperature map has been observed in 2-D and 3-D PIC simulations [116, 117] and can reconcile opposite trends found in recent ILTS experiments on the same thruster design as the one in this work [118,119]. While Ref. 118 measured electron temperatures increasing away from the channel centerline, Ref. 119 measured electron temperature decreasing away from the channel centerline. However, Ref. 118 operated the thruster at 150 V and 40 A, and Ref. 119 operated the thruster at 300 V and 15 A. As a result, Ref. 118 only measured the electron temperature upstream of the peak electron temperature along the channel centerline, while Ref. 119 only measured the electron temperature downstream of the peak temperature along the channel centerline. While our data is noisy, these trends are exactly what is seen in Fig. 7-11 which contains data across the entire acceleration region. That is, when the high temperature region has a bowed shape curving away from the thruster, upstream of the peak electron temperature along the channel centerline, the electron temperature will increase away from the channel centerline, and downstream of the peak electron temperature along the channel centerline, the electron temperature will decrease away from the channel centerline.

Regarding what causes this bowed shape in the electron temperature 2-D map, Ref. 117 recovered this bowed shape in their radial-axial PIC simulation. Since the magnetic field in Ref. 117 was purely radial, the authors found that the radial electron heat flux deviated from the classical conductive heat flux required for isothermal magnetic field lines. In addition, because Ref. 117 used a radial-axial PIC simulation, they could not self-consistently model anomalous electron momentum transport or anomalous electron heating, meaning that they needed to define single anomalous collision frequency. This formulation results in the phenomenological model of anomalous electron heating of $Q_a = \eta_a j_{e\theta}^2$, meaning that the bowed shape in the electron temperature map can be explained only by electron heat flux and does not require an alternative model for anomalous electron heating.

Because this bowed shape implies a deviation from isothermal magnetic field lines, it is instructive to interpolate our measured electron temperature on magnetic field lines. In Figs. 7-12 and 7-13, we have interpolated our measurements onto six field lines, with the number of the field lines increasing with distance from the channel exit plane. Among the field lines, field line 2 has the highest electron temperature at the channel centerline. Field line 1 exhibits a clear increase in electron temperature away from the channel centerline, which makes sense since it is upstream of field line 2. For field line 2, the electron temperatures at the inner and outer edges of the channel are higher than at the centerline, but the electron temperature confidence intervals for the centerline and the outer edge overlap. For field line 3, the electron temperatures at the inner and outer edges of the channel are lower than at the centerline, but the electron temperature confidence intervals for the centerline and inner edge overlap. For field line 4, the electron temperature is highest at the channel centerline. Lastly, for field lines 5 and 6, there is an approximately linear trend in the electron temperature between the inner and outer edges of the channel. We find that the magnetic field lines are non-isothermal and that whether electron temperatures increase or decrease away from the channel centerline depends on whether the field line is upstream or downstream of the field line with the peak electron temperature along the channel centerline.

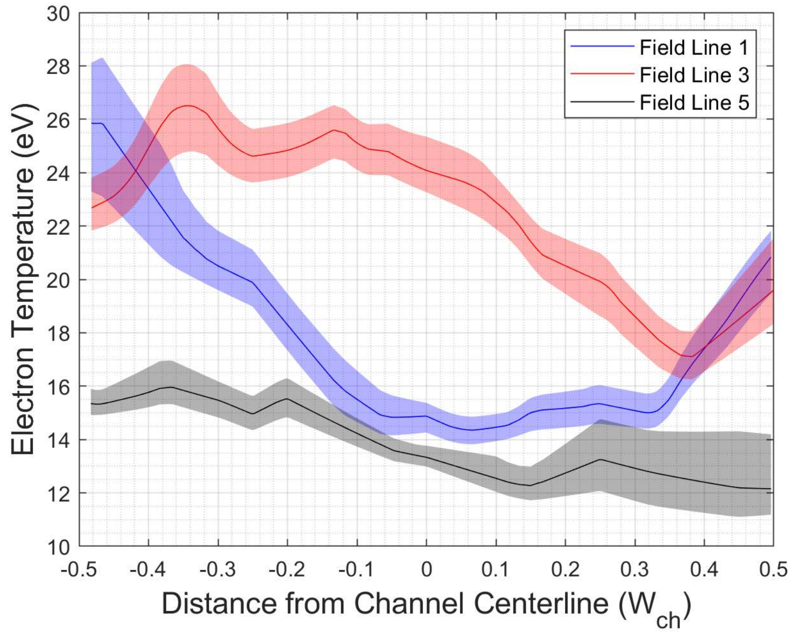

Figure 7-12: Radial variation of electron temperature along magnetic field lines 1, 3, and 5. Radial coordinate is normalized by the channel width.

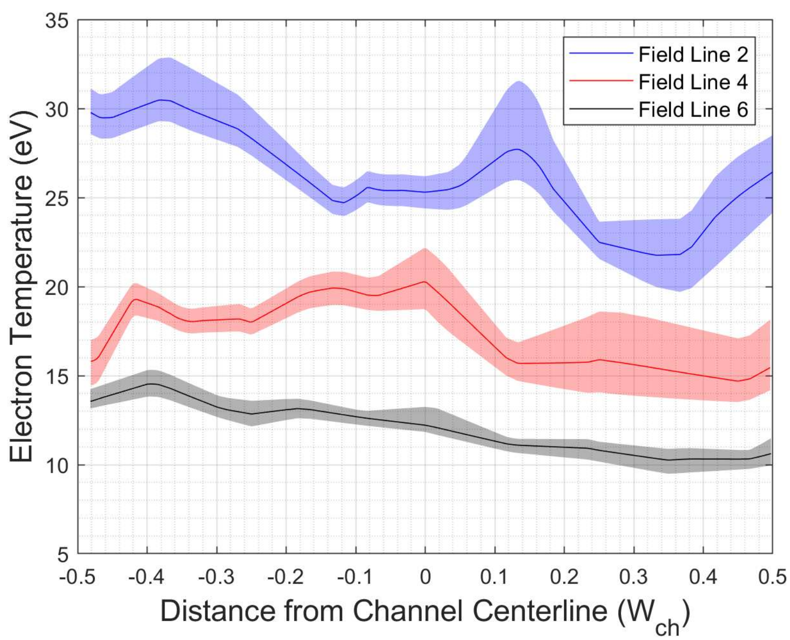

Figure 7-13: Radial variation of electron temperature along magnetic field lines 2, 4, and 6. Radial coordinate is normalized by the channel width.

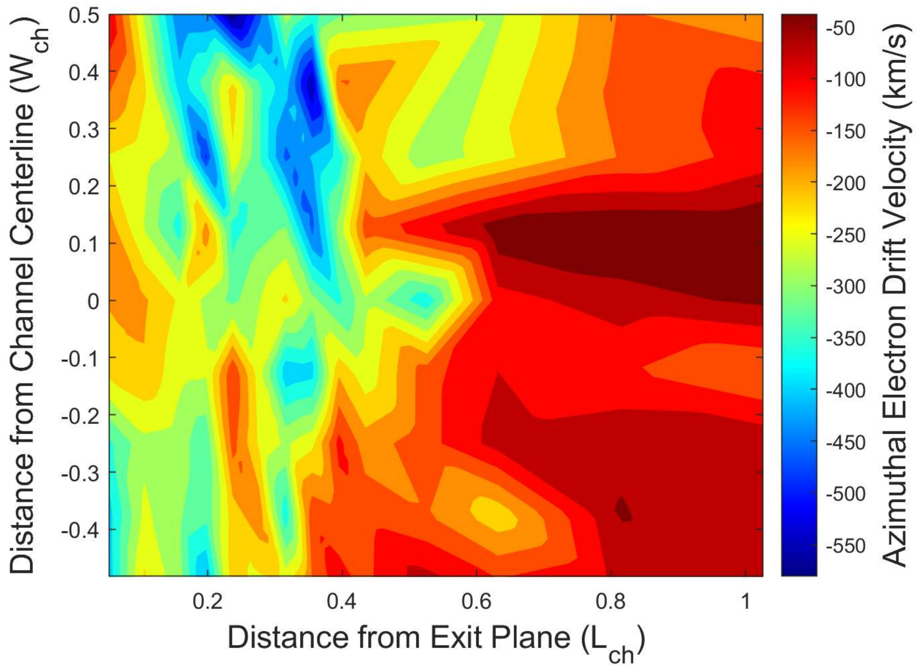

Figure 7-14: 2-D map of ILTS measurements of azimuthal electron drift velocity. Axial coordinate is normalized by the channel length, and the radial coordinate is normalized by the channel width.

In Fig. 7-14, the region of high $|u_{e\theta}|$ seems to have a similar bowed shape as that of the electron temperature, although a definite conclusion is challenging due to the noisy data. The peak $|u_{e\theta}|$ is around 550 km/s. In the outer two-thirds of the channel, we observe the rise and fall of $|u_{e\theta}|$ characteristic of probing across the axial extent of the acceleration region. However, for the inner third of the channel, $|u_{e\theta}|$ is already high at the exit plane, meaning that the upstream portion of the acceleration region is inside the channel for this region of the channel. As a result, in order to probe the entire 2-D extent of the acceleration region with conventional ILTS, the thruster would need to be operated at an even more extreme discharge condition that pushes the acceleration region even farther out. Furthermore, the bowed shape of the $|u_{e\theta}|$ map could have a similar effect of 2-D map of anomalous electron momentum transport, which will explore in Section 7.3. Lastly, the highest azimuthal current density is around 70×10^4 A/m^2, which is around 50 times less than that in Ref. 188, suggesting that the induced magnetic field should be negligible compared to the applied magnetic field within the experimental domain.

Figures 7-15 and 7-16 show a negative skew (aligned with the direction of $u_{e\theta}$) and positive excess kurtosis of the azimuthal EVDF near the thruster exit plane and near zero skew and negative excess kurtosis in the downstream region. Interestingly, the values of the excess kurtosis in the downstream region are close to the -0.532 value for a 1-D Druyvesteyn EVDF. Regarding similar experimental findings, Ref. 22 used ILTS to measure a skewed azimuthal EVDF aligned with the direction of $u_{e\theta}$ near the channel exit plane at 150 V and a standard current density, and Ref. 189 found that Druyvesteyn EEDFs provided good fits of Langmuir probe data in the far plume of a 5 kW HET at a nominal operating condition. Regarding similar findings to our skew measurements in simulations, the PIC simulation of Ref. 117 produced an axial EVDF with a pronounced skew aligned with the axial drift in the upstream of the acceleration region but with pronounced skew further downstream. Regarding similar findings to our excess kurtosis measurements in simulations, Ref. 117 only showed EVDFs upstream of the peak electron temperature, but all the axial EVDFs shown have positive excess kurtosis and with the excess kurtosis decreasing for locations further downstream. Similarly, the PIC simulation from Ref. 190 showed EEDFs with positive excess kurtosis closer to the anode, with excess kurtosis dropping with distance from the anode, and even showed a significant flat top EEDF in the farthest point from the anode, resembling our measured EVDF in Fig. 7-6.

The spatial evolution of the skew and excess kurtosis can be explained by the 2-D maps of the electron temperature and of $u_{e\theta}$ and the fact that higher energy electrons equilibrate slower [191]. Different electron populations within regions of the EVDF self-equilibrate at the rate of the local (in velocity space) electron-electron collision frequency of

$$\nu_{ee,L} = 7.7 \times 10^{-6} \frac{n_{e,L}\Lambda}{E_L^{3/2}}, \tag{7-1}$$

where Λ is the Coulomb logarithm, $n_{e,L}$ is the electron density of the local population, and E_L is the average electron energy of the local population [191]. In addition, electrons are back-streaming towards the anode, such that, for electrons, the exit plane is downstream of the regions of high electron temperature and $|u_{e\theta}|$. When electrons travel from a high temperature region to a low temperature region and the high energy portions of the EVDF are not able to equilibrate, these high energy electrons from the high temperature region remain as a high temperature population in a low temperature EVDF, generating positive excess kurtosis. Similarly, when electrons travel from a high temperature, high drift region to a low temperature, low drift region and the high energy portions of the EVDF are not able to equilibrate, these high energy electrons from the high temperature, high drift region remain as a high temperature, high drift population but are now in a low temperature, low drift EVDF, generating skew that is aligned with the drift velocity. In the region of our measurement domain far from the thruster, the electrons are traversing a region with smaller gradients, such that the gradients have a reduced or negligible effect on non-Maxwellian nature of the EVDF. Instead, far from the thruster, the process of inelastic collisions causing a Druyvesteyn EEDF dominates the non-Maxwellian effects. This explanation for the cause of significant departures from Maxwellian EVDFs can also explain why the ILTS measurements in Ref. 187 did not observe non-Maxwellian features, since the authors were only able to make measurements upstream (for electrons) of the peak electron temperature. One important consequence of this explanation for non-Maxwellian electrons is that it would suggest that the electrons heat flux is related to gradients in both the drift velocity and the temperature and that the excess kurtosis is related to the gradient in the electron temperature.

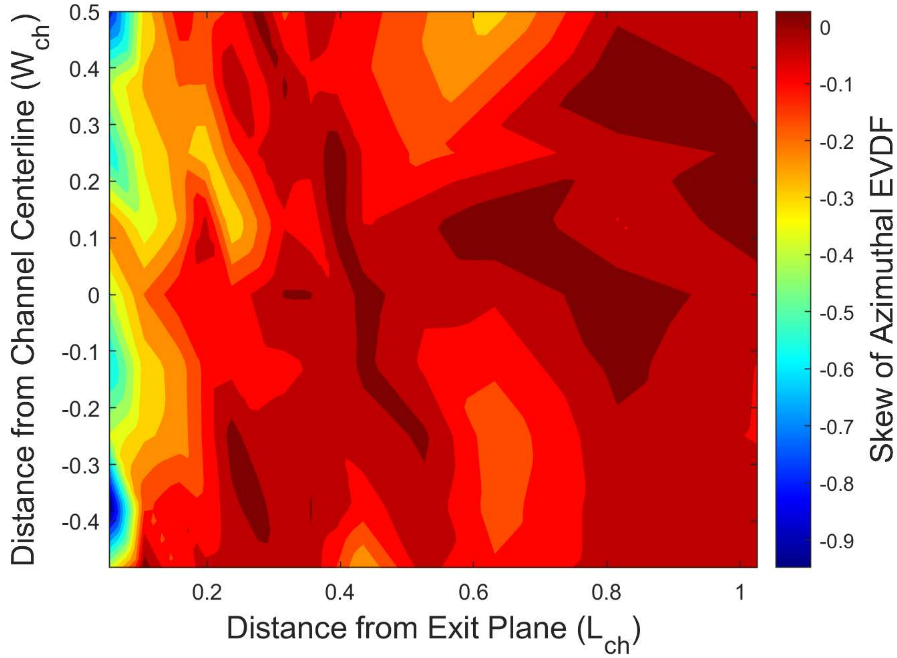

Figure 7-15: 2-D map of ILTS measurements of skew of the azimuthal EVDF. Axial coordinate is normalized by the channel length, and the radial coordinate is normalized by the channel width.

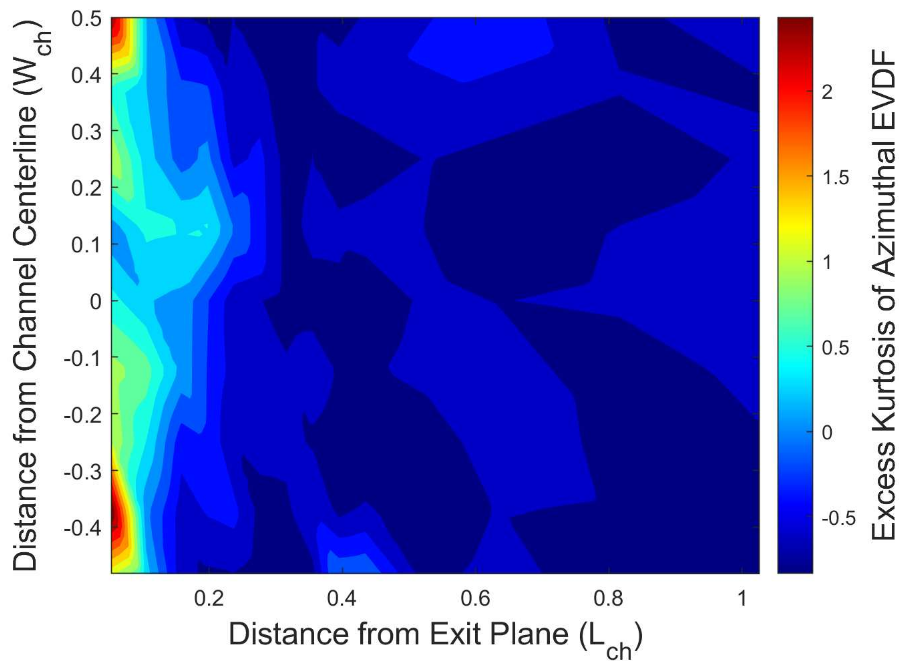

Figure 7-16: 2-D map of ILTS measurements of azimuthal electron drift velocity. Axial coordinate is normalized by the channel length, and the radial coordinate is normalized by the channel width.

Another important consequence is that if the EVDF is more non-Maxwellian upstream (for the electrons) of the peak electron temperature, then the EVDFs are highly non-Maxwellian in the ionization region. This suggests that simulations need to accurately capture non-Maxwellian EVDFs to accurately predict the ionization rate and particle densities. For example, Fig. 7-17 shows that the difference between the ionizations rate calculated from Maxwellian and non-Maxwellian EVDFs can reach around 10% close to thruster face. We also expect the degree of electron nonequilibrium to increase at more nominal conditions, since higher voltages and lower flow rates will increase the gradients and lower the electron-electron collision frequency in the acceleration region.

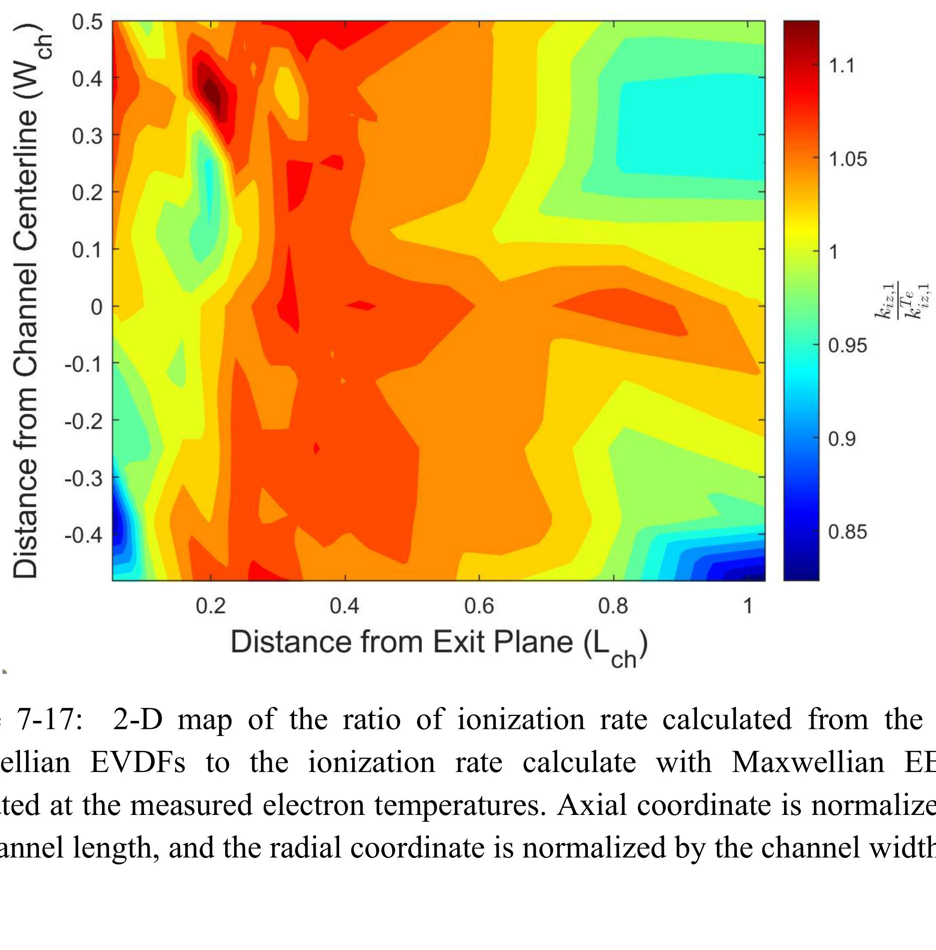

Figure 7-17: 2-D map of the ratio of ionization rate calculated from the non-Maxwellian EVDFs to the ionization rate calculate with Maxwellian EEDFs evaluated at the measured electron temperatures. Axial coordinate is normalized by the channel length, and the radial coordinate is normalized by the channel width.

In addition, it is important to consider the effect that discharge oscillations have on our time-averaged ILTS measurements. This is especially important because the time-averaged ILTS spectrum is the time-averaged product of the electron density and the normalized EVDF, and electron density and temperature are known to oscillate in HETs [39]. However, the operating condition of 150 V and 30 A on the H9 has a low level of oscillations, with a ratio of the rms of the discharge current oscillations to the mean discharge current of 2%. This means that the importance of correlations such as $\frac{\langle \delta n_e \delta T_e \rangle}{\langle n_e T_e \rangle}$ should scale with 0.04%, and higher order correlations would be even smaller. Since all corrections to our measurements would scale with 0.04%, we do not believe that correlations of oscillations play a significant role in our measurements.

7.1.2.1. Radial EVDF Measurements

While we did not make a 2-D map of measurements of the radial EVDF, we did measure the radial EVDF along the channel centerline. When comparing the measurements from the radial EVDF with those of the azimuthal EVDF, we include the outliers in the data. The strong agreement between the electron density for the radial and azimuthal measurements in Fig. 7-18 indicates azimuthal uniformity in the time-averaged electron density and repeatability in our density measurements. The radial electron temperature is generally higher than the azimuthal electron temperature in Fig. 7-19, which is opposite of what Ref. 22 found. The higher radial temperature may be indicative of stronger radial instabilities at this operating condition, since radial instabilities can increase the radial electron temperature [80]. While Ref. 22 also operated at 150 V, our operating condition has a higher current density, which may be responsible for the higher radial temperatures compared to azimuthal temperatures. Regarding the drift velocities, Fig. 7-20 shows a lower radial drift velocity compared to azimuthal drift velocity, as expected, but the magnitudes of radial drift velocities seem high if they are assumed to scale with the radial ion velocity.

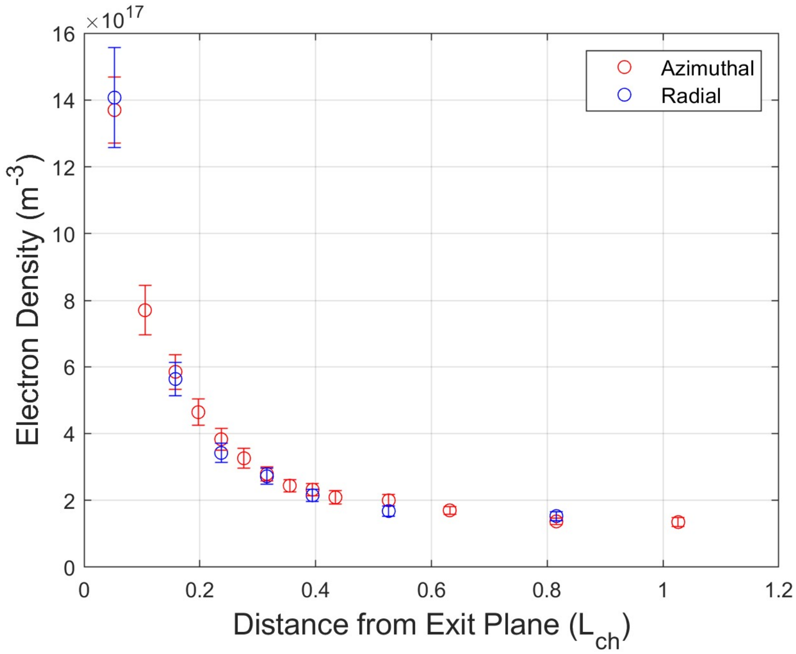

Figure 7-18: Electron density calculated from the channel centerline measurements of the radial and azimuthal EVDFs.

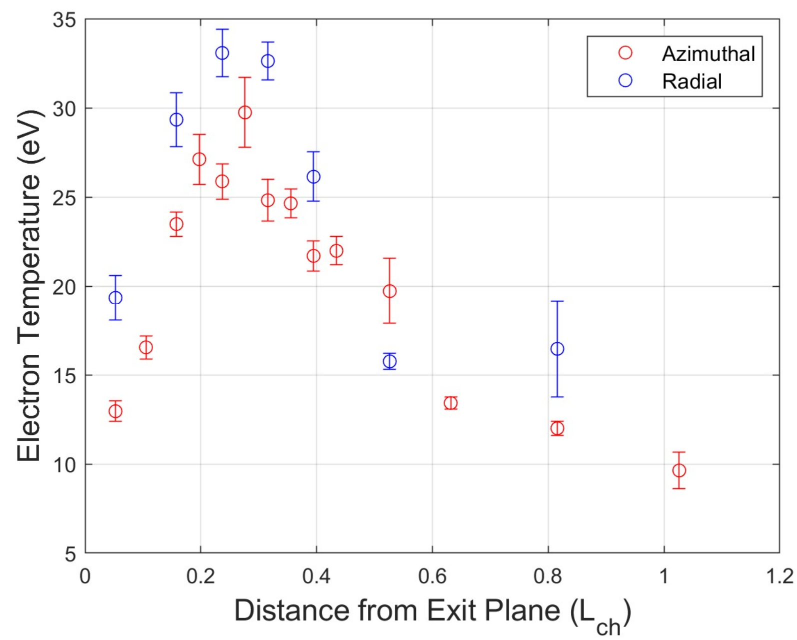

Figure 7-19: Electron temperature calculated from the channel centerline measurements of the radial and azimuthal EVDFs.

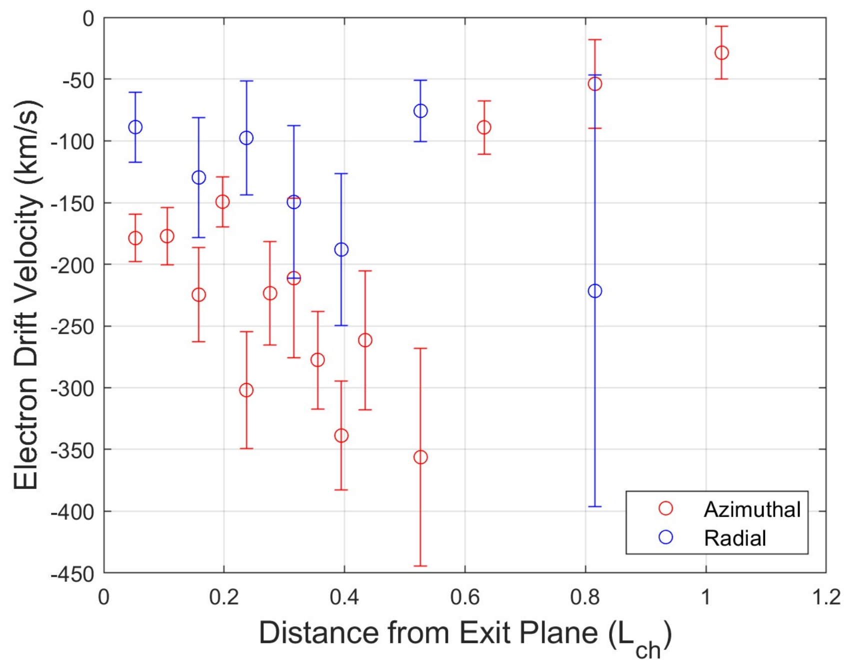

Figure 7-20: Electron drift velocity calculated from the channel centerline measurements of the radial and azimuthal EVDFs.

Regarding the non-Maxwellian properties of the radial EVDF, the skew and excess kurtosis of the radial EVDF follow similar trends as that of the azimuthal EVDF. Similar trends for the excess kurtosis make sense, since the radial electron temperature has similarly strong axial gradients as the azimuthal electron temperature. However, the radial drift velocity does not have as strong an axial gradient as the azimuthal drift velocity, so our previous explanation for the cause of skew in the EVDFs does not explain the similarities between the radial and azimuthal skews. Interestingly, for radial magnetic field lines, this measurement of the radial skew can provide a direct measurement of the deviation from the classical conductive heat flux along magnetic field lines.

Given that the radial electron temperature is generally higher than the azimuthal electron temperature, we likely underestimate the ionization rates using Eq. 5-16 for the 3D EVDF. To illustrate this anisotropic effect, we compare two different calculations for the ionization rate in Appendix D.

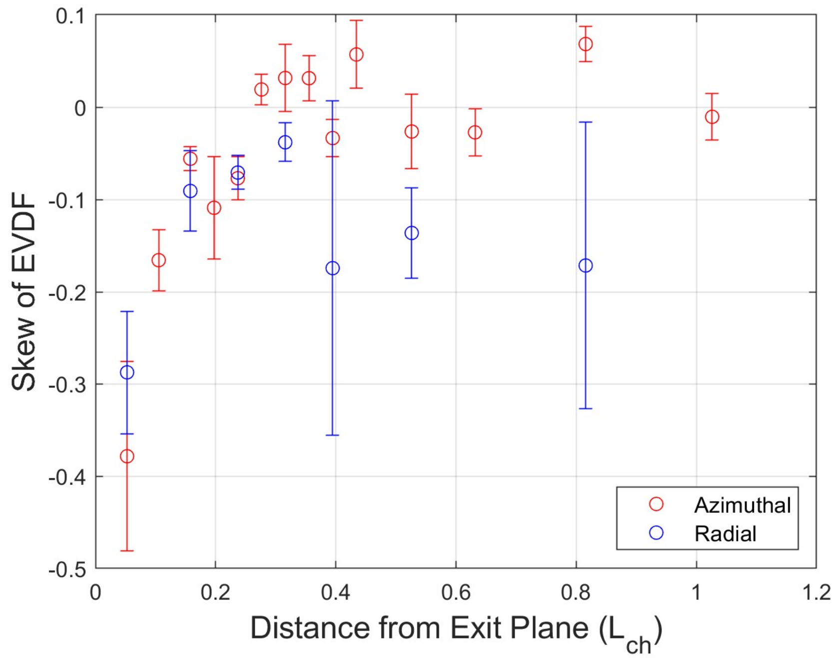

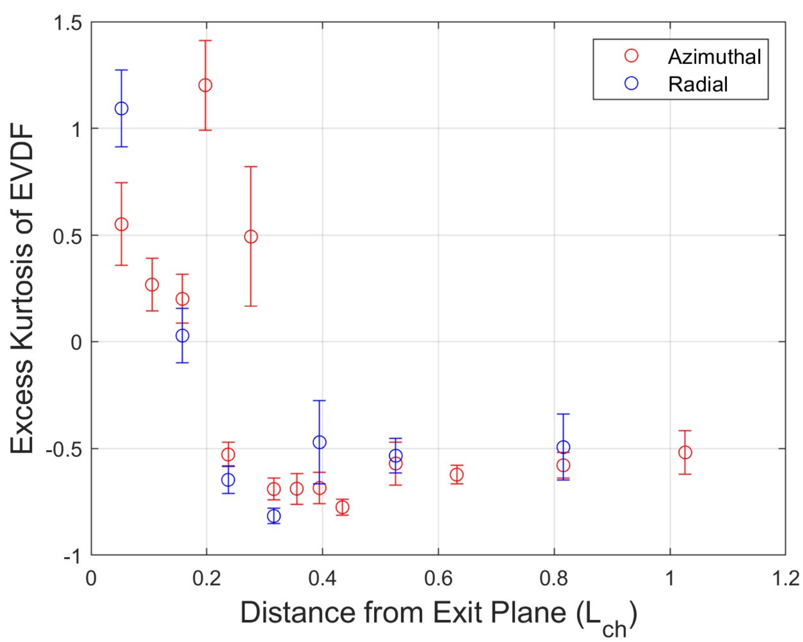

Figure 7-22: Excess kurtosis of the radial and azimuthal EVDFs.

7.1.2.2. Repeatability

Figures 7-23 - 7-27 show that while the electron density measurements show the highest degree of repeatability, followed by the electron temperature, the general trends and shapes of the other profiles along the channel centerline are repeatable. Figures 7-23 - 7-27 also provide a scale for the measurement uncertainty not accounting for repeatability.

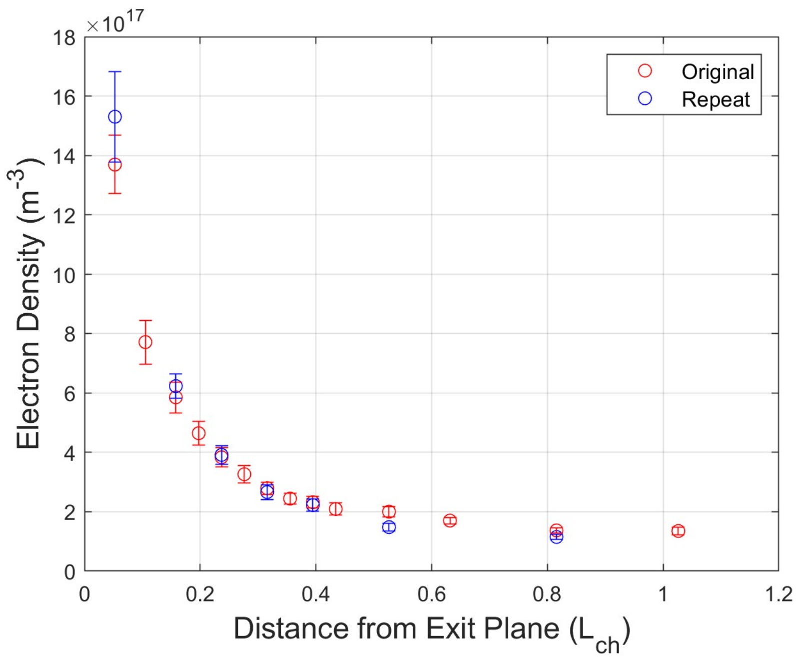

Figure 7-23: Comparison of electron density measurements taken from the original 2-D map and from a set of repeated measurements along the channel centerline.

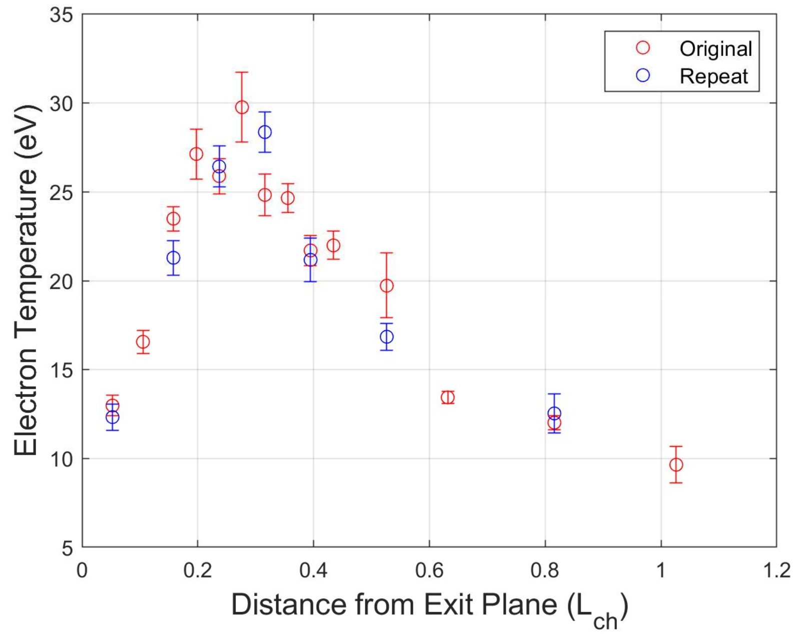

Figure 7-24: Comparison of electron temperature measurements taken from the original 2-D map and from a set of repeated measurements along the channel centerline.

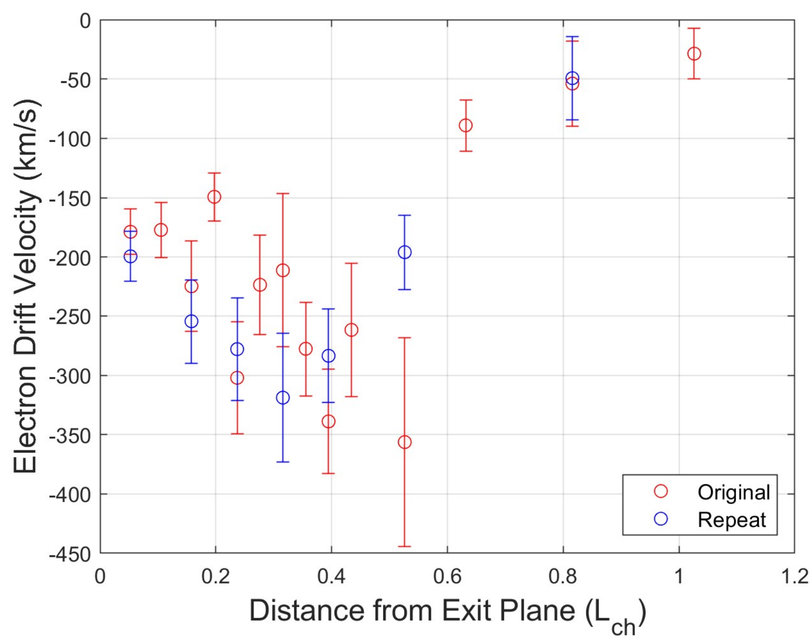

Figure 7-25: Comparison of azimuthal electron drift velocity measurements taken from the original 2-D map and from a set of repeated measurements along the channel centerline.

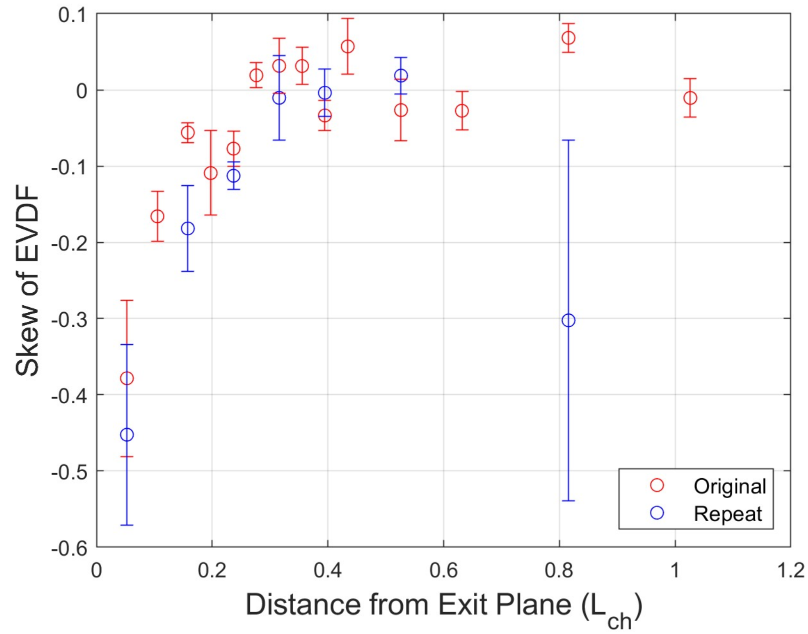

Figure 7-26: Comparison of skew of the azimuthal EVDF taken from the original 2-D map and from a set of repeated measurements along the channel centerline.

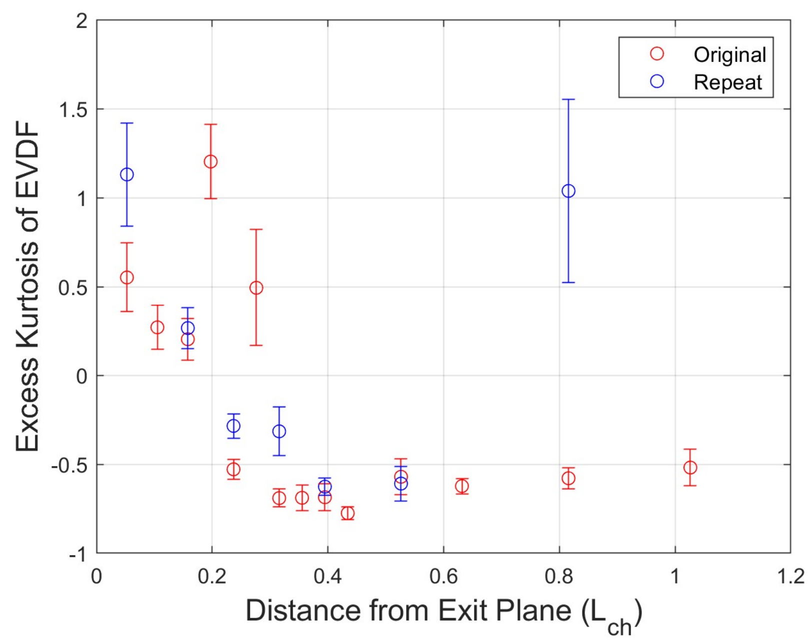

Figure 7-27: Comparison of excess kurtosis of the azimuthal EVDF taken from the original 2-D map and from a set of repeated measurements along the channel centerline.

7.2. Solver Results

In this section, we present the results of our 2-D solver. We begin by presenting the intermediate results, such as the electric field, ion velocity field, neutral velocity field, neutral density, and axial electron drift velocity. We then briefly present results that justify the use of our approach and present the importance of certain features of the 2-D solver. We then finish with the inference of the anomalous electron Hall parameter, the comparison with closure models, and the inference of anomalous electron heating. The intermediate results and the anomalous heating results are primarily shown as 2-D maps, so Appendix C shows how the intermediate properties and the anomalous electron heating (and their uncertainty) vary along magnetic field lines. Similarly, the comparison to closure models is shown along magnetic field lines, so Appendix C shows the comparison as 2-D maps.

7.2.1. Intermediate Results

Figure 7-28 confirms that we measured across the axial extent of the acceleration region for the outer two-thirds of the channel but not for the inner third of the channel. In addition, the axial electric field is strongest at the inner edge of the channel near the exit plane. For the radial electric field in Fig. 7-29, in the downstream region, the outer half of the channel predominantly has a positive radial electric field, and the inner half has a negative radial electric field. However, for the upstream portion of the domain, the opposite is found, where the outer half of the channel has a negative radial electric field and the inner half of the channel has a positive radial electric field.

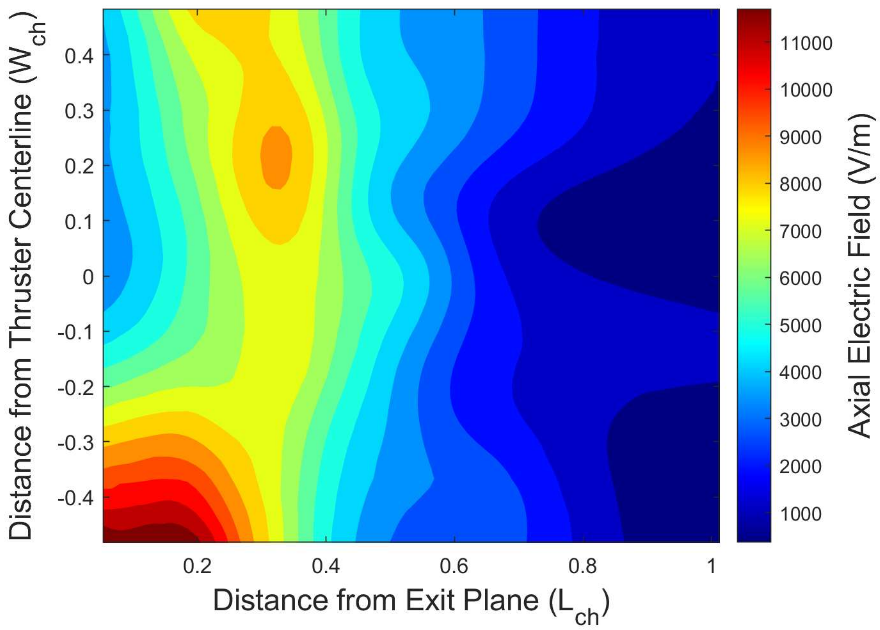

Figure 7-28: 2-D map of the inferred axial electric field.

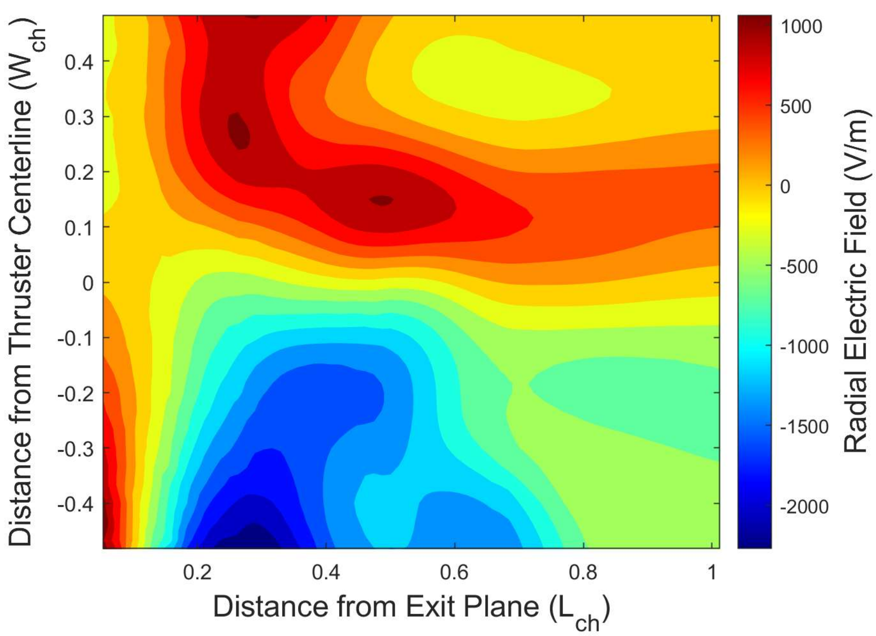

Figure 7-29: 2-D map of the inferred radial electric field.

In Fig. 7-30, the axial ion velocity generally is minimized near the channel centerline, and this feature becomes more accentuated in the downstream region. The minimum axial ion velocity near the channel centerline in the downstream region cannot be explained by the 2-D map of the axial electric field. Instead, this minimum is linked to the radial ion velocity map in Fig. 7-31. The larger radial ion velocities in the downstream region cause radial convection of the axial ion momentum away from channel centerline, resulting in larger axial ion velocities away from the channel centerline. The mean ion velocity at the downstream axial boundary is 19.5 km/s, corresponding to an acceleration voltage of 167 V. This acceleration voltage is higher than expected for a discharge voltage of 150 V, which may indicate some inaccuracy in our measurements. However, LIF measurements have measured axial ion velocities that also correspond to acceleration potentials larger than the discharge voltage [21].

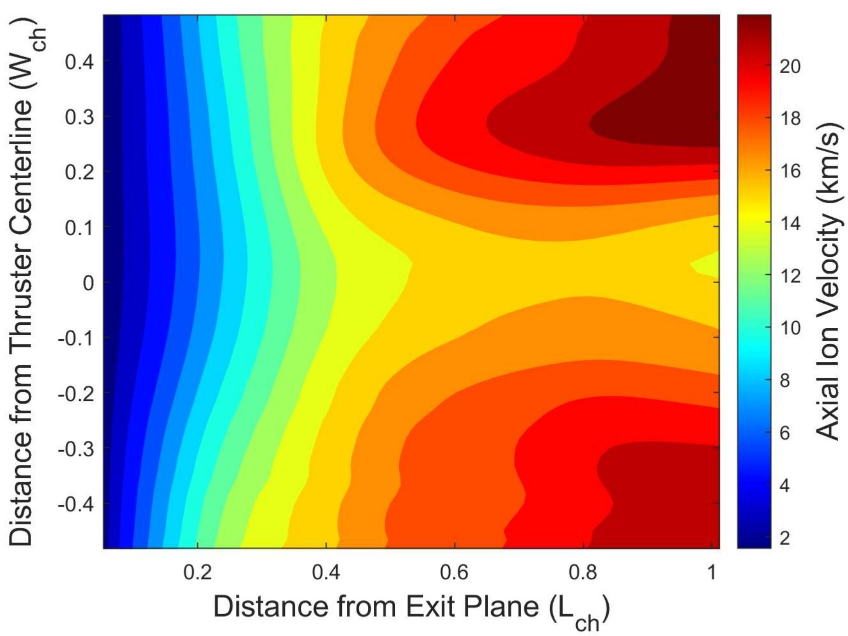

Figure 7-30: 2-D map of the inferred axial ion velocity.

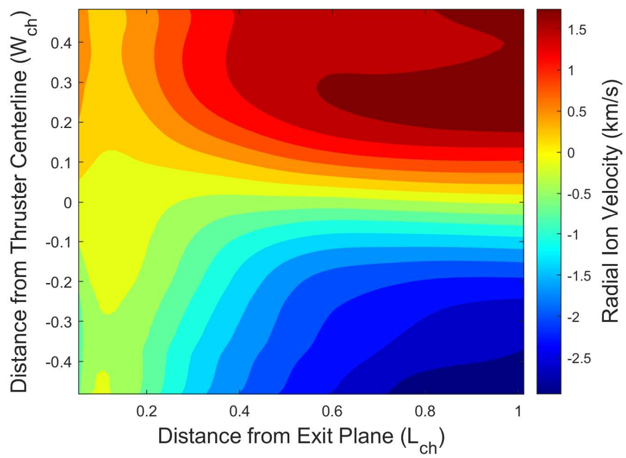

Figure 7-31: 2-D map of the inferred radial ion velocity.

The axial neutral velocity map in Fig. 7-32 shows moderate acceleration and peak axial velocity near the channel centerline. While LIF measurements of axial neutral velocities do not measure as far out as our axial downstream boundary, they do show moderate acceleration of the axial neutral fluid velocity and a drop in axial neutral fluid velocity towards the edges of the channel [192]. The peak of the axial neutral velocity near the channel centerline can also be explained through radial convection of axial neutral momentum, since the radial neutral velocity map in Fig. 7-33 shows a primarily negative radial velocity above the centerline and a primarily positive radial velocity below the centerline. In addition, farther downstream, the radial location of the peak axial neutral velocity moves towards the inner channel edge, just like the boundary between positive and negative radial neutral velocity. We do note, however, that the radial neutral velocity map has significant noise. Lastly, in Fig. 7-34, the neutral density tends to increase away from the channel centerline. This increase in neutral density away from the channel centerline was also observed in LIF measurements [192].

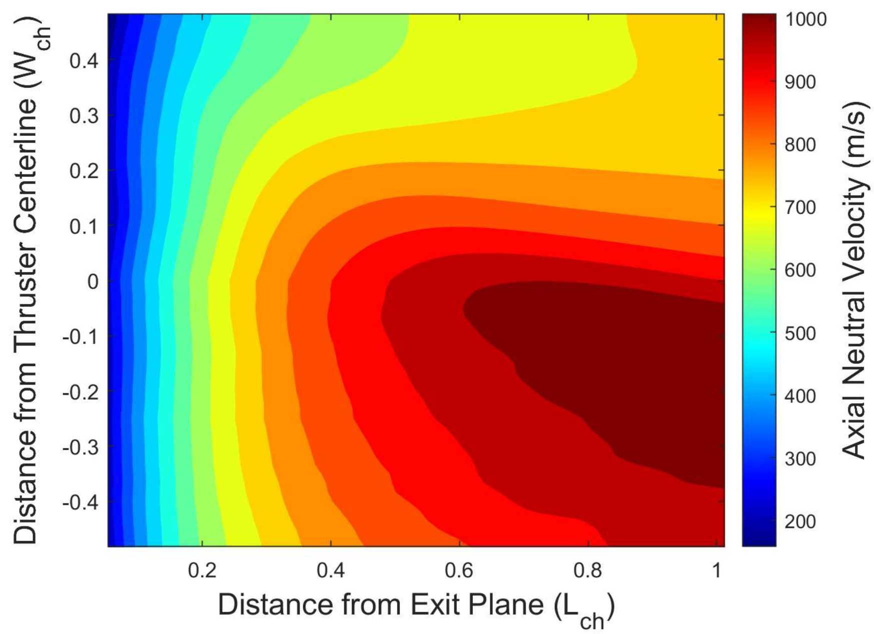

Figure 7-32: 2-D map of the inferred axial neutral velocity.

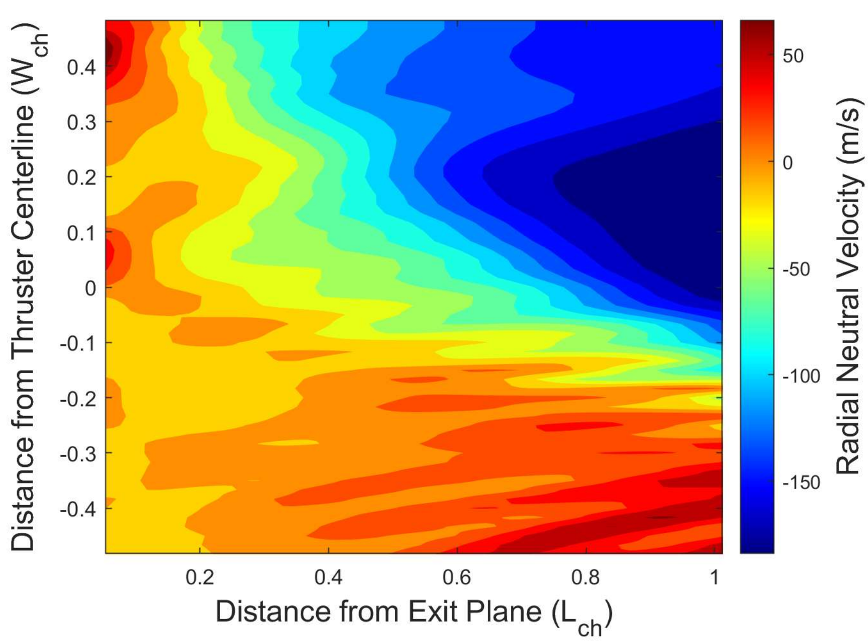

Figure 7-33: 2-D map of the inferred radial neutral velocity.

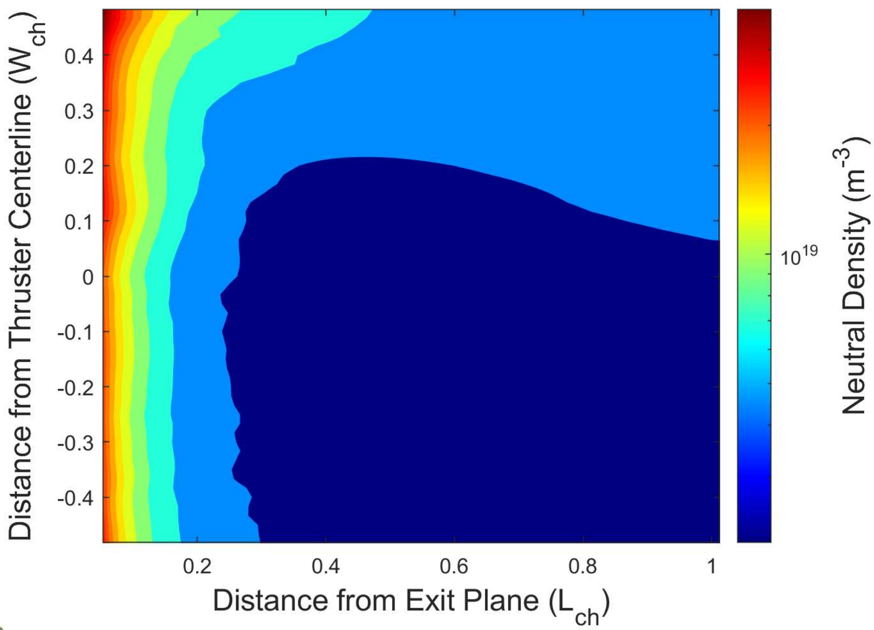

Figure 7-34: 2-D map of the inferred neutral density.

In Fig. 7-35, the axial electron drift velocity generally decreases in magnitude closer to thruster and increase in magnitude away from the channel centerline. The increase in magnitude away from the channel centerline is likely driven the 2-D map of radial electron drift velocity, where we recall that we have assumed $u_{er} = -u_{ir} \pm 0.2u_{ir}$. When compared to an inference of the axial electron drift velocity from channel centerline measurements of LIF and ILTS [40], our inference of the axial electron drift velocity is around four times higher than in Ref. 40, and we do not observe a local minimum in magnitude of the axial electron drift velocity.

7.2.2. Justification for Solver

The main justification for using a custom solver to infer the anomalous electron Hall parameter is that the electric field due to the measured Lorentz force and electron pressure gradient is not exactly conservative, even with measurements of relatively high precision and accuracy. Using the electric field in Figs. 7-28 and 7-29, we calculated the potential difference between the bottom left corner of our measurement domain and every other point using two different integration paths. One path integrated first along the lower boundary and then integrated upwards, and the second path integrated first along the left boundary and then integrated rightwards. As seen in Fig. 7-36, there is high percent difference between the integration along the two paths, indicating that our measurements produce a highly non-conservative electric field. This is another indication of inaccuracy and imprecision in our measurements.

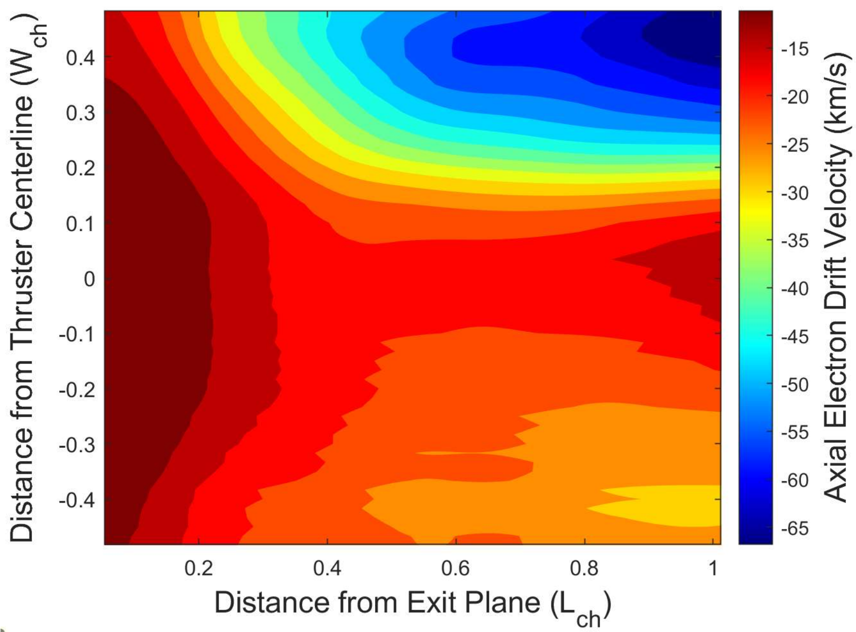

Figure 7-35: 2-D map of the inferred axial electron drift velocity.

In addition, Fig. 7-37 shows that when we use our ILTS measurements to calculate the neutral density from the ion continuity equation, the neutral density is negative over a large part of the domain. This, again, is another indication of inaccuracy and imprecision in the measurements. However, we recall that the upstream values one cell inside in the upstream boundary in Fig. 7-37 are used as the upstream boundary condition for neutral density.

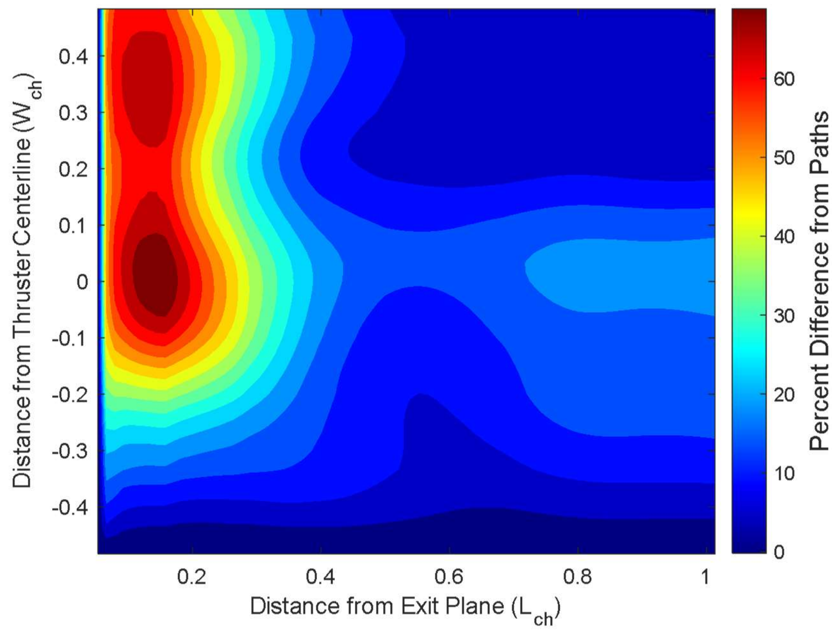

Figure 7-36: 2-D map of the percent difference of the integration along two different paths from the electric field in Figs. 7-28 and 7-29.

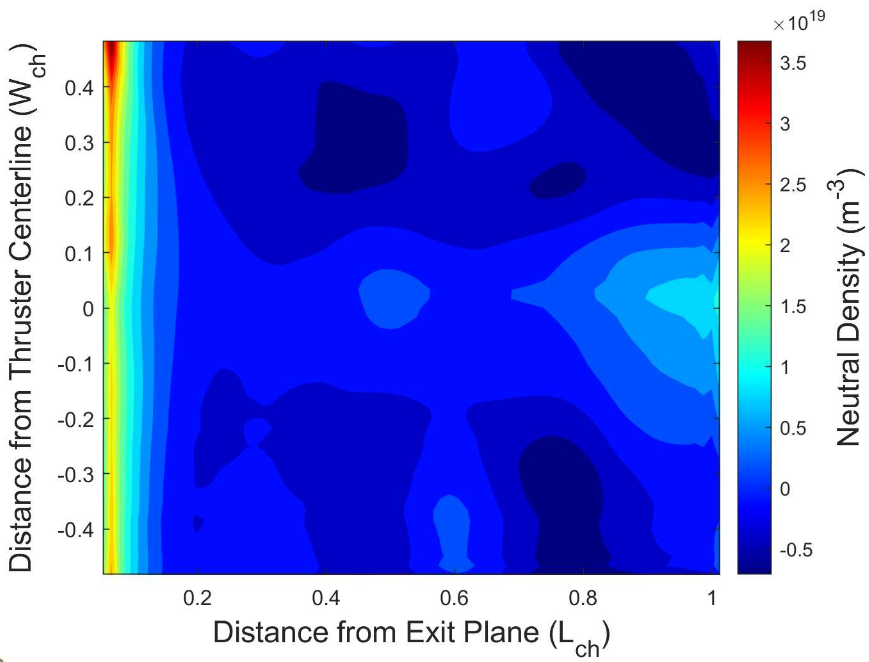

Figure 7-37: 2-D map of the neutral density calculated from the ion continuity equation.

7.2.3. Importance of Electron Inertia

Considering that electron inertia terms due to the azimuthal drift velocity should have the largest importance among the electron inertia terms, we included electron inertia in the azimuthal electron momentum equation and included the centrifugal force in the radial electron momentum equation. Fig. 7-38 shows that the azimuthal electron shear is negligible, contributing less than 1% to the azimuthal electron momentum equation within the experimental domain. The low discharge voltage is expected to reduce axial gradients [14,21], such that the azimuthal electron shear should be more important at more nominal discharge conditions. As shown in Fig. 7-39, the electron centrifugal force is unsurprisingly important in regions where the radial electric field is near zero. However, the electron centrifugal force is large negligible in most of the measurement domain, and the radial ion velocity map has no noticeable change if the centrifugal force is neglected.

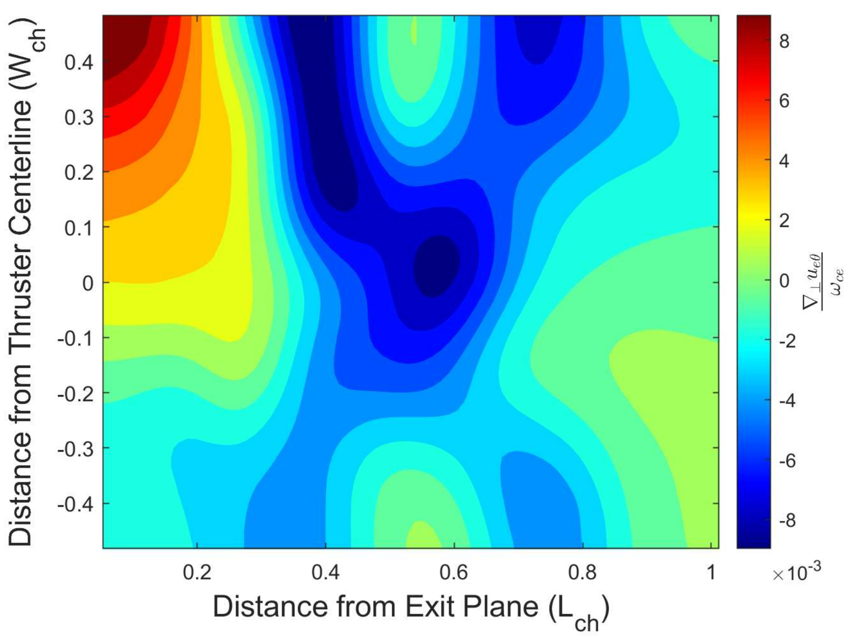

Figure 7-38: 2-D map of the ratio of azimuthal electron inertia to the azimuthal Lorentz force.

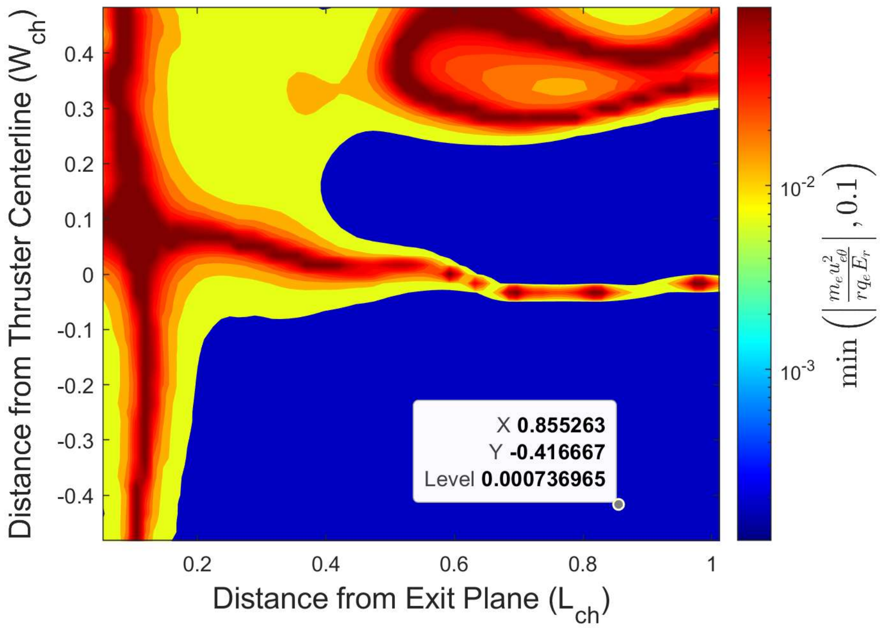

Figure 7-39: 2-D map of the absolute value of the ratio of electron centrifugal force and the radial electrostatic force. The minimum between 0.2 and the absolute value is shown for visualization purposes.

7.3. Inferred Anomalous Momentum Transport

The 2-D inference of the Ω_{ea} has a maximum Ω_{ea} of around 35, as seen in Fig. 7-40. Interestingly, the region of high Ω_{ea} does not directly follow the region of high $|u_{e\theta}|$, and is instead upstream of the region of high $|u_{e\theta}|$ because the axial electron drift velocity continues to decrease towards the channel exit plane. As seen Figs. 7-41 and 7-42, Ω_{ea} varies by around 50% of the peak values on all field lines. However, because of the high uncertainty of the inference, we cannot confidently say that Ω_{ea} varies on Field Line 5. However, from all other field lines, we can confidently say that Ω_{ea} is not generally constant along magnetic field lines. This is significant because calibrated fluid or hybrid HET simulations often assume that the Ω_{ea} is constant along magnetic field lines.

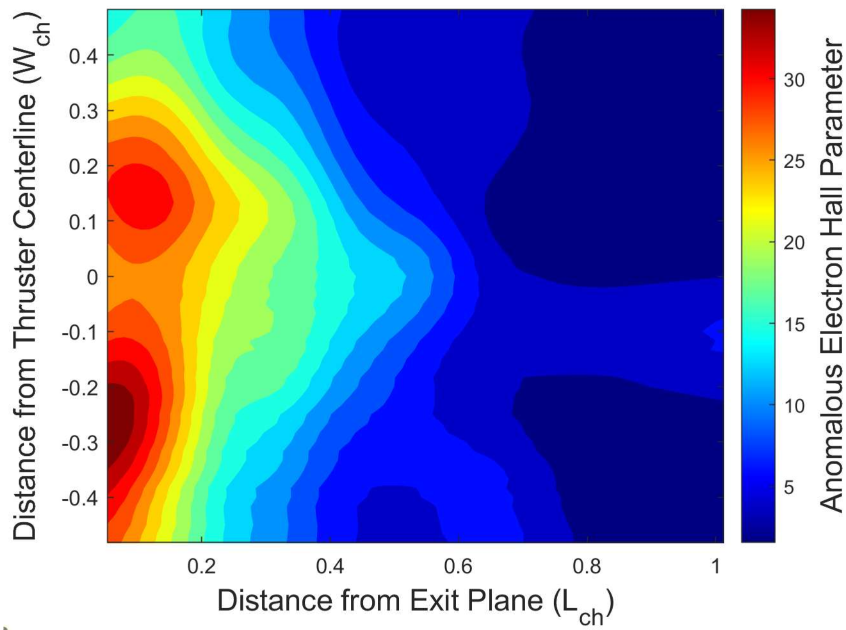

Figure 7-40: 2-D map of the inferred anomalous electron Hall parameter.

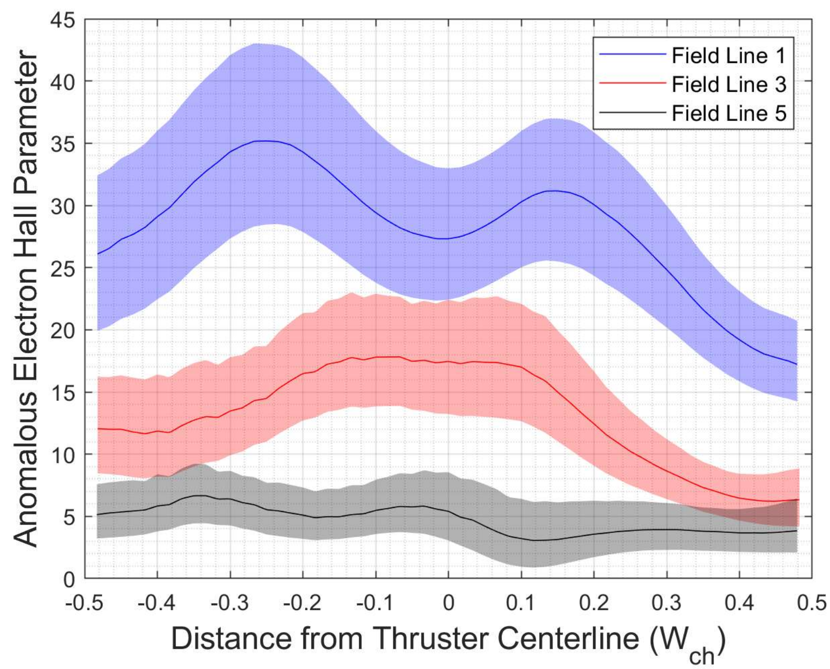

Figure 7-41: Radial variation of the anomalous electron Hall parameter along magnetic field lines 1, 3, and 5. Radial coordinate is normalized by the channel width.

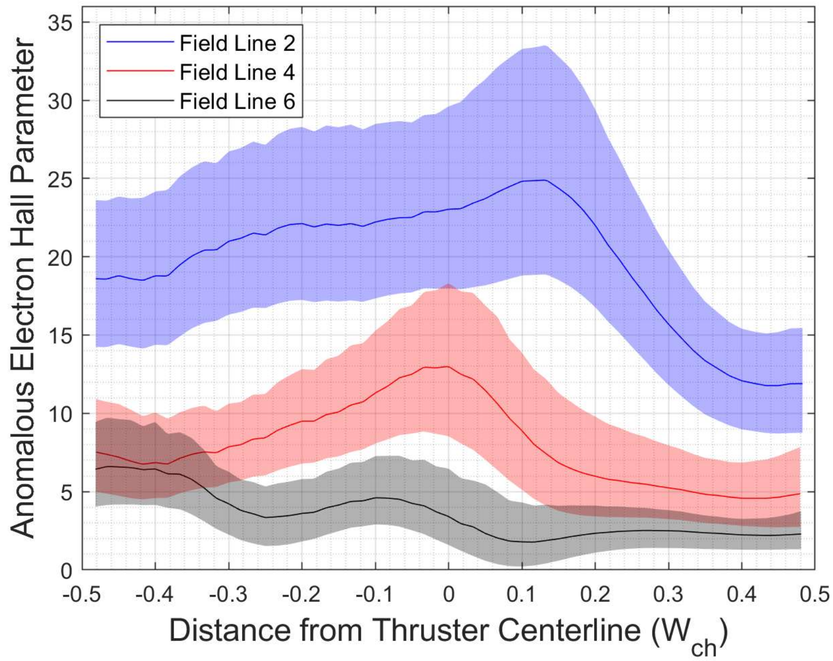

Figure 7-42: Radial variation of the anomalous electron Hall parameter along magnetic field lines 2, 4, and 6. Radial coordinate is normalized by the channel width.

In addition, comparing the uncertainty bounds in Fig. 7-43 and 7-41, we find that the uncertainty in $u_{e\theta}$ dominates the uncertainty in Ω_{ea}. It would then be useful to consider an alternative normalization of anomalous electron momentum transport that does not require using $u_{e\theta}$. In fact, $u_{e\theta}$ only appears in Ω_{ea} due to the assumption that the anomalous azimuthal force density, R_{ea}, can be modeled as a collisional term. In addition, when $u_{e\theta}$ changes sign without a corresponding change in sign in R_{ea}, the anomalous collision frequency is undefined; this was observed in a PIC simulation [193], and in our measurements a handful of points had $u_{e\theta} = 0$ within the uncertainty bounds. Therefore, in addition to reducing uncertainty, an alternative normalization of R_{ea} makes fewer assumptions and is well-defined over the entire domain. Figures 7-44 and 7-45 show that $\hat{R}_{ea} = \frac{R_{ea}}{m_e \omega_{ce} n_e u_{iB}}$ has a relatively low uncertainty, is approximately constant along the magnetic field lines in the inner half of the channel and varies less over the domain than Ω_{ea}. $\hat{R}_{ea}$ has a low uncertainty in part because it has weak dependence on $u_{e\theta}$. This weak dependence is because $u_{e\theta}$ only role in calculating R_{ea} is through the calculation of u_{ir}, and because $u_{ez}B_r$ generally dominates over $u_{er}B_z$, R_{ea} has a weak dependence on u_{ir}. Lastly, because the closure models of Eqs. 6-20 and 6-21 are based on models of R_{ea} that are proportional to u_{iB} and because Ref. 119 found that Ω_e scales approximately with the azimuthal Mach number, the inclusion of u_{iB} in the normalization of R_{ea} makes $\hat{R}_{ea}$ closely related to existing theories of anomalous transport in HETs.

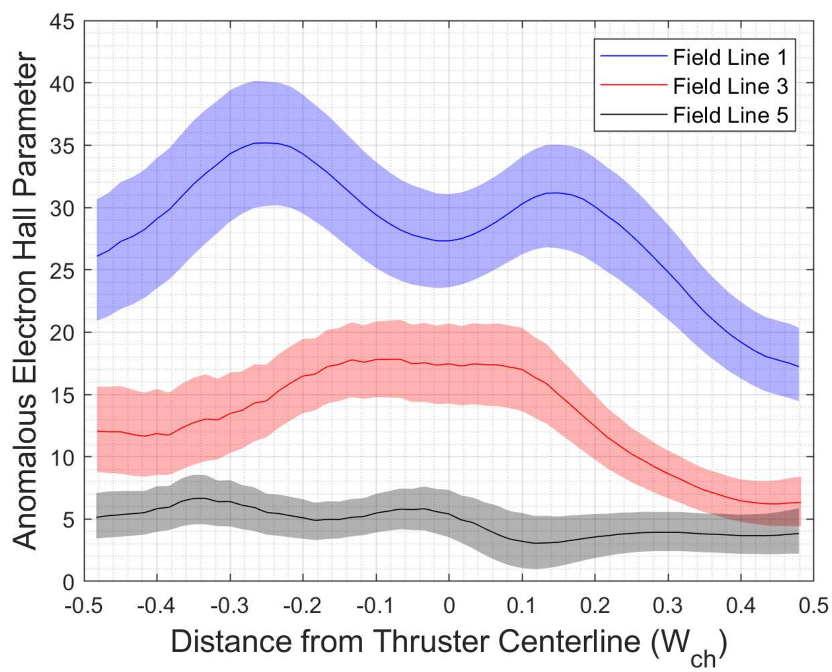

Figure 7-43: Radial variation of the anomalous electron Hall parameter along magnetic field lines 1, 3, and 5. Radial coordinate is normalized by the channel width. Only includes uncertainty due to the uncertainty of the measured $u_{e\theta}$

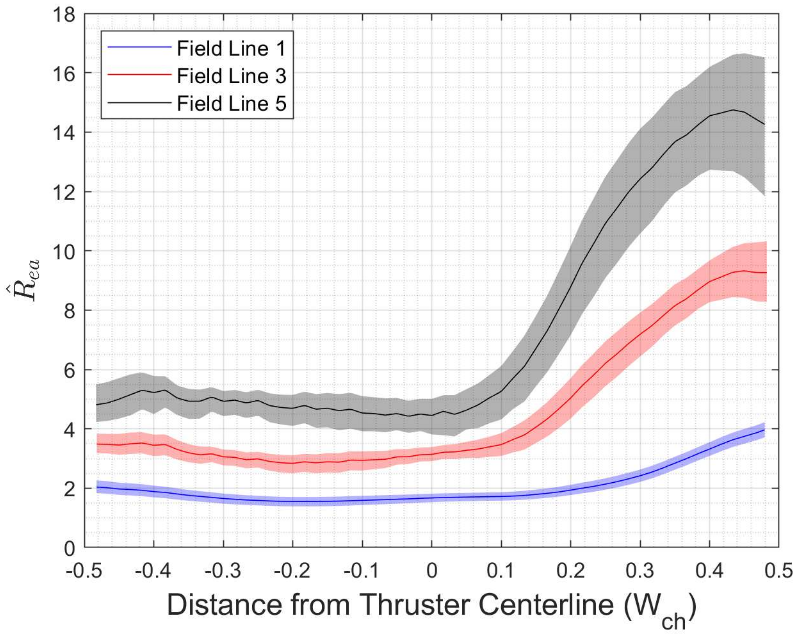

Figure 7-44: Radial variation of the normalized anomalous force density along magnetic field lines 1, 3, and 5. Radial coordinate is normalized by the channel width.

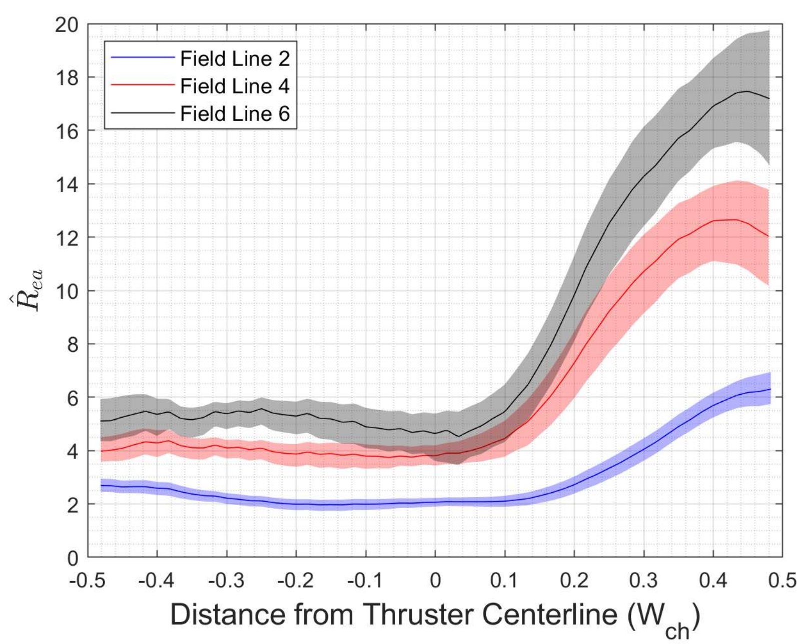

Figure 7-45: Radial variation of the normalized anomalous force density along magnetic field lines 2, 4, and 6. Radial coordinate is normalized by the channel width.

7.4. Answer to Research Question

As defined in Chapter 4, the research question was the following:

In a HET, is the anomalous electron Hall parameter directly proportional to the azimuthal electron drift velocity along magnetic field lines?

Our hypothesis was the following:

In a HET, the anomalous electron Hall parameter is directly proportional to the azimuthal electron drift velocity along magnetic field lines.

As seen in Figs. 7-46 and 7-47, $\frac{u_{e\theta}}{\Omega_{ea}}$ is not constant along any field line, such that we can conclude that the Ω_{ea} is not directly proportional to $u_{e\theta}$ along magnetic field lines. As a result, our measurements to not provide an improvement on the common assumption used in calibrated simulations that Ω_{ea} is constant along magnetic field lines.

While for field lines 1-4, $\frac{u_{e\theta}}{\Omega_{ea}}$ varies by about 50% of the maximum, for field lines 5 and 6, there is more significant variation, including a change in sign in $\frac{u_{e\theta}}{\Omega_{ea}}$. Regarding possible reasons for the asymmetry in $\frac{u_{e\theta}}{\Omega_{ea}}$ across the channel centerline, the asymmetry in the magnetic field topology across the channel centerline is the likely underlying cause, with this likely being reflected in the asymmetry across the channel centerline in our measurements of electron density, temperature, and drift velocity. We see that field lines 5 and 6 also have significantly higher uncertainty than the other field lines, especially at around $0.1W_{ch}$ from the channel centerline. This is because Ω_{ea} is lowest on field lines 5 and 6, and the large increase in uncertainty occurs because Ω_{ea} is close to zero. It is also important to note that although $\frac{u_{e\theta}}{\Omega_{ea}}$ changes sign, u_{ez} does not change sign even when accounting for uncertainty in Figs. C-21 and C-22, meaning that the change in sign is not necessarily unphysical and is due to a change in sign in $u_{e\theta}$ being within the measurement uncertainty, as seen in in Figs. C-3 and C-4.

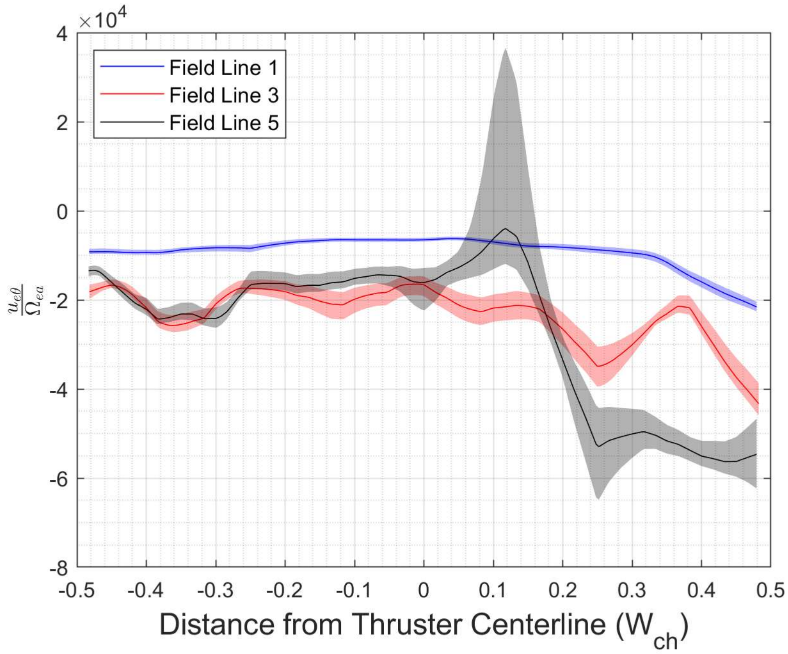

Figure 7-46: Radial variation of $\frac{u_{e\theta}}{\Omega_{ea}}$ along magnetic field lines 1, 3, and 5. Radial coordinate is normalized by the channel width.

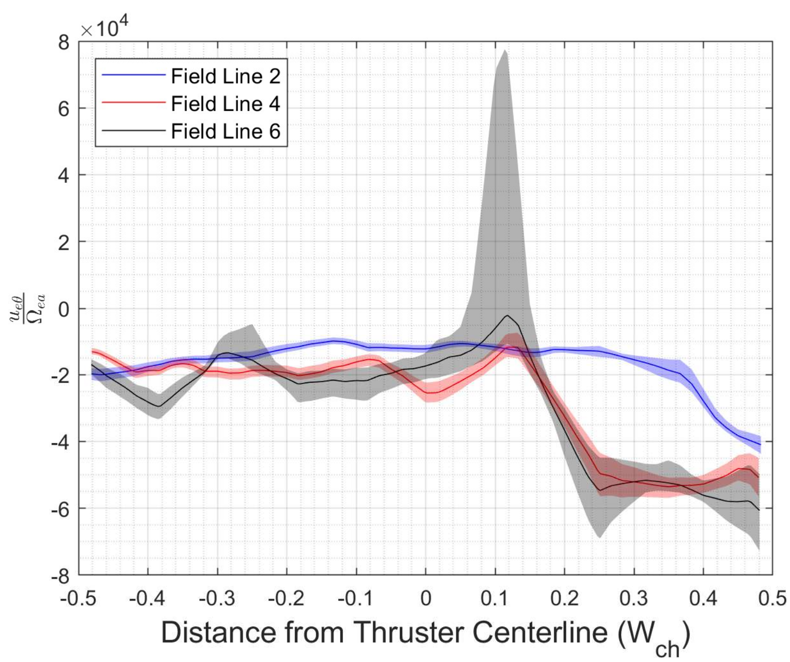

Figure 7-47: Radial variation of $\frac{u_{e\theta}}{\Omega_{ea}}$ along magnetic field lines 2, 4, and 6. Radial coordinate is normalized by the channel width.

7.5. Comparison to Closure Models

Using the coefficients used in Refs. 45 and 49 for their respective closure models for Ω_{ea} (as defined in Section 6.1.3), we find that the MTSI closure model has orders of magnitude of less relative error than the ECDI model, as seen in Figs. 7-48 - 7-51. The error in the MTSI model is essentially a scaled-up form of $\hat{R}_{ea}$ in Figs. 7-48 and 7-49. Considering the significantly smaller range in the error in of the MTSI closure, the MTSI closure seems to capture anomalous electron momentum transport at this discharge condition better than the ECDI closure.

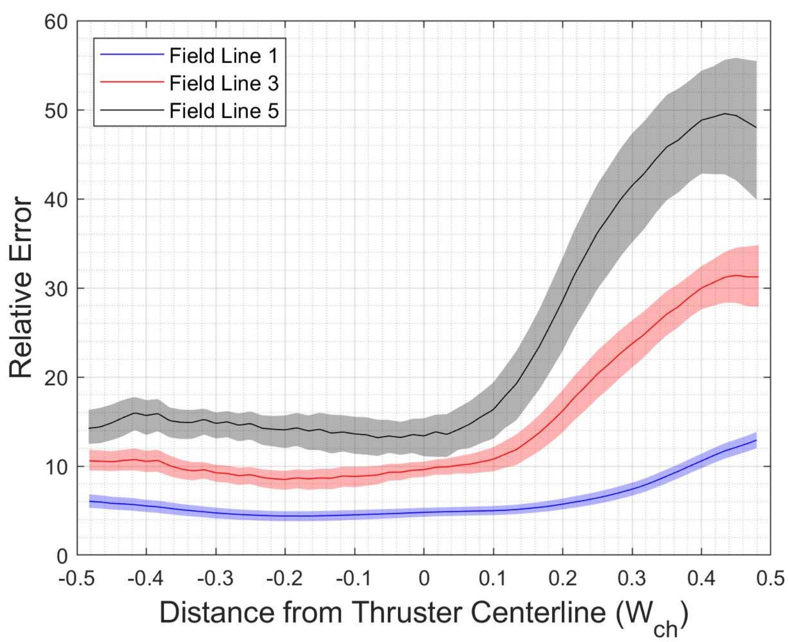

Figure 7-48: Radial variation of the relative error of the MTSI closure with C_1= 0.28 and C_2 = 2.5 × 10^{-3} versus the inferred Ω_{ea} along magnetic field lines 1, 3, and 5. Radial coordinate is normalized by the channel width.

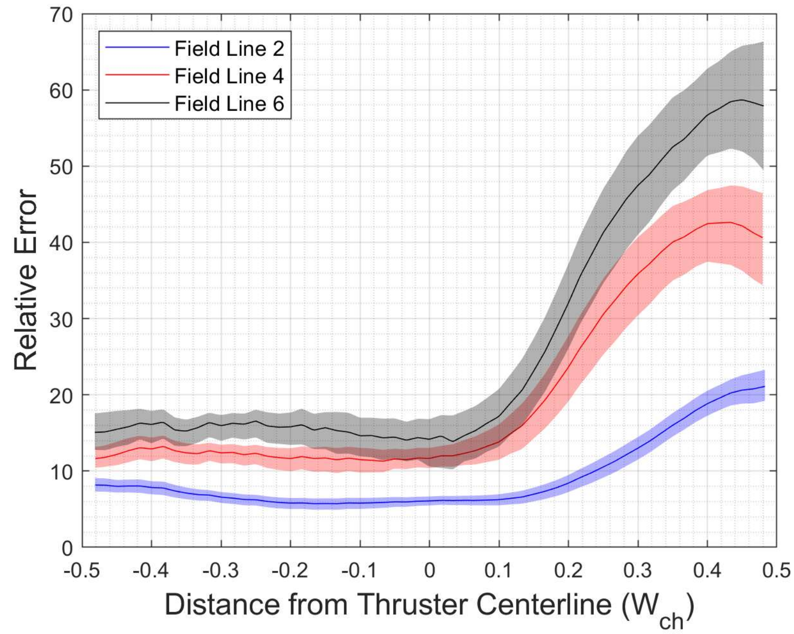

Figure 7-49: Radial variation of the relative error of the MTSI closure with C_1= 0.28 and C_2 = 2.5 × 10^{-3} versus the inferred Ω_{ea} along magnetic field lines 2, 4, and 6. Radial coordinate is normalized by the channel width.

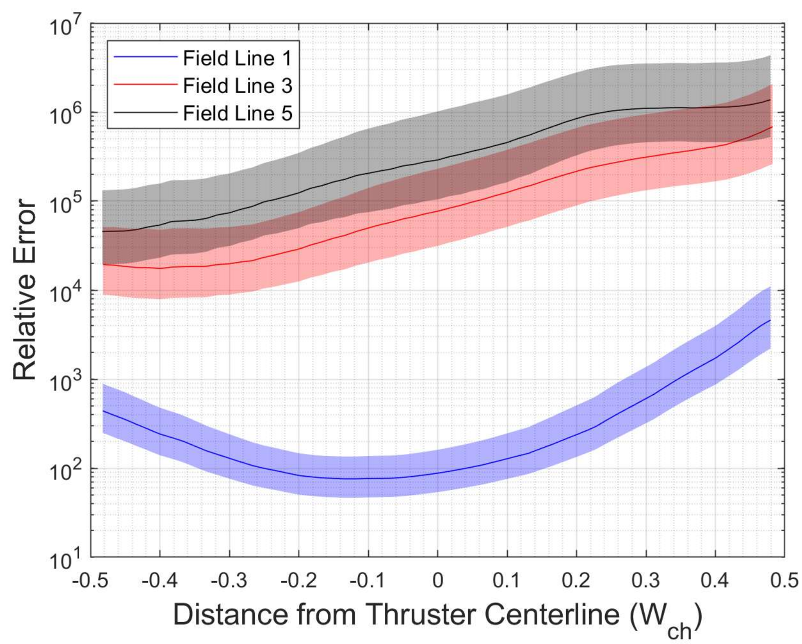

Figure 7-50: Radial variation of the relative error of the ECDI closure with C_3 = 130, C_4 = 0.01, and C_5 = 400 versus the inferred Ω_{ea} along magnetic field lines 1, 3, and 5. Radial coordinate is normalized by the channel width.

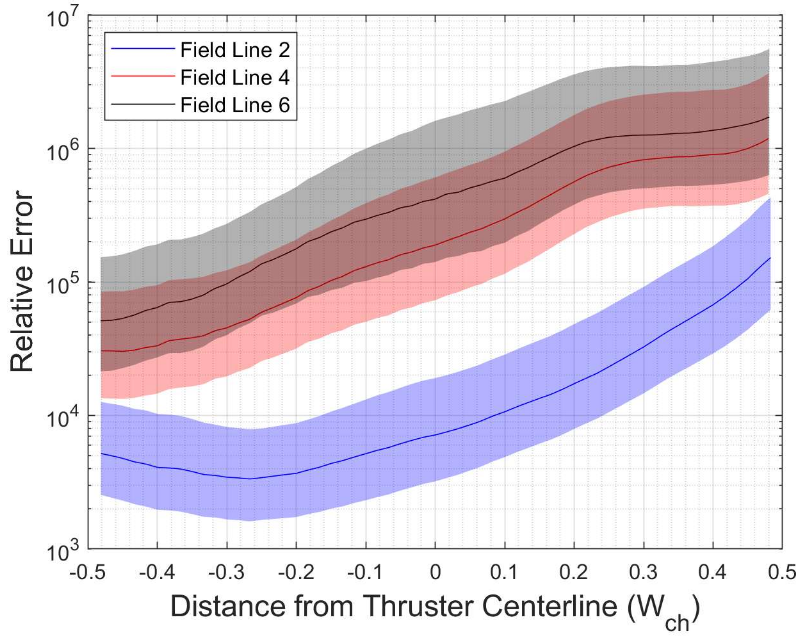

Figure 7-51: Radial variation of the relative error of the ECDI closure with C_3 = 130, C_4 = 0.01, and C_5 = 400 versus the inferred Ω_{ea} along magnetic field lines 2, 4, and 6. Radial coordinate is normalized by the channel width.

However, it is worth exploring the performance of both closures upon fitting of the coefficients in each closure, especially since the coefficients for the ECDI closure are based on one discharge condition and those coefficients were not unique in their suitability to that one discharge condition [45]. We only fit the closure models with the main 2-D maps, that is, with no uncertainty. For the MTSI closure model, we get C_1= 4.01 and C_2 = 6.8 × 10^{-3}. For the ECDI closure model, we get C_3 = 150.6, C_4 = 0.285, and C_5 = 62.4. Interestingly, while the MTSI fit mainly corrected the leading constant in Eq. 6-20, the ECDI fit only changed the leading constant in Eq. 6-21 by around 13% and instead changed made larger changes to the constants in the transport equations of Eqs. 6-22 and 6-23. As seen in Figs. 7-52 and 7-53, the relative error in the MTSI with fitted coefficients is larger towards the outer channel. On the other hand, as seen in Figs. 7-54 and 7-55, the relative error in the ECDI closure with fitted coefficients is distributed relatively symmetrically across the channel centerline for each magnetic field line. Over the entire domain, the MTSI closure with fitted coefficients has an average relative error of 0.23, while the ECDI closure with fitted coefficients has an average relative error of 0.38. Even with fitted coefficients, the MTSI closure better represents our measurements than the ECDI closure.

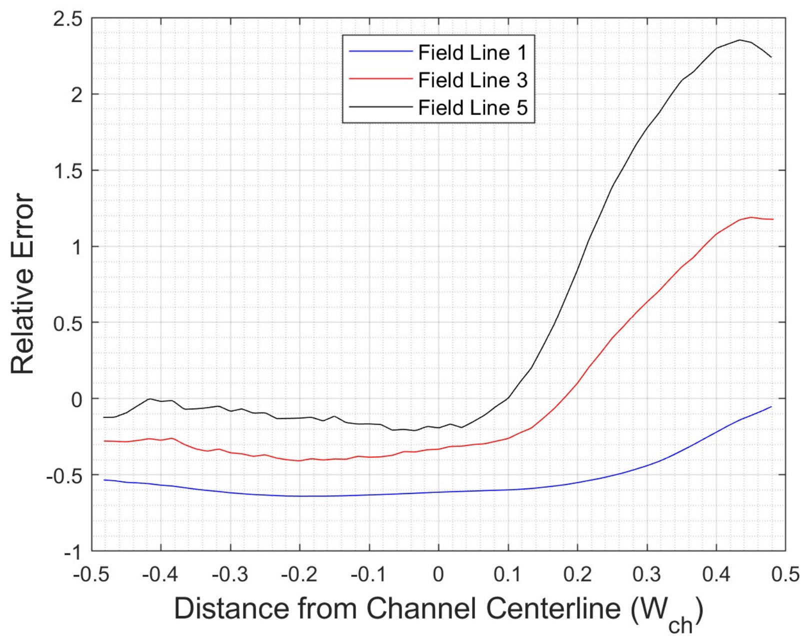

Figure 7-52: Radial variation of the relative error of the MTSI closure with C_1= 4.01 and C_2 = 6.8 × 10^{-3} versus the inferred Ω_{ea} along magnetic field lines 1, 3, and 5. Radial coordinate is normalized by the channel width.

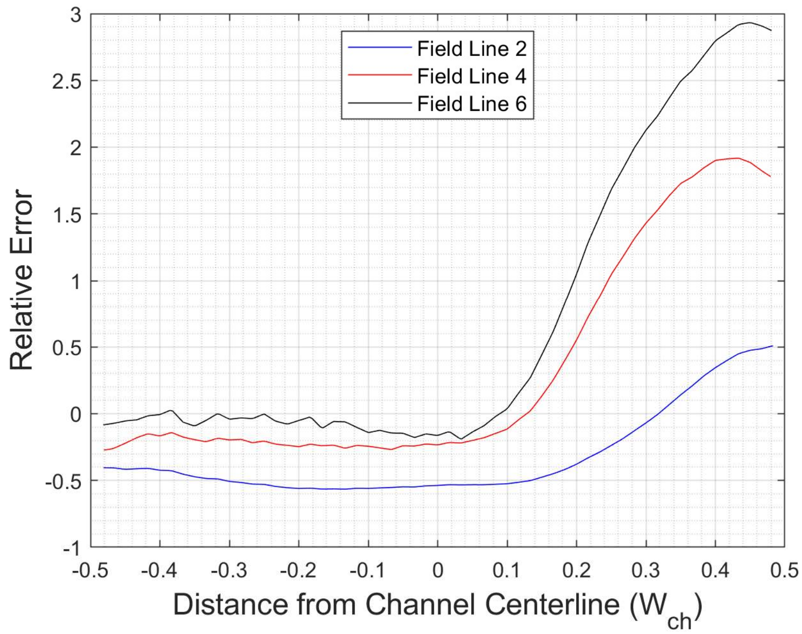

Figure 7-53: Radial variation of the relative error of the MTSI closure with C_1= 4.01 and C_2 = 6.8 × 10^{-3} versus the inferred Ω_{ea} along magnetic field lines 2, 4, and 6. Radial coordinate is normalized by the channel width.

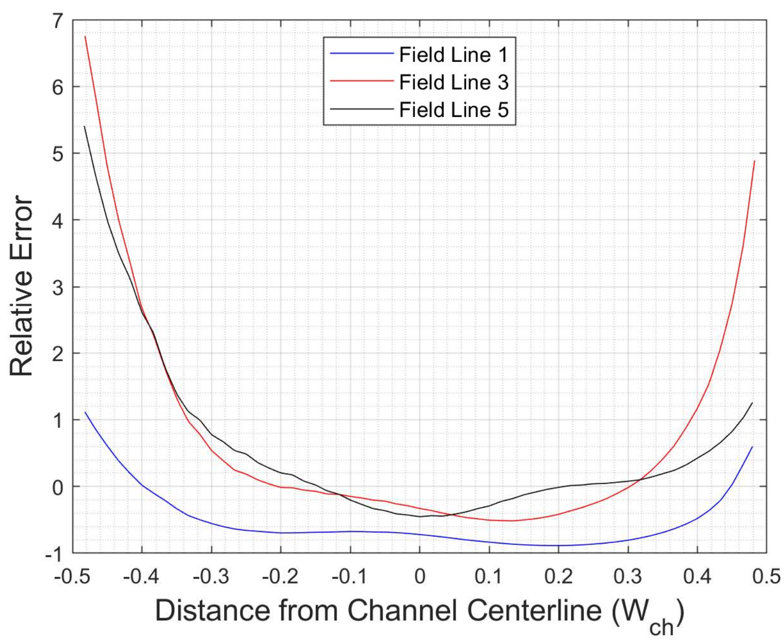

Figure 7-54: Radial variation of the relative error of the ECDI closure with C_3 = 150.6, C_4 = 0.285, and C_5 = 62.4 versus the inferred Ω_{ea} along magnetic field lines 1, 3, and 5. Radial coordinate is normalized by the channel width.

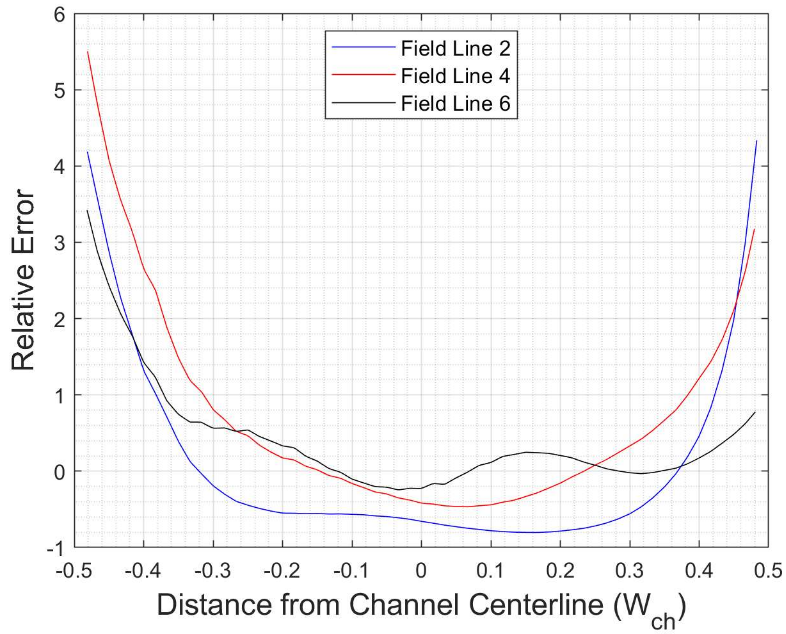

Figure 7-55: Radial variation of the relative error of the ECDI closure with C_3 = 150.6, C_4 = 0.285, and C_5 = 62.4 versus the inferred Ω_{ea} along magnetic field lines 2, 4, and 6. Radial coordinate is normalized by the channel width.

7.6. Inferred Anomalous Electron Heating

Figures 7-56 - 7-60 show how the 2-D map of the ratio of anomalous electron heating to the phenomenological anomalous Joule heating, $\frac{Q_a}{\eta_a j_{e\theta}^2}$, depends strongly on the electron heat flux model. Figure 7-56 shows that when the classical conductive heat flux along magnetic field lines is used, $\frac{Q_a}{\eta_a j_{e\theta}^2}$ becomes unphysically large. Figures 7-57 and 7-58 show that going from a convective heat flux along magnetic field lines to zero heat flux along magnetic field lines has small but minor effect on $\frac{Q_a}{\eta_a j_{e\theta}^2}$. Figures 7-58 and 7-59 show that going from a conductive heat flux across magnetic fields with the phenomenological model of $q_{e\hat{\perp},anom} = \left(\frac{1}{1+\Omega_e\Omega_c} - \frac{1}{1+\Omega_c^2}\right) q_{e\hat{\perp},cond}$ to a heat flux combining classical cross-field conductive heat flux with $q_{e\hat{\perp},conv} = \frac{5}{2}\frac{p_e u_{\hat{\perp}}}{(1+\Omega_c^2)}$ and $q_{e\hat{\perp},azim} = \frac{5}{2}\frac{p_e u_{e\vartheta}\Omega_c}{(1+\Omega_c^2)}$ results in a 2-D map of $\frac{Q_a}{\eta_a j_{e\theta}^2}$ with values mostly between -1 and

1; this range of values is closest among Figures 7-56 - 7-60 to those in the PIC simulation of Ref. 107. Figures 7-59 and 7-60 show that adding the phenomenological model of anomalous heat flux to the heat flux of Fig. 7-59 makes $\frac{Q_a}{\eta_a j_{e\theta}^2}$ more oscillatory and span a wider range of values. Lastly, the change in sign of Q_a in Figs. 7-57 - 7-60 indicates that Q_a cannot be accurately modeled by resistive heating, since resistive heating would require an anomalous energy-transfer collision frequency that is negative in certain regions, which is unphysical.

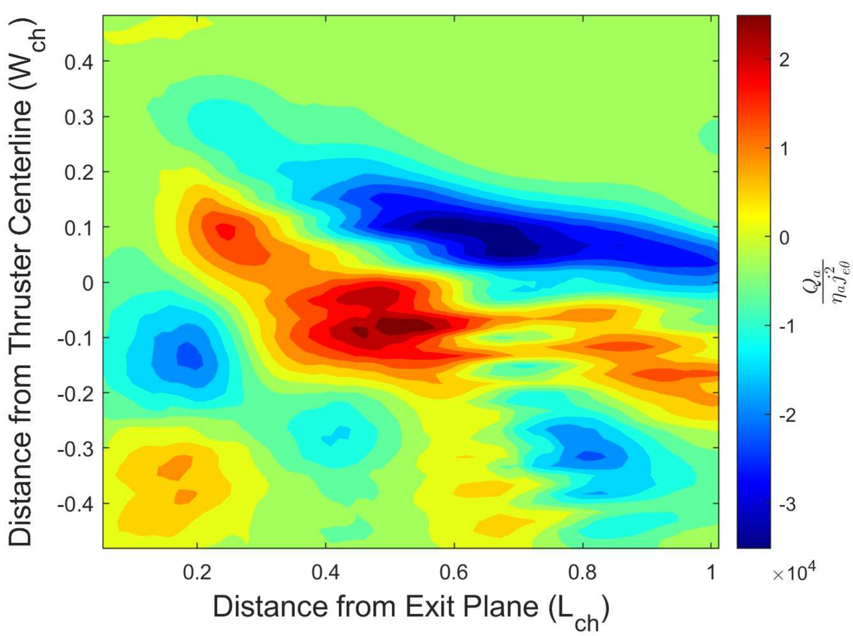

Figure 7-56: 2-D map of $\frac{Q_a}{\eta_a j_{e\theta}^2}$ for heat flux model $\vec{q}_e^{\,1}$.

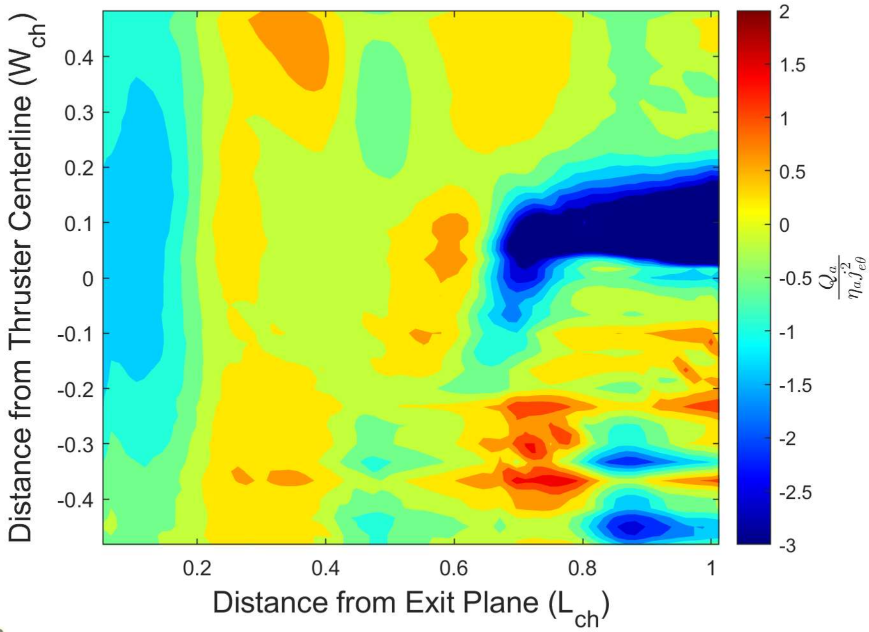

Figure 7-57: 2-D map of $\frac{Q_a}{\eta_a j_{e\theta}^2}$ for heat flux model $\vec{q}_e^2$.

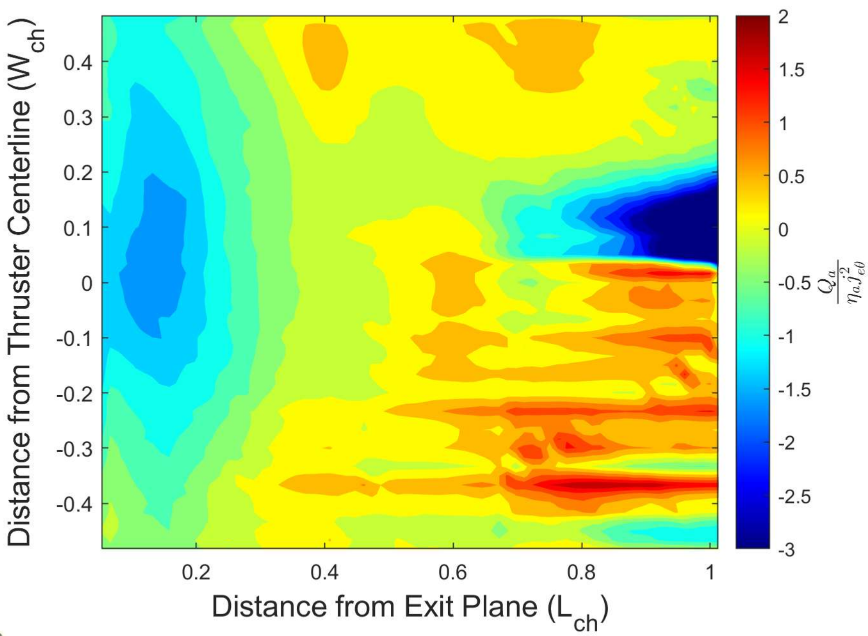

Figure 7-58: 2-D map of $\frac{Q_a}{\eta_a j_{e\theta}^2}$ for heat flux model $\vec{q}_e^3$.

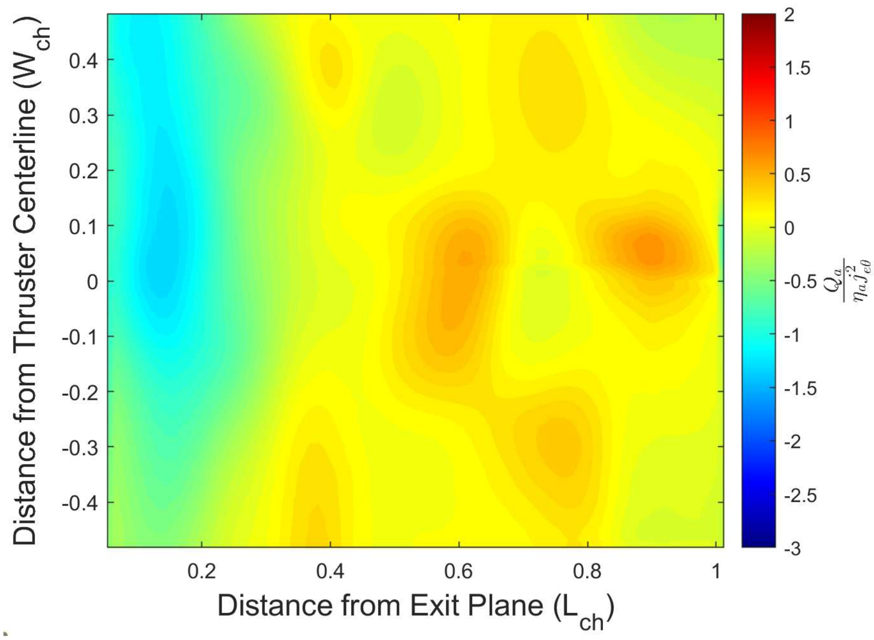

Figure 7-59: 2-D map of $\frac{Q_a}{\eta_a j_{e\theta}^2}$ for heat flux model $\vec{q}_e^{\,4}$.

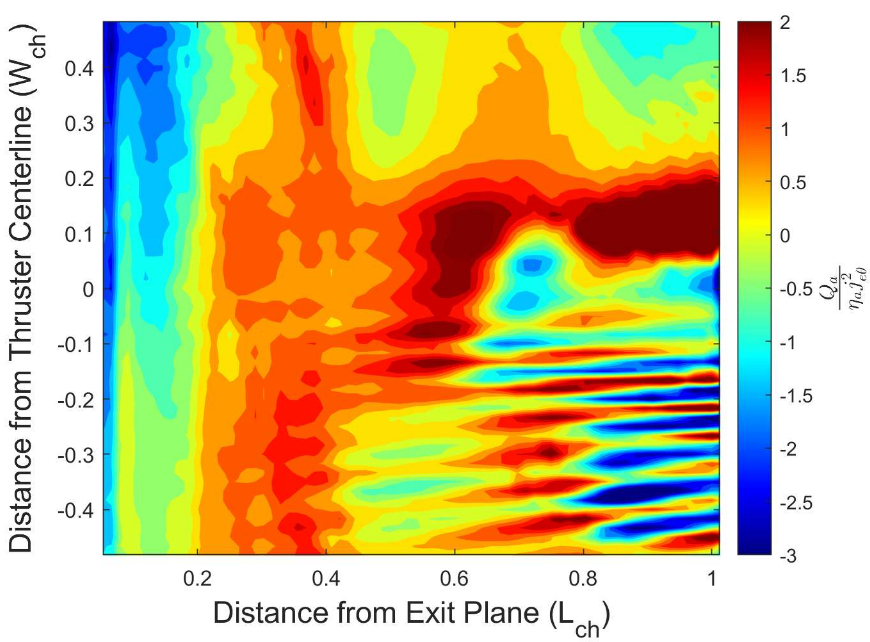

Figure 7-60: 2-D map of $\frac{Q_a}{\eta_a j_{e\theta}^2}$ for heat flux model $\vec{q}_e^{\,5}$.

7.7. Chapter Summary

In this chapter, we presented the 2-D maps of ILTS measurements and of the inference of Ω_{ea}. Most importantly, we disproved our research hypothesis that Ω_{ea} is proportional to $u_{e\theta}$ along magnetic field lines. We also found that Ω_{ea} is not constant along magnetic field lines. In addition, we confirmed how the electron temperature changes away from the channel centerline in the two different regimes of upstream of peak electron temperature and downstream of the peak electron temperature. We also found significant deviations from Maxwellian EVDFs and illustrated the importance of the electron heat flux in the calculation of the anomalous electron heating. Lastly, we discussed how previous measurements and PIC simulations support many aspects of our ILTS measurements.

CHAPTER 8. Conclusion

8.1. Research Contributions

The main purpose of this thesis was to investigate the 2-D behavior of anomalous electron momentum transport across the acceleration of a HET. Seeking accurate quantification of anomalous electron momentum transport, we elected to make measurements using ILTS and to develop a custom solver to infer anomalous electron momentum transport from the measurements. With our measurements and custom solver, we were also able to investigate the additional anomalous electron phenomena of anomalous electron heating and nonequilibrium phenomena. The main contributions from this thesis are the following:

1. Development of a Bayesian data processing method for ILTS measurements that accounts for non-Maxwellian EVDFs and allows for the measurements of higher-order moments of the EVDF
2. Development of a solver to infer anomalous electron momentum transport from ILTS measurements
3. 2-D map of ILTS measurements of electron density, temperature, and azimuthal drift velocity across the acceleration region of HET
4. 2-D map of ILTS measurements of high-order moments of the EVDF
5. Inference of the 2-D map of the anomalous electron Hall parameter
6. Inference of the 2-D map of anomalous electron heating for different heat flux models

The first contribution significantly expanded the measurement capabilities of ILTS and enabled us to make the fourth contribution. The second contribution allows ILTS to be a stand-alone diagnostic for anomalous electron momentum transport in a HET, which allowed us to make the first 2-D inference of the anomalous electron Hall parameter using a non-invasive diagnostic. The third contribution confirms previous experimental and simulation findings regarding how the electron temperature varies along magnetic field lines. We found that, in the acceleration region and for magnetic field lines upstream of the field line with the peak electron temperature along the channel centerline, the electron temperature increases away from the channel centerline. Conversely, in the acceleration region and for magnetic field lines downstream of the field line with the peak electron temperature along the channel centerline, the electron temperature increases away from the channel centerline. These electron temperature measurements indicate that the electron fluid models should not use a conductive electron heat flux along magnetic field lines.

Our measurements of higher-order moments of the EVDF agree qualitatively with previous simulation findings regarding how the EVDF becomes more skewed and with heavier tails further upstream. We provided a qualitative explanation for why the EVDF becomes more non-Maxwellian upstream, which may explain why some ILTS measurements have not measured highly non-Maxwellian EVDF when operating at more nominal discharge voltages. Furthermore, the high degree of electron nonequilibrium indicates that fully predictive HET simulations must capture electron nonequilibrium effects, either through kinetic simulations or higher-order fluid simulations.

The inference of the 2-D map of the anomalous electron Hall parameter showed that the anomalous electron Hall parameter varies along magnetic field lines. This is significant given the following: calibrated simulations often assume a constant anomalous electron Hall parameter along magnetic field lines; this variation along magnetic field lines affects simulated erosion rates; and these calibrated simulations are often used to estimate the lifetime of flight thrusters. While we have not found an alternative assumption for the off-centerline variation of the anomalous electron Hall parameter that is valid, this uncertainty in the off-centerline variation should be accounted for in the estimates of erosion rates from calibrated simulations.

The inference of the 2-D map of the anomalous electron heating indicates that regardless of what electron heat flux model is used, the anomalous electron heating does not follow the phenomenological anomalous Joule heating with the same collision frequency used for anomalous momentum transport. In addition, we find that regardless of the electron flux model used, modeling the anomalous electron heating with resistive heating would require a negative collision frequency in certainty regions, which would be unphysical. This indicates that for the purpose of fully predictive HET simulations, significant advancement of the understanding of anomalous electron heating is required.

8.2. Future work

There are several natural extensions of this work that we think should be pursued. The first should be to verify our inference methodology with an inference that relies on LIF measurements or on a combination of LIF and ILTS measurements. This would be done by either using our methodology and alternatives on a different thruster or discharge condition or by applying our methodology and alternatives on the same thruster and discharge condition. While there a number of ways to combine LIF and ILTS, one simple way is to use LIF to provide the upstream boundary conditions for u_{iz} and u_{ir}. In addition, while we are unsure how, a measurement that can provide an estimate of the radial distribution of the total current density at either an upstream or downstream boundary would also be useful. The second extension would be to investigate the 2-D behavior of anomalous electron phenomena at other discharge conditions and on other thrusters; this should include studying the 2-D behavior of the radial EVDF and its moments. Measurements and inferences on additional thrusters and discharge conditions could help identify certain trends and see if certain findings in this work are observed at nominal discharge conditions. The third extension, which may be necessary to extract meaningful results at highly oscillatory discharge conditions, would be to make time-resolved ILTS measurements, following a technique outlined in Ref. 187 or perhaps using other techniques. The fourth extension would be to take ILTS measurements with sufficiently high spectral resolution to significantly lower the uncertainty of the drift velocity measurements. This could allow meaningful direct measurements of u_{ez}, u_{er}, and $u_{e\hat{1}}$, which would significantly simplify the solver. A fifth extension would be to make two-photon absorption LIF to make neutral density measurements, which would remove the need for the neutral solver in our methodology.

To help make measurements at certain discharge conditions, time-resolved measurements, and to generally reduce the uncertainty in our measurements, a few upgrades to the ILTS system are necessary. First, while we use an ICCD detector, a more sensitive EM-ICCD is on the market. A more sensitive detector would have a more noticeable effect on spectra or spectral regions that are read-noise dominated, such as for the tails of a Thomson spectrum or for single-shot acquisitions necessary for time-resolved measurements. Second, a laser with a similar MJ per pulse value as the laser used in this work, but with five times the repetition rate, is available on the market. A faster repetition rate would enable faster measurements (given our average of 3,000 shots at 10 Hz), allowing for an increased test matrix. However, switching to a higher repetition laser may require changing some of the optics in the interrogation beam due to the increased laser power. Lastly, the laser and perhaps all the optics used for the interrogation beam should be in a temperature-controlled environment. A temperature-controlled environment should increase the alignment stability of the system. Increased alignment stability will not only increase the time for which good alignment holds, which will further increase the accuracy of density measurements.

More importantly, increased alignment stability should make the full stray light spectrum (not just around 532) more repeatable, which would improve the accuracy of subtracting the stray light spectrum, resulting in more accurate ILTS measurements in the tails of the spectrum.

APPENDIX A: Electron Collisions in Plasmas

In this appendix, we will summarize the types of electron collisions in a partially ionized plasma, and we present equations for each type of collision. Collisions can be classified as either elastic or inelastic. In addition, plasmas also contain a combination of short-range and long-range collisions.

A short-range collision is a standard collision event represented by a collision cross-section, σ. Collision cross-sections for short-range collisions are typically found experimentally, and they depend on the size of the colliding particles, relative energy of the colliding particles, and the probability that the collision event occurs given the relative energy of the particles and the type of collision. As we are often concerned with the transport of averaged properties of electrons, it is necessary to consider the collision frequency averaged over the electron velocity distribution,

$$\nu_s = n_s \langle \sigma v_e \rangle, \tag{A-1}$$

where n_s is the density of the collision partner and $\langle \sigma v_e \rangle$ is the product of collision cross-section and electron velocity averaged over the electron velocity distribution.

Electron-impact ionization events are particularly important in plasmas as they generate charged particles, and as such, ionization events appear as source or sink terms in the particle continuity equation. In the electron momentum equation, the effects of elastic and inelastic electron-neutral collisions are combined in a momentum-transfer cross-section. In the electron energy equation, all inelastic collisions are considered sinks of electron energy, as electrons lose the equivalent of the threshold energy at the rate of the collision frequency. Apart from ionization events, electron-impact electron excitation is also a significant source of energy loss, and for molecular plasmas, electron-impact events can also dissociate molecular or excite internal energy modes. Elastic electron collisions with other species also appear in the electron energy equation and represent the tendency for all species to reach thermal equilibrium.

In plasmas, long-range collisions are a consequence of the electrostatic forces between charged particles. As such, these collisions are called Coulomb collisions. The Coulomb collision frequencies relevant to electrons are ν_{ee}, ν_{ei}^{m}, and ν_{ei}^{ε}. ν_{e} is the electron-electron collision frequency that determines the thermal relaxation time of electrons, ν_{ei}^{m} is the electron-ion momentum collision frequency that determines the rate of electron momentum loss to ions, and ν_{ei}^{ε} is the electron-ion energy collision frequency that determines the rates of energy transfer from electrons to ions. We note that electron-electron collision frequency is the same for momentum transfer as it is for energy transfer. Assuming that $T_e \gg T_i$ and $m_i \gg m_e$, ν_{ee}, ν_{ei}^{m}, and ν_{ei}^{ε} are given by [194]

$$\nu_{ee} = \frac{n_e e^4 \ln \Lambda_{ee}}{12\pi^{3/2}\varepsilon_0^2 m_e^{1/2} T_e^{3/2}} \tag{A-2}$$

$$\nu_{ei}^{m} = \frac{2^{1/2} n_i Z^2 e^4 \ln \Lambda_{ei}}{12\pi^{3/2}\varepsilon_0^2 m_e^{1/2} T_e^{3/2}} \tag{A-3}$$

and

$$\nu_{ei}^{\varepsilon} = \frac{2^{1/2} m_e^{1/2} n_i Z^2 e^4 \ln \Lambda_{ei}}{6\pi^{3/2}\varepsilon_0^2 m_i T_e^{3/2}}. \tag{A-4}$$

$\ln \Lambda_{ee}$ and $\ln \Lambda_{ei}$ are given by

$$\ln \Lambda_{ee} \approx \begin{cases} 30 - \ln\left(n_e^{1/2} T_{eV}^{-3/2}\right), \; T_e < 10\ eV \\ 31 - \ln\left(n_e^{1/2} T_{eV}^{-1}\right), \; T_e > 10\ eV \end{cases} \tag{A-5}$$

and

$$\ln \Lambda_{ei} \approx \begin{cases} 30 - \ln\left(n_e^{1/2} T_{eV}^{-3/2} Z\right), & \frac{T_i m_e}{m_i} < T_e < 10Z^2 \, eV \\ 31 - \ln\left(n_e^{1/2} T_{eV}^{-1}\right), & \frac{T_i m_e}{m_i} < 10Z^2 eV < T_e \end{cases}, \tag{A-6}$$

where n_e is expressed in m^{-3}. In addition, since electron-electron collision frequencies are relevant in the relaxation of anisotropic electron temperatures, we present the equation for ν_{ee} in the case of anisotropic electron temperatures, [112]

$$\nu_{ee} = \frac{n_e e^4 \ln \Lambda_{ee}}{12\pi^{3/2} \varepsilon_0^2 m_e^{1/2} T_{e\perp} T_{e\parallel}^{1/2}}. \tag{A-7}$$

Since $\ln \Lambda_{ee}$ in Eq. A-5 is weakly dependent on the electron temperature, we can approximate $\ln \Lambda_{ee}$ in Eq. A-7 by using $T_e = \frac{2T_{e\perp} + T_{e\parallel}}{3}$.

APPENDIX B: Laser Raman Scattering Model Equations

To calibrate the ILTS diagnostic, we implement laser rotational Raman scattering (LRS). Raman scattering is the inelastic scattering of incident light off molecules that occurs via the excitation of the molecules' rotational or vibrational energy modes [132]. Rotational Raman scattering is used instead of vibrational Raman scattering to calibrate ILTS systems because the spectral shifts associated with rotational Raman scattering are similar to those expected in ILTS. Alternatively, Rayleigh scattering has been used to calibrate ILTS systems, but Rayleigh scattering is elastic scattering off of molecules and the spectral broadening observed in Rayleigh scattering is small, such that Rayleigh scattering can be difficult to distinguish from stray light reflections. In addition, to observe Rayleigh scattering, the stray light filtering used from ILTS needs to be removed, such that the detection system for Rayleigh scattering is not the exact same as for ILTS. For these reasons, LRS is the best choice to calibrate ILTS.

Raman scattering occurs in two variants, Stokes and anti-Stokes Raman scattering. The Stokes case corresponds to when an incident photon excites a ground (or reference) state molecule which then relaxes to a lower (but higher energy than ground state) excited state; the scattered photon is then at a lower energy than incident photon, which corresponds to a larger wavelength compared to the incident wavelength. The anti-Stokes case correspond to when the molecule starts in an excited state relative to the ground (or reference) state and then relaxes to the ground (or reference) state; in this case, the scattered photon is at higher energy than the incident photon, such that the scattered photon is at smaller wavelength than the incident wavelength.

As we are concerned with LRS on an air mixture, the spectral density of the photon counts in the signal measured from LRS is combination of the contributions from the individual gas species of the air mixture, such that

$$P_s^R = P_{s,N_2}^R + P_{s,O_2}^R, \tag{B-1}$$

where we neglect all other molecular species of air. For rotational Raman scattering of diatomic molecules, there is only one allowable Stokes transition and one allowable anti-Stokes transition [132], such that the spectral density of the photon counts from LRS on a given species, j, as a function of wavelength is given by [132]

$$P_{s,j}^R(\lambda) = \eta \frac{\lambda_i}{hc} E_i L_{det} \Delta\Omega \sum_{J=0}^{\infty} n_{j,J} \frac{d\sigma_{j,J\to J\pm 2}^R}{d\Omega} S^R\left(\lambda, \lambda_{j,J\to J\pm 2}\right), \tag{B-2}$$

where the summation accounts for the LRS of every rotationally excited state as the reference state, J is the rotational quantum number of an excited state, $n_{j,J}$ is the species number density in excited state J, $\frac{d\sigma_{j,J\to J\pm 2}^R}{d\Omega}$ is the species differential rotational Raman cross section, where $+$ corresponds to the Stokes transition and $-$ corresponds to the anti-Stokes transition, and $S^R\left(\lambda, \lambda_{j,J\to J\pm 2}\right)$ is the species spectral redistribution function of a given transition. $n_{j,J}$ is given by

$$n_{j,J} = \frac{n_{j,g} g_{j,J} (2J+1)}{Q_j} \exp\left(-\frac{E_{j,J}}{k_b T_g}\right), \tag{B-3}$$

where $g_{j,J}$ is the species degeneracy of rotational state J, Q_j is the rotational partition function of species j, $n_{j,g}$ is the species number density, $E_{j,J}$ is the species' rotational energy of state J, and T_g is the neutral gas temperature. $n_{j,g}$ is given by the combination of the ideal gas law and the law of partial pressure,

$$n_{j,g} = \chi_j \frac{k_b T_g}{p_g}, \tag{B-4}$$

where χ_j is the species fraction in the air mixture and p_g is the gas pressure. When taking our LRS measurements on the residual air at 10 Torr, we assume χ_j of N_2 and O_2 remain unchanged from their values at atmosphere, such that $\chi_{N_2} = 0.79$ and $\chi_{O_2} = 0.21$. For the rotational degeneracies, $g_{N_2,J}$ is 3 when J is odd and 6 when J is even, and $g_{O_2,J}$ is 1 when J is odd and 0 when J is even. The rotational partition functions are given by

$$Q_j = \left(2I_j + 1\right)^2 \frac{k_b T_g}{B_j} \tag{B-5}$$

where I_j is the species nuclear spin degeneracy, $I_{N_2} = 1$, $I_{O_2} = 0$, B_j is the species rotational constant, $B_{N_2} = 1.98973$ cm^{-1}, and $B_{O_2} = 1.4378$ cm^{-1}. $E_{j,J}$ is given by

$$E_{j,J} = J(J+1)B_j. \tag{B-6}$$

Regarding the differential Raman cross section, in the perpendicular scattering geometry used for our ILTS and LRS measurements, $\frac{d\sigma^R_{j,J\to J\pm2}}{d\Omega}$ is given by [171]

$$\frac{d\sigma^R_{j,J\to J\pm2}}{d\Omega} = \frac{3}{4}\frac{d\sigma^R_{\perp j,J\to J\pm2}}{d\Omega}, \tag{B-7}$$

where $\frac{d\sigma^R_{\perp j,J\to J\pm2}}{d\Omega}$ is the perpendicular Raman cross section and is given by

$$\frac{d\sigma^R_{\perp j,J\to J\pm2}}{d\Omega} = \frac{64 \quad {}^{4}}{45}\frac{\gamma_j^2}{\varepsilon_0^2}\frac{b_{J\to J\pm2}}{\lambda^4_{j,J\to J\pm2}}, \tag{B-8}$$

where $\frac{\gamma_j^2}{\varepsilon_0^2}$ is the anisotropy of the polarizability tensor of species j, $b_{J\to J\pm2}$ are the Placzek-Teller coefficients, and $\lambda_{j,J\to J\pm2}$ are the wavelengths of the scattered photons. $\frac{\gamma_j^2}{\varepsilon_0^2}$ is interpolated to 532 nm from the data in Ref. 195, and is $5.02 \times 10^{-59} \pm 8\%$ m^6 for N_2 and $1.29 \times 10^{-60} \pm 10\%$ m^6 for O_2. $b_{J\rightarrow J\pm 2}$ and $\lambda_{j,J\rightarrow J\pm 2}$ are given by

$$b_{J\rightarrow J\pm 2} = \frac{3(2J+1\pm 1)(2J+1\pm 3)}{4(2J+1)(2J+1\pm 2)} \tag{B-9}$$

$$\lambda_{j,J\rightarrow J\pm 2} = \lambda_i \pm \lambda_i^2 \frac{B_j}{hc}(4J+2\pm 4). \tag{B-10}$$

The photons are scattered to a discrete set of wavelengths, but the scattered light is spectrally broadened by the instrument function, which is a consequence of the finite detection optics. The instrument function is the dominant source of spectral broadening of the LRS signal, and we assume a Gaussian instrument function, such that the spectral redistribution function of a given transition can then be represented by

$$S^R(\lambda, \lambda_{j,J\rightarrow J\pm 2}) = \frac{1}{\sqrt{2\pi}\sigma_{IF}} \exp\left(-\frac{1}{2}\frac{\left(\lambda - \lambda_{j,J\rightarrow J\pm 2}\right)^2}{\sigma_{IF}^2}\right), \tag{B-11}$$

where σ_{IF} is the standard deviation of the Gaussian instrument function.

APPENDIX C: Additional 2-D Maps and Variations Along Magnetic Field Lines

This appendix serves three purposes. The first is to plot the variation of certain properties along magnetic field lines. This is done for the properties for which we only showed 2-D color maps in Chapter 7. The data along magnetic field lines will contextualize the 2-D maps for those that do not have access to the H9 magnetic field topology will also show the level of uncertainty in the 2-D maps. The second purpose of this appendix is to show 2-D color maps for the data that was only shown as along magnetic field lines in Chapter 7. The third purpose of this appendix is to show alternative results for the 2-D solver with different sized windows for the gaussian filter.

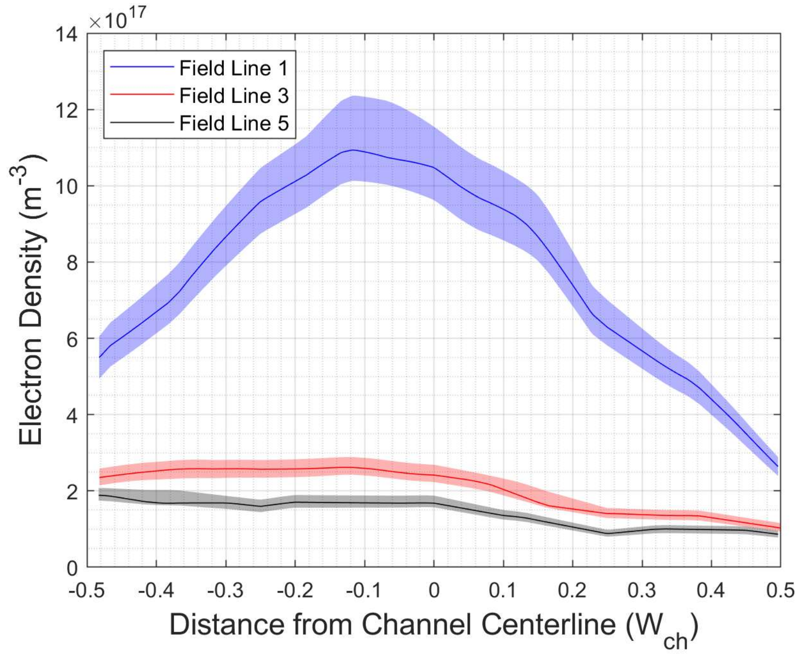

Figure C-1: Radial variation of electron density along magnetic field lines 1, 3, and 5. Radial coordinate is normalized by the channel width.

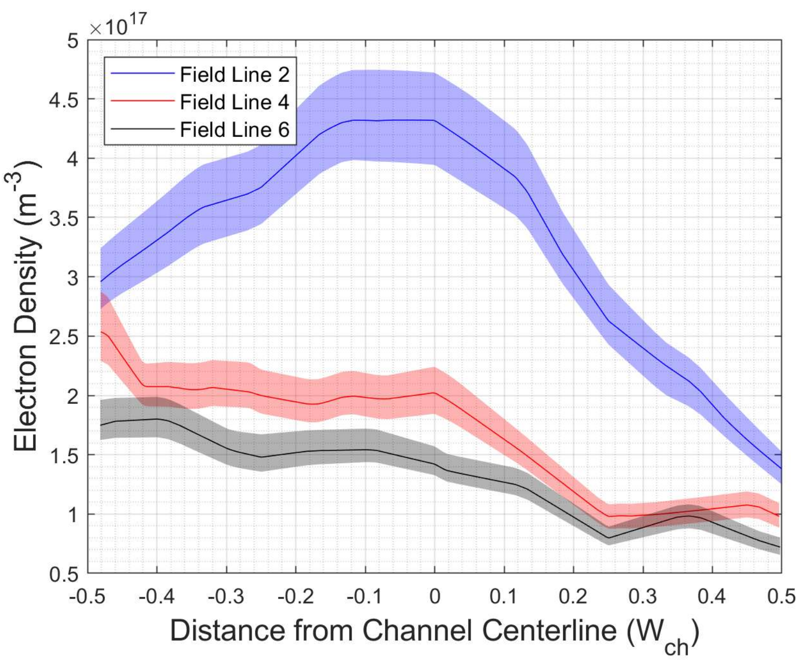

Figure C-2: Radial variation of electron density along magnetic field lines 2, 4, and 6. Radial coordinate is normalized by the channel width.

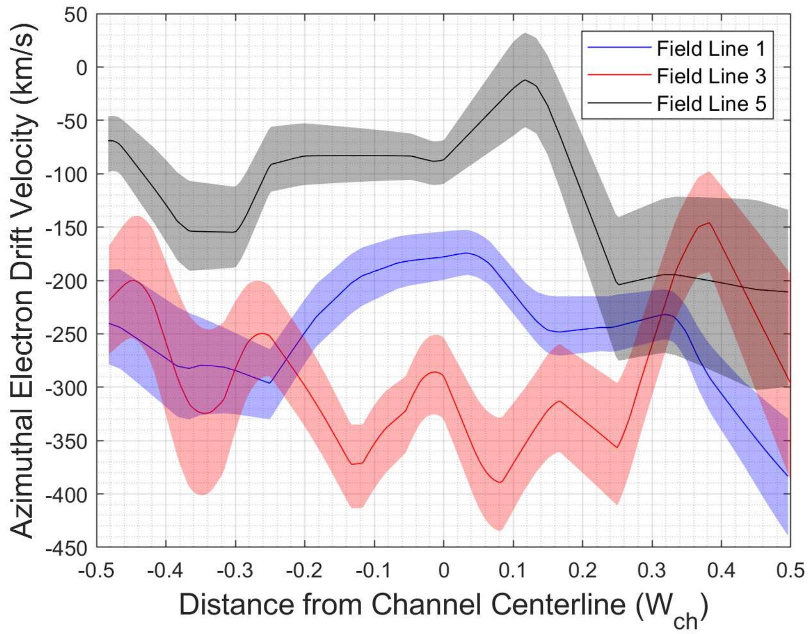

Figure C-3: Radial variation of azimuthal electron drift velocity along magnetic field lines 1, 3, and 5. Radial coordinate is normalized by the channel width.

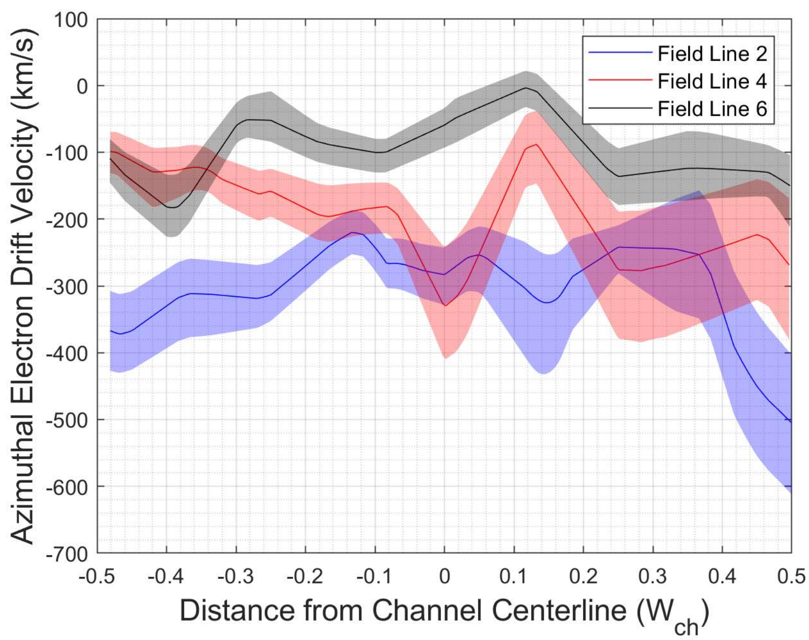

Figure C-4: Radial variation of azimuthal electron drift velocity along magnetic field lines 2, 4, and 6. Radial coordinate is normalized by the channel width.

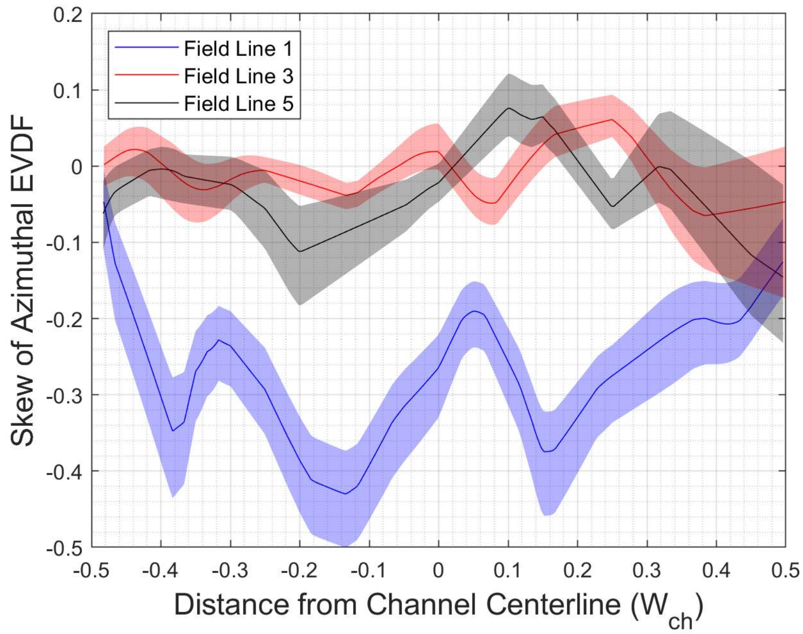

Figure C-5: Radial variation of skew of azimuthal EVDF along magnetic field lines 1, 3, and 5. Radial coordinate is normalized by the channel width.

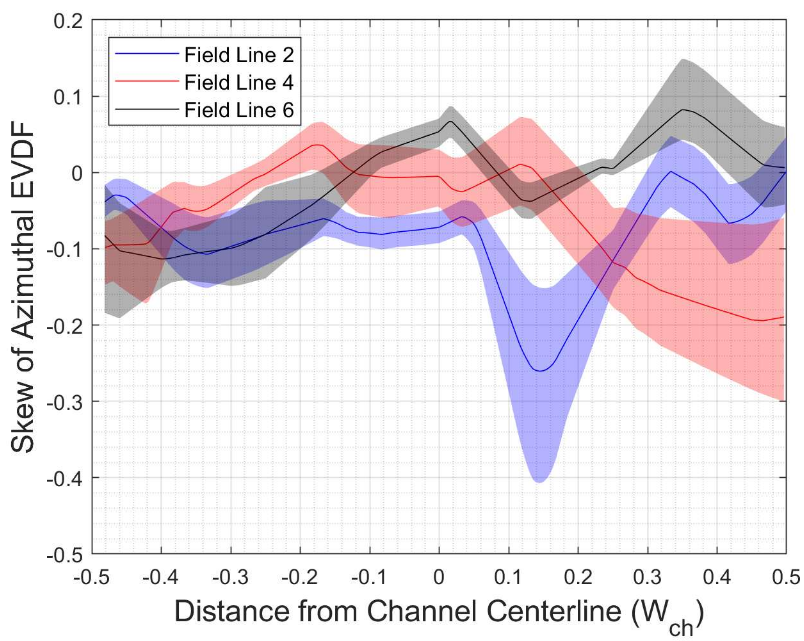

Figure C-6: Radial variation of skew of azimuthal EVDF along magnetic field lines 2, 4, and 6. Radial coordinate is normalized by the channel width.

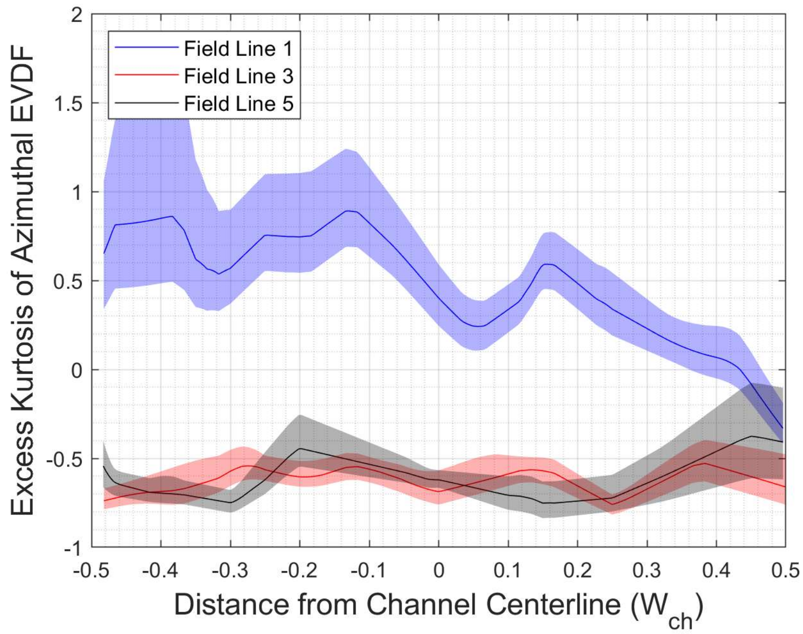

Figure C-7: Radial variation of excess kurtosis of azimuthal EVDF along magnetic field lines 1, 3, and 5. Radial coordinate is normalized by the channel width.

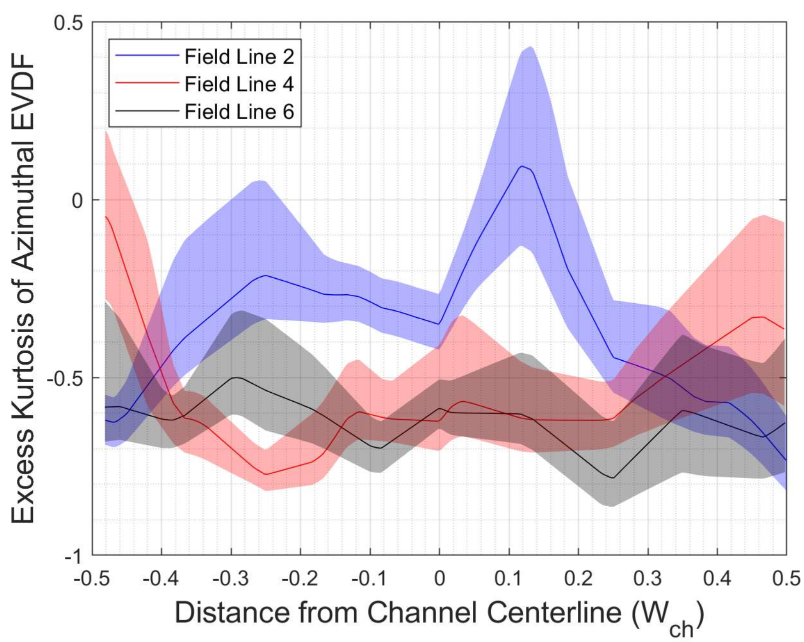

Figure C-8: Radial variation of excess kurtosis of azimuthal EVDF along magnetic field lines 2, 4, and 6. Radial coordinate is normalized by the channel width.

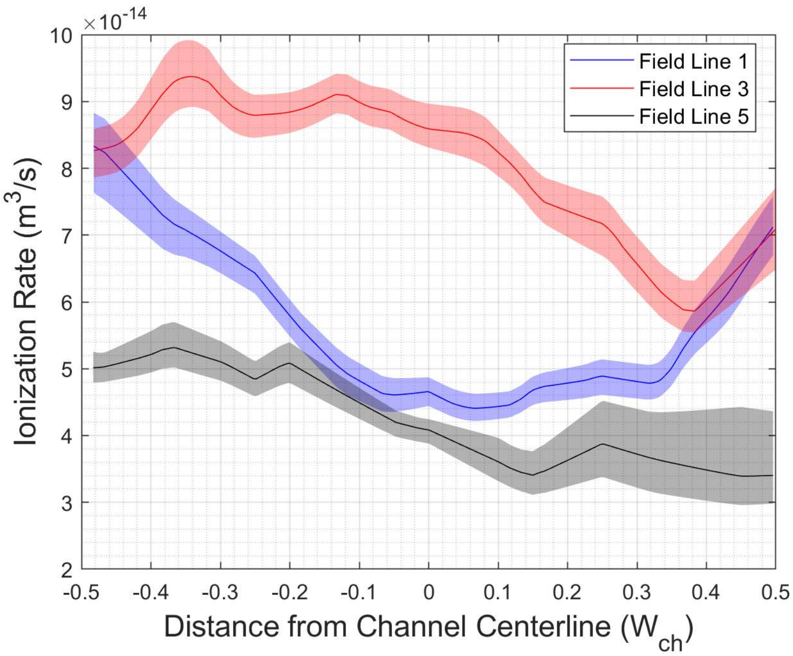

Figure C-9: Radial variation of single ionization rate of neutral krypton along magnetic field lines 1, 3, and 5. Radial coordinate is normalized by the channel width.

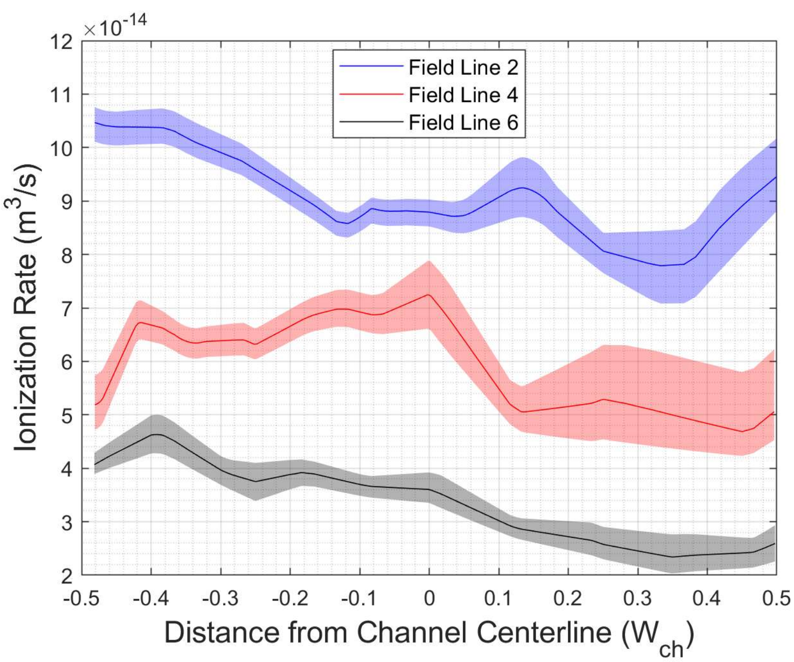

Figure C-10: Radial variation of single ionization rate of neutral krypton along magnetic field lines 2, 4, and 6. Radial coordinate is normalized by the channel width.

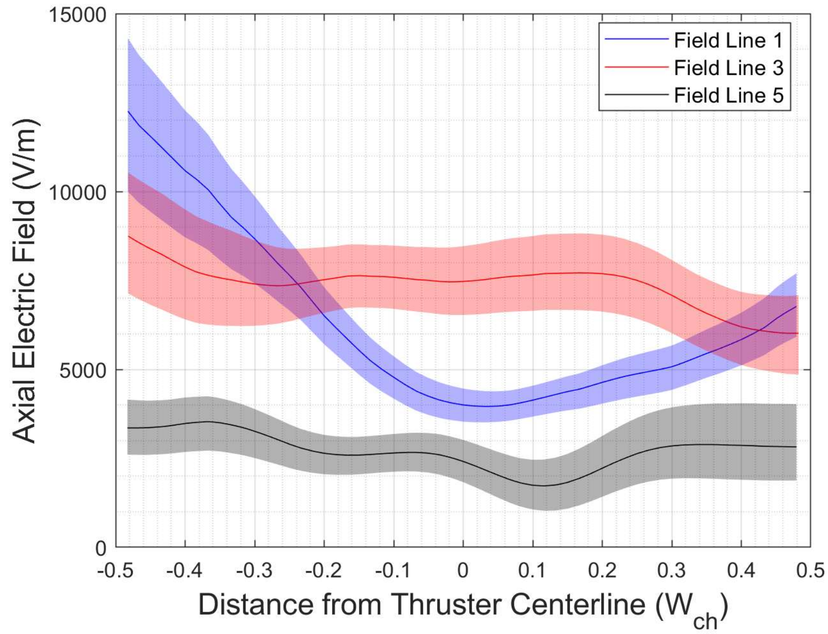

Figure C-11: Radial variation of axial electric field along magnetic field lines 1, 3, and 5. Radial coordinate is normalized by the channel width.

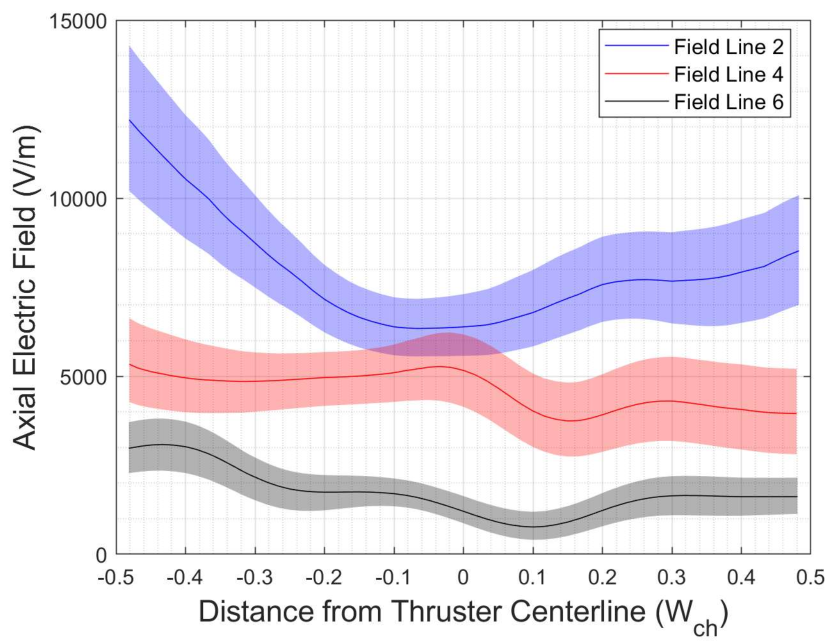

Figure C-12: Radial variation of axial electric field along magnetic field lines 2, 4, and 6. Radial coordinate is normalized by the channel width.

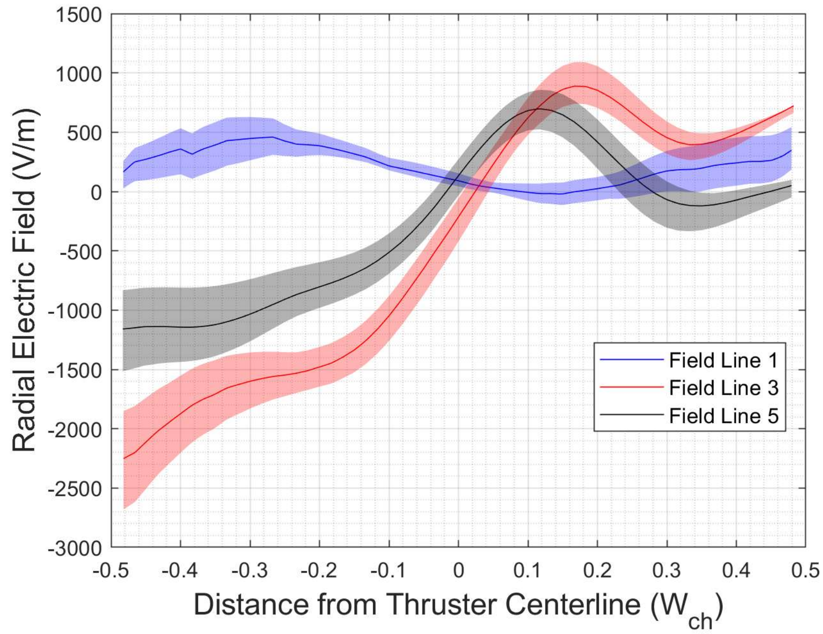

Figure C-13: Radial variation of radial electric field along magnetic field lines 1, 3, and 5. Radial coordinate is normalized by the channel width.

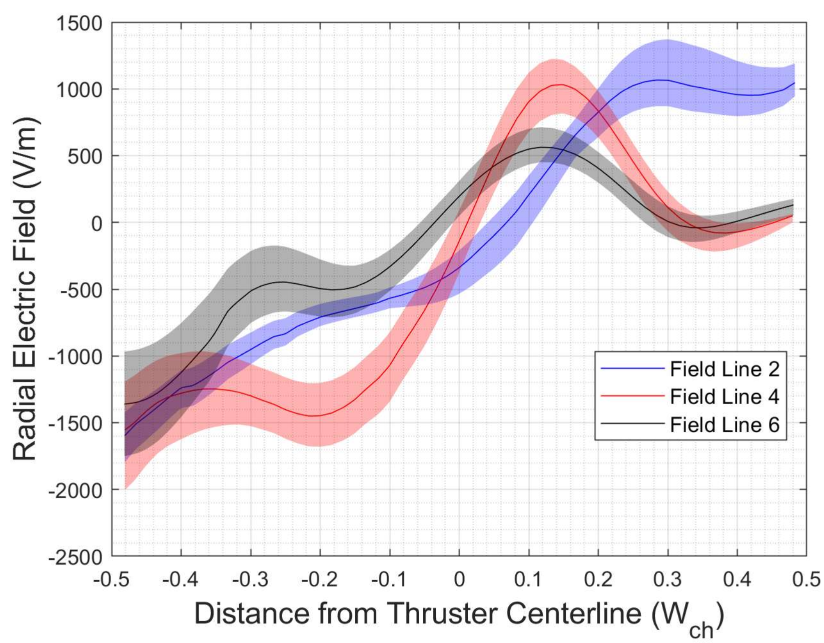

Figure C-14: Radial variation of radial electric field along magnetic field lines 2, 4, and 6. Radial coordinate is normalized by the channel width.

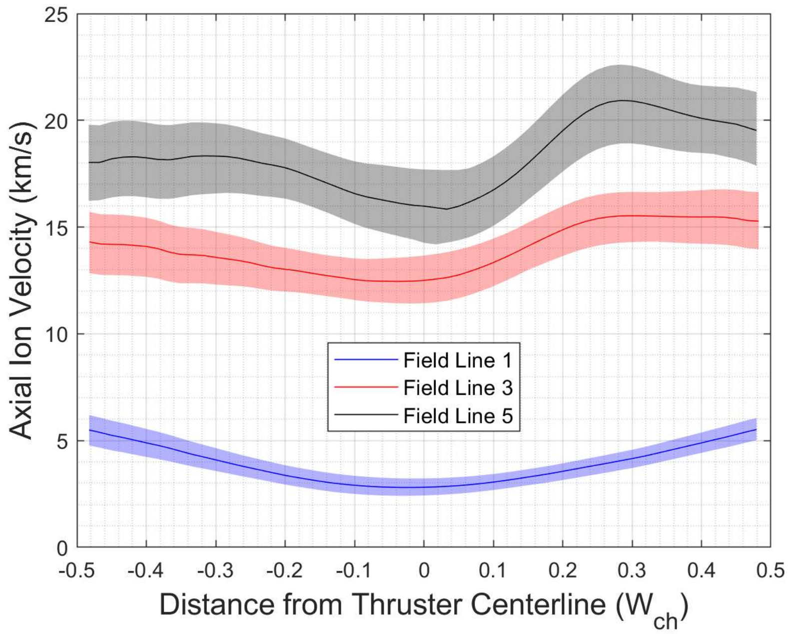

Figure C-15: Radial variation of axial ion velocity along magnetic field lines 1, 3, and 5. Radial coordinate is normalized by the channel width.

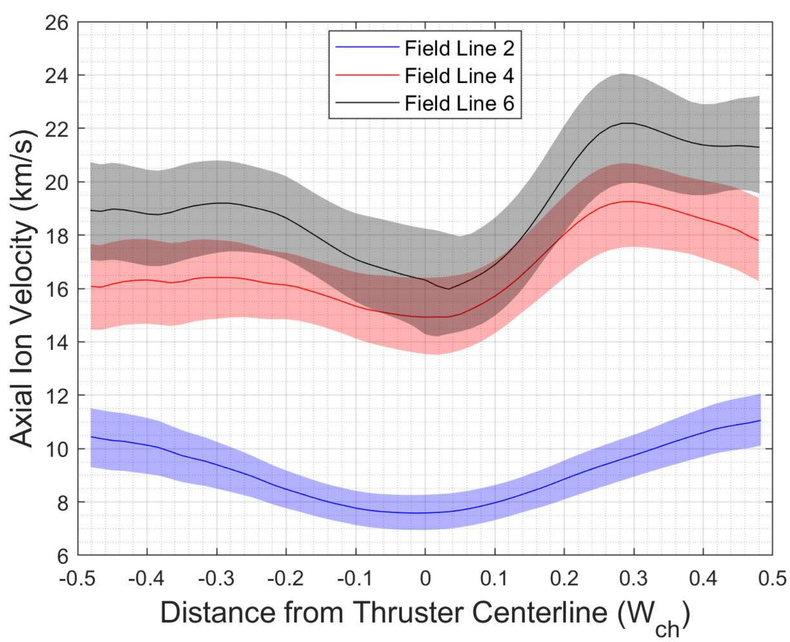

Figure C-16: Radial variation of axial ion velocity along magnetic field lines 2, 4, and 6. Radial coordinate is normalized by the channel width.

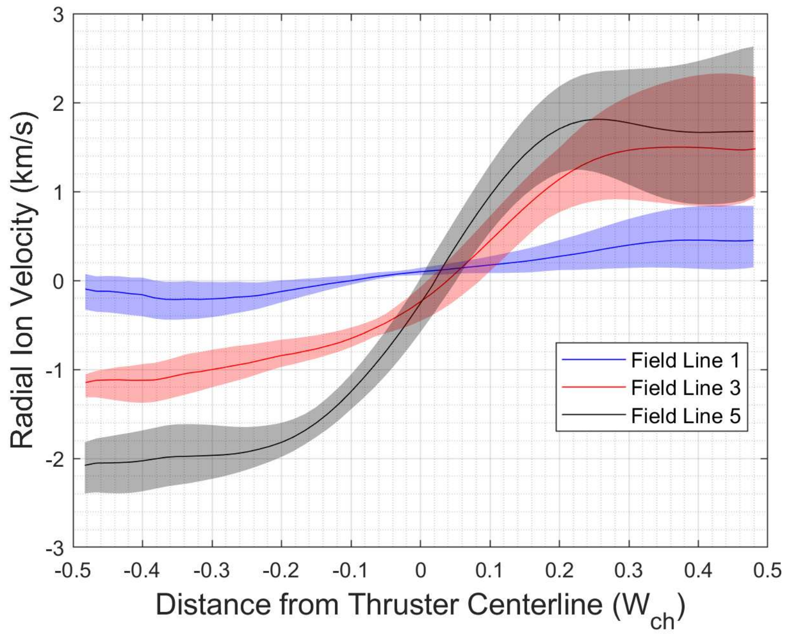

Figure C-17: Radial variation of radial ion velocity along magnetic field lines 1, 3, and 5. Radial coordinate is normalized by the channel width.

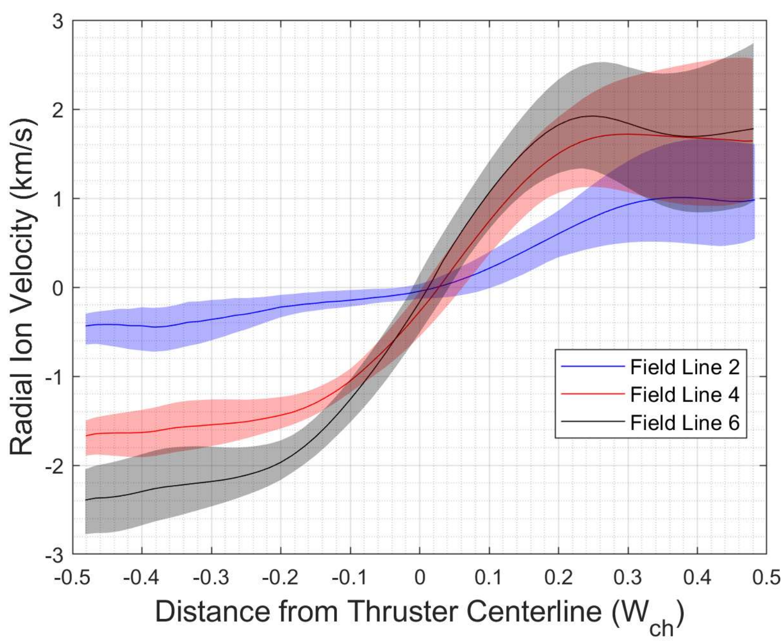

Figure C-18: Radial variation of radial ion velocity along magnetic field lines 2, 4, and 6. Radial coordinate is normalized by the channel width.

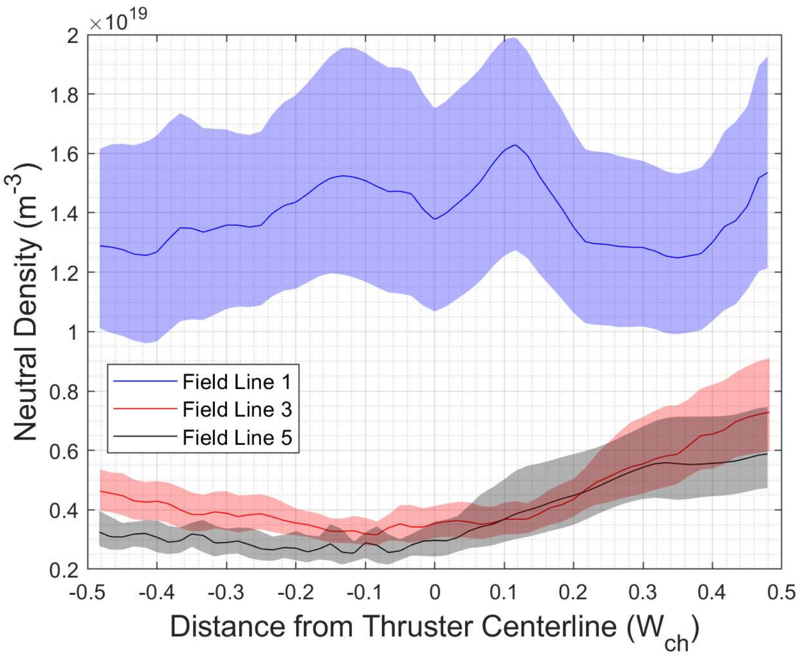

Figure C-19: Radial variation of neutral density along magnetic field lines 1, 3, and 5. Radial coordinate is normalized by the channel width.

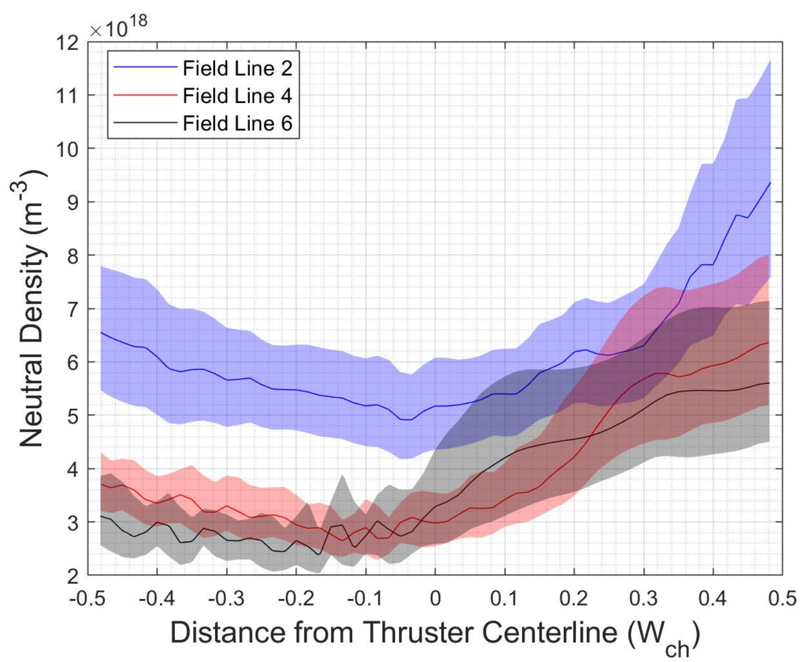

Figure C-20: Radial variation of neutral density along magnetic field lines 2, 4, and 6. Radial coordinate is normalized by the channel width.

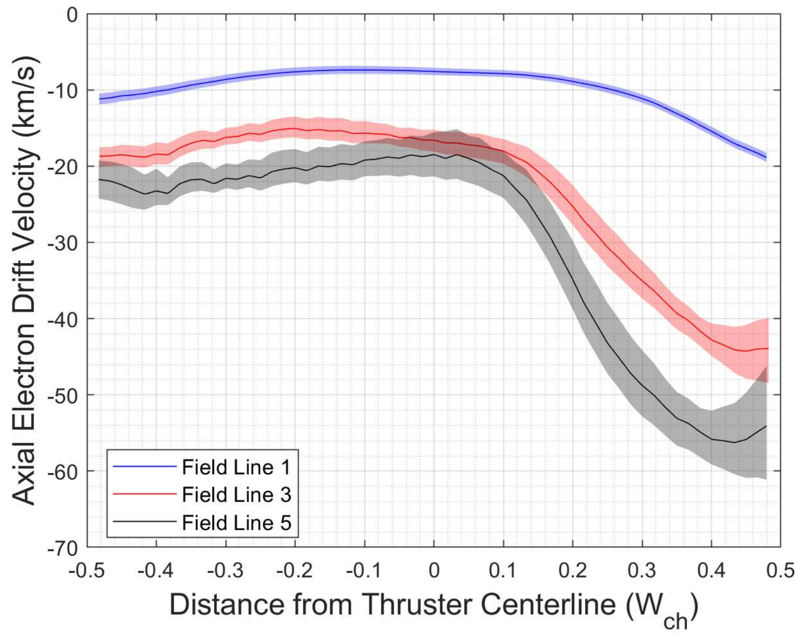

Figure C-21: Radial variation of axial electron drift velocity along magnetic field lines 1, 3, and 5. Radial coordinate is normalized by the channel width.

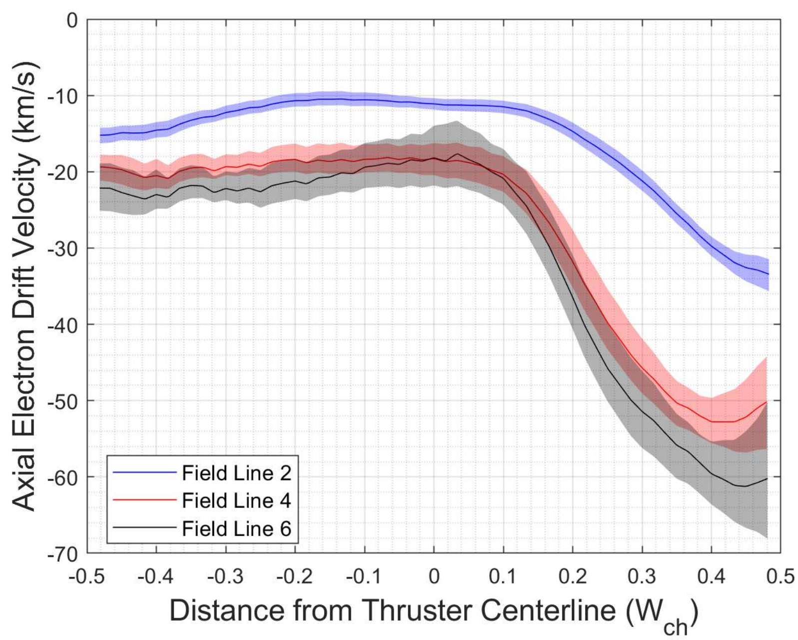

Figure C-22: Radial variation of axial electron drift velocity along magnetic field lines 2, 4, and 6. Radial coordinate is normalized by the channel width.

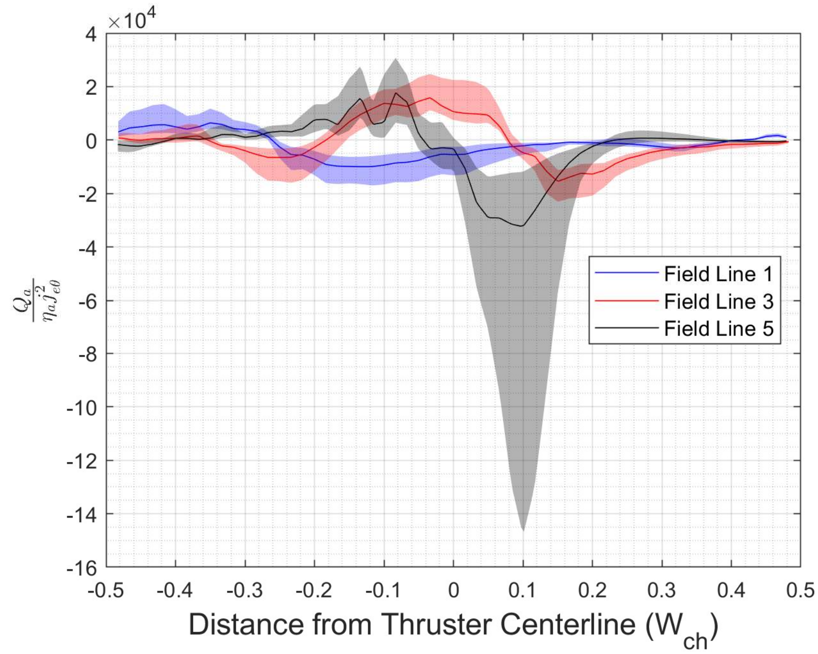

Figure C-23: Radial variation of $\frac{Q_a}{\eta_a j_{e\theta}^2}$ for heat flux model $\vec{q}_e^{\,1}$ along magnetic field lines 1, 3, and 5. Radial coordinate is normalized by the channel width.

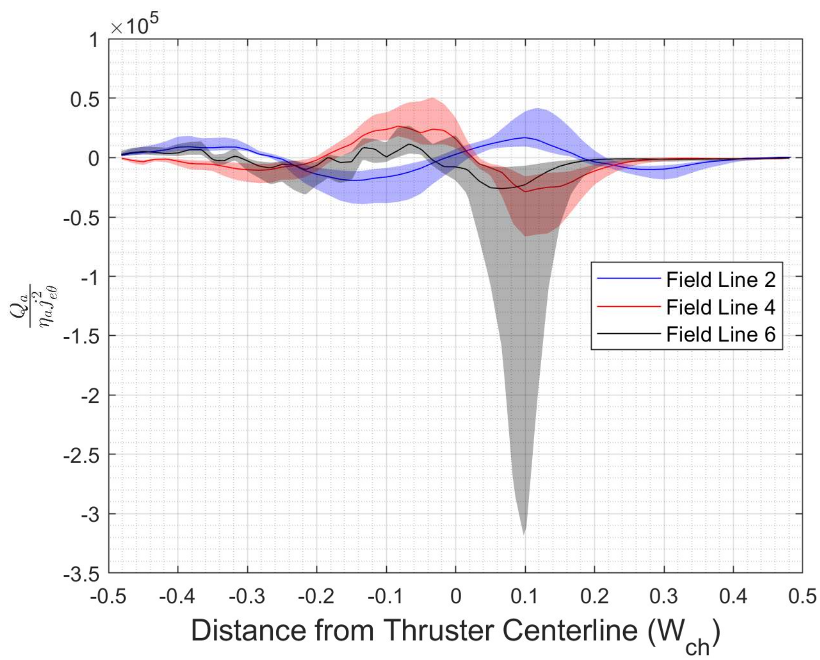

Figure C-24: Radial variation of $\frac{Q_a}{\eta_a j_{e\theta}^2}$ for heat flux model $\vec{q}_e^{\,1}$ along magnetic field lines 2, 4, and 6. Radial coordinate is normalized by the channel width.

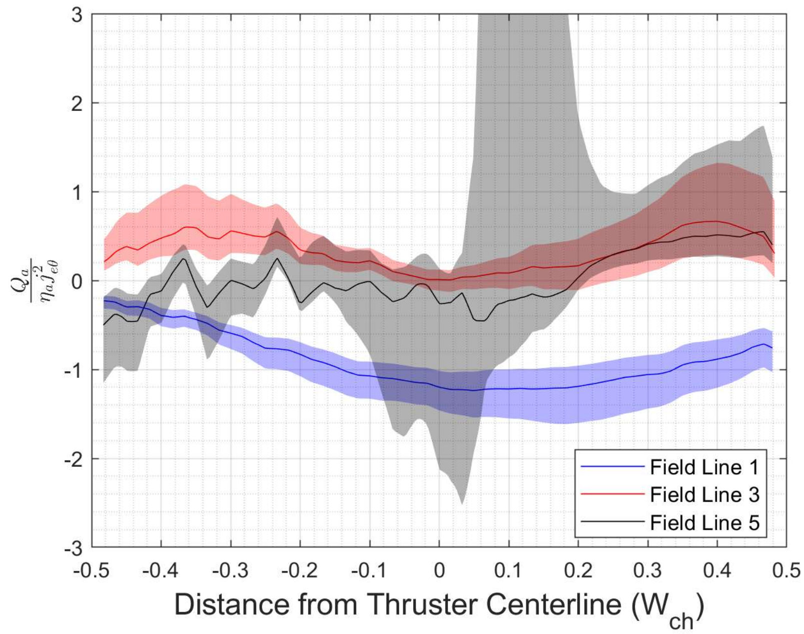

Figure C-25: Radial variation of $\frac{Q_a}{\eta_a j_{e\theta}^2}$ for heat flux model $\vec{q}_e^{\,2}$ along magnetic field lines 1, 3, and 5. Radial coordinate is normalized by the channel width.

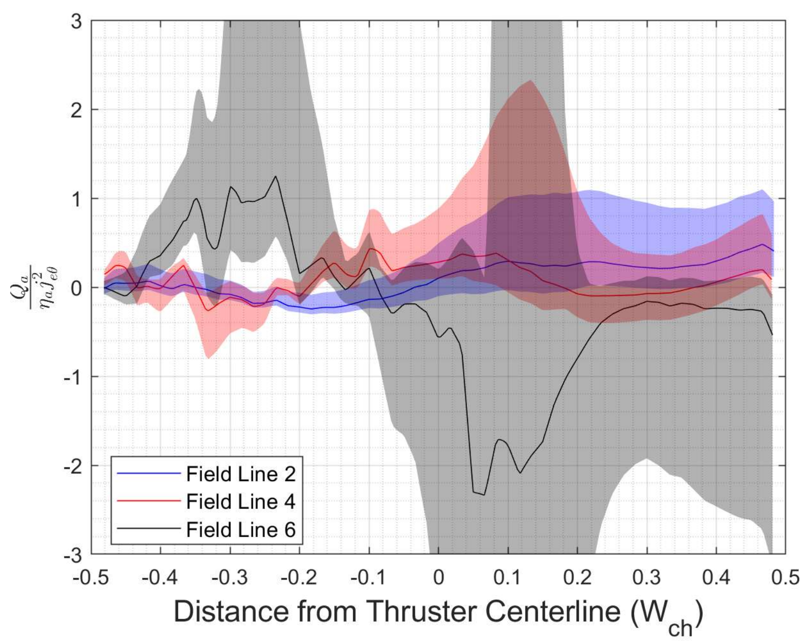

Figure C-26: Radial variation of $\frac{Q_a}{\eta_a j_{e\theta}^2}$ for heat flux model $\vec{q}_e^{\,2}$ along magnetic field lines 2, 4, and 6. Radial coordinate is normalized by the channel width.

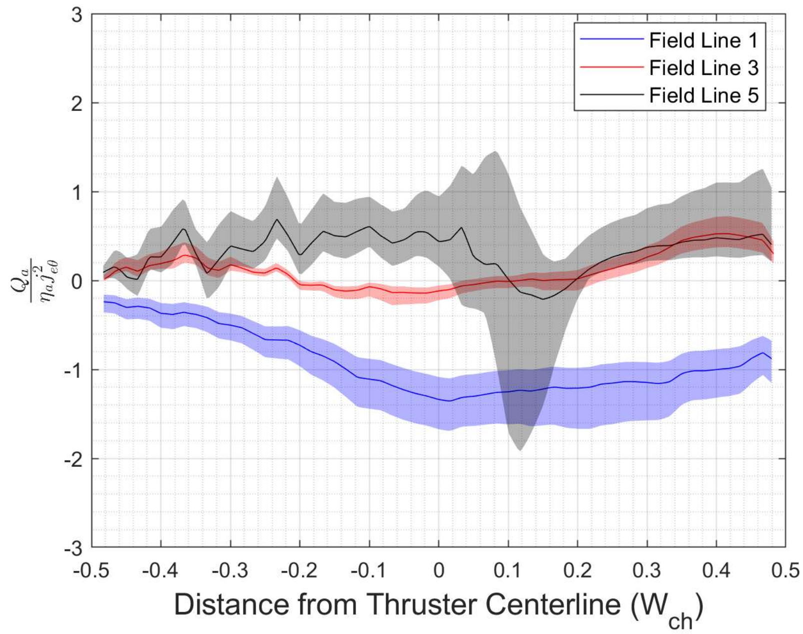

Figure C-27: Radial variation of $\frac{Q_a}{\eta_a j_{e\theta}^2}$ for heat flux model $\vec{q}_e^{\,3}$ along magnetic field lines 1, 3, and 5. Radial coordinate is normalized by the channel width.

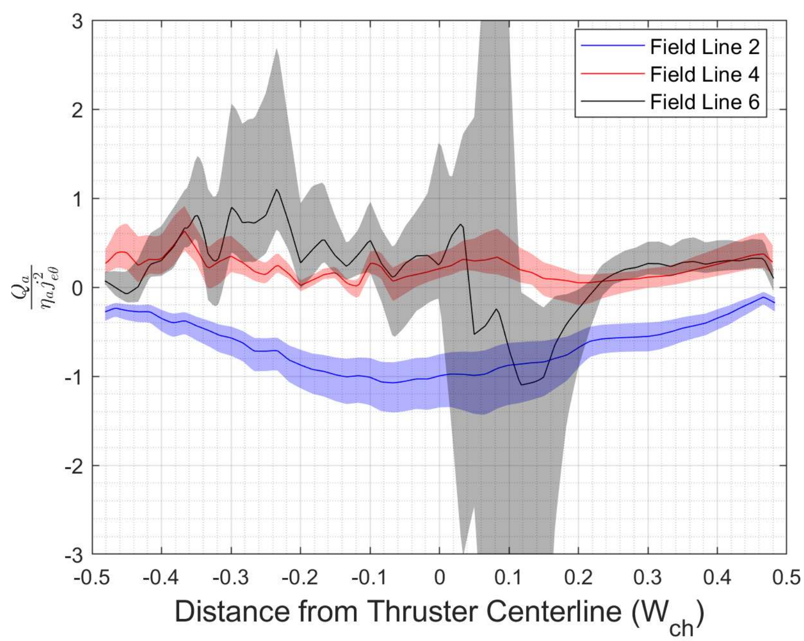

Figure C-28: Radial variation of $\frac{Q_a}{\eta_a j_{e\theta}^2}$ for heat flux model $\vec{q}_e^{\,3}$ along magnetic field lines 2, 4, and 6. Radial coordinate is normalized by the channel width.

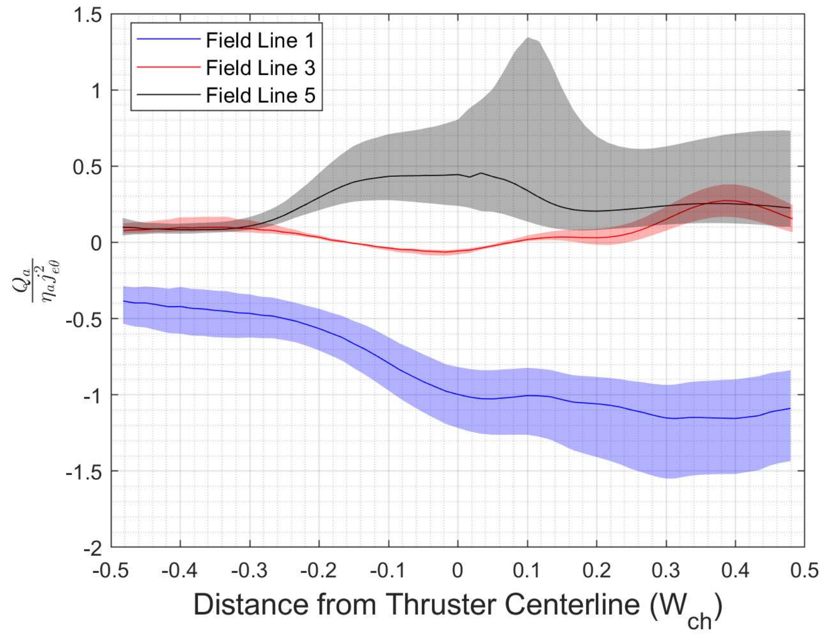

Figure C-29: Radial variation of $\frac{Q_a}{\eta_a j_{e\theta}^2}$ for heat flux model $\vec{q}_e^{\,4}$ along magnetic field lines 1, 3, and 5. Radial coordinate is normalized by the channel width.

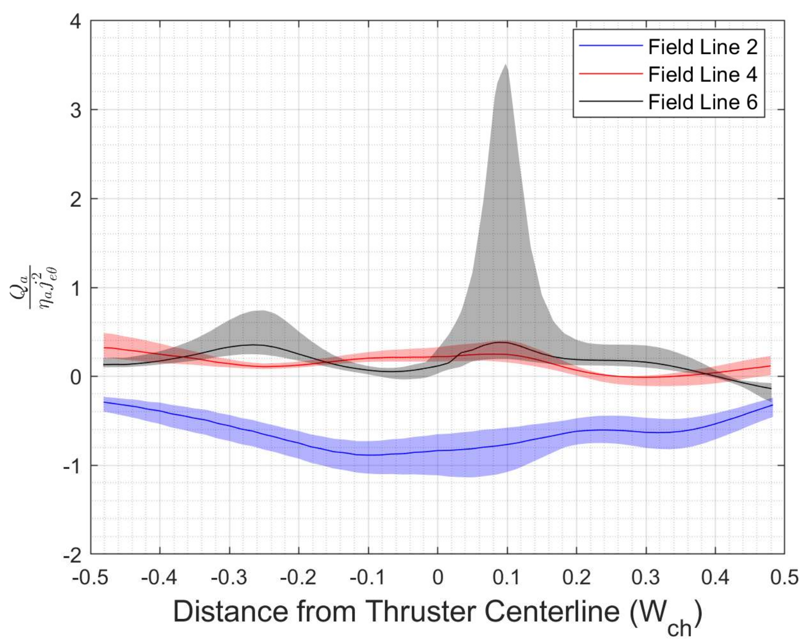

Figure C-30: Radial variation of $\frac{Q_a}{\eta_a j_{e\theta}^2}$ for heat flux model $\vec{q}_e^{\,4}$ along magnetic field lines 2, 4, and 6. Radial coordinate is normalized by the channel width.

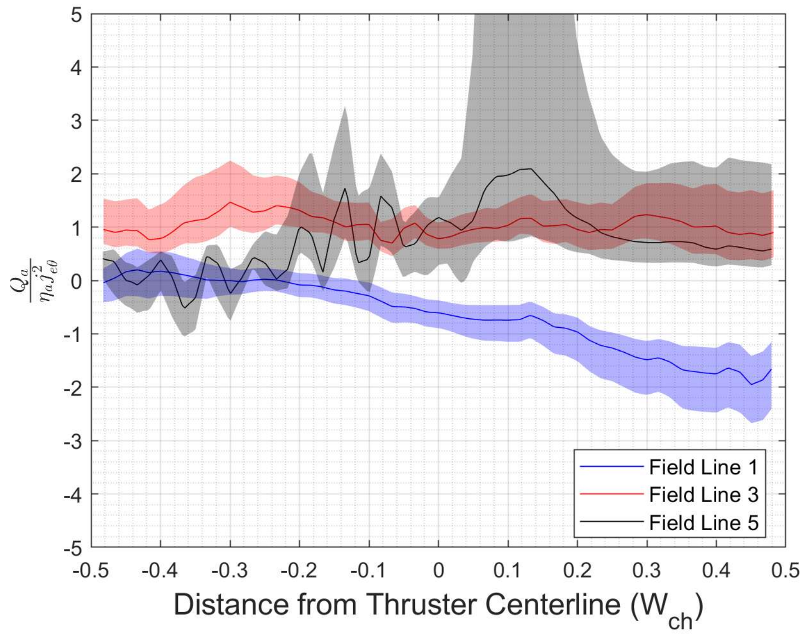

Figure C-31: Radial variation of $\frac{Q_a}{\eta_a j_{e\theta}^2}$ for heat flux model $\vec{q}_e^{\,5}$ along magnetic field lines 1, 3, and 5. Radial coordinate is normalized by the channel width.

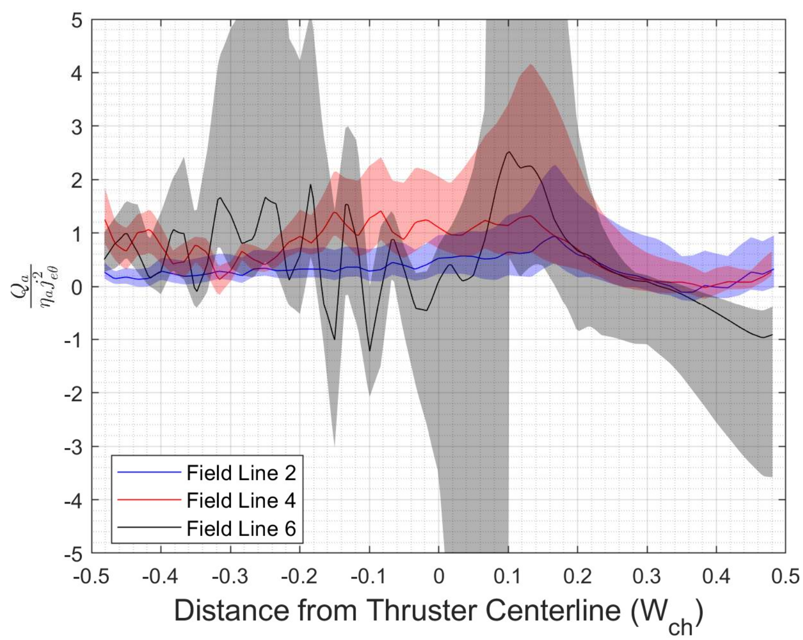

Figure C-32: Radial variation of $\frac{Q_a}{\eta_a j_{e\theta}^2}$ for heat flux model $\vec{q}_e^{\,5}$ along magnetic field lines 2, 4, and 6. Radial coordinate is normalized by the channel width.

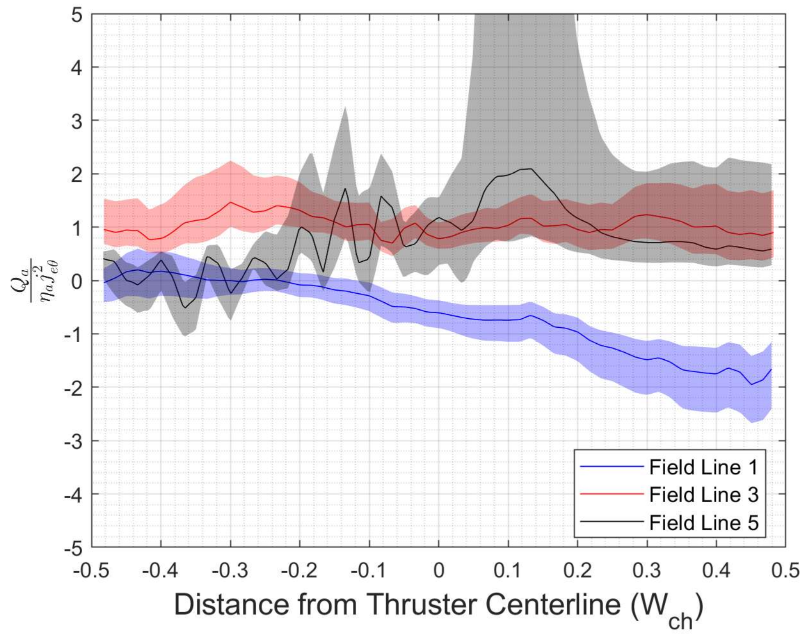

Figure C-33: 2-D map of the normalized anomalous force density. Axial coordinate is normalized by the channel length. Radial coordinate is normalized by the channel width.

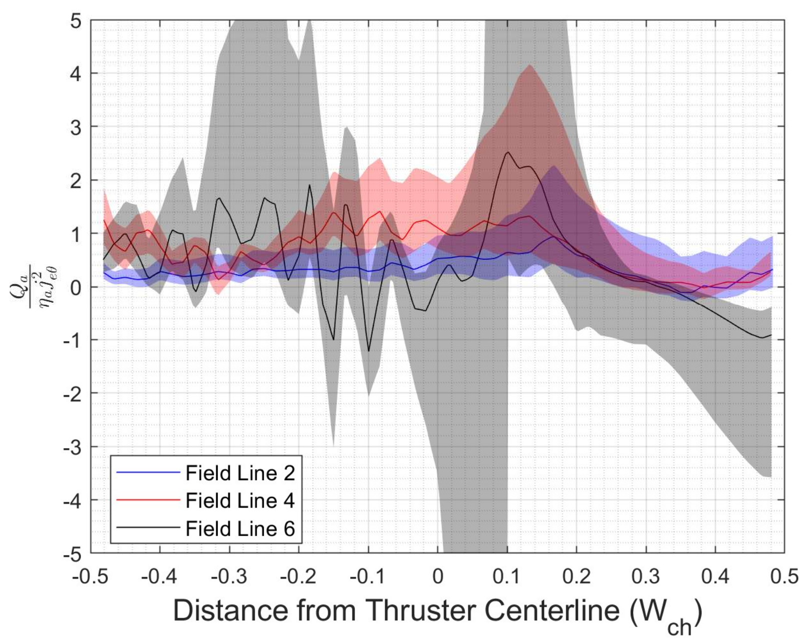

Figure C-34: 2-D map of $\frac{u_{e\theta}}{\Omega_{ea}}$. Axial coordinate is normalized by the channel length. Radial coordinate is normalized by the channel width.

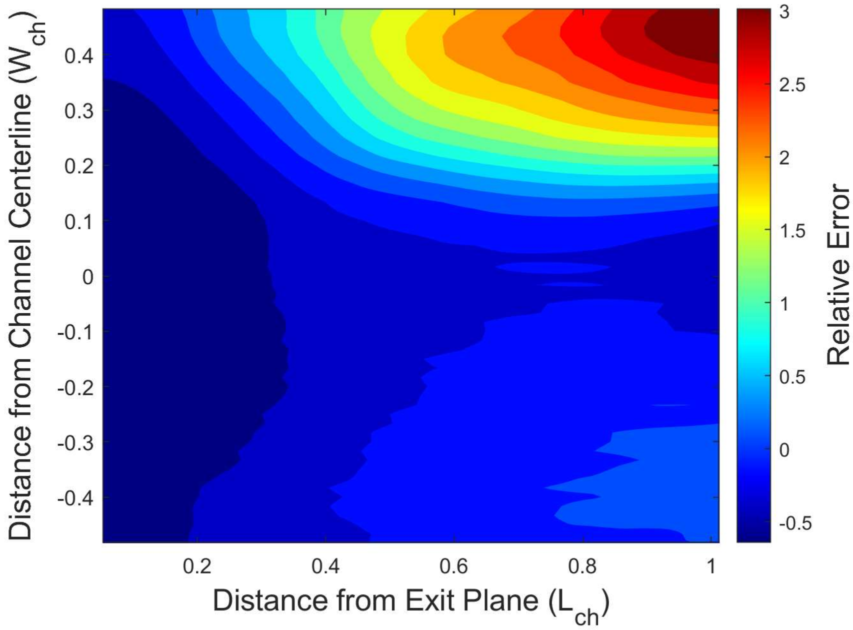

Figure C-35: 2-D map of the relative error of the MTSI closure with C_1= 0.28 and C_2 = 2.5 × 10^{-3} versus the inferred Ω_{ea}. Axial coordinate is normalized by the channel length. Radial coordinate is normalized by the channel width.

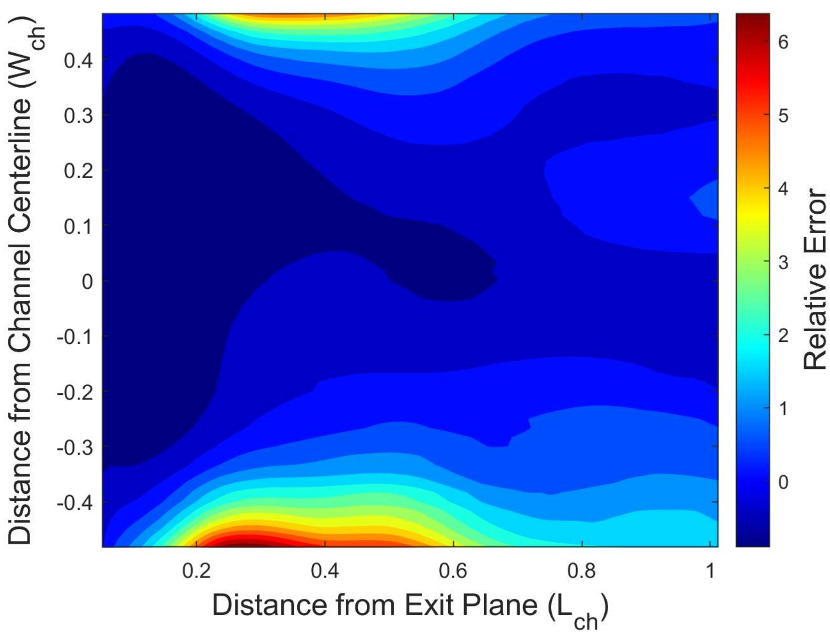

Figure C-36: 2-D map of the relative error of the ECDI closure with C_3 = 150.6, C_4 = 0.285, and C_5 = 62.4 versus the inferred Ω_{ea}. Axial coordinate is normalized by the channel length. Radial coordinate is normalized by the channel width.

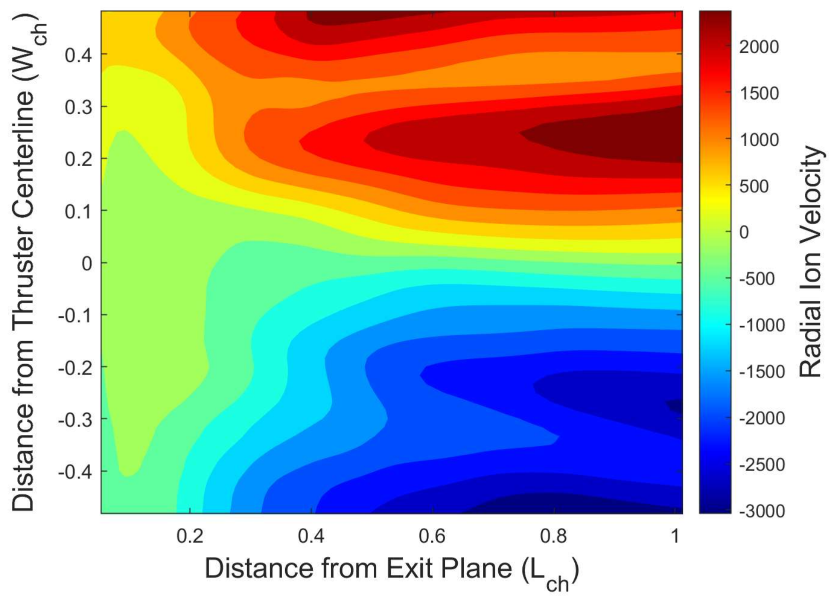

Figure C-37: 2-D map of the radial ion velocity inferred by the solver when a gaussian filter with a window of 10 grid points is used.

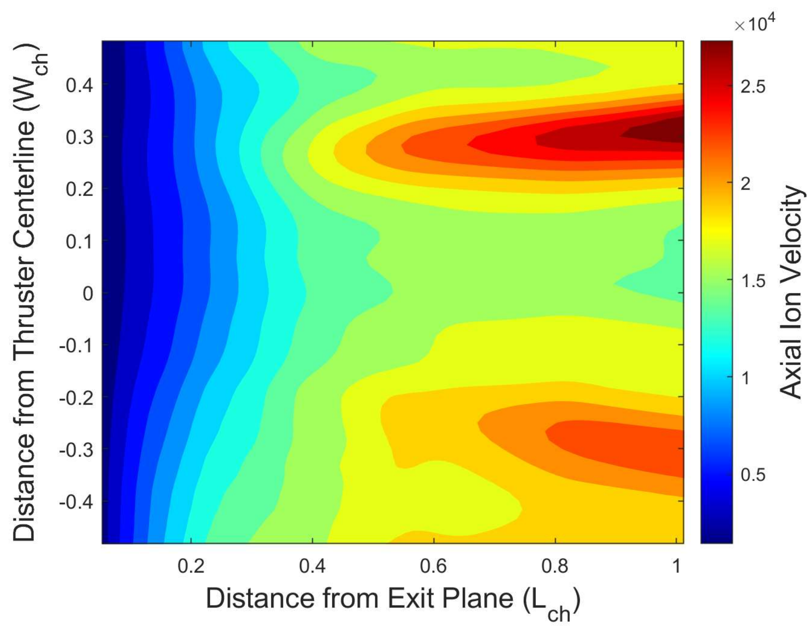

Figure C-38: 2-D map of the axial ion velocity inferred by the solver when a gaussian filter with a window of 10 grid points is used.

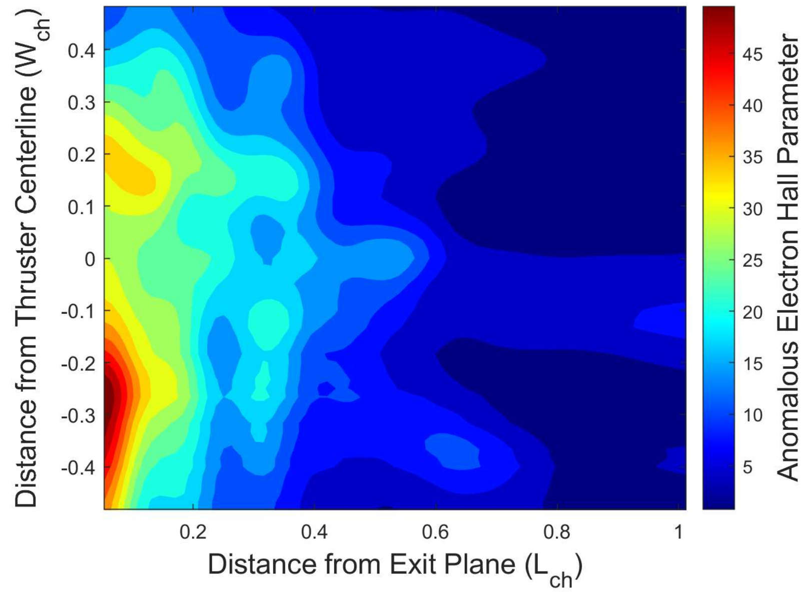

Figure C-39: 2-D map of the anomalous electron Hall parameter inferred by the solver when a gaussian filter with a window of 10 grid points is used.

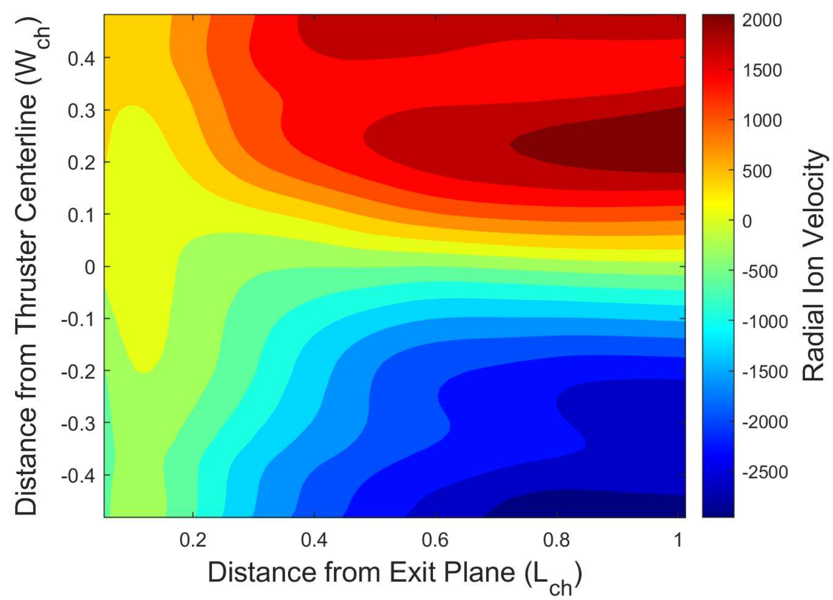

Figure C-40: 2-D map of the radial ion velocity inferred by the solver when a gaussian filter with a window of 15 grid points is used.

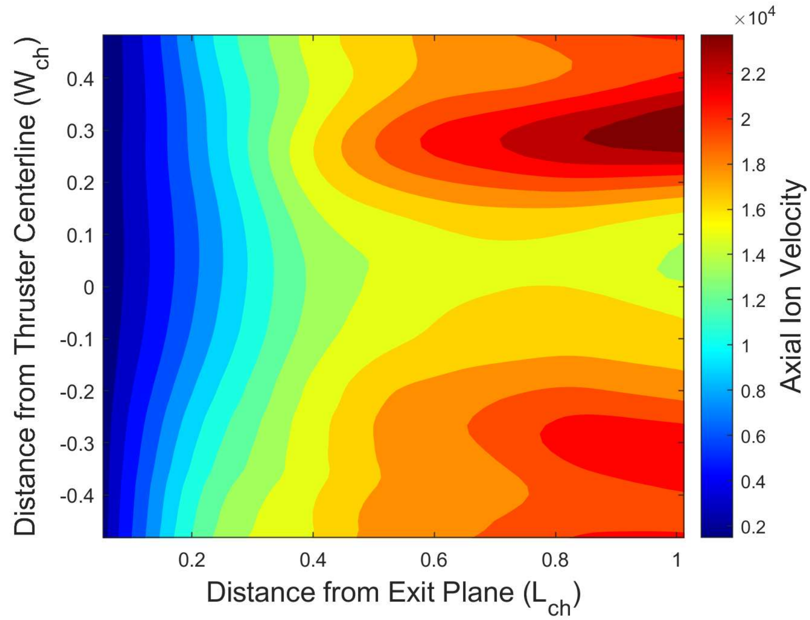

Figure C-41: 2-D map of the axial ion velocity inferred by the solver when a gaussian filter with a window of 15 grid points is used.

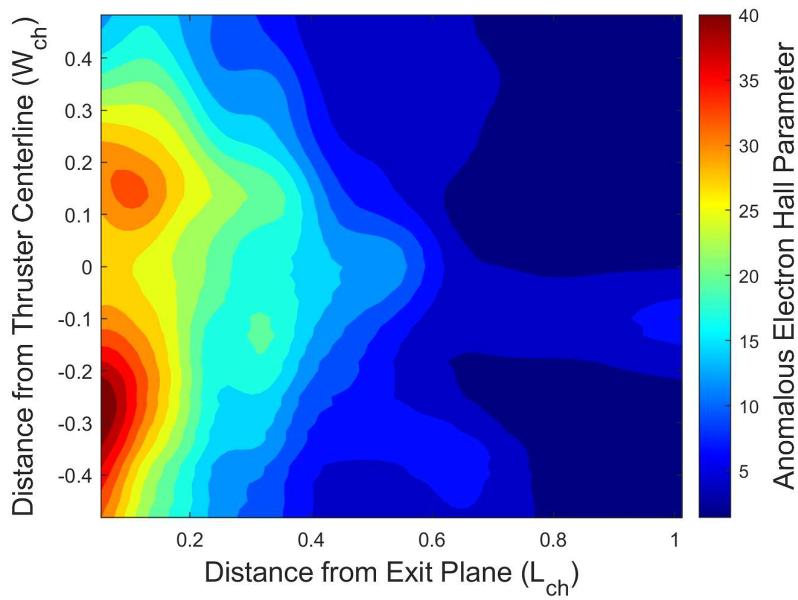

Figure C-42: 2-D map of the anomalous electron Hall parameter inferred by the solver when a gaussian filter with a window of 15 grid points is used.

APPENDIX D: Anisotropic Ionization Rate Calculation

Due to the anisotropic electron temperature, we decided to compare two different methods to calculate the ionization rate. For simplicity, and to focus on the effect of anisotropy in the electron temperature, we will assume Maxwellian EVDFs for both methods. Method 1 will only use the measured azimuthal electron temperature and assume an isotropic electron temperature. Method 2 will use both the measured azimuthal and radial electron temperatures. For Method 2, a similar approach to Eqs. 5-16 - 5-18, but where f_{3D} is instead calculated as

$$f_{3D}(v_z, v_r, v_\theta) = f_\theta^M(v_z) f_\theta^M(v_\theta) f_r^M(v_r), \tag{D-1}$$

where f_θ^M and f_r^M are the radial and azimuthal Maxwellian EVDFs calculated at the corresponding electron temperature. In Eq. D-1, we assume that the axial temperature is equal to azimuthal temperature, since the magnetic field is predominantly radial, and electron cyclotron motion tends isotropize the electron temperatures in the plane perpendicular to the magnetic field.

For both methods, we use the set of azimuthal electron temperatures shown as "Repeat" in Fig. 7-24, and for Method 2, we use the radial electron temperature measurements from Fig. 7-19. As expected, we find that Method 2 results in a higher ionization rate in regions where the radial electron temperature is higher than the azimuthal electron temperature.

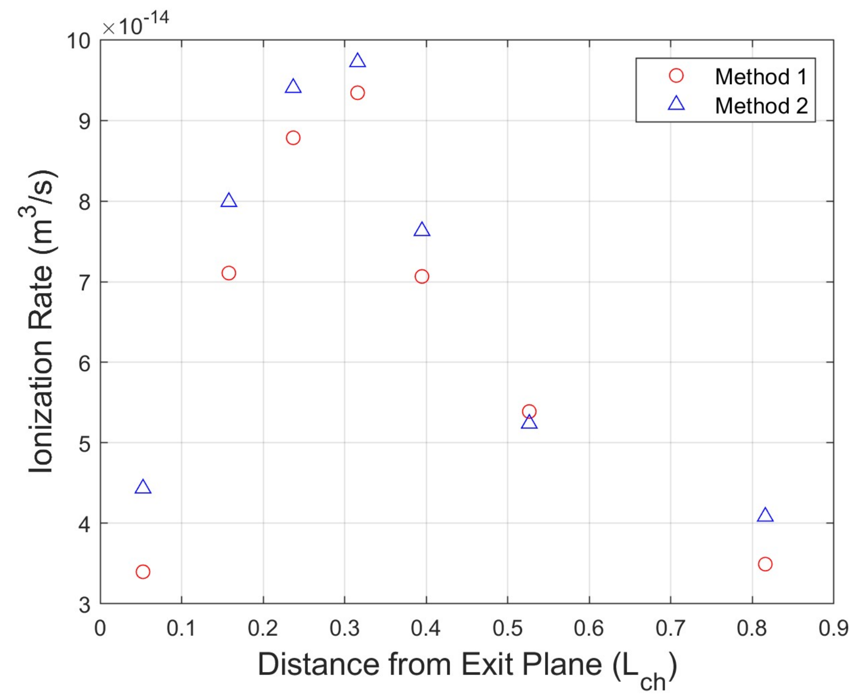

Figure D-1: Comparison of ionization rate calculations along the channel centerline. Method 1 assumes electron temperature isotropy, and method 2 accounts for electron temperature anisotropy.

REFERENCES

[1] J. E. Prussing, B. A. Conway *Orbital Mechanics* (Oxford University Press, 2012).

[2] T. N. Edelbaum, "Propulsion Requirements for Controllable Satellites," American Rocket Society Journal **31**(8), 1079-1088 (1961).

[3] D. F. Landau, J. M Longuski, "Trajectories for Human Missions to Mars, Part 2: Low-Thrust Transfers," Journal of Spacecraft and Power **43**(5), 1043-1047 (2006).

[4] H. Pernicka, D. Scarberry, S. Marsh, T. Sweetser, "A Search for Low Delta-V Earth-to-Moon Trajectories," AIAA Astrodynamics Conference, AIAA 1994-3772.

[5] A. Miele, M. Ciarcia, J. Mathwig, "Reflections on the Hohmann Transfer," Journal of Optimization Theory and Applications **123**, 233-253 (2004).

[6] J. D. Mattingly, K. M. Boyer *Elements of Propulsion: Gas Turbines and Rockets* (American Institute of Aeronautics, 2016).

[7] S. Kumar, L. Thomas, J. T. Cassibry, R. A. Frederick, "Review of Nuclear Thermal Propulsion Technology for Deep Space Missions," AIAA Joint Propulsion Conference, AIAA 2020-3915.

[8] K. A. Polzin, C. Russell Joyner, T. Kokan, A. Irvine, M. Rodriguez, M. Houts, "Enabling Deep Space Science Missions with Nuclear Thermal Propulsion," White Paper in Response to Planetary Science and Astrobiology Decadal, 2020.

[9] D. R. Jovel, M. L. R. Walker, D. Herman, "Review of High-Power Electrostatic and Electrothermal Electric Propulsion," Journal of Propulsion and Power **38**(6), 1051-1081 (2022).

[10] D. M. Goebel, I. Katz, I. G. Mikellides *Fundamentals of Electric Propulsion* (Wiley, 2023).

[11] L. L. Su, "Performance of a Magnetically Shielded Hall Thruster Operating on Krypton at High Powers," Ph.D. dissertation (University of Michigan, 2023).

[12] I. G. Mikellides, I. Katz, R. R. Hofer, D. M. Goebel, "Magnetic Shielding of a Laboratory Hall Thruster. I. Theory and Validation," Journal of Applied Physics **115**, 043303 (2014).

[13] R. R. Hofer, D. M. Goebel, I. G. Mikellides, I. Katz, "Magnetic Shielding of a Laboratory Hall Thruster. II. Experiments," Journal of Applied Physics **115**, 043304 (2014).

[14] V. H. Chaplin, B. A. Jorns, A. Lopez Ortega, I. G. Mikellides, R. W. Conversano, R. B. Lobbia, R. R. Hofer, "Laser-Induced Fluorescence Measurements of Acceleration Zone Scaling in the 12.5 kW HERMeS Hall Thruster," Journal of Applied Physics **124**, 183302 (2018).

[15] B. Vincent, S. Tsikata, S. Mazouffre, "Incoherent Thomson Scattering Measurements of Electron Properties in a Conventional and Magnetically-Shielded Hall Thruster," Plasma Sources Science and Technology **29**, 035015 (2020).

[16] L. L. Su, B. A. Jorns, "Performance at High Current Densities of a Magnetically-Shielded Hall Thruster," AIAA Joint Propulsion Conference, AIAA 2021-3405.

[17] R. R. Hofer, "Development and Characterization of High-Efficiency, High-Specific Impulse Xenon Hall Thrusters," Ph.D. dissertation (University of Michigan, 2004).

[18] I. D. Kaganovich, A. Smolyakov, Y. Raitses, E. Ahedo, I. G. Mikellides, B. Jorns, F. Taccogna, *et al*., "Physics of E × B Discharges Relevant to Plasma Propulsion and Similar Technologies," Physics of Plasmas **27**, 120601 (2020).

[19] R. J. Goldston, P. H. Rutherford, *Introduction to Plasma Physics* (CRC Press, 1995).

[20] I. G. Mikellides, I. Katz, "Numerical Simulations of Hall-Effect Plasma Accelerators on a Magnetic-Field-Aligned Mesh," Physical Review E **86**, 046703 (2012).

[21] D. Gawron, S. Mazouffre, N. Sadeghi, A. Heron, "Influence of Magnetic Field and Discharge Voltage on the Acceleration Layer Features in a Hall Effect Thruster," Plasma Sources Science and Technology **17**, 025001 (2008).

[22] B. Vincent, S. Tsikata, S. Mazouffre, C. Boniface, "Thomson Scattering Investigations of a Low-Power Hall Thruster in Standard and Magnetically-Shielded Configurations," International Electric Propulsion Conference, IEPC-2019-384.

[23] J. Polk, J. Anderson, J. Brophy, V. Rawlin, M. Patterson, J. Sovey, J. Hamley, "An Overview of the Results from an 8200 Hour Wear Test of the NSTAR Ion Thruster," AIAA Joint Propulsion Conference, AIAA 1999-2446.

[24] G. C. Soulas, H. Kamhawi, M. J. Patterson, M. A. Britton, M. M. Frandina, "NEXT Ion Engine 2000 Hour Wear Test Results," AIAA Joint Propulsion Conference, AIAA 2004-3791.

[25] J. D. Frieman, H. Kamhawi, J. Mackey, T. Haag, P. Y. Peterson, D. Herman, *et al*. "Completion of the Long Duration Wear Test of the NASA HERMeS Hall Thruster," AIAA Joint Propulsion Conference, AIAA 2019-3895.

[26] J. R. Brophy, J. E. Polk, T. M. Randolph, J. W. Dankanich, "Lifetime Qualification of Electric Thrusters for Deep-Space Missions," AIAA Joint Propulsion Conference, AIAA 2008-5184.

[27] J. J. Szabo, B. Pote, R. Tedrake, S. Paintal, L. Byrne, V. J. Hruby, *et al*., "High Throughput 600 Watt Hall Effect Thruster for Space Exploration," AIAA Joint Propulsion Conference, AIAA 2016-4830.

[28] F. Salz, R. Meyerand, E. Lary, "Ion Acceleration in a Gyro-Dominated Neutral Plasma – Experiment," Bulletin of the American Physical Society, Series II, **7**(7), 441 (1962).

[29] G. S. Janes, T. Wilson, "Electrostatic Acceleration of Neutral Plasmas -Momentum Transfer through Magnetic Fields" Third Symposium on Advanced Propulsion Concepts (1962).

[30] N. B. Meezan, W. A. Hargus, Jr., M. A. Cappelli, "Anomalous Electron Mobility in a Coaxial Hall Discharge Plasma," Physical Review E **63**, 026410 (2001).

[31] J. A. Linnell, A. D. Gallimore, "Hall Thruster Electron Motion Characterization Based on Internal Probe Measurements," International Electric Propulsion Conference, IEPC-2009-105.

[32] L. Grimaud, A. Petin, J. Vaudolon, S. Mazouffre, "Perturbations Induced by Electrostatic Probe in the Discharge of Hall Thrusters," Review of Scientific Instruments 87, 043506 (2016).

[33] B. A. Jorns, D. M. Goebel, R. R. Hofer, "Plasma Perturbations in High-Speed Probing of Hall Thruster Discharge Chambers: Quantification and Mitigation," AIAA Joint Propulsion Conference, AIAA 2015-4006.

[34] R. B. Lobbia, B. E. Beal, "Recommended Practice for Use of Langmuir Probes in Electric Propulsion Testing," Journal of Propulsion and Power **33**(3), 566-581 (2017).

[35] J. P. Sheehan, Y. Raitses, N. Hershkowitz, M. McDonald, "Recommended Practice for Use of Emissive Probes in Electric Propulsion Testing," Journal of Propulsion and Power **33**(3), 614-637 (2017).

[36] P. J. Ryan, J. W. Bradley, M. D. Bowden, "Comparison of Langmuir Probe and Laser Thomson Scattering for Electron Property Measurements in Magnetron Discharges," Physics of Plasmas **26**, 073515 (2019).

[37] J. M. Haas, A. D. Gallimore, K. McFall, G. Spanjers, "Development of a High-Speed, Reciprocating Electrostatic Probe System for Hall Thruster Interrogation," Review of Scientific Instruments **71**, 4131-4138 (2000).

[38] K. Dannenmayer, S. Mazouffre, "Compact High-Speed Reciprocating Probe System for Measurements in a Hall Thruster Discharge and Plume," Review of Scientific Instruments **83**, 123503 (2012).

[39] E. T. Dale, B. A. Jorns, "Non-Invasive Time-Resolved Measurements of Anomalous Collision Frequency in a Hall Thruster," Physics of Plasmas **26**, 013516 (2019).

[40] P. J. Roberts, B. A. Jorns, "Laser Measurement of Anomalous Electron Diffusion in a Crossed-Field Plasma," Physical Review Letters **132**, 135301 (2024).

[41] I. G. Mikellides, A. Lopez Ortega, "Challenges in the Development and Verification of First-Principles Models in Hall-Effect Thruster Simulations that are Based on Anomalous Resistivity and Generalized Ohm's Law," Plasma Sources Science and Technology **28**, 014003 (2019).

[42] L. Garrigues, J. Perez-Luna, J. Lo, G. J. M. Hagelaar, J. P. Boeuf, S. Mazouffre, "Empirical Electron Cross-Field Mobility in a Hall Effect Thruster," Applied Physics Letters 95, 141501 (2009).

[43] I. G. Mikellides, A. Lopez Ortega, I. Katz, B. A. Jorns, "Hall2De Simulations with a First-Principles Electron Transport Model Based on the Electron Cyclotron Drift Instability," 52nd AIAA/SAE/ASEE Joint Propulsion Conference, 4618, 2016.

[44] I. Katz, I. G. Mikellides, B. A. Jorns, A. Lopez Ortega, "Hall2De Simulations with an Anomalous Transport Model Based on the Electron Cyclotron Drift Instability," International Electric Propulsion Conference, IEPC-2015-402.

[45] B. A. Jorns, "Two Equation Closure Model for Plasma Turbulence in a Hall Effect Thruster," International Electric Propulsion Conference, IEPC-2019-129.

[46] B. Jorns, "Predictive, Data-Driven Model for the Anomalous Electron Collision Frequency in a Hall Effect Thruster," Plasma Sources Science and Technology **27**, 104007 (2018).

[47] A. Lopez Ortega, I. Katz, V. H. Chaplin, "Application of a First-Principles Anomalous Transport Model for Electrons to Multiple Hall Thrusters and Operating Conditions," AIAA Joint Propulsion Conference, AIAA 2018-4903.

[48] T. A. Marks, B. A. Jorns, "Challenges with the Self-Consistent Implementation of Closure Models for Anomalous Electron Transport in Fluid Simulations of Hall Thrusters," Plasma Sources Science and Technology **32**, 045016 (2023).

[49] I. G. Mikellides, A. Lopez Ortega, V. H. Chaplin, "Theory of the Anomalous Momentum Exchange from Wave-Particle Interactions in Hall-Effect Ion Accelerators and Comparisons with Measurements," Physics of Fluids **36**, 074121 (2024).

[50] A. Lopez Ortega, I. G. Mikellides, "Erosion Mechanisms at the Outer Front Pole Cover of a Magnetically Shielded Hall Thruster," International Electric Propulsion Conference, IEPC-2024-264.

[51] A. Lopez Ortega, I. G. Mikellides, M. J. Sekerak, B. A. Jorns, “Plasma Simulations in 2-D (r-z) Geometry for the Assessment of Pole Erosion in a Magnetically Shielded Hall Thruster,” Journal of Applied Physics **125**, 033302 (2019).

[52] A. Lopez Ortega, I. G. Mikellides, “Investigations of Pole Erosion Mechanisms in the 12.5 kW HERMeS Hall Thruster Using Numerical Simulations and Ion Velocity Measurements,” AIAA Joint Propulsion Conference, AIAA 2018-4647.

[53] I. G. Mikellides, A. Lopez Ortega, “Growth of the Modified Two-Stream Instability in the Plume of a Magnetically Shielded Hall Thruster,” Physics of Plasmas **27**, 100701 (2020).

[54] I. G. Mikellides, A. Lopez Ortega, “Growth of the Lower Hybrid Drift Instability in the Plume of a Magnetically Shielded Hall Thruster,” Journal of Applied Physics **129**, 193301 (2021).

[55] A. Lopez Ortega, I. G. Mikellides, V. H. Chaplin, W. Huang, J. D. Frieman, “Anomalous Ion Heating and Pole Erosion in the 12.5-kW Hall Effect Rocket with Magnetic Shielding (HERMeS),” AIAA Joint Propulsion Conference, AIAA 2020-3620.

[56] F. F. Chen *Introduction to Plasma Physics and Controlled Fusion* (Springer, 2015).

[57] R. Z. Sagdeev, “Cooperative Phenomena and Shock Waves in Collisionless Plasmas,” in *Reviews of Plasma Physics* **4**, edited by M. A. Leontovich (Consultants Bureau, 1966), pages 23-91.

[58] C. F. Chew, M. L. Goldberger, F. E. Low, “The Boltzmann Equation and the One-Fluid Hydromagnetic Equations in the Absence of Particle Collisions,” Proceedings of the Royal Society A **236**(1204), 112-118 (1956).

[59] R. Balescu *Transport Processes in Plasmas. Classical Transport Theory* (Elsevier, 1988), pages 163-209.

[60] A. Alvarez Laguna, B. Esteves, A. Bourdon, P. Chabert, "A Regularized High-Order Moment Model to Capture Non-Maxwellian Electron Energy Distribution Function Effects in Partially Ionized Plasmas," Physics of Plasmas **29**, 083507 (2022).

[61] A. Alvarez Laguna, K. Hara, "High-Order Moment Closure for Nonmagnetized Electrons in Partially Ionized Plasmas," Physical Review E **113**, 025207 (2026).

[62] J.-P. Boeuf, A. Smolyakov, "Physics and Instabilities of Low-Temperature E × B Plasmas for Spacecraft Propulsion and Other Applications," Physics of Plasmas **30**, 050901 (2023).

[63] M. J. Sekerak, B. W. Longmier, A. D. Gallimore, D. L. Brown, R. R. Hofer, J. E. Polk, "Azimuthal Spoke Propagation in Hall Effect Thruster," IEEE Transactions on Plasma Science **45**(1), 72-85 (2015).

[64] K. Hara, S. Tsikata, "Cross-Field Electron Diffusion due to the Coupling of Drift-Driven Microinstabilities," Physical Review E **102**, 023202 (2020).

[65] S. Tsikata, N. Lemoine, V. Pisarev, D. M. Gresillon, "Dispersion Relations of Electron Density Fluctuations in a Hall Thruster Plasma, Observed by Collective Light Scattering," Physics of Plasma **16**, 033506 (2009).

[66] S. Tsikata, C. Honore, N. Lemoine, D. M. Gresillon, "Three-Dimensional Structure of Electron Density Fluctuations in the Hall Thruster Plasma: E × B Mode," Physics of Plasmas **17**, 112110 (2010).

[67] J. Cavalier, N. Lemoine, G. Bonhomme, S. Tsikata, C. Honore, D. Gresillon, "Hall Thruster Plasma Fluctuations Identified as the E × B Electron Drift Instability: Modeling and Fitting on Experimental Data," Physics of Plasmas **20**, 082107 (2013).

[68] Z. A. Brown, B. A. Jorns, "Spatial Evolution of Small Wavelength Fluctuations in a Hall Thruster," Physics of Plasmas **26**, 113504 (2019).

[69] J. C. Adam, A. Heron, G. Laval, "Study of Stationary Plasma Thrusters Using Two-Dimensional Fully Kinetic Simulations," Physics of Plasmas **11**, 295-305 (2004).

[70] A. Ducroq, J. C. Adam, A. Heron, G. Laval, "High-Frequency Electron Drift Instability in the Cross-Field Configuration of Hall Thrusters," Physics of Plasmas **13**, 102111 (2006).

[71] A. Heron, J. C. Adam, "Anomalous Conductivity in Hall Thrusters: Effects of the Non-Linear Coupling of the Electron-Cyclotron Drift Instability with Secondary Electron Emission of the Walls," Physics of Plasmas **20**, 082313 (2013).

[72] A. Tavant, V. Croes, R. Lucken, T. Lafleur, A. Bourdon, P. Chabert, "The Effects of Secondary Electron Emission on Plasma Sheath Characteristics and Electron Transport in an E × B Discharge via Kinetic Simulations," Plasma Sources Science and Technology **27**, 124001 (2018).

[73] T. Lafleur, S. D. Baalrud, P. Chabert, "Theory for the Anomalous Electron Transport in Hall Effect Thrusters. I. Insights from Particle-in-Cell Simulations," Physics of Plasmas **23**, 053502 (2016).

[74] T. Lafleur, S. D. Baalrud, P. Chabert, "Theory for the Anomalous Electron Transport in Hall Effect Thrusters. II. Kinetic Model," Physics of Plasmas **23**, 053503 (2016).

[75] T. Lafluer, R. Martorelli, P. Chabert, A. Bourdon, "Anomalous Electron Transport in Hall-Effect Thrusters: Comparison Between Quasi-Linear Kinetic Theory and Particle-in-Cell Simulations," Physics of Plasmas **25**, 061202 (2018).

[76] T. Lafluer, P. Chabert, "The Role of Instability-Enhanced Friction on 'Anomalous' Electron and Ion Transport in Hall-Effect Thrusters," Plasma Sources Science and Technology **27**, 015003 (2017).

[77] T. Charoy, T. Lafleur, A. Tavant, P. Chabert, A. Bourdon, "A Comparison Between Kinetic Theory and Particle-in-Cell Simulations of Anomalous Electron Transport in E × B Plasma Discharges," Physics of Plasmas **27**, 063510 (2020).

[78] T. Charoy, T. Lafleur, A. Alvarez Laguna, A. Bourdon, P. Chabert, "The Interaction Between Ion Transit-Time and Electron Drift Instabilities and their Effect on Anomalous Electron Transport in Hall Thrusters," Plasma Sources Science and Technology **30**, 065017 (2021).

[79] S. Janhunen, A. Smolyakov, O. Chapurin, D. Sydorenko, I. Kaganovich, Y. Raitses, "Nonlinear Structures and Anomalous Transport in Partially Magnetized E × B Plasma," Physics of Plasmas **25**, 011608 (2018).

[80] S. Janhunen, A. Smolyakov, D. Sydorenko, M. Jimenez, I. Kaganovich, Y. Raitses, "Evolution of the Electron Cyclotron Drift Instability in Two-Dimensions," Physics of Plasmas **25**, 082308 (2018).

[81] A. Tavassoli, A. Smolyakov, M. Shoucri, R. J. Spiteri, "Nonlinear Regimes of the Electron Cyclotron Drift Instability in Vlasov Simulations," Physics of Plasmas **29**, 030701 (2022).

[82] A. Smolyakov, T. Zintel, L. Couedel, D. Sydorenko, A. Umnov, E. Sorokina, N. Marusov, "Anomalous Electron Transport in One-Dimensional Electron Cyclotron Drift Turbulence," Plasma Physics Reports **46**, 496-505 (2020).

[83] F. Taccogna, P. Minelli, Z. Asadi, G. Bogopolsky, "Numerical Studies of the ExB Electron Drift Instability in Hall Thrusters," Plasma Sources Science and Technology **28**, 064002 (2019).

[84] F. Taccogna, P. Minelli, "Three-Dimensional Particle-in-Cell Model of Hall Thruster: The Discharge Channel," Physics of Plasmas **25**, 061208 (2018).

[85] Z. Asadi, F. Taccogna, M. Sharifian, "Numerical Study of Electron Cyclotron Drift Instability: Application to Hall Thruster," Frontiers of Physics **7**, 140 (2019).

[86] G. S. Janes, R. S. Lowder, "Anomalous Electron Diffusion and Ion Acceleration in a Low-Density Plasma," Physics of Fluids **9**, 1115-1123 (1966).

[87] T. Marks, "Modeling Anomalous Electron Transport in a Fluid Hall Thruster Code," Ph.D. dissertation (University of Michigan, 2023).

[88] S. Barral, K. Makowski, Z. Peradzynski, N. Gascon, M. Dudeck, "Wall Material Effects in Stationary Plasma Thrusters. II. Near-Wall and in-Wall Conductivity," Physics of Plasmas **10**, 4137-4152 (2003).

[89] E. Ahedo, J. M. Gallardo, M. Martinez-Sanchez, "Effects of the Radial Plasma-Wall Interaction on the Hall Thruster Discharge," Physics of Plasmas **10**, 3397-3409 (2003).

[90] R. Hofer, I. Katz, D. Goebel, K. Jameson, R. Sullivan, L. Johnson, I. Mikellides, "Efficacy of Electron Mobility Models in Hybrid-PIC Hall Thruster Simulations," AIAA Joint Propulsion Conference, AIAA 2008-4924.

[91] A. I. Morozov, V. V. Savel'ev, "Theory of the Near-Wall Conductivty," Plasma Physics Reports **27**, 570-575 (2001).

[92] D. Sydorenko, A. Smolyakov, I. Kaganovich, Y. Raitses, "Kinetic Simulation of Secondary Electron Emission Effects in Hall Thrusters," Physics of Plasmas **13**, 014501 (2006).

[93] I. D. Kaganovich, Y. Raitses, D. Sydorenko, A. Smolyakov, "Kinetic Effects in a Hall Thruster Discharge," Physics of Plasmas **14**, 057104 (2007).

[94] N. Gascon, M. Dudeck, S. Barral, "Wall Material Effects in Stationary Plasma Thrusters. I. Parametric Studies of an SPT-100," Physics of Plasmas **10**, 4123-4136 (2003).

[95] D. M. Goebel, R. R. Hofer, I. G. Mikellides, I. Katz, J. E. Polk, B. N. Dotson, "Conducting Wall Hall Thrusters," IEEE Transactions on Plasma Science **43**(1), 118-126 (2015)

[96] L. Grimaud, S. Mazouffre, "Conducting Wall Hall Thrusters in Magnetic Shielding and Standard Configurations," Journal of Applied Physics **122**, 033305 (2017).

[97] C. A. Thomas, "Anomalous Electron Transport in the Hall-Effect Thruster," Ph.D. dissertation (Stanford University, 2007).

[98] P. W. Terry, "Suppression of Turbulence and Transport by Sheared Flow," Review of Modern Physics **72**, 109 (2000).

[99] M. K. Scharfe, C. A. Thomas, D. B. Scharfe, N. Gascon, M. A. Cappelli, E. Fernandez, "Shear-Based Model for Electron Transport in Hybrid Hall Thruster Simulations," IEEE Transactions on Plasma Science **36**(5), 2058-2068 (2008).

[100] D. Bohm, in *The Characteristics of Electrical Discharges in Magnetic Fields*, edited by A. Guthrie, R. K. Wakerling (McGraw-Hill, 1949), Chap. 2, p. 65.

[101] L. Spitzer Jr., "Particle Diffusion Across a Magnetic Field," Physics of Fluids **3**, 659-661 (1960).

[102] J. Perales-Diaz, A. Dominguez-Vazquez, P. Fajardo, E. Ahedo, F. Faraji, M. Reza, T. Andreussi, "Hybrid Plasma Simulations of a Magnetically Shielded Hall Thruster," Journal of Applied Physics **131**, 103302 (2022).

[103] D. L. Brown, C. W. Larson, B. E. Beal, A. D. Gallimore, "Methodology and Historical Perspective of a Hall Thruster Efficiency Analysis," Journal of Propulsion and Power **25**(6), 1163-1177 (2009).

[104] R. H. Comfort, "The Magnetic Mirror Force in Plasma Fluid Models," in *Geophysical Monograph Series* 44, edited by T.E. Moore, J. H. Moorehead, W. B. Hanson (American Geophysical Union, 1988), pages 51-53.

[105] A. Dominguez-Vazquez, F. Taccogna, E. Ahedo, "Particle Modeling of Radial Electron Dynamics in a Controlled Discharge of a Hall Thruster," Plasma Source Science and Technology **27**, 064006 (2018).

[106] M. Keidar, I. D. Boyd, "On the Magnetic Mirror Effect in Hall Thrusters," Applied Physics Letters **87**, 121501 (2005).

[107] G. Cuerva-Lazaro, A. Marin-Cebrian, M. P. Encinar, E Ahedo, "Characterizing the Anomalous Transport in E×B Plasmas via GPU-Accelerated PIC Simulations," International Electric Propulsion Conference, IEPC-2025-362.

[108] G. Guest *Electron Cyclotron Heating of Plasmas* (Wiley, 2009).

[109] B. T. Tsurutani, G. S. Lakhina, "Some Basic Concepts of Wave-Particle Interactions in Collisionless Plasmas," Reviews of Geophysics **35**(4), 491-502 (1997).

[110] D. Biskamp, R. Chodura, "On the Non-Linear Electron-Cyclotron Drift Instability," Nuclear Fusion **12**, 485 (1972).

[111] D. Forslund, R. Morse, C. Nielson, J. Fu, "Electron Cyclotron Drift Instability and Turbulence," Physics of Fluids **15**, 1303-1318 (1972).

[112] R. Chodura, F. Pohl, "Hydrodynamic Equations for Anisotropic Plasmas in a Magnetic Field. II. Transport Equations Including Collisions," Plasma Physics **13**, 645 (1971).

[113] J. J. Ramos, "Fluid Formalism for Collisionless Magnetized Plasmas," Physics of Plasmas **12**, 052102 (2005).

[114] A. Dominguez-Vazquez, "Axisymmetric Simulation Codes for Hall Effect Thrusters and Plasma Plumes," Ph.D. dissertation (Universidad Carlos III de Madrid, 2019).

[115] A. I. Morozov, S. V. Lebedev, "Plasma Optics," in *Reviews of Plasma Physics* **8**, edited by M. A. Leontovich (Springer, 1980), pages 301-460.

[116] W. Villafana, B. Cuenot, O. Vermorel, "3D Particle-In-Cell Study of the Electron Drift Instability in a Hall Thruster Using Unstructured Grids," Physics of Plasmas **30**, 033503 (2023).

[117] A. Marin-Cebrian, E. Bello-Benitez, A. Dominguez-Vazquez, E. Ahedo, "Non-Maxwellian Electron Effects on the Macroscopic Response of a Hall Thruster Discharge from an Axial-Radial Kinetic Model," Plasma Sources Science and Technology **33**, 025008 (2024).

[118] J. L. Suazo Betancourt, N. Butler-Craig, J. Lopez-Uricoechea, A. M. Steinberg, M. L. R. Walker, “Laser Thomson Scattering Measurements Indicate Non-Isothermal Magnetic Field Lines in Magnetically Shielded Hall Effect Thrusters,” Physics of Plasmas **31**, 113106 (2024).

[119] P. J. Roberts, M. G. Allen, D. C. Brick, B. A. Jorns, “Empirical Closures for Momentum and Energy Transport in Hall Thrusters based on Thomson Scattering Measurements,” International Electric Propulsion Conference, IEPC-2024-393.

[120] M. Reza, F. Faraji, A. Knoll, “Influence of the Magnetic Field Curvature on the Radial-Azimuthal Dynamics of a Hall Thruster Plasma Discharge with Different Propellants,” Journal of Applied Physics **134**, 233303 (2023).

[121] S. Hamasaki, N. A. Krall, “Relaxation of Anisotropic Collisionless Plasma,” Physics of Fluids **16**, 145-149 (1973).

[122] G. F. Karabadzhak, Y.-H Chiu, R. A. Dressler, “Passive Optical Diagnostic of Xe Propelled Hall Thrusters. II. Collisional-Radiative Model,” Journal of Applied Physics **99**, 113305 (2006).

[123] J. Kim, D. Lee, G. Doh, S. Park, H. Kim, W. Choe, “Three-Dimensional Tomographically Reconstructed Optical Emission Profiles of Hall Thruster Plasmas,” Plasma Sources Science and Technology **31**, 015013 (2022).

[124] D. Lee, J. Kim, G. Doh, C. Shin, W. Choe, “Two-Dimensional Electron Temperature and Density Profiles of Hall Thruster Plume Plasmas Using Tomographically Reconstructed Optical Emission Spectroscopy,” Plasma Sources Science and Technology **31**, 125004 (2022).

[125] S. Mazouffre, “Laser-Induced Fluorescence Diagnostics of the Cross-Field Discharge of Hall Thrusters,” Plasma Sources Science and Technology **22**, 013001 (2013).

[126] M. A. Cappelli, N. Gascon, W. A. Hargus Jr., “Millimetre Wave Plasma Interferometry in the Near Field of a Hall Plasma Accelerator,” Journal of Physics D: Applied Physics **39**, 4582 (2006).

[127] B. Vincent, “Incoherent Thomson Scattering Investigations in Hall Thruster, Planar Magnetron and ECR Ion Source Plasmas,” Ph.D. dissertation (Université D’Orléans, 2019).

[128] M. Mitchner, C. H. Kruger *Partially Ionized Gases* (Wiley, 1973).

[129] W. Huang, “Study of Hall Thruster Discharge Channel Wall Erosion via Optical Diagnostics,” Ph.D. dissertation (University of Michigan, 2011).

[130] J. Sheffield, D. Froula, S. H. Glenzer, N. C. Luhmann, Jr. *Plasma Scattering of Electromagnetic Radiation: Theory and Measurement Techniques*, (Elsevier Science, 2018).

[131] T. Dubois, S. Tsikata, M. Chung To Sang, L. Garrigues, “Insights into Hall Thruster Radial Physics via Incoherent Thomson Scattering,” International Electric Propulsion Conference, IEPC-2022-331.

[132] J. L. Suazo Betancourt, “Laser Thomson Scattering Measurements of the Plasma Structure in the Front Pole Region of a Magnetically-Shielded Hall Effect Thruster,” Ph.D. dissertation (Georgia Institute of Technology, 2024).

[133] I. G. Mikellides, A. Lopez Ortega, B. Jorns, “Assessment of Pole Erosion in a Magnetically Shielded Hall Thruster,” AIAA Joint Propulsion Conference, AIAA 2014-3897.

[134] A. Lopez Ortega, I. G. Mikellides, I. Katz, “Hall2De Numerical Simulations for the Assessment of Pole Erosion in a Magnetically Shielded Hall Thruster,” International Electric Propulsion Conference, IEPC-2015-249.

[135] B. Jorns, C. A. Dodson, J. R. Anderson, D. M. Goebel, R. R. Hofer, M. J. Sekerak, *et al*. "Mechanisms for Pole Piece Erosion in a 6-kW Magnetically-Shielded Hall Thruster," AIAA Joint Propulsion Conference, AIAA 2016-4839.

[136] R. Rejoub, B. G. Lindsay, R. F. Stebbings, "Determination of the Absolute Partial and Total Cross Sections for Electron-Impact Ionization of the Rare Gases," Physical Review A **65**, 042713 (2002).

[137] R. R. Hofer, "The H9 Magnetically Shielded Hall Thruster," International Electric Propulsion Conference, IEPC-2017-232.

[138] J. L. Suazo Betancourt, J. Lopez-Uricoechea, N. Butler-Craig, A. Steinberg, M. L. R. Walker, "An Incoherent Thomson Scattering System for Plasma Boundary Studies," Review of Scientific Instruments **95**, 043001 (2024).

[139] M. J. van de Sande, J. J. A. M. van der Mullen, "Thomson Scattering on a Low-Pressure, Inductively-Coupled Gas Discharge Lamp," Journal of Physics D: Applied Physics **35**, 1381 (2002).

[140] J. Bak, J. L. Suazo Betancourt, A. Rekhy, A. Abbasszadehrad, R. B. Miles, C. M. Limbach, M. L. R. Walker, "High-Resolution Spatially Extended 1D Laser Scattering Diagnostics using Volume Bragg Grating Notch Filters," Review of Scientific Instruments **94**, 023003 (2023).

[141] J. Lopez-Uricoechea, J. L. Suazo Betancourt, N. Butler-Craig, M. L. R. Walker, "Spatially-Resolved Thomson Scattering Measurements of Electron Properties Across the Acceleration Region of a High-Power Magnetically Shielded Hall Effect Thruster," Journal of Applied Physics **136**, 113303 (2024).

[142] J. Lopez-Uricoechea, M. L. R. Walker, "Statistical Infernce of Higher-Order Moments of Electron Velocity Distribution Functions from Incoherent Thomson Scattering Spectra," Physics of Plasmas **32**, 103502 (2025).

[143] V. Kolobov, V. Godyak, "Electron Kinetics in Low-Temperature Plasmas," Physics of Plasmas **26**, 060601 (2019).

[144] G. J. M. Hagelaar, L. C. Pitchford, "Solving the Boltzmann Equation to Obtain Transport Coefficients and Rate Coefficients for Fluid Models," Plasma Sources Science and Technology **14**, 722 (2005).

[145] A. M. Castillo and K. Hara, "Loss Cone Effects and Monotonic Sheath Conditions of a Partially Magnetized Plasma Sheath," Physics of Plasmas **31**, 030701 (2024).

[146] S. R. Cranmer, A. J. Schiff, "Electron Heat Flux in the Solar Wind: Generalized Approaches to Fluid Transport with a Variety of Skewed Velocity Distributions," Journal of Geophysical Research: Space Physics **126**, e2021JA029666 (2021).

[147] E. Ahedo, S. Correyero, J. Navarro-Cavalle, M. Merino, "Macroscopic and Parametric Study of Kinetic Plasma Expansion in a Paraxial Magnetic Nozzle," Plasma Sources Science and Technology **29**, 045017 (2020).

[148] D. A. Kuldinow, Y. Yamashita, K. Hara, "Ten-Moment Fluid Model for Low-Temperature Magnetized Plasmas," Physics of Plasmas **31**, 123506 (2024).

[149] L. L. Alves, A. Bogaerts, V. Guerra, M. M. Turner, "Foundations of Modeling of Nonequilibrium Low-Temperature Plasmas," Plasma Sources Science and Technology **27**, 023002 (2018).

[150] V. A. Godyak, R. B. Piejak, B. M. Alexandrovich, "Measurement of Electron Energy Distribution in Low-Pressure RF Discharges," Plasma Sources Science and Technology **1**, 36 (1992).

[151] T. K. Popov, M. Dimitrova, P. Ivanova, J. Kovacic, T. Gyergyek, R. Dejarnac, J. Stockel, M. A. Pedrosa, D. Lopez-Bruna, C. Hidalgo, "Advances in Langmuir Probe Diagnostics of the Plasma Potential and Electron-Energy Distribution Function in Magnetized Plasma," Plasma Sources Science and Technology **25**, 061205 (2018).

[152] M. Tichy, A. Petin, P. Kudrna, M. Horky, S. Mazouffre, "Electron Energy Distribution Function in a Low-Power Hall Thruster Discharge and Near-Field Plume," Physics of Plasmas **25**, 061205 (2018).

[153] T. I. Cox, V. G. I. Deshmukh, D. A. O. Hope, A. J. Hydes, N. S. Braithwaite, N. M. P. Benjamin, "The Use of Langmuir Probes and Optical Emission Spectroscopy to Measure Electron Energy Distribution Functions in RF-Generated Argon Plasmas," Journal of Physics D: Applied Physics **20**, 820 (1987).

[154] N. Bibinov, H. Halfmann, P. Awakowicz, "Determination of the Electron Energy Distribution Function via Optical Emission Spectroscopy and Langmuir Probe in an ICP," Plasma Sources Science and Technology **17**, 035004 (2008).

[155] J. B. Boffard, R. O. Jung, C. C. Lin, A. E. Wendt, "Optical Emission Measurements of Electron Energy Distributions in Low-Pressure Argon Inductively Coupled Plasmas," Plasma Sources Science and Technology **19**, 065001 (2010).

[156] A. Dwivedi, K. Hara, "Estimation of Electron Kinetics in Low-Temperature Plasmas Using Data Assimilation," Journal of Physics D: Applied Physics **58**, 175203 (2025).

[157] M. Huang, K. Warner, S. Lehn, G. M. Hieftje, “A Simple Approach to Deriving an Electron Energy Distribution from an Incoherent Thomson Scattering Spectrum,” Spectrochimica Acta Part B: Atomic Spectroscopy **55**(9), 1397-1410 (2000).

[158] T. Hori, M. Kogano, M. D. Bowen, K. Uchino, K. Muraoka, “A Study of Electron Energy Distributions in an Inductively Coupled Plasma by Laser Thomson Scattering,” Journal of Applied Physics **83**, 1909-1916 (1998).

[159] J. L. Suazo Betancourt, S. Grauer, J. Bak, A. Steinberg, M. Walker, “Bayesian Model Selection for Thomson Scattering,” Review of Scientific Instruments **95**, 043004 (2024).

[160] G. Zhuang, R. Behn, I. Klimanov, P. Nikkola, O. Sauter, “Influence of Non-Maxwellian Velocity Distributions During ECRH and ECCD on Electron Temperature Measurements by Thomson Scattering,” Plasma Physics and Controlled Fusion **47**, 1539-1558 (2005).

[161] B. C. Foo, D. B. Schaeffer, P. V. Heuer, “Recovering Non-Maxwellian Particle Velocity Distribution Functions from Collective Thomson Scattered Spectra,” AIP Advances **13**, 115328 (2023).

[162] A. L. Milder, S. T. Invancic, J. P. Palastro, D. H. Froula, “Impact of Non-Maxwellian Electron Velocity Distribution Functions on Inferred Plasma Parameters in Collective Thomson Scattering,” Physics of Plasmas **26**, 022711 (2019).

[163] J. Zheng, C. X. Yu, Z. J. Zheng, “Effects of Non-Maxwellian (Super Gaussian) Electron Velocity Distribution on the Spectrum of Thomson Scattering.” Physics of Plasmas 4, 2736-2740 (1997).

[164] Y. Y. Yamaguchi, "Nondiagonalizable and Nondivergent Susceptibility Tensor in the Hamiltonian Mean-Field Model with Asymmetric Momentum Distributions," Physical Review E **92**, 032109 (2015).

[165] F. LeBlanc, D. Hubert, "A Generalized Model for the Proton Expansion in Astrophysical Winds. I. The Velocity Distribution Function Representation," Astrophysical Journal **483**, 464 (1997).

[166] A. A. Abid, M. Z. Khan, Q. Lu, S. L. Yap, "A Generalized AZ-Non-Maxwellian Velocity Distribution Function for Space Plasmas," Physics of Plasmas **24**, 033702 (2017).

[167] J. C. Raymond, P. A. Isenberg, J. M. Laming, "Non-Maxwellian Proton Velocity Distributions in Nonradiative Shocks," Astrophysics Journal **682**, 408 (2008).

[168] A. L. Milder, J. Katz, R. Boni, J. P. Palastro, M. Sherlock, W. Rozmus, D. H. Froula, "Statistical Analysis of Non-Maxwellian Electron Distribution Functions Measured with Angularly Resolved Thomson Scattering," Physics of Plasmas **28**, 082102 (2021).

[169] L. B. Wilson III, L.-J. Chen, S. Wang, S. J. Schwartz, D. L. Turner, M. L. Stevens, J. C. Kasper, A. Osmane, D. Caprioli, S. D. Bale, "Electron Energy Partition Across Interplanetary Shocks. I. Methodology and Data Product," Astrophysical Journal Supplement Series **243**, 8 (2019).

[170] L. B. Wilson III, L.-J. Chen, S. Wang, S. J. Schwartz, D. L. Turner, M. L. Stevens, J. C. Kasper, A. Osmane, D. Caprioli, S. D. Bale, "Electron Energy Partition Across Interplanetary Shocks. II. Statistics," Astrophysical Journal Supplemental Series **245**, 24 (2019).

[171] M. J. van de Sande, "Laser Scattering on Low Temperature Plasmas: High Resolution and Stray Light Rejection," Ph.D. dissertation, (Technische Universiteit Eindhoven, 2002).

[172] M. Hoffman, P. Sountsov, J. V. Dillon, "NeuTra-lizing Bad Geometry in Hamiltonian Monte Carlo Using Neural Transport," arXiv:1903.03704 (2019).

[173] See https://num.pyro.ai/en/stable/examples/neutra.html for "Example: Neural Transport," NumPyro Documentation (2019).

[174] M. D. Hoffman, A. Gelman, "The No-U-Turn Sampler: Adaptively Setting Path Lengths in Hamiltonian Monte Carlo," Journal of Machine Learning Research **15**, 1593-1623 (2014).

[175] See https://num.pyro.ai/en/latest/tutorials/bayesian_regression.html for "Bayesian Regression Using NumPyro," NumPyro Documentation (2019).

[176] A. L. Milder, A. S. Joglekar, W. Rozmus, D. H. Froula, "Qualitative and Quantitative Enhancement of Parameter Estimation for Model-Based Diagnostics Using Automatic Differentiation with an Application to Inertial Fusion," Machine Learning Science and Technology **5**, 015026 (2024).

[177] G. Livadiotis, "Kappa Distributions: Thermodynamic Origin and Generation in Space Plasmas," Journal of Physics: Conference Series **1100**, 012017 (2018).

[178] B. Vincent, S. Tsikata, S. Mazouffre, T. Minea, J. Fils, "A Compact New Incoherent Thomson Scattering Diagnostic for Low-Temperature Plasma Studies," Plasma Sources Science and Technology **27**, 055002 (2018).

[179] J. Lopez-Uricoechea, J. L. Suazo Betancourt, N. Butler-Craig, M. L. R. Walker, "Spatially Resolved Laser Thomson Scattering Measurements in a Negative Glow and Cathode Presheath to Investigate a 1D Sheath Model," Physics of Plasmas **31**, 033503 (2024).

[180] V. A. Godyak, R. B. Piejak, B. M. Alexandrovich, "Electron Energy Distribution Function Measurements and Plasma Parameters in Inductively Coupled Argon Plasmas," Plasma Sources Science and Technology **11**, 525 (2002).

[181] S. Mazouffre, G. Bourgeois, L. Garrigues, E. Pawelec, "A Comprehensive Study on the Atom Flow in the Cross-Field Discharge of a Hall Thruster," Journal of Physics D: Applied Physics **44**, 105203 (2011).

[182] Biagi-V7.1 database, retrieved from LxCat.net April, 2026.

[183] K. Tinschert, A. Muller, G. Hofman, C. Achenbach, R. Becker, E. Salzborn, "Electron Impact Single Ionisation of Multiply Charged Krypton Ions," Journal of Physics B: Atomic and Molecular Physics **20**, 1121 (1987).

[184] R. C. Wetzel, F. A. Baiocchi, T. R. Hayes, R. S. Freund, "Absolute Cross Sections for Electron-Impact Ionization of the Rare-Gas Atoms by the Fast-Neutral-Beam Method," Physical Review A **35**, 559 (1987).

[185] M. L. Hause, B. D. Prince, R. J. Bemish, "Krypton Charge Exchange Cross Section for Hall Effect Thruster Models," Journal of Applied Physics **113**, 163301 (2013).

[186] J. Bak, A. Abbasszadehrad, A. Rekhy, C. Limbach, R. B. Miles, "Demonstration of Low Angle Thomson Scattering for Background Interference Suppression," AIAA SCITECH, AIAA 2023-1859.

[187] P. J. Roberts, “Characterization of Momentum and Heat Flow in Hall Thrusters with Laser Scattering,” Ph.D. dissertation (University of Michigan, 2025).

[188] W. Huang, B. B. Ngom, A. D. Gallimore, “Using Nonlinear Zeeman Spectroscopy to obtain In-Situ Magnetic Field Measurement in a Hall Thruster,” International Electric Propulsion Conference, IEPC-2009-088.

[189] S. Mazouffre, V. Delbosq, “Electron Parameters in the Plasma Plume of a 5 kW Hall Thruster Firing with Xenon and Krypton,” International Electric Propulsion Conference, IEPC-2024-866.

[190] F. Petronio, A. Alvarez Laguna, A. Bourdon, T. Lafluer, P. Chabert, “Hall Thruster Modeling with Multiple Simulation Techniques: Modeling Benchmarking, Fluid-Kinetic Consistency, and Experimental Validation,” Journal of Applied Physics **139**, 093303 (2026).

[191] W. Villafana, A. T. Powis, S. Sharma, I. D. Kaganovich, A. V. Khrabrov, “Establishing Criteria for the Transition from Kinetic to Fluid Modeling in Hollow Cathode Analysis,” Physics of Plasmas **31**, 093504 (2024).

[192] W. Huang, A. D. Gallimore, “Laser-Induced Fluorescence Study of Neutral Xenon Flow Evolution Inside a 6-kW Hall Thruster,” International Electric Propulsion Conference, IEPC-2009-087.

[193] F. Petronio, A. Alvarez Laguna, M. J. Guillon, A. Bourdon, “Refining the Modeling Strategy for Anomalous Electron Transport in Fluid Simulations of Hall Thrusters via Insights from PIC Simulations,” Physics of Plasmas **32**, 073513 (2025).

[194] W. Fundamenski, O. E. Garcia, “Comparison of Coulomb Collision Rates in the Plasma Physics and Magnetically Confined Fusion Literature,” EFDA-JET Report, (2007).

[195] C. M. Penney, R. L. St. Peters, M. Lapp, “Absolute Rotational Raman Cross Sections for N_2, O_2, and CO_2,” Journal of the Optical Society of America **64**, 712-716 (1974).